Strål
säkerhets
myndigheten
Swedish Radiation Safety Authority

Research

# Earthquake stationarity and distributed fault displacements, Forsmark repository site

## 2024:02

**Author:** James P. McCalpin GEO-HAZ Consulting, Inc.
P.O. Box 837, Crestone, Colorado. 81131 USA
**Date:** February 2024
**Report number:** 2024:02
**ISSN:** 2000-0456
**Available at www.ssm.se**

Strål
säkerhets
myndigheten
Swedish Radiation Safety Authority

Author: James P. McCalpin GEO-HAZ Consulting, Inc.
P.O. Box 837, Crestone, Colorado. 81131 USA

# 2024:02

# Earthquake stationarity and distributed fault displacements, Forsmark repository site

**Date:** February 2024
**Report number:** 2024:02
**ISSN:** 2000-0456
**Available at** www.stralsakerhetsmyndigheten.se

## SSM perspective

### Background and objective

Large earthquakes occur predominantly along plate boundaries. Due to this, much of the research have been directed towards this tectonic setting. Also, the general lack of seismicity data in stable continental interiors, such as the Baltic Shield, have impeded estimations, as well as the understanding, of the seismic hazard in these tectonic settings. Large earthquakes at plate margins tend to be stationary phenomena recurring at the same fault system. Observations of the recent seismicity and paleoseismic records in intraplate settings suggests a more migrating earthquake pattern (Stein et al., 2009). It has even been argued that earthquakes in stable continental interiors can occur in regions with no previous seismicity and no surface evidence for strain accumulation (Calais et al. 2016).

The proposed project will amalgamate information concerning the present understanding of the stationarity of earthquake occurrence in intraplate tectonic settings and maximum possible magnitudes. It will also compare the shear displacements on target fractures predicted by SKBs rock mechanics approach, to observed distributed fault displacements in historic earthquakes. In this comparison an assessment shall be made about the relevance of this comparison with the Forsmark site regarding the tectonic setting, geological complexity, recent seismicity and paleoseismic records. These questions are of importance for the safety analysis of radioactive waste repository since they can be used to check the reliability of SKBs assumptions regarding secondary shear displacements in relation to the distance to the primary shearing event and the presumed long term stability of the Forsmark site.

### Results and conclusions

Based on recent work by the Scandinavian geological surveys, SKB and POSIVA, we now see a pattern of large-magnitude seismicity from today back to the end of the middle Weichselian (ca. 57 ka). It appears that surface ruptures have remained in the same areas during this time, which suggests spatial stationarity and not unpredictable migration.

Digital Surface Rupture Databases containing rupture maps and dis-placement measurements, and recently-published statistical analyses of off-fault displacements were used to predict off-fault displacements as a function of distance from the Principal (coseismic, activated) fault. The prediced off-fault displacements were compared to numerical displacements, for the same earthquake magnitude and distances from the fault.

Nurminen et al. (2020) and Moss et al. (2022) (for reverse faults) and Petersen et al. (2011) present equations for distributed displacement as a function of magnitude and distance. In every case their predictions are larger, usually much larger, than the target fracture displacements predicted by SKB using the 3DEC software. Compared to the displacements predicted by Yoon et al. (2014) and Yoon and Zang (2019) using Particle Flow Code 3D v4, the empirical displacements were a closer match. The closest match was between empirical displacements and Particle Flow Code -predicted displacements on other named faults (deformation zones, not smooth fractures). This suggests that most empirical displacements in the databases represent reactivation of pre-existing deformation zones, not of smooth fractures. If this is the case, then there is no conflict between the (larger) empirical and (smaller) numerical displacements, because they are measuring different phenomena.

## Recommendations

Issue 1-Establish exactly how PFC modelling of induced displacement on other DZs (which matches empirical displacements) differs from PFC modelling of induced displacement on smooth target fractures (which underestimates empirical displacements). Is it because the DZs were assigned different geotechnical properties than the smooth joints in the PFC model? And if not that, what causes the difference?

Issue 2-Having answered Issue 1, can 3DEC modelling be similarly reconfigured to output induced displacements on DZs more in line with empirical displacements?

Issue 3-When additional PGFs are mapped in Sweden using lidar, investigators should look for possible DFs associated with the main PGF scarp. If trenching is performed, on the PGF scarp, consider also trenching the possible DF scarps. Some care should be taken: (1) lengthen the trenches away from the PF scarp to look for evidence of DFs which might have been obscured by weathering and erosion, and (2) document the type of bedrock structure that underlies any DFs. The more surface rupture data we can obtain from the Fennoscandian SCR, the less we will have to rely on analogs from other SCRs (such as Australia), which possibly might not be appropriate for use in Fennoscandia.

## Project information

Contact person SSM: Carl-Henrik Pettersson
Reference: SSM2021-3335/ 3030045-61

# SSM perspektiv

## Bakgrund och syfte

Stora jordbävningar inträffar huvudsakligen längs plattgränser. På grund av detta har mycket av forskningen riktats mot denna tektoniska miljö. Den allmänna bristen på seismicitet i stabila kontinentala områden, såsom Baltiska Skölden, har försvårat uppskattningar, såväl som förståelsen, av den seismiska faran i dessa tektoniska miljöer. Stora jordbävningar vid plattgränser tenderar att vara stationära fenomen som återkommer vid samma förkastningssystem. Observationer av nutida, historiska och paleoseismiska jordbävningar inom plattorna tyder på ett mer migrerande jordbävningsmönster (Stein et al., 2009). Det har till och med hävdats att jordbävningar i stabila kontinentala områden kan inträffa i regioner utan tidigare seismicitet och inga indikationer av ackumulerad deformation vid markytan (Calais et al. 2016).

Det föreslagna projektet sammanställer information om den nuvarande förståelsen av jordbävningars stationäritet och maximala möjliga magnituder i stabila kontinentala områden. Den jämför även SKB:s modellering av sprickrörelser med observerade förkastningsrörelser i historiska jordbävningar. Vid denna jämförelse har en värdering gjorts rörande relevansen av jämförelsen med avseende tektonisk miljö, geologisk komplexitet, nutida och dåtida seismicitet. Studien är av betydelse för säkerhetsanalysen av slutförvaret för radioaktivt avfall eftersom den kan användas för att värdera tillförlitligheten av SKB:s antaganden om sekundära rörelser i förhållande till avståndet till den primära rörelsen och Forsmarksplatsens förmodade långsiktiga stabilitet.

## Resultat och slutsatser

Nyligen utfört arbete av de geologiska undersökningarna i Skandinavien, SKB och POSIVA, visar ett mönster av seismicitet från idag tillbaka till slutet av mellersta Weichsel (ca 57 tusen år sedan) med stora skalv strax efter att inlandsisen smälte bort. Detta tyder på en rumslig stationäritet och inte oförutsägbar migration.

*Digital Surface Rupture Databases*, databaser som innehåller observationer av förkastningsbranter, och nyligen publicerade statistiska analyser av sekundära förskjutningar, användes för att förutsäga sekundära rörelser som en funktion av avståndet från den förkastning som hyser jordskalvet. De förutspådda sekundära rörelserna jämfördes med modellerade förskjutningar, för samma jordbävningsmagnitud och avstånd från förkastningen.

Nurminen et al. (2020) och Moss et al. (2022) (för reversa förkastningar) och Petersen et al. (2011) presenterar ekvationer för sekundära rörelser som en funktion av storlek och avstånd. Deras förutsägelser är större, vanligtvis mycket större, än de inducerade sprickrörelser som förutspåtts av SKB med hjälp av 3DEC-mjukvaran. De rörelser som förutspåtts av Yoon et al. (2014) och Yoon och Zang (2019) med hjälp av Particle Flow Code 3D v4 (PFC), fanns ligga närmare observationerna av sekundära rörelser. Framförallt för större spröda strukturer, dvs. förkastningar och inte enskilda sprickor, fanns matchningen mellan empiri och PFC vara som störst. Detta tyder på att de flesta observationerna som ligger till grund för databaserna representerar reaktivering av redan existerande förkastningar, inte av sprickor. Om så är fallet finns det ingen konflikt mellan de (större) empiriska och (mindre) modellerade förskjutningarna, eftersom de mäter olika fenomen.

## Rekommendationer

Fråga 1 – Etablera hur PFC-modellering av inducerade förkastningsrörelser (som matchar empiriska förskjutningar) skiljer sig från PFC-modellering av inducerad sprickförskjutning (vilket underskattar empiriska förskjutningar). Beror det på att förkastningarna tilldelades andra mekaniska egenskaper än sprickorna i PFC-modellen? Och om inte det, vad orsakar skillnaden?

Fråga 2 – Efter att ha besvarat fråga 1, kan 3DEC-modellering reproducera observerade sekundära förkastningsrörelser?

Fråga 3 – Om ytterligare postglaciala förkastningar kartläggs i Sverige med hjälp av LiDar, bör undersökningar genomföras i syfte att leta efter möjliga sekundära rörelser associerade med den primära förkastningsbranten. Om grävning utförs, överväg att även gräva ut möjliga sekundära förkastningsstrukturer. Viss försiktighet bör iakttas: (1) förläng dikena bort från den primära branten för att leta efter tecken på sekundära, och (2) dokumentera vilken typ av berggrundsstruktur som är kopplad med eventuella sekundära rörelser. Ju mer information om förkastningsbranter vi kan få från den Baltiska Skölden, desto mindre kommer vi att behöva förlita oss på analoger från andra stabila kontinentala regioner (som Australien),

## Projekt information

Kontakt person SSM: Carl-Henrik Pettersson
Referens: SSM2021-3335/ 3030045-61

# Innehåll

# Executive summary

This report addresses two questions:

(1) Is seismicity spatially stationary in Sweden and adjoining Stable Continental Region (SCR) countries?
(2) Are target fracture displacements predicted by numerical models similar in size to distributed fault displacements observed in historic surface ruptures?

Question 1 arose due papers of Stein (2009) and Calais et al. (2016) who proposed that large-magnitude earthquakes in SCRs migrate spatially in unpredictable patterns, not coincident with the more common low- and moderate-magnitude earthquakes. Based on recent work by the Scandinavian geological surveys and SKB and POSIVA, we now see a pattern of large-magnitude seismicity from today back to the end of the middle Weichselian (ca. 57 ka). It appears that surface ruptures have remained in the same areas during this time, which are also areas of high historic and instrumental seismicity. This looks more like spatial stationarity to me, not unpredictable migration.

Question 2 takes up most of the report, because it has to describe historic reverse- and strike-slip surface ruptures to non-specialists, and to explain how distributed faulting is analyzed in PFDHA (Probabilistic Fault Displacement Hazard Analysis). The complexity of Principal and Distributed surface faulting may surprise numerical modelers. Fortunately, there are now two digital Surface Rupture Databases (SURE 2.0 [Nurminen et al., 2022] and FDHI, 2021) containing rupture maps and displacement measurements, plus recently-published statistical analyses of off-fault displacements (2021, 2022). We used these data sets to predict off-fault displacements as a function of distance from the Principal (coseismic, activated) fault, and then compared them to numerical displacements, for the same earthquake magnitude and distances from the fault.

Nurminen et al. (2020) and Moss et al. (2022) (for reverse faults) and Petersen et al. (2011) present equations for distributed displacement as a function of magnitude and distance. In every case their predictions are larger, usually much larger, than the target fracture displacements predicted by SKB using the 3DEC software. Compared to the displacements predicted by Yoon et al. (2014) and Yoon and Zang (2019) using Particle Flow Code 3D v4, the empirical displacements were a closer match. The closest match was between empirical displacements and PFC-predicted displacements on other named faults (deformation zones, not smooth fractures). This suggests that most empirical displacements in the databases represent reactivation of preexisting deformation zones, not of smooth fractures. If this is the case, then there is no conflict between the (larger) empirical and (smaller) numerical displacements, because they are measuring different phenomena.

# 1. Introduction

## 1.1. Scope of this review

According to the 2021 contract between SSM and GEO-HAZ Consulting, this report has two goals:

1. Amalgamate information concerning the present understanding of the stationarity of earthquake occurrence in intraplate settings and maximum possible magnitudes, with any implications for Forsmark.
2. Compare the shear displacements on target fractures predicted by SKB's rock mechanics approach, to observed distributed fault displacements in historic earthquakes. In this comparison an assessment shall be made about the relevance of this comparison with the Forsmark site regarding the tectonic setting, geological complexity, recent seismicity and paleoseismic records.

The origin of the above goals is documented in Chapman et al. (2014, p. 8), where 2013 my recommendation for future work was as follows:

1. *Use LiDAR DEMs to confirm whether post-glacial faults exist in the same seismic source zone that contains Forsmark*
2. *If they do, use PFDHA to assess the probability and displacement of distributed faulting within the repository area (the PFDHA method also accommodates distributed faulting on both pre-existing fractures and new faults)*
3. *Compare PFDHA displacements/frequencies to those from SKB's rock mechanics approach. If they are the same, there is no problem.*
4. *Rather than predicting the return period of M>5 earthquakes from strain rates (500,000 years) and assuming that earthquake probability is uniform in space and time and can be scaled down from large areas to small ones without limit—predict it from a more traditional seismological basis. That is, define the magnitude-frequency distributions of the smaller areal seismic source zone in which Forsmark lies, during the Interglacial, Glacial Buildup/Maximum, and Rapid Deglaciation periods (as defined in SKB's Reference Glacial Model). If the M>5 earthquake rates are the same, there is no problem.*

In the nine years between 2013 and this report, several advances have been made. Relative to Recommendation #1, LiDAR surveys were performed over Sweden and Finland and interpreted by their respective geological surveys. No postglacial faults were found near Forsmark, as concluded by Öhrling et al., 2018:

”*We essentially confirmed previous assessments since no mapped landforms are clearly indicative of postglacial seismicity (i.e. glacial landforms displaced by faults) and have not unambiguously identified any glacially induced fault scarps or landslide scarps. However, two scarps require additional analyses by means of a field reconnaissance and excavation program to unambiguously determine if they are of a non- seismic origin, or not. None of these scarps are obvious or distinct in their appearance but cannot without further work be completely depreciated.*”

The two ambiguous scarps were studied further by Öhrling and Smith (2020), who concluded:

*“The sedimentological investigations together with the lack of a crack structure in the bedrock mean that we exclude that the investigated landform is caused by a triggered fault in the bedrock.*”

As to recommendations 2 and 3, they are addressed in Part 2 of this report.
Recommendation 4 is addressed in part in Part 1 of this report.

## 1.2. Detailed topics covered in this review

To accomplish the two goals above, it was necessary to update McCalpin, 2013 in several topic areas which had significant advances since 2013 (Section 2.1) However, one topic that has not changed is the definition of a Stable Continental Region (SCR) used in this report (Coppersmith, 1994). He defines an SCR as follows:

1-It is continental crust, including continental shelves, slopes, and attenuated continental crust.

2-It has no orogenic activity younger than early Cretaceous. Orogenic activity includes major magmatism, deformation, or dynamic metamorphism of basement, related to a compressional or transpressional event.

3-It has no deformed forelands of orogenic belts younger than early Cretaceous.

4-It has no major anorogenic intrusions (sufficient to overprint basement) younger than early Cretaceous.

5-It has no rifting or major extension or transtension younger than Paleogene.

In a more recent publication, Schulte & Mooney (2005) introduced the term “non-extended continental crust” to differentiate the non-extended interiors of SCRs from their rifted margins. That term was not really necessary, since almost all pre-Paleogene rifted margins are excluded by Coppersmith’s requirement #5 for SCRs. Later papers have used the phrase “non-extended SCRs”, which again is an uneccessary redundancy. The only useful thing about such terms is that they should remind us that the “non-extended” parts of most SCRs show a contemporary weak, compressional stress field (such as central USA and Scandinavia), whereas rifted margins (such as the Norwegian coast) have contemporary extensional stress fields. In Section 3.3 of this report we discuss in more detail the contact between the Fennoscandian SCR and its western rifted margin, and Forsmark’s location relative to seismotectonic zonation of the contact area.

# 2. Stationarity of earthquake occurrence in Sweden

The stationarity principle broadly states that any given geographic area (or polygon) will tend to release a certain amount of seismic energy (moment) consistently through time. Thus plate boundary areas will consistently release more annual seismic moment than plate interiors. This pattern can be observed in any map of global seismicity, regardless of the time span covered (years, decades, or centuries). Progressively more strict definitions of stationarity require the magnitude-frequency relationship (a- and b-values), and the maximum possible earthquake magnitude, within the given area be more or less constant through time. Once seismologists determine how strict their working definition will be, they can define spatial areas (seismic source areas) within which instrumental and historic seismicity is thought to be ”stationary.” The corollary is that within the boundaries of any seismic source area thus defined, the a- and b-values and the maximum magnitude are roughly fixed, and earthquakes of any given magnitude have a uniform probability of occurrence throughout the polygon. Thus, the principle of ”stationarity” permits drawing seismic source areas that can be used in Probabilistic Seismic Hazard Assessment (PSHA).

Between 2009 and 2016 two papers were published that questioned whether ”stationarity” as described above exists in Stable Continental Regions (SCRs). Instead, the authors proposed a very different paradigm of seismicity for SCRs, where the magnitude-frequency curve and maximum magnitude in an SCR zone migrate spatially within the source zone through time. If their speculations are correct, then ”normal” (uniform probability) seismic source zones cannot be defined in SCRs, which would create a huge problem in PSHA.

The conundrum was first proposed by Stein (2009), based on observations from North America:

*”The paradox arises from a series of GPS studies across the New Madrid seismic zone (NMSZ). Large (magnitude >7) earthquakes felt across the Midwest occurred here in 1811 and 1812, small earthquakes occur today, and paleoseismic records show evidence of large earthquakes about 500 years apart in the past 2,000 years. We thus expected to see strain building up for a future large earthquake, but found none. Successive studies confirm this surprising result with progressively higher precision. The most recent analysis shows that present-day motions within 200 km of the NMSZ are indistinguishable from zero and less than 0.2 mm/yr. The NMSZ is thus deforming far more slowly—if at all—than expected if large earthquakes continue to occur as they have. Hence the high strain rates required by paleoearthquakes in the NMSZ must have been transient and have ended. This observation is consistent with the absence of fault-related topography, the small deformation that has accumulated over the fault system's long life, and the jagged nature of the faults thought to have broken in 1811 and 1812. All of these indicate that the cluster of large-magnitude events in the past few thousand years does not reflect the faults' long-term behaviour.*

*Such variable fault behavior is being widely recognized in continental interiors. In many places large earthquakes cluster on specific faults for some time and then migrate to others. Some faults that appear inactive today, such as the Meers fault in Oklahoma, have clearly been active within the past few thousand years. Thus mid-continental faults "turn on" and "turn off" on timescales of hundreds or thousands of years, causing large earthquakes that are episodic, clustered, and migrating.*

*We hypothesize that this spatio-temporal variability results from interactions among the faults in a region. The faults form a complex system, in the sense that the system's evolution cannot be understood by considering an individual fault."* [Underlining added by the author]

In 2016 Calais et al. (2016) expanded on this concept:

*"Large earthquakes within stable continental regions (SCR) show that significant amounts of elastic strain can be released on geological structures far from plate boundary faults, where the vast majority of the Earth's seismic activity takes place. SCR earthquakes show spatial and temporal patterns that differ from those at plate boundaries and occur in regions where tectonic loading rates are negligible. However, in the absence of a more appropriate model, they are traditionally viewed as analogous to their plate boundary counterparts, occurring when the accrual of tectonic stress localized at long-lived active faults reaches failure threshold. Here we argue that SCR earthquakes are better explained by transient perturbations of local stress or fault strength that release elastic energy from a prestressed lithosphere.*

*As a result, SCR earthquakes can occur in regions with no previous seismicity and no surface evidence for strain accumulation. They need not repeat, since the tectonic loading rate is close to zero. Therefore, concepts of recurrence time or fault slip rate do not apply. As a consequence, seismic hazard in SCRs is likely more spatially distributed than indicated by paleoearthquakes, current seismicity, or geodetic strain rates."* [Underlining added by the author]

Between the publication of the two papers cited above, Coppersmith et al. (2012) published the landmark report on seismic hazards in the Stable Continental Region of the United States. Although they acknowledged the new concept of Stein (2009), they did not abandon the traditional PSHA method, which assumes stationarity within defined seismic source zones. They make remarks of a general nature that are applicable to the Fennoscandian Shield.

*"Sec. 5.3 Earthquake Recurrence Assessment*

*5.3.1 Smoothing to Represent Spatial Stationarity*

*The CEUS [Central and Eastern USA) SSC [seismic source characterization] model is based to a large extent on an assessment that spatial stationarity of seismicity will persist for time periods of interest for PSHA (approximately the next 50 years for engineered structures)."*

This 50-year planning period is the default in the USA, where structures built on the surface are assumed to have an average useful life of 50 years. During this planning period, the acceptable seismic hazard to a surface nuclear facility is an external event with an annual exceedance probability of $10^{-4}$ to $10^{-6}$. It is assumed in the PSHA that in 50 years there will be no significant changes in the geologic environment and in seismotectonic processes (e.g., the rate of plate tectonic motions). In contrast, the underground part of a sealed nuclear repository is planned to "function" for a planning period of ~$10^4$ to $10^5$ years, rather than $5x10^1$ years.

*"Stationarity in this sense does not mean that future locations and magnitudes of earthquakes will occur exactly where they have occurred in the historical and instrumental record. Rather, the degree of spatial stationarity varies as a function of the type of data available to define the seismic source. RLME (repeated large-magnitude earthquake) sources are based largely on paleoseismic evidence for repeated large-magnitude ($M \geq 6.5$) earthquakes that occur in approximately the same location over*

*periods of a few thousand years. Uncertainties in the locations and sizes of these events are a function of the types of data available. [...] Because the record that defines the RLME sources spans a relatively long time period and records large-magnitude events, repeated events for these sources are expected to occur within a restricted location defined by the RLME source."* [Underlining added by the author]

In other words, the authors assume that future surface-rupturing earthquakes will occur where past surface-ruptures occurred. For Fennoscandia, this assumption is equivalent to saying future surface-ruptures will occur at or near where prehistoric fault scarps exist.

## 2.1. Impacts of recent work on SCRs: Fennoscandia and USA

### 2.1.1. Recognition of preserved, pre-late Weichselian landscapes in Fennoscandia

Smith et al. (2022b) describe how pre-late Weichselian landscapes were preserved under the late Weichselian ice sheet, and how that affects PGFs.

*"During the same period that glacially induced faults were being mapped and excavated in northern Sweden, a paradigm shift in the interpretation of the region's glacial geology was underway. Following extensive mapping, coring and excavating it was demonstrated that much of the glacial geomorphology believed to date to the Late Weichselian deglaciation was in fact older (Lagerbäck, l988a, b; Lagerbäck & Robertsson, 1988). Widespread geologic evidence indicates that Early and Middle Weichselian glacial landforms have been preserved beneath at least one cold-based ice sheet with little or no erosive effect (Sigfusdottir, 2013). Landforms created during the Late Weichselian deglaciation often overlie the older landforms. The implications of these findings for glacially induced faults are twofold. First, a scarp that cross-cuts a glacial landform is not necessarily younger than the Late Weichselian deglaciation (~ 10 ka). Rather, it may only be younger than the early Weichselian (~ 80 ka). Second, if glacial landforms composed of unconsolidated sediment could be preserved beneath ice sheets, then fault scarps could be preserved beneath ice sheets.*

*The discovery of preserved glacial landscapes in northern Sweden, however, did not change the interpretation of glacially induced faults. Lagerbäck and Sundh (2008) point to a lack of evidence indicating multiple ruptures and the stratigraphic evidence from Lansjarv to suggest single ruptures occurred on all glacially induced faults during or shortly after the Late Weichselian deglaciation.*

*More recently, the availability of high-resolution digital elevation models (DEM) derived from light detection and ranging (LiDAR) data has revolutionized the way geomorphology is studied in Fennoscandia (Johnson et al., 2015). High-resolution shaded relief imagery was used in a nationwide mapping effort that refined the catalogue of scarps and scarp segments by both adding and removing features.... (Smith et al., 2014; Mikko et al., 2015).*

*DEMs also allow for detailed examination of geomorphology and cross-cutting relationships that can refine the interpretations of both the number of fault ruptures and the relative timing of the ruptures. Although based on field observations, Smith et al. (2018) use LiDAR-derived imagery to illustrate multiple ruptures of the Merasjarvi Fault. The current study [Smith et al., 2022b] expands on this work to explore evidence of multiple ruptures, differential timing of rupture on different segments, and a more prolonged period of postglacial seismicity than previously understood."*

In the following section, we describe how this last paragraph changes the ’rules of the game’ for PGFs in Fennoscandia.

### 2.1.2. Multiple slip events on postglacial faults in Fennoscandia

In the past few years the ”single-rupture hypothesis” of Fennoscandian PGFs has been questioned by multiple authors, based on both lidar geomorphology and trenching. Smith et al. (2022b) summarizes the ”new paradigm” of multiple ruptures (Fig. 2-1) on PGFs which were recognized in the 1970s, but assumed to have been created in a single, huge earthquake. New geomorphic studies using lidar DEMs show that some scarp segments on long fault zones must be of different ages, based on cross-cutting relationships with moraines, shorelines and outwash terraces. This is primary, on-fault evidence.

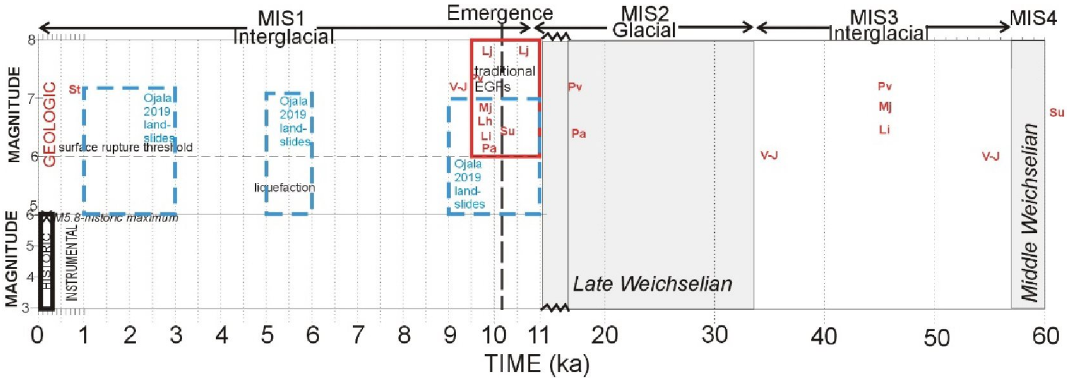

Figure 2-1. Timeline of scarp-forming events (red) on Scandinavian fault scarps, and times of earthquake-triggered (?) landslides in Finland close to scarps (blue). St, Stouragurra NO; Li, Lainio SE; Lj, Lansjärv SE; Mj, Merasjärvi SE; Pv, Pärvie, SE; Pa, Pasmajärvi FI; Su, Suasselka FI; Venejärvi–Jauhojärvi, FI. Middle Weichselian= MIS4= 57-71 ka.

Summary of named faults and their multiple events:

- Merasjärvi- 2 events post-middle Weichselian
- Lainio- 1 event post-late Weichselian, 1 event post-middle Weichselian
- Pärvie- 1 post-late Weichselian, 1 late Weichselian (sub-glacial), 1 post middle-Weichselian
- Lansjärv- post-late Weichselian, 1 pre-emergence, 1 post emergence (all above from Smith et al., 2022b)
- Suasselka- 1 early? Weichselian, 1 post-late Weichselian (Ojala a et al., 2019)
- Pasmajärvi- 1 post-late Weichselian, 1 late Weichselian (sub-glacial)
- Venejärvi–Jauhojärvi- 3 events, 1 of which was post-late Weichselian (Mattila et al 2019)

As shown in blue on Fig. 2-1, some of the evidence for middle and late Holocene earthquakes is secondary, off-fault evidence, mainly landslides. Ojala et al. (2019) summarize the evidence that these landslides are likely earthquake-triggered, while admitting ”*a seismogenic origin cannot be unequivocally established.* ” (p. 34; see also Fig. 2-2). At this time Swedish paleoseismologists have not made the same assumption and don’t include landslides in their PGF chronologies.

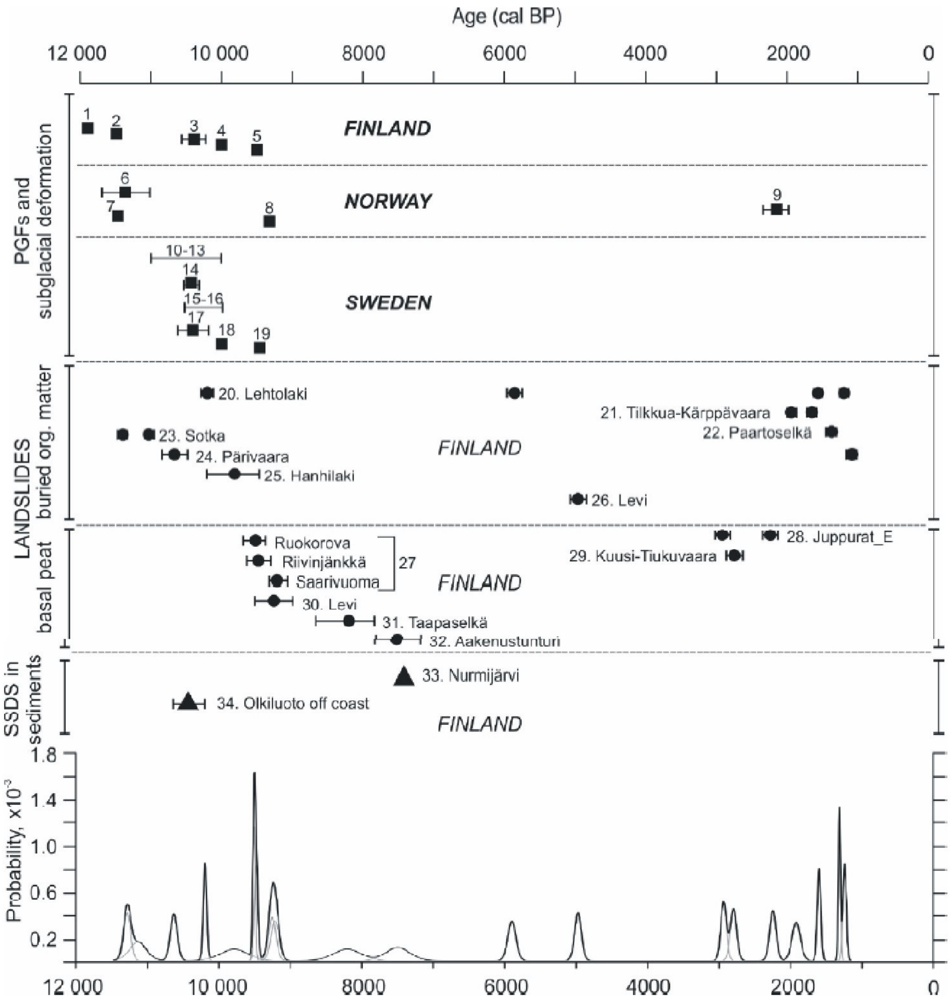

Figure 2-2. Top, calibrated radiocarbon ages on the latest movement of PGFs in Finland, Norway, and Sweden (from pre-2018 publications). Middle, calibrated radiocarbon ages on suspected coseismic landslides and soft-sediment deformation structures (SSDS) in Finland. Bottom, cumulative distribution of new landslide ages (thicker line) compared to previously published PGFs in Finland, Norway, and Sweden. From Ojala et al., 2019, their Fig. 3-3.

The ambiguity about landslide origin will remain until the ”triggering earthquakes” are confirmed by contemporaneous C-14 dates from fault trenches near the slides. Such a rigorous comparison has not yet been made in Sweden, where most of the trenching has been done, due to few dating studies on landslides. In Finland it is the opposite; the Finns have devoted much work to map and date landslides, but dug fewer fault trenches. With a more sophisticated approach to dating in fault trenches, it should be possible to test whether these landslides near PGFs are in fact coseismic.

The reason these comparative studies are important, is because they are the only sure test of several long-held hypotheses, such as the ”single-rupture hypothesis.” If PGF scarps were in fact created by multiple ruptures which involved only certain segments, those per-event scarp heights and lengths (being smaller) might fall more closely to the global averages. The more events are identified, the smaller the displacements will be, which results in shorter recurrence for smaller earthquakes. In other words, the PGF systems will begin to look more like repeating fault systems elsewhere and not merely a seismotectonic fluke unique to Fennoscandia.

### 2.1.3. The 2019 Sparta Earthquake, North Carolina, USA

On August 6, 2020 an M5.1 earthquake occurred near Sparta, North Carolina, USA. As documented by Figueiredo et al. (2022), this was the first historic coseismic surface rupture in the eastern USA. The rupture extended for ~2 km, with reverse faulting and folding creating a scarp averaging 8-10 cm high, with maximum height of 25 cm (Fig. 2-3).

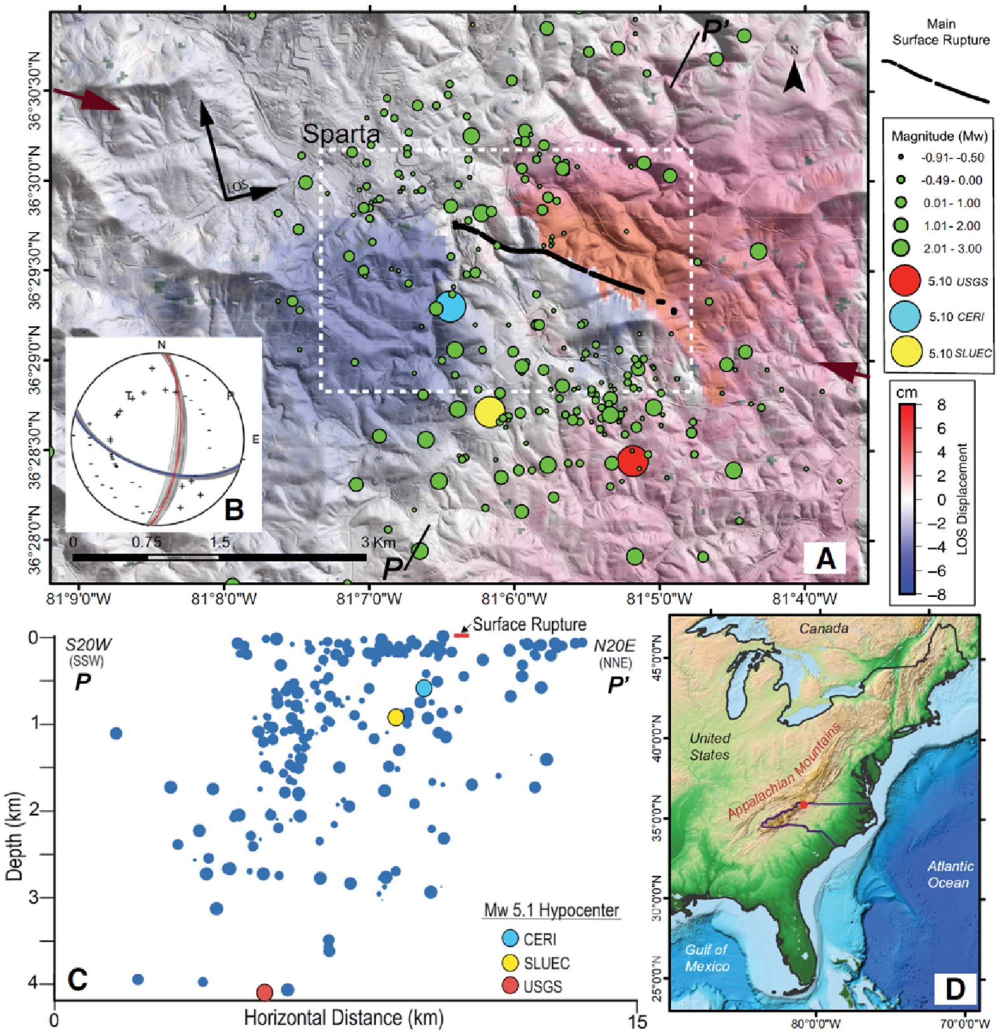

Figure 2-3. Location, earthquake sequence, and interferometric synthetic aperture radar interferogram for the Sparta earthquake. (A) Unwrapped phase interferogram overlaying a lidar-derived hillshade model with the main surface rupture (black line) and August 2020–February 2021 instrumental seismicity (circles; USGS catalog). Topographic lineament marked by brown arrows on right and left margins. Line P–P' indicates the projection plane for seismicity. (B) Focal mechanism solution (Horton et al., 2021). (C) Projection of seismic sequence (USGS catalog) into a plane with azimuth N20°E. (D) Location of the earthquake (red) in eastern North America, with North Carolina outlined. LOS—line of sight; CERI—Center for Earthquake Research and Information, University of Memphis; SLEUC—Saint Louis University Earthquake Center. From Figueiredo et al., 2022.

This earthquake and its surface rupture are relevant to Forsmark in two ways. First, it fills in the gap between low-magnitude (<M5) earthquakes that are not preserved in the geologic record, and high magnitude (M>6) surface-rupturing events. It is this gap that is causing uncertainty in characterizing Scandinavian seismicity, with its abundant small earthquakes that leave no trace, and huge endglacial surface rupturing earthquakes, but nothing in-between. The lesson of this earthquake is that if you wait long enough, earthquakes will occur in that ”magnitude gap”, and you will approach a normal frequency-magnitude relationship.

The second relevance is that this M5.1, shallow (3 km focal depth), moderately-dipping (48°-60°) reverse-fault earthquake is similar to some of the numerically-modeled earthquakes at Forsmark. As shown later in Section 3, the Sparta earthquake is just above the threshold for surface rupture, and unsurprisingly, lacks distributed faulting.

## 2.2. Previous seismic source zonation of Fennoscandia

In theory, if earthquake occurrence in the instrumental and historic periods in Fennoscandia has not been stationary, it would have been very difficult to identify seismic source zones (SSZs). However, neither the GSHAP Project or the SHARE Project (now European Seismic Hazard Model, ESHM20; see Danciu et al, 2021) reported any difficulties defining SSZs in Fennoscandia, compared to the rest of Europe. In our area of interest, the GSHAP and SHARE SSZs look very similar (Fig. 2-4). This means that two different groups of experts came to essentially the same conclusion about seismic zonation, at least for geologically ”short-term” seismicity.

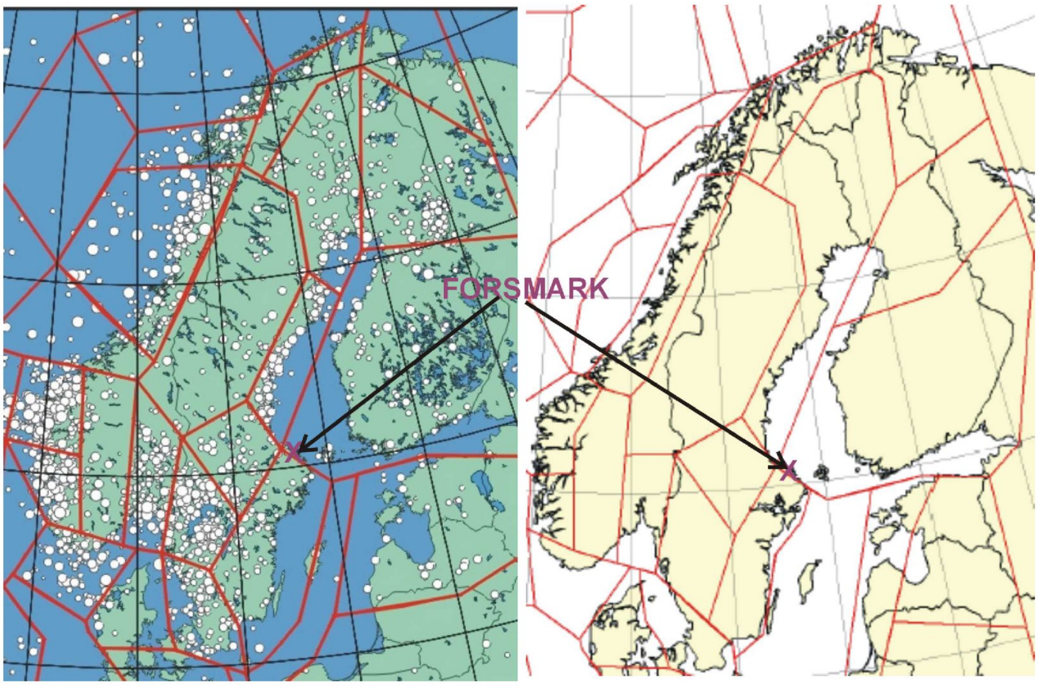

Figure 2-4. Seismic Source Zones in Fennoscandia as interpreted by the GSHAP Project (left; from Grunthal, 1999) and SHARE-ESHM20 (right; downloaded 2022; see Danciu et al., 2021). Earthquake epicenters shown by white circles. For Fennoscandia, the source catalog is described by Grunthal only as ”Institute of Seismology, Univ. Of Helsinki, 1997”. The area immediately surrounding Forsmark has essentially the same seismic source zones defined by the two different groups of collaborators.

On both maps Forsmark lies very near to the junction point of four SSZs. Forsmark lies just within the extreme SW margin of Zone 32 (see Fig. 2-5), which occupies most of southern Finland and part of the Gulf of Bothnia, with just a thin sliver of the Swedish

Coast. As seen in Fig. 2-4 (left image), Zone 32 contains widely-spread seismicity in Finland with no particular strong concentrations or lineations. The pattern is similar to that of Zone 33, which lies west of Forsmark in southern Sweden. To the south of Forsmark lies the zone containing Stockholm and the SE coast of Sweden; about half this zone is under water.

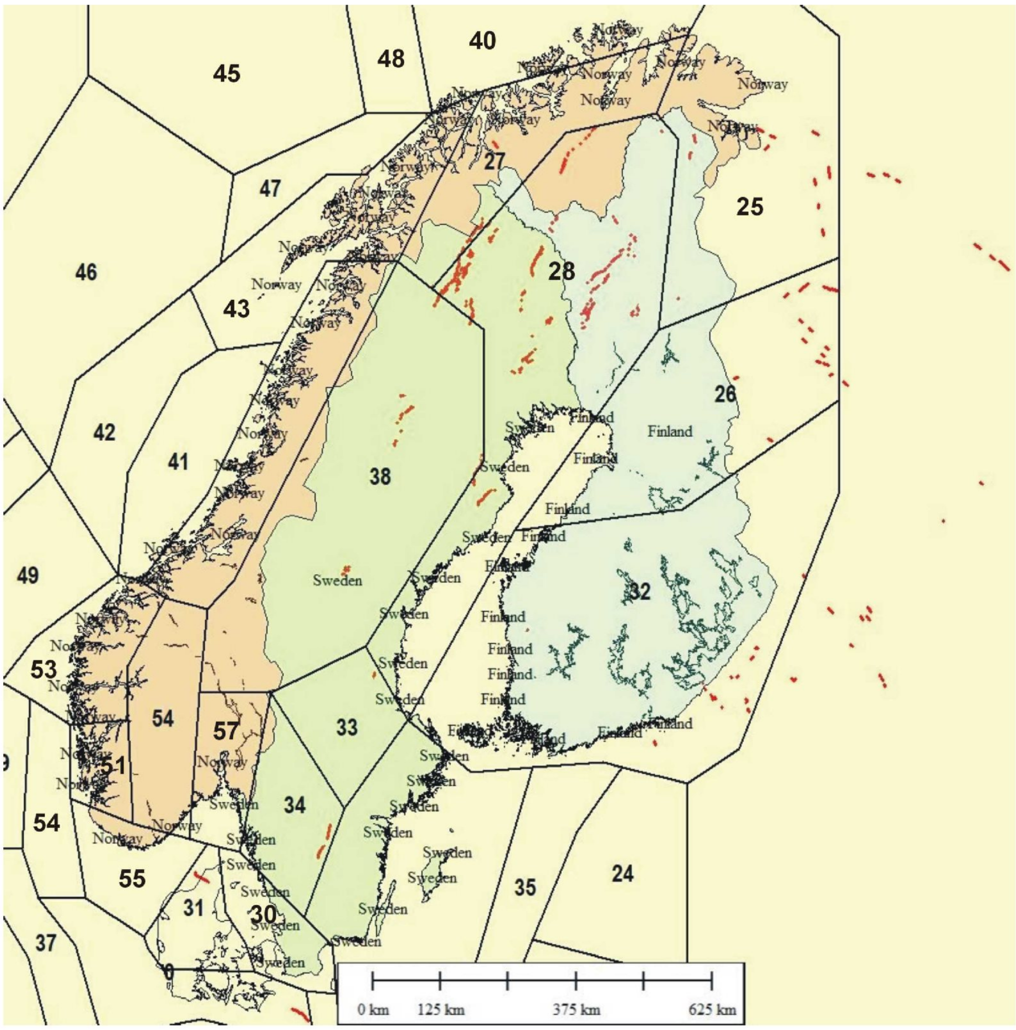

Figure 2-5. Seismic source zones and their numbers from the SHARE Project. The newer ESHM20 zones are identical but use longer ID numbers; for convenience I use the older numbers.

The historic seismic output of these three zones (32, 33, and the unnumbered one containing Stockholm) is similar, as shown by the a-values in Fig. 2-6. Zone 32 has an a-value of 2.1 (the highest of the 3), Zone 33 has the lowest a-value (1.9), and the ”Stockholm zone” is intermediate at a=2.04.

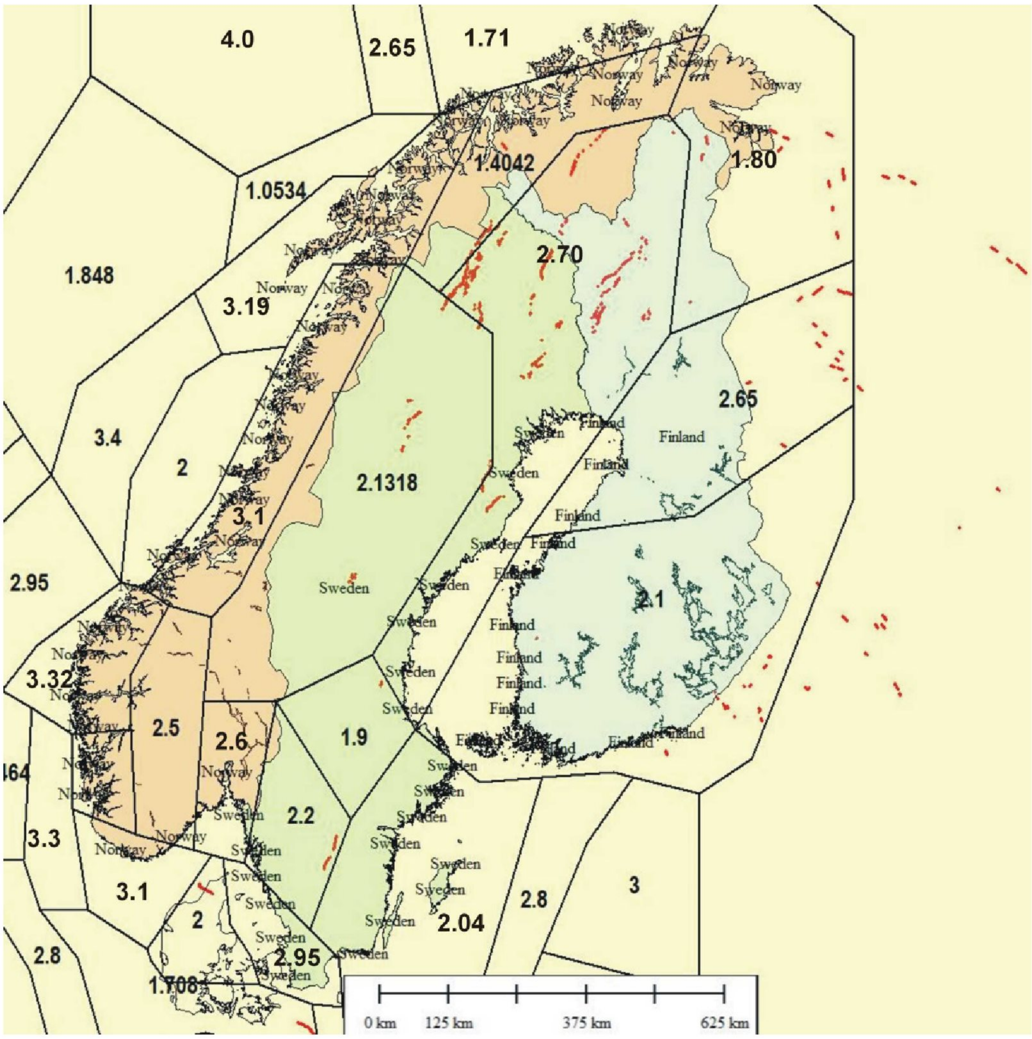

Figure 2-6. Seismic source zones and their a-intercept values on the frequency-magnitude curve. From the SHARE-ESHM20 project.

The fourth zone that nearly touches Forsmark is the active area of the Höga Kusten (Zone 28 on the SHARE map). On the SHARE map this zone extends all the way to the head of the Gulf of Bothnia and then inland, encompassing almost all of the Lapland PGFs in Norway, Sweden, and Finland. Its a-value is 2.7, the highest of all the SSZs in Sweden (Fig. 2-6), and higher than the Oslo Graben (Zone 57, a=2.6). The only SSZs with higher a-values are on the west coast of Norway.

With the boundary of seismically active Zone 28 so close to Forsmark, we should ask ourselves how confident are we about the exact location of the zone boundaries? In the old days of Seismic Hazard Assessment, zone boundaries were strictly observed, and higher (or lower) seismicity in adjacent zones was not allowed to impact the assessment. In the case where the a-values of the zones were not much different, this was an acceptable procedure. However, since Zone 28 has an a-value nearly 30% higher than Zone 32, we would want to assure ourselves that the higher seismicity of Zone 28 cannot drift over into Zone 32. In other words, is there a structural reason that the linear zone of Zone 28 seismicity is abruptly truncated just NW of Forsmark?

As discussed later (Sec. 3.3, Fig. 3-7b), Zone 28 seismicity is apparently truncated at the Singö-Eckarfjärden-Forsmark shear zone, a major tectonic domain boundary. Thus there is a structural argument for having ”hard” SSZ boundaries around Forsmark.

If this had not been the case, the potential seismicity at Forsmark might benefit from ”softer” treatment of the four zone boundaries close to the repository site. This process of ”spatial smoothing” of seismicity across SSZ boundaries is a common practice in SCR areas (e.g., Coppersmith et al., 2012), and somewhat covers the possibility that the boundaries might not be exactly correct. The latest version of ESHM20 includes a smoothed seismicity option; see Danciu et al., 2021, p.53; Nandan et al., 2022).

### 2.2.1. Longer-term stationarity considering glacial isostatic adjustments

The concept of ”stationarity” was based on patterns of seismicity from the instrumental and historic periods, i.e. 50 years to a few centuries. During that time span few seismically-active parts of the world were being affected by Glacial Isostatic Adjustments (GIA). Even those few areas affected by GIA could assume that, over a planning period of 50-100 years, the GIA rate would be essentially constant (i.e., a background process).

But at Forsmark we have to examine a different situation, where over a time span of ~100 kyr, the repository will go from: (a) its present interglacial stress condition, to (b) the next glaciation (crustal subsidence), and then (c) through the next deglaciation (crustal rebound). Our analysis above concluded that Swedish seismicity has been stationary enough in the past few centuries to permit seismic source zones to be defined. But that conclusion only supports stationarity for time span (a) above. Will the present (interglacial) seismic zones continue to generate unique moment release through time spans (b) and (c)?

As shown in Fig. 2-1, we have seismicity data for a ~50-year instrumental period (complete to M3 or 4), and a ~300 year historical period (complete to 4 or 5). Then we have prehistoric data going back to 11 ka (complete from M5.5? to M7.5 only), and a fragmentary record going back to perhaps 57 ka (end of Middle Weichselian).

The first pattern to recognize is that the zones with highest instrumental and historic seismicity (past 300 years) are also the zones containing the PGFs (ca. 9.5-11 ka) (Fig. 2-6). Even though we are uncertain about seismicity patterns in the late and middle Holocene (Fig. 2-1), it is a remarkable coincidence that the PGFs fall into today’s most active seismic regions. This is probably the strongest evidence that present SSZs will persist into the next deglaciation. And this pattern refutes the contentions of Stein (2009) and Calais et al. (2016) that surface-rupturing earthquakes in SCRs migrate randomly and unpredictably in space.

Obviously, during the rapid rebound of the deglaciation, the Mmax in the more active SSZs will increase (as it did in the past deglaciation), to produce surface-rupturing earthquakes (M>6). And the a-value will have to increase to account for the increased annual seismic moment release during the deglaciation. But will the b-values have to change? Not necessarily; larger Mmax and higher a-values could accommodate the increased seismic moment without changing the b-value.

### 2.2.2. Maximum magnitudes in Swedish SSZs

The SHARE Project SSZs (Figs. 2-5, 2-6) all have different Mmax limits, which generally take into account whether the Zone contains a PGF, and how long (or high) that PGF is.  In the top row of Table 2-1 you can see that 50% of the Swedish SSZs are assigned an Mmax of 6.4-6.6. This is roughly the threshold range for surface rupture, so was assigned to SSZs without any known PGFs. The SSZs containing known PGFs were assigned Mmax between 6.6 and 7.2, depending on PGF frequency, length, and height.

Table 2-1. Comparison of SHARE Mmax frequencies in Swedish SSZs with estimated magnitudes of the 13 PGFs in Sweden.

| Magnitudes | <6.4 | 6.4-6.6 | 6.6-6.8 | 6.8-7.0 | 7.0-7.2 | 7.2-7.4 |
|---|---|---|---|---|---|---|
| SHARE-SSZ | - | 50% | 20% | 20% | 10% | - |
| PGF | 30% | 8% | 8% | 15% | 23% | 15% |

Of the 13 known PGFs in Sweden, each has an estimated Magnitude of surface rupture based on scarp length and/or height. The frequency of these empirically-estimated magnitudes is bimodal (bottom row), with modes at M<6.4, and from M6.8-7.4. This creates an apparent mismatch in the frequencies, but only because the PGFs are not uniformly spread within each zone. For example, Zone 28 contains all the longer PGFs, whereas other SSZs may contain only a single, short PGF. Apparently the SHARE seismologists wished to be rather conservative in their Mmax assignments, so for SSZs not containing a known surface rupture, they assigned an Mmax of slightly larger than the threshold for surface faulting (M6.5±0.1). The values in Table 2-1 should be revisited by taking into account the latest papers on probability of reverse-surface faulting as a function of magnitude (e.g. Pizza et al., 2023).

### 2.2.3. Earthquake distributions in time and frequency

In SKB report TR-11-01, p. 466, it is reported that: ”*There have been few attempts to estimate the earthquake frequency for time periods relevant to SR-Site [that is, 100,000 to 1 million years]. To our knowledge, these are restricted to the ones listed in Table 10-14”.*

SKB report TR-11-01 goes on to explain how these earthquake frequencies for the 5 km-radius area were derived by dividing the frequencies of earthquakes of a given magnitude in the 650 km-radius circle, by the proportional area of a 5 km-radius circle. *“The frequencies shown in Table 10-14 were, for comparative reasons, normalised by averaging the original frequencies predicted by each estimate over the area covered by each assessment [a 650 km radius circle] and here rescaled to an area corresponding to a circle with 5 km radius. It is emphasised that estimates of anticipated earthquakes at Forsmark, based on frequencies in Table 10-14, are associated with some yet unresolved uncertainties and fundamental assumptions*.”[underlining added]

Table 2-2 (same as Table 10-14 in SKB (2011), TR-11-01). Estimated annual frequency of earthquakes ≥ M5 within a 5 km radius area. These frequencies are then divided (f) amongst the 30 local deformation zones susceptible to reactivation (see Table 10-15 and /Fälth et al. 2010/), out of the 36 deformation zones intersecting the area (Figure 10-128).

| Reference | Earthquake frequency (M≥ 5/year) for the 5 km radius area around Forsmark | f (annual frequency) |
|---|---|---|
| Böðvarsson et al. 2006 | $2.4\cdot10^{-6}$ | $7.8\cdot10^{-8}$ |
| La Pointe et al. 2000, 2002 | $8.7\cdot10^{-7}$ | $2.9\cdot10^{-8}$ |
| Hora and Jensen 2005[1] | $2.5\cdot10^{-6}$ | $8.3\cdot10^{-8}$ |
| Fenton et al. 2006[2] | $2.0\cdot10^{-6}$ | $6.8\cdot10^{-8}$ |

[1] The frequency estimates of Hora and Jensen (2005) concern earthquakes of magnitude M6 or larger. The references therein were not readily scalable to ≥ M5 but, as the slope of the logarithmic G-R relationship is close to unity (Scholz, 2002), we increased the frequencies in the Table by a factor 10 to incorporate earthquakes of magnitude M5 or larger as an approximation.

[2] In Fenton et al. (2006) frequency estimates ≥ M4.9 were provided and we choose to use the original values rather than rescaling to M5. This will slightly overestimate the frequency.

The method of calculating temporal probability of earthquakes near Forsmark, used in SKB (2011) for the next 100 kyr, rather ignored the SSZs of the original SHARE Project (2010). Now that the new ESHM20 has recalculated seismicity statistics both the traditional way and with spatial smoothing, it is probably time to ”retire” these old probabilities (Table 2-2) from 20 years ago and replace them with updated values.

Our conclusions about long-term seismicity patterns are currently limited, because the Holocene record of seismicity comes mainly from fault scarps, so only captures M>5.5 earthquakes and larger. Most postglacial scarps are now known to consist of multiple segments, but the complete rupture history of each segment is unknown. We might be able to fill in the knowledge gaps if we could prove that all landslides near PGFs were coseismic, and then simply date the landslides as has been done in Finland. But even the Finns have not performed a rigorous comparison between landslide ages and the age of the nearest fault ruptures (from scarp trenching).

### 2.2.4. Reconciling Mörner’s observed liquefaction evidence with a more uniform seismic history

Mörner (2003) hypothesized that >60 large (M7 to 8+) postglacial earthquakes caused liquefaction, soft-sediment deformation, and tsunamiites in postglacial time. This conclusion created much skepticism amongst Fennoscandian geologists and even myself (based on what I saw during the 2008 field trip prior to the International Geological Congress, when Mörner refused to explain why there were no surface ruptures). Almost all of his inferred rupture magnitudes exceeded the threshold for surface rupture (as we understood it in 2008), yet he could not explain where these ruptures were.

The new paradigm of multiple surface ruptures extending throughout the Holocene (described previously) offers an alternative explanation for the abundant secondary features observed by Mörner. Green and Bommer (2019) concluded that ”*earthquakes as small as moment magnitude 4.5 can trigger liquefaction in extremely susceptible soil deposits*.” In comparison, Pizza et al. 2023 (see our Fig. 5-11a) show that probability of surface faulting does not even rise to 50% until Magnitude reaches M7.5. What this means is, there is potentially a magnitude range spanning three magnitude units (M4.5 to M7.5), in which liquefaction can occur, but the earthquake is too small to rupture the surface and create a fault scarp. Near the epicenter such mid-magnitude, sub-rupture earthquakes could produce ground motions strong enough to cause local liquefaction and secondary deformation. For example, in an area that generated one M7.5 earthquake, it should have generated 10 M6.5 events, 100 M5.5 events, and 1000 M4.5 earthquakes. Given these numbers, it would be easy to explain Mörner’s 60 large paleoearthquakes as the result of a much larger number of smaller earthquakes, still large enough to cause liquefaction in their epicentral areas.

## 2.3. Summary of evidence for stationary seismicity in Fennoscandia

Scandinavian publications over the past 8 years (cited previously), and my interpretation thereof, seem to support the spatial stationarity of seismicity between the present and ~57ka (end of the middle Weichselian). It has been known since the 1980s that instrumental and historic seismicity clustered around PGFs. Newly-discovered PGFs have not changed that pattern. It now appears that PGFs have been active in the same locations over >50 ka.

# 3. The geologic approach to predicting distributed faulting

At present, potential earthquake-induced displacements within the Forsmark repository have been calculated in a deterministic manner, using numerical models. SKB has developed several earthquake scenarios by identifying and characterising faults favorably oriented to slip in the present and in anticipated stress field. Given the permanent slip deformation in such events, they calculate the amount of induced displacement on preexisting fractures at various distances from the principal (seismogenic) fault plane.

The SKB approach contrasts with the empirical approach used by geologists and seismic hazard analysts, called Probabilistic Fault Displacement Hazard Analysis (PFDHA). In the Section 3 we will describe the PFDHA method and apply it to the geological setting at Forsmark. Then in Section 4 we will compare the PFDHA displacements with those predicted by various numerical models, for the same set of scenario earthquakes.

## 3.1. Early development of probabilistic fault displacement hazard analysis

In its first versions PFDHA aimed mainly at predicting future surface displacement on known seismogenic faults (called ”principal faults” in PFDHA). The temporal probability of displacement was directly determined by the annual frequency (or return period) of earthquakes on the principal fault of a large enough magnitude to rupture to the surface. The spatial probability of surface displacement was determined statistically by comparison with other historic surface-rupturing earthquakes of the same magnitude (probability of surface rupture, as a function of earthquake magnitude). Assuming that surface rupture did occur, displacements along-strike on the principal fault were assessed statistically based on patterns observed in historic earthquakes of similar magnitude and slip sense.

There was little emphasis in early PFDHAs (e.g. Youngs et al., 2003 for normal faults; Petersen et al. 2011 for strike-slip faults; Moss and Ross, 2011, for reverse faults) on secondary faulting that occurred away from the trace of the Principal (or Primary; Fig. 3-1a) seismogenic fault (PF), because the database of historic surface ruptures contained very little data on secondary faulting. Prior to the 1980s most historic rupture maps did not show secondary faults at all. Once they began to be shown, only the larger ones would be mapped, and only rarely were displacements measured on them. This situation changed in the 2000s with the advent of lidar, which eased mapping of even small-displacement secondary faulting. Together with drone imagery and InSAR, by the 2010s displacements could be measured or estimated for even small secondary faults. This new data has revolutionized PFDHA by adding enough measurements on these secondary faults to permit their statistical characterization.

The International Atomic Energy Agency (IAEA, 2021) recently wrote this about characterizing secondary faulting:

” *Besides primary ruptures, historical and certainly many recent events show the occurrence of off-fault deformation and faulting on connected segments, such as splays, parallel branches or other structurally connected-to-primary fault segments. The displacement amount on these off-fault ruptures is generally less than on the primary fault and the continuity of the segments is normally reduced on those so-called ‘secondary’ ruptures. During large events, minor displacements (several mm to several cm) of tectonic origin might also occur along mapped faults at large distances, on clearly* *non-connected strands. Hosted on segments without any structural relationships with the primary fault, the slip events are suspected to occur on faults that are close to failure. These remote ruptures are suspected to have been 'triggered' by seismic waves or strain. Triggered aseismic faulting occurred on historically active faults of southern California after the 2010 Mw 7.2 El Mayor-Cucapah earthquake in northern Mexico, at distances exceeding 100 km. Petersen et al. (2011) were the first to separate the two kinds of off-fault distributed rupture in their dataset. These authors defined triggered rupture when it occurs at a distance of more than 2 km from the main (primary) fault. The corresponding data were not included to derive empirical regressions of off-fault displacement with distance. As stated in Petersen et al. (2011): "adjacent faults are an important source of fault-rupture hazard and should be considered in the analysis"; and they need to be considered separately because they respond to different processes than typical secondary faulting."*

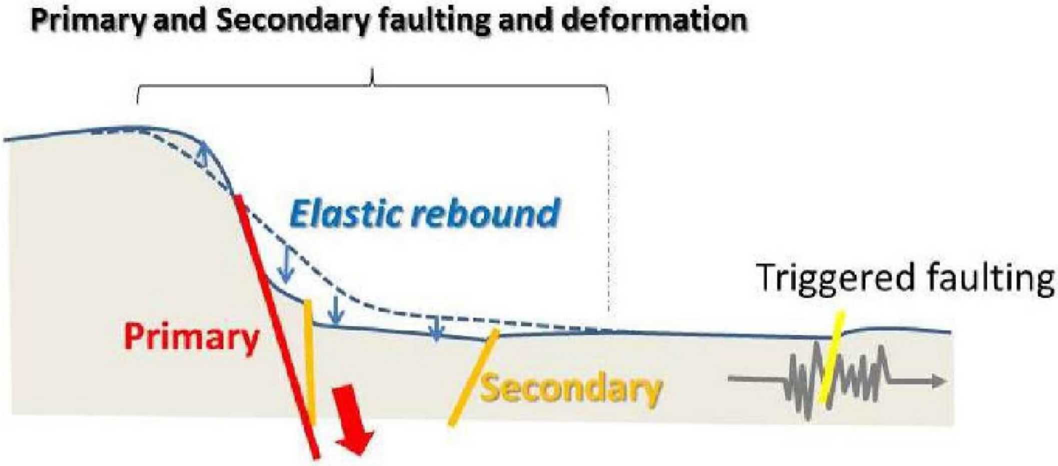

*Figure 3-1a. Schematic diagram illustrating how and where secondary (orange lines) and triggered rupture (yellow line) can occur off the principal fault, for the case of normal faulting. From IAEA, 2021.*

IAEA (2021) continues:

” *With a dipping principal fault, it has been observed that the rupture generally propagates into the hanging wall block and creates distributed faulting like during the 1999 Mw 7.7 Chi-Chi earthquake in Taiwan.... (Kelson et al., 2001). Fault geometry at depth, similarly to near surface, largely controls surface-faulting pattern and the most striking cases are those occurring on shallow faults with very low dip in compressional flat-and-ramp tectonic environments....Principal fault changes in strike or continuity (bends, step-over) usually induce slip transfer across these discontinuities leading to rupture complexity: this is clearly shown by cases like the 1954 surface wave magnitude (Ms) 6.8 Dixie Valley, Nevada earthquake (USA) (Caskey et al, 1996). For building a worldwide database, the along-strike structural pattern of a principal fault is a parameter that can control surface rupture because faulting is much more distributed at fault tips, stepovers, bends and other geometric irregularities (simple vs complex ruptures, e.g. 2010 El Mayor-Cucapah earthquake; Fletcher et al, 2014). To account for this, it is suggested to include the location of the site with respect to structural entities of the principal fault in future databases: a regular site is near a linear, well-defined portion of principal fault; and a complex site is located in stepovers, relays or bends, within a fault gap or at a fault tip.”*

NOTE: at present neither the SURE 2.0 or FDHI databases contain such an attribute field, unfortunately.

Consider this example of modern data collection on a surface rupture. After the 2016 M6.6 Norcia earthquake in Italy, field surveys on the ground plus lidar and drone measurements totalled 5200 surface displacements, roughly half of which were on distributed faults (Fig. 3-1b).

In this report we generally follow the IAEA definitions, with a few exceptions. We disagree with the strict requirement that all secondary faults more than 2 km from the principal fault (PF) should be treated as ”triggered faults”, as done by Petersen et al. (2011) for strike-slip faults. Strike-slip faults normally dip very steeply to vertical. But as shown later, it is easy for low-angle faults (such as reverse/thrust faults) >2 km from the PF to be directly connected to the PF at depth. Direct connection would make them secondary faults, as shown in Fig. 3-1a, not triggered faults (which are not physically connected to the PF).

Second, recent papers use the term ”secondary faulting” to cover ”distributed faulting” and ”triggered faulting”, the former divided into multiple sub-classes depending on rupture type. The classification scheme as applied to reverse faults is shown below (from Nurminen et al., 2020):

- -Principal (seismogenic) Fault (Rank 1)
- -Secondary Faults
    - -Triggered Faults (Rank 3)
    - -Distributed Faults
        - -Primary distributed faults (backthrusts and sympathetic thrusts (Rank 1.5)
        - -Simple distributed faults (Rank 2)
        - -Bending-moment faults (Rank 21)
        - -Flexural-slip faults (Rank 22)

### 3.1.1. New research in distributed faulting, 2013-2021

Subsequent to McCalpin, 2013 there has been great improvement in characterizing distributed faulting in PFDHA, in many different tectonic settings, as seen below:

- All fault types: American Nuclear Society, 2015; Baize et al., 2020 (SURE 2020 surface-rupture database); Sarmiento et al., 2021 (FDHI global surface-rupture database); IAEA, 2019, 2021, 2022; Nurminen et al., 2022 (SURE 2.0 surface-rupture database); Takao et al., 2013, 2014, 2016.
- Dip-slip faults: Nurminen et al., 2020
- Normal faults: Ferrario and Livio, 2021
- Reverse faults: Moss et al., 2013; Boncio et al., 2018; Nurminen, 2018; Nurminen et al, 2020; Moss et al, 2022.

Some of these publications characterize only the probability of distributed faulting (e.g., Moss et al., 2011); and some characterize only the width of surface rupture zone (WRZ) but not displacement (e.g. Boncio et al, 2018). More recent papers characterize both probability and displacement as a function of distance away from the PF (e.g. Nurminen et al, 2020, 2022; Moss et al., 2022).

Most post-2013 papers on distributed faulting have characterized only one type of fault (reverse, normal, and strike-slip). This follows the earliest characterization of principal surface ruptures by Wells and Coppersmith (1994), who showed that empirical scaling relationships between earthquake magnitude (Mw), surface rupture length (SRL), average displacement (AD), and maximum displacement (MD) were very different among fault types. Fig. 3-2 shows how different the patterns of distributed faulting can be between normal, reverse, and strike-slip faults.

Because the Fennoscandian Shield is dominantly under compressive stress, and all postglacial fault scarps in Scandinavia are reverse faults, early numerical models mainly simulate activation of low-angle reverse faults in and near the repository. The latest models however (Yoon and Zang, 2019) activate vertical faults in addition to low-angle faults. This affects how we make our comparison with the appropriate historic surface rupture data sets, as explained in the next section.

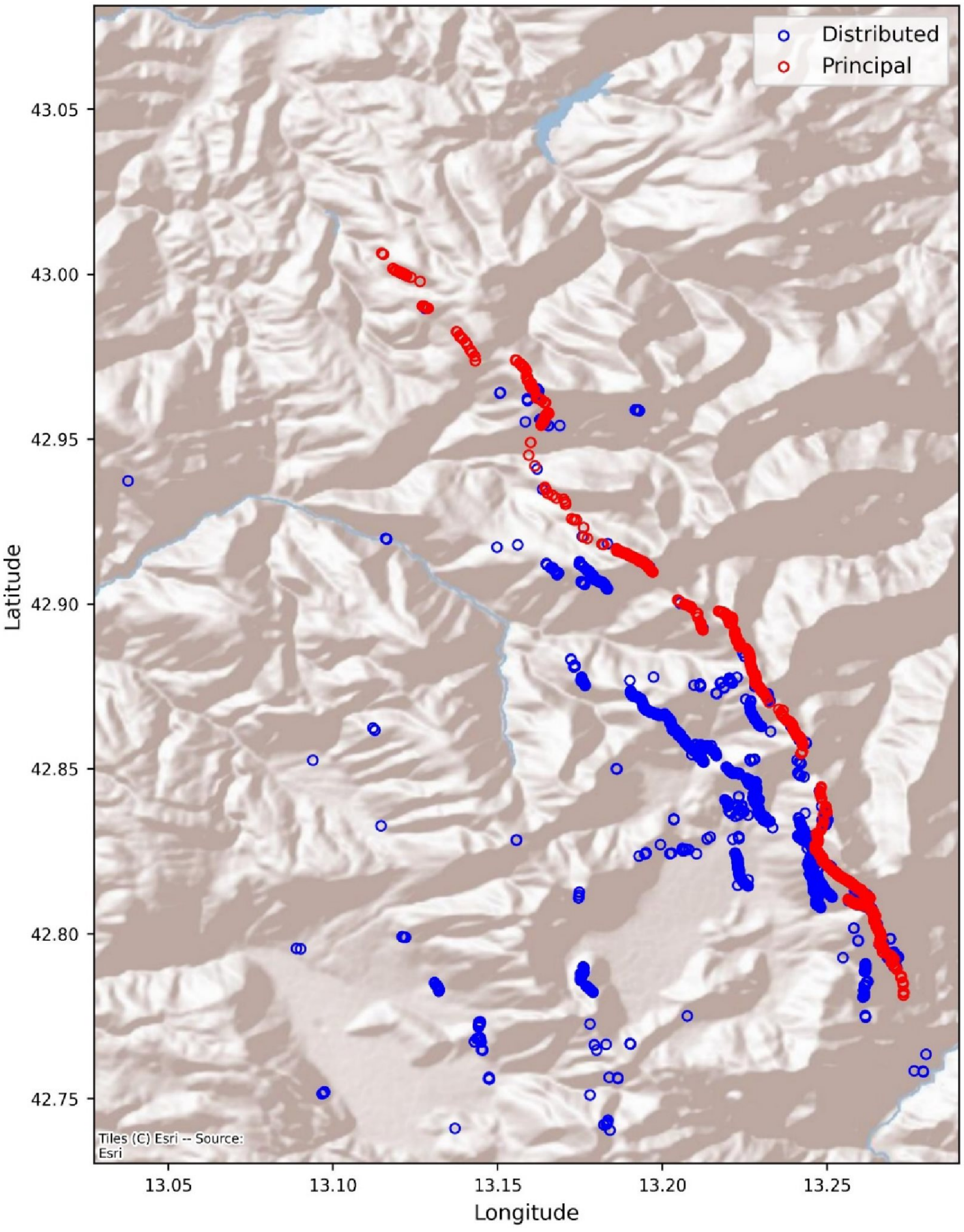

Norcia3, EQ_ID=23
Meas. Group: 23_01

*Figure 3-1b Map of surface ruptures from the 2016 M6.6 Norcia earthquake, Italy, showing locations of the 5200 displacement measurements. Red, on the principal fault; Blue, on distributed faults. In most areas there are so many overlapping open circles, that the measurement points appear as a solid red or blue line on the map. From Sarmiento et al., 2021*

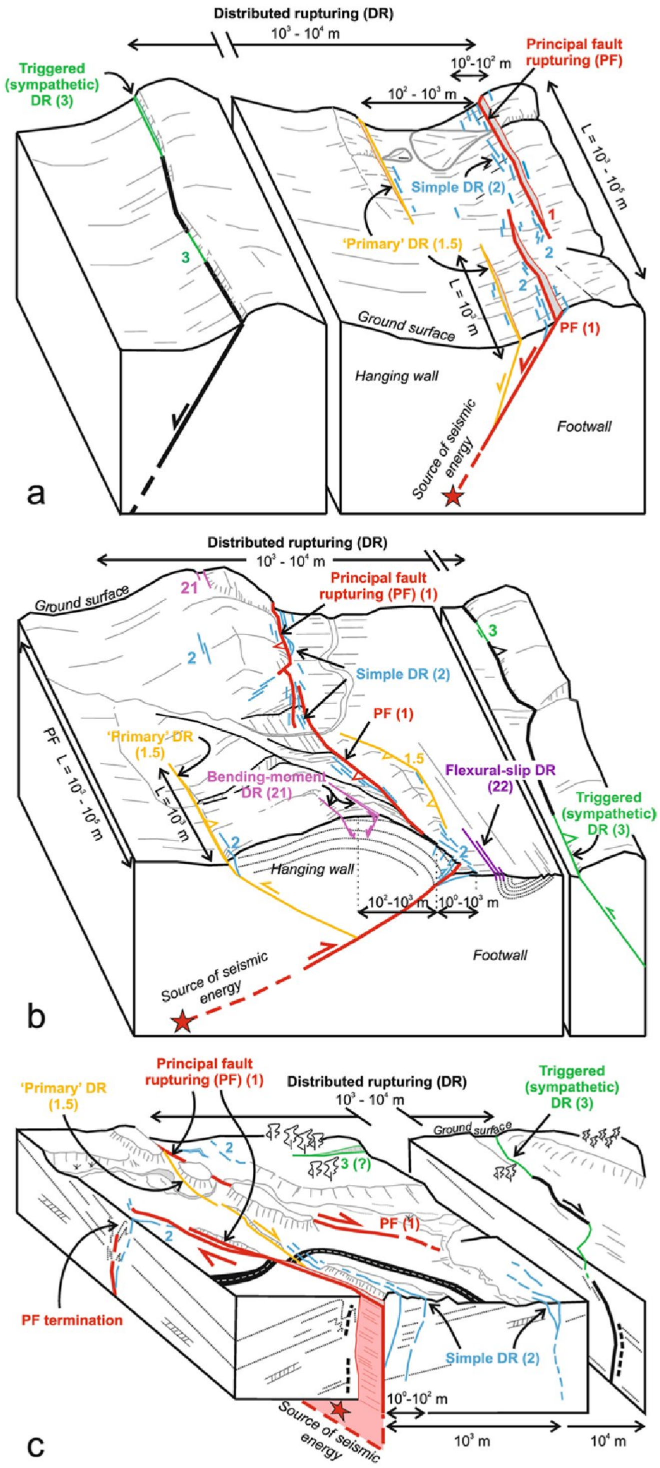

*Figure. 3-2. Schematic illustration of fault ranking for (a) normal, (b) reverse, and (c) strike-slip faults. Principal fault (rank 1) is the surface expression of the fault responsible for the earthquake, the other ranking categories refer to various types of distributed rupturing present in different kinematic settings. Primary distributed rupturing (rank 1.5) refers to distributed rupturing along a pre-existing fault that is connected to the principal fault in depth. Simple distributed rupturing (rank 2) is the most common type of distributed rupturing, occurring in unpredictable locations. Triggered rupturing (rank 3) occurs along a pre-existing fault that is not directly connected to the principal fault. Bending-moment (rank 21) and flexural-slip (rank 22) rupturing are both related to large-scale folding associated to reverse faulting. From Nurminen et al., 2022.*

### 3.1.2. What types of faulting can we expect at Forsmark in the future?

Yoon and Zang (2019) contrast three stress states under which Forsmark earthquakes could occur:

1. Present day, reverse faulting stress field; "Stress Model 1, S1" (Martin, 2007);
2. ice cover forebulge="Stress Model 1, S2": Glacially induced stress model in relation to forebulge;
3. ice cover retreat="Stress Model 1, S3", Stress model in relation to the ice cover retreat (deglaciation).

In each of these idealized stress states the relative magnitude of the two horizontal and one vertical stress components are assumed to vary, but their orientation would remain the same. Table 3-1 lists the seven earthquake scenarios for which Yoon and Zang computed fracture displacements, which we will compare in Section 4 to empirical distributed fault displacements.

Yoon and Zang 2019 (and prior SKB reports) chose to model reactivations of faults which, in their opinion, were favorably oriented in the current and future stress fields to experience coseismic slip. The faults fall into two categories: low-angle faults that strike 080°-082°, and vertical faults that strike 116°-120°. The low-angle faults strike perpendicular to the maximum horizontal stress (SH, 145°), making them favorable to activation as reverse faults (Fig. 3-3). The vertical faults strike ~30° away from the strike of SH, making them susceptible to reactivation as conjugate, right-lateral strike-slip faults (red fault in Fig. 3-3). There do not appear to be any mapped fault sets at Forsmark with a strike near to the other possible conjugate set (175°, blue fault on Fig. 3-3.)

In Fig. 3-3 the green lines with triangles represent potential reverse faults striking perpendicular to SH. The blue and red lines represent conjugate strike slip faults, striking 30° to right and left of the SH direction, with the blue (left-lateral) fault at azimuth 175°, and the red (right-lateral) fault at azimuth 115°. Low-angle (22°-45°dip) faults such as ZFMA1, 2, and 3 strike near to 55° and are prone to reactivation as reverse faults. Vertical faults such as ZFMWNW0809A and ZFMWNW0001 (Singö fault) strike near to 115°and are prone to reactivation as right-lateral strike-slip faults.

In the past 4 years two surface-rupturing earthquakes of M6.4-7.1 have occurred where Shmax is oriented roughly N-S, but they were not expressed as reverse faults perpendicular to Shmax. Instead, they were nearly-simultaneous ruptures on two faults nearly perpendicular to each other (a conjugate fault set) and were strike-slip ruptures. These were the 2019 Ridgecrest, USA ruptures (M6.4 on July 4, M7.1 on July 6; DuRoss et al., 2020), and the M6.4 Petrinja, Croatia earthquake (December 29, 2021; Markusic et al., 2021). These mid-magnitude ruptures on strike-slip faults are the hardest to preserve in the geologic record, due to their small displacements (a few decimeters) and lack of vertical relief across the rupture. Weathering and erosion can remove the surface evidence in just a few years. They are the geomorphic opposite to the long and high reverse-fault scarps in Fennoscandia. If such ruptures had occurred in Sweden at the endglacial, they would be impossible to detect today.

In the following sections we describe how distributed faulting has occurred in historic reverse and strike-slip faults, and how fault analysts have devised methods for predicting the probability of occurrence, and displacement on secondary (distributed) faults away from the activated (Principal) fault.

Table 3-1. Earthquake scenarios used in Yoon and Zang, 2019, their Table 8-7. SSM report 2019-15.

| Model[1] | In situ stress[2] | Primary Fault | RA[3] (km$^2$) | Fault Strike | Fault Dip[4] | Sense of Slip | Median Fault Slip (m) | Earthquake Moment Magnitude |
|---|---|---|---|---|---|---|---|---|
| LSM | Present day | ZFMWNW0809A | 11.42 | 116° | 90 | SS | 0.35 | 5.39 |
| LSM | ice cover forebulge | ZFMWNW0809A | 11.42 | 116° | 90 | SS | 0.15 | 5.14 |
| RSM | Present day | ZFMWNW0001<br>(Singö fault) | 55.14 | 120° | 90 | SS | 0.72 | 6.05 |
| RSM | ice cover forebulge | ZFMWNW0001<br>(Singö fault) | 55.14 | 120° | 90 | SS | 1.03 | 6.15 |
| RSM | Present day | ZFMA2 | 18.34 | 080 | 24 | R | 0.32 | 5.50 |
| RSM | Present day | ZFMA3 | 31.48 | 082* | 22 | R | 0.44 | 5.75 |
| RSM | Ice cover retreat | ZFMA3 | 31.48 | 082* | 22 | R | 0.63 | 5.85 |

[1] LSM, local scale model; RSM, regional scale model

[2] Present day=reverse faulting stress field; “Stress Model 1, S1” (Martin, 2007); ice cover forebulge=“Stress Model 1, S2”: Glacially induced stress model in relation to forebulge; ice cover retreat=”Stress Model 1, S3”, Stress model in relation to the ice cover retreat (deglaciation).
in front of the ice cover (glaciations);

[3] Rupture Area

[4] in degrees

* Yoon and Zang (2019, their Table 4-2) list strike as 046, but their Fig. 4-3 shows strike to be 082, essentially the same as ZFMA2.

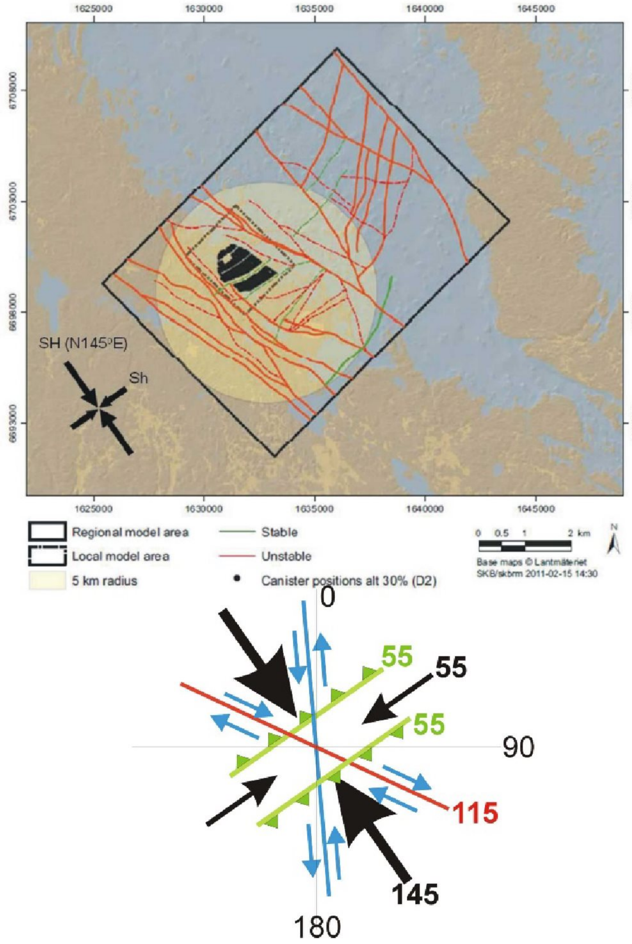

*Figure 3-3. Top half, Stable (green) and unstable (red) deformation zones at Forsmark and the orientation of maximum (SH, azimuth 145°) and minimum (Sh, azimuth 55°) horizontal stresses today at the depth of the repository (modified after SKB, 2011). From Yoon and Zang, 2019, their Fig. 3-4. Bottom half, favorable orientation of faults in the given stress field. See text below.*

### 3.1.3. Reverse earthquakes and their surface expression

Fig. 3-4 is a composite diagram showing all the different ways that surface rupture has occurred in historic reverse-faulting surface ruptures. Obviously most surface ruptures do not display all of these secondary rupture types. Probably the most common secondary ruptures are close to and parallel to the Principal (seismogenic) fault (PF). These are the ”simple DRs” (distributed ruptures) that are short and discontinuous, and decrease rapidly away from the PF. The origin of simple DFs is not always clear. In some cases it appears that simple DFs must project downward to intersect the PF, and thus are subsidiary faults that move along with the PF. In other cases simple DFs might be purely superficial, ”rootless” features created by violent shaking of the regolith and unconsolidated deposits. In most cases there are not good enough vertical exposures to determine the structural origin of every simple DF. The assumption is that most of them were created by slip on underlying bedrock faults.

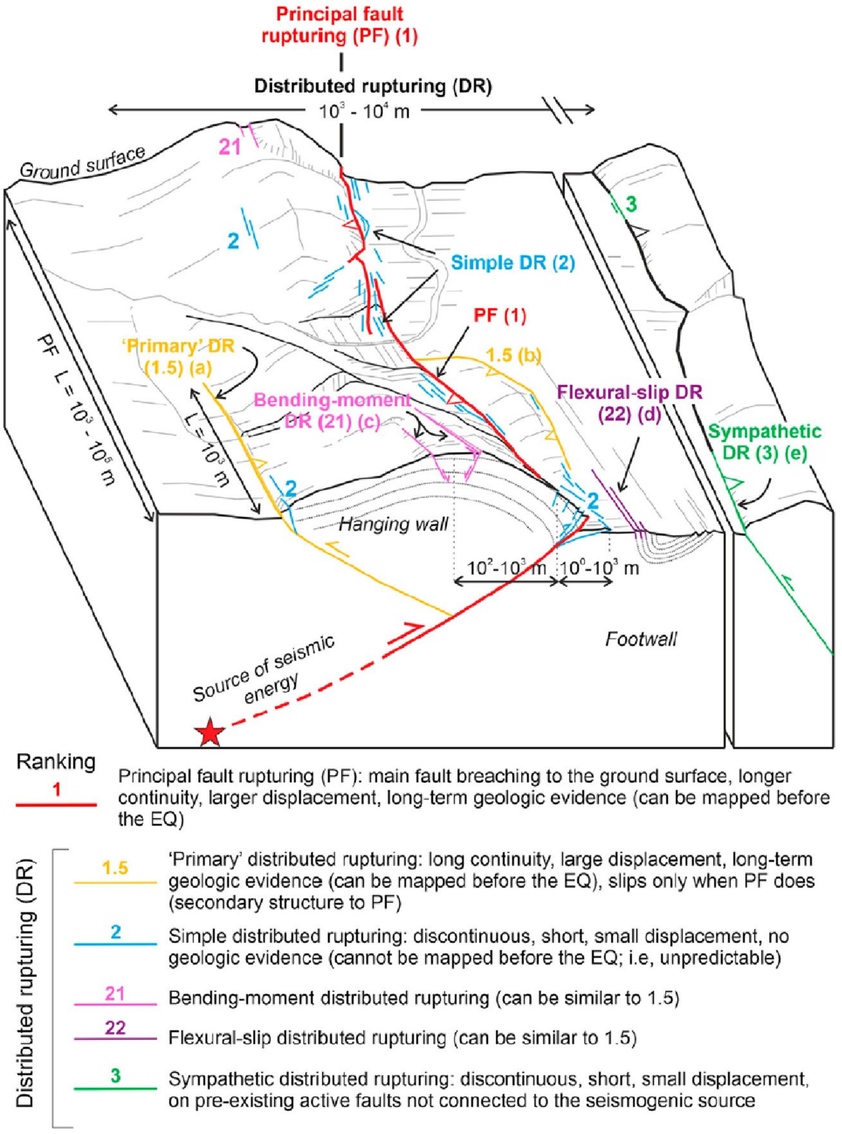

Figure. 3-4. Original caption of Nurminen et al, 2020, Supplementary Figure S1. *"Schematic illustration of fault ranking for reverse faults. Principal fault rupture (1) is the surface expression of the fault responsible for the earthquake, the other fault types being various kind of off-fault rupturing. Primary distributed rupturing (1.5) refers to the pre-existing faults that are connected to the principal fault in depth. These, however, rupture only together with the PF. Simple distributed rupturing (2) is the most general case of off-faulting, referring to the surface rupturing on unpredictable locations (not pre-existing faulting, or hidden small pre-existing faults). Bending-moment (21) and flexural-slip (22) rupturing are both responses to large scale folding. Sympathetic rupturing (3) occurs along a pre-existing fault that is triggered usually for rather discontinuous rupturing. Complex DR inspired by (a) Tsauton back-thrust and (b) Tsauton frontal synthetic splay of Chi 1999 rupture (Ota et al., 2007); (c) central zone (normal faults at extrados of folds in the hanging wall of the main thrust), (d) northern zone (bedding plane slips in the sub-vertical limb of a footwall syncline), and (e) distant ruptures east of central zone of El Asnam 1980 rupture (Philip and Meghraoui, 1983)."*

Fig. 3-4 comes from a breakthrough paper appeared by Nurminen et al. (2020), based on the 2018 thesis of Fiia-Charlotta Nurminen of the Oulu Mining School, University of Oulu, Finland. The 2020 paper was a refinement of her thesis carried out under her supervisor Paolo Boncio at University "G. d'Annunzio" of Chieti-Pescara, Chieti, Italy. This paper laid out a new classification scheme for distributed faults formed in reverse surface ruptures, following previous naming conventions from structural geology (Fig. 3-4). Starting with Rank 1 for the PF, DFs are divided into Rank 1.5 (”primary distributed ruptures”) which splay off the PF at depth, including backthrusts into the hanging wall [HW] and sympathetic thrusts into the footwall [FW]; Rank 2 (”simple distributed ruptures”), discontinuous, short, small-displacement fractures and scarplets which may or may not be connected to the PF; Rank 21, bending-moment faults (normal faults in the HW); Rank 22, flexural-slip ruptures caused by folding and bedding-plane faulting on the FW; and Rank 3, sympathetic distributed ruptures not connected at the surface or in the subsurface to the PF.

Using this ranking scheme, Nurminen et al. analyzed many historic reverse ruptures as contained in the SURE 1.0 database of Baise et al (2021). They derived empirical equations for the probability of various types of DFs, and the displacement on DFs as a function of: (a) closest distance to the PF, (b) displacement on the PF at its closest point, and (c) earthquake magnitude. These equations were made based on a subset of ”simple reverse ruptures” containing only ranks 1 and 2 (and not Ranks 1.5, 21, 22, or 3).

We considered whether our comparison of empirical DF displacements with the numerical model predictions should be based on Nurminen’s simple rupture data set, or on a dataset of DFs only from Stable Continental Regions (SCRs) composed of non-extended cratons. Obviously her simple dataset would contain a larger number of data points, but most of those data points would be from surface ruptures in tectonic and geological settings very different than the Fennoscandian Shield. Her simple data set omits Ranks 1.5, 21, 22, and 3, which are most prominent in areas of thick sedimentary rocks above basement rocks. Still, most of her simple DF measurements would not be from shields in SCRs. An SCR-only dataset would appear most applicable to the Fennoscandian Shield, but there have been few historic surface ruptures in SCRs, and even fewer where DFs were measured. We ultimately decided to use her ”simple data set” equations, and then derive our own version of her Equation 6 using only SCR input data. This task required looking at the Worldwide Database of Reverse-Fault Surface Ruptures to identify ruptures in settings most like Forsmark and the Fennoscandian Shield (see following section).

## 3.2. Worldwide database of reverse-fault surface ruptures

The SURE 1.0/2.0 (Baise et al. (2021) and FDHI (2021) databases contain data from 17 and 60 historic reverse-fault surface ruptures, respectively. Table 3-2 shows the FHDI list, in which ruptures span the period 1847 to 2019 and range in estimated moment magnitude from MW 4.7 to 8.02. Most of these ruptures occurred in highly seismic plate boundary zones of continental collision (e.g., Iran), oceanic subduction zones (e.g., Japan), or strike-slip plate boundaries (e.g., New Zealand). A slight majority (31 of 60) are from active crustal settings other than Iran, with most of these from China (6), Japan (5), New Zealand (4), and USA (3; all California). Only 16 of the 60 events occurred in plate interiors where crystalline basement rocks lie at the surface and form a stable craton (or Stable Continental Region, SCR) similar to the Fennoscandian Shield. Fourteen of these ruptures were in Australia, with one each in Canada and India.

Table 3-2. Historic reverse-faulting surface ruptures contained in the FDHI database (Moss et al, 2022). None of the ruptures prior to 1968 have published displacement measurements on secondary faults. Ruptures in bold are used for the SCR data subset; focal depths are given in Table 3-7

| No. | Date | Event | Location | MW | AD[1] (m) | MD[1] (m) | Sources | Displacement Measurements[2] | | | | |
|---|---|---|---|---|---|---|---|---|---|---|---|---|
| | | | | | | | | Total | PF | PDF | DF2 | DF2+ |
| 1 | 05/08/1847 | Zenkoji | Japan | 7.4 | | 2.4 | L97 | | | | | |
| 2 | 08/31/1896 | Rikuu | Japan | 7.2 | 2.1 | 3.6 | FDHI | | | | | |
| 3 | 12/23/190 | Manas | China | 7.95 | | *5* | L97 | | | | | |
| 4 | 1/23/1909 | Silakhar | Iran | 7.2 | | *2.5* | L97 | | | | | |
| 5 | 1/3/1911 | Chon Kemin | Kyrgyzstan | 8.02 | 3.5 | 9.0 | FDHI | | | | | |
| 6 | 4/18/1911 | Raver | Iran | 6.2 | | *0.5* | L97 | | | | | |
| 7 | 5/1/1929 | Baghan | Iran | 7.51 | | *2.1* | L97 | | | | | |
| 8 | 6/17/1929 | White Creek | New Zealand | 7.89 | | *5.2* | L97 | | | | | |
| 9 | 5/6/1930 | Salmas | Iran | 7.6 | | 5 | L97 | | | | | |
| 10 | 2/2/1931 | Hawkes Bay | New Zealand | 7.89 | | *4.6* | L97 | | | | | |
| 11 | 12/25/1932 | Changma | China | 7.82 | *2.0* | 4.0 | WC94, L97 | | | | | |
| 12 | 11/28/1933 | Behabad | Iran | 6.29 | | *1.0* | L97 | | | | | |
| 13 | 4/21/1935 | Tuntzhuchio | Taiwan | 7.23 | | 3.0 | L97 | | | | | |
| 14 | 1/15/1944 | San Juan | Argentina | 7.6 | | 0.6 | L97 | | | | | |
| 15 | 1/13/1945 | Mikawa-Fukozu | Japan | 6.7 | 1.2 | 2.4 | FDHI | | | | | |
| 16 | 3/17/1947 | Dari | China | 7.89 | | *5.0* | L97 | | | | | |
| 17 | 7/21/1952 | Kern County | California, USA | 7.36 | 0.42 | 1.2 | FDHI | | | | | |
| 18 | 2/12/1953 | Torud | Iran | 6.6 | | *1.4* | L97 | | | | | |
| 19 | 12/13/1957 | Farsinaj | Iran | 6.91 | | *1.0* | L97 | | | | | |
| 20 | 9/1/1962 | Ipak | Iran | 7.4 | | *0.8* | L97 | | | | | |
| 21 | 5/24/1968 | Inangahua | New | 7.1 | | 0.52 | L97 | | | | | |
| **22** | **10/14/1968** | **Meckering** | **Australia** | **6.59** | **0.96** | **2.0** | **FDHI** | **96** | **81** | **0** | **5** | **10** |
| 23 | 7/24/1969 | Pariahuanca | Peru | 6.1 | | 0.4 | L97 | | | | | |
| 24 | 10/1/1969 | Pariahuanca | Peru | 6.6 | | 1.2 | L97 | | | | | |
| **25** | **3/10/1970** | **Calingiri** | **Australia** | **5.03** | **0.18** | **0.33** | **FDHI** | **41** | **35** | **0** | **6** | **0** |
| 26 | 2/9/1971 | San Fernando | California, USA | 6.61 | 0.47 | 1.0 | FDHI | 153 | 60 | 4 | 59 | 30 |
| 27 | 4/10/1972 | Qir | Iran | 6.8 | | *0.1* | L97 | | | | | |
| 28 | 9/6/1975 | Lice | Turkey | 6.6 | *0.5* | 0.6 | WC94, L97 | | | | | |
| 29 | 1/1/1977 | Mangya | China | 6.1 | | *0.3* | L97 | | | | | |
| 30 | 9/16/1978 | Tabas | Iran | 7.4 | *1.5* | *3.0* | WC94, L97 | | | | | |
| **31** | **6/2/1979** | **Cadoux** | **Australia** | **6.1** | **0.4** | **1.4** | **FDHI** | **54** | **38** | **4** | **12** | **0** |
| 32 | 10/10/1980 | El Asnam | Algeria | 7.3 | 1.8 | 5.0 | FDHI | 51 | 31 | | 1 | 19 |
| 33 | 6/11/1981 | Golbaf | Iran | 6.6 | | *0.11* | L97 | | | | | |
| 34 | 7/27/1981 | Sirch | Iran | 7.1 | | *0.50* | L97 | | | | | |
| 35 | 6/11/1983 | Coalinga Nuñez | California, USA | 5.4 | | *0.64* | L97 | 60 | 45 | | 15 | |
| 36 | 8/23/1985 | Wuqai | China | 6.89 | | *1.6* | WC94) | | | | | |
| 37 | 3/30/1986 | Marryat Creek | Australia | 5.7 | 0.34 | 1.1 | FDHI | 74 | 73 | | 1 | |

| | | | | | | | | | | | | |
|---|---|---|---|---|---|---|---|---|---|---|---|---|
| **38** | **1/22/1988** | **Tennant Creek 1** | **Australia** | **6.27** | **0.39** | **0.9** | **FDHI** | **64** | **58** | **0** | **0** | **6** |
| **39** | **1/22/1988** | **Tennant Creek 2** | **Australia** | **6.44** | **0.58** | **1.1** | **FDHI** | | | | | |
| **40** | **1/22/1988** | **Tennant Creek 3 (LSE)** | **Australia** | **6.58** | **0.61** | **1.8** | **FDHI** | | | | | |
| 41 | 12/7/1988 | Spitak | Armenia | 6.77 | 0.90 | 1.6 | FDHI | 17 | 17 | | | |
| 42 | 10/29/1989 | Chenoua | Algeria | 6.0 | | 0.12 | L97 | | | | | |
| 43 | 12/25/1989 | Ungava | Canada | 6.0 | *0.80* | 1.8 | WC94, L97 | | | | | |
| 44 | 6/20/1990 | Rudbar- Tarom | Iran | 7.4 | | **1.0** | L97 | | | | | |
| 45 | 8/19/1992 | Suusamyr | Kyrgyzstan | 7.2 | | *4.2* | L97 | | | | | |
| 46 | 9/29/1993 | Killari-Latur | India | 6.2 | 0.49 | 0.80 | FDHI | 12 | 6 | | 6 | |
| 47 | 9/3/1998 | Iwate (Inland) | Japan | 5.8 | 0.22 | 0.38 | FDHI | | | | | |
| 48 | 9/21/1999 | Chi-Chi | Taiwan | 7.62 | 2.6 | 9.8 | FDHI | 172 | 99 | 9 | 64 | |
| 49 | 6/22/2002 | Avaj | Iran | 6.5 | *0.7* | *0.8* | W05 | | | | | |
| 50 | 2/22/2005 | Zarand | Iran | 6.4 | | *1.0* | T06 | | | | | |
| 51 | 10/8/2005 | Kashmir | Pakistan | 7.6 | 1.5 | 7.1 | FDHI | 84 | 61 | | 3 | 20 |
| 52 | 10/10/2007 | Katanning | Australia | 4.7 | *0.17* | *0.3* | KY) | | | | | |
| 53 | 5/12/2008 | Wenchuan | China | 7.9 | 2.2 | 6.0 | FDHI | 356 | 251 | 67 | 38 | |
| 54 | 3/23/2012 | Pukatja | Australia | 5.18 | 0.15 | 0.48 | FDHI | 24 | 24 | | | |
| 55 | 10/15/2013 | Bohol | Philippines | 7.1 | 1.4 | 5.2 | FDHI | | | | | |
| 56 | 11/22/2014 | Nagano | Japan | 6.2 | 0.48 | 1.2 | FDHI | 48 | 33 | | 15 | |
| **57** | **5/20/2016** | **Petermann** | **Australia** | **6.0** | **0.25** | **0.90** | **FDHI** | **104** | **99** | **0** | **13** | **0** |
| 58 | 11/13/2016 | Kaikoura | New Zealand | 7.8 | 2.2 | 10.3 | FDHI | | | | | |
| 59 | 11/8/2018 | Lake Muir | Australia | 5.3 | *0.28* | *0.75* | KY) | | | | | |
| 60 | 11/11/2019 | Le Teil | France | 4.9 | 0.05 | 0.11 | FDHI | 22 | 12 | | 10 | |
| | TOTALS | | | | | | | 1432 | 1023<br>*71%* | 84<br>*6%* | 248<br>*17%* | 85<br>*6%* |

[1] Average displacement (AD) and maximum displacement (MD) values, in meters.

[2] PF, principal fault; PDF, primary distributed fault, Rank 1.5 of Nurminen et al., 2020; DF2, simple distributed fault, Rank 2; DF2+, distributed faults of Ranks 21, 22, and 3.

Reverse ruptures in all tectonic settings yielded 1432displacement measurements in the FDHI database, of which 1023 (71%) were on the PF. [This is the same percentage cited by Nurminen et al. (2022) for their smaller data set of 16 reverse ruptures]. Of the 417measurements on DFs, 20% were on ”primary distributed faults” (rank 1.5 of Nurminen et al., 2020); 60% on simple distributed faults (Rank 2 of Nurminen et al., 2020); and 20% on more complex distributed faults (Rank 21 [bending-moment faults], Rank 22 [flexural-slip faults], and Rank 3 [sympathetic distributed faults]).

The total number of distributed fault measurements in all FDHI reverse ruptures was 417. However, as can be seen in Table 3-2, far right columns, most of these measurements came from ruptures 26, 32, 35, 41, 48, 51, 53, and 56 which lie in active fold-and-thrust belts at plate margins. Only events 22, 25, 31, 38-40, 43, 46, 52, 54, 57, and 59 occurred in Stable Continental Regions in non-extended cratons. Unfortunately, of those 12 events in SCRs, only two (46, Killari-Latur, INDIA; 57, Petermann, AUSTRALIA) appeared to have measurements of DFs in the FDHI database, totalling 11 measurements. This was too small a number to make a statistically valid comparison with the 3DEC fracture displacements.

Therefore, we went back to the original published literature on the 12 SCR earthquakes to see if there was additional surface-rupture data. The best analogy with Fennoscandia seemed to be the 1989 Ungava rupture in the Canadian Shield, a non-extended shield currently undergoing postglacial isostatic rebound. Unfortunately, the reconnaissance study of the Ungava rupture did not identify any DFs (Adams et al., 1991). Our effort therefore shifted to the nine well-studied earthquakes in the Australian craton which ranged from M4.7 to M6.59. But before putting our reliance heavily on an analogy with Forsmark and Australia, we had to assure ourselves that the seismotectonic setting of these two areas were sufficiently similar.

## 3.3. Is the crustal setting of Forsmark similar to that of Australia?

Both Sweden and Australia are considered Stable Continental Regions (SCRs), composed of Precambrian crystalline basement rocks that have not been extended since early Cretaceous time (Johnston et al., 1994a). But is this true? This question is a critical for our study, because all historic SCR earthquakes that have ruptured the surface and have displacement measurements on distributed faults occurred in Australia. The only justification for using Australian displacement data as a proxy for future ruptures at Forsmark, would be that Sweden and Australia are very similar in geological and seismotectonic setting. If we cannot demonstrate such similarity, then we cannot use a targeted empirical SCR dataset, and would be forced to use Nurminen's predictive equations from a global dataset.

### 3.3.1. The issue of extension

Post-early-Cretaceous extension has not affected interior Australia (Harry et al., 2020), but it has affected the western parts of the Fennoscandian Shield (Atlantic margin; Redfield and Osmundsen, 2014; see our Fig. 3-5, below). Given that, did the extension extend as far eastward as the Forsmark area? Redfield and Osmundsen (2014) subdivide the Atlantic margin of the Fennoscandian Shield as follows:

*"Three distinct belts of earthquakes strike sub-parallel to the generalized line of breakup. The outermost seismic belt (SB1) marks the Taper Break (TB), or the zone of flexural coupling/decoupling between the distal (seaward) and proximal/necking (landward) domains. A coastal belt (SB2) follows the Innermost Limit of Extension, defined as the onset of 39 km-thick crystalline continental crust. An interior belt (SB3) follows the Hinterland Break in Slope, or the landward limit of the Scandinavian rifted margin. Between each belt, large portions of the necking, proximal, and hinterland domains are seismically quiescent. Evaluation of the 'Cumulative Seismic Moment' (CSMw) per unit area indicates that the release of seismic energy is asymmetric. Although some of Fennoscandia's largest seismic events occur in the dominantly Proterozoic to Archean lithosphere of the eastern craton, 80% of Fennoscandian CSMw maps to the domain boundaries of the western rifted margin. CSMw energy tends to be highest at the TB and decreases systematically towards the continental interior.* [underlining added]

*[...] Our data imply that ridge push does not contribute significantly to Fennoscandia's seismicity. Rather, we find that thin-plate bending stresses stemming from offshore depositional loading conspire with unbuttressed Gravitational Potential Energy (GPE),*

*onshore erosion, and post-glacial isostatic rebound to generate Fennoscandia's earthquakes.*

*We present a conceptual seismological model for Fennoscandia that is consistent with modern hypotheses of extended margin evolution, including post-breakup reactivation by footwall uplift in regions adjacent to sharp crustal taper. Illustrated by simple concepts of elastic thin-plate theory, the model honors our conclusion that Fennoscandian seismicity is principally the product of locally derived stress fields and that far field stress from the oceanic domain is unlikely to penetrate deeply into a hyperextended continental margin. [...]".*

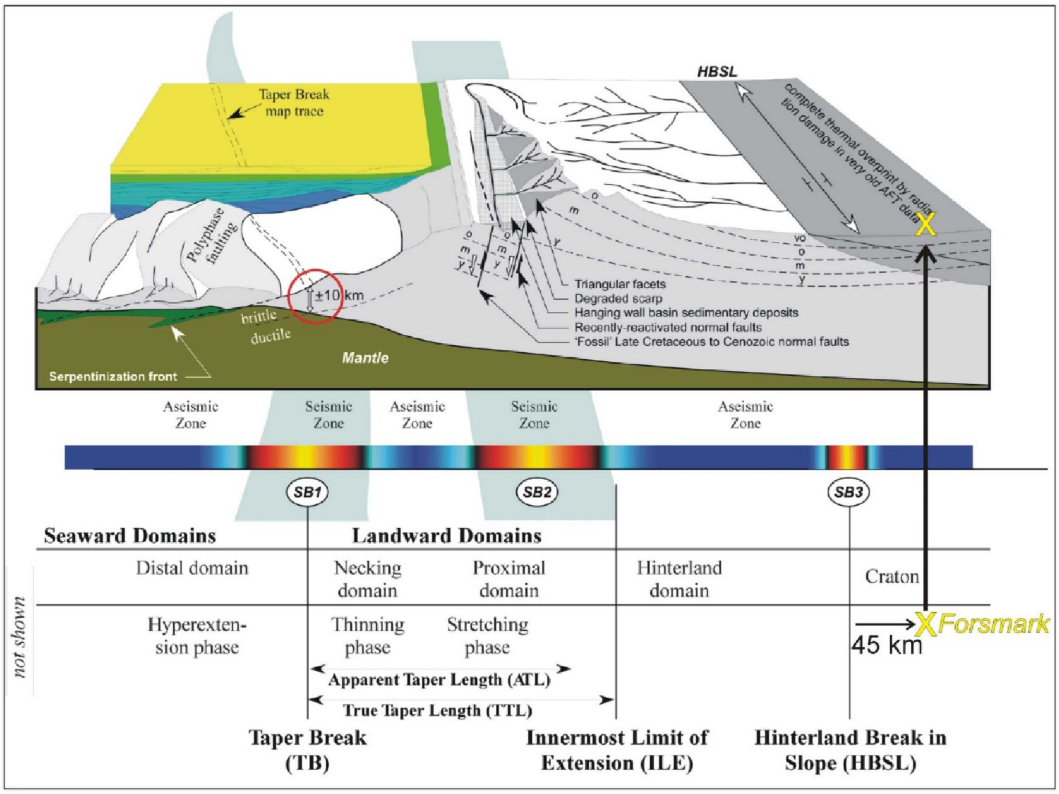

Figure.3-5. Cross-section of named structural domains and sub-domains in an extended continental margin, modeled after the Norwegian-Atlantic margin (from Redfield and Osmunsen [2014], as modified from Redfield et al. (2005a, b), Osmundsen and Ebbing (2008), Redfield and Osmundsen (2013) and Osmundsen (unpublished). Forsmark (yellow X) lies 45 km into the craton, unaffected by either direct rift faulting or by indirect footwall uplift. See details below. [Original caption of Redfield and Osmunsen, 2014, Figure 2: "*The landward domains are composed of continental crust affected by stretching-phase and thinning-phase deformation whereas the continental crust of the seaward domains was affected by hyperextension and possibly exhumation-phase deformation (not shown). The Taper Break (TB; red circle) marks the conceptual point of total crustal embrittlement during extension, and conceptually forms the boundary between the landward and seaward domains. We define the True Taper Length (TTL) to be the absolute width of the landward (proximal plus necking) domains, measured from the TB to the point where the crystalline continental crust has not undergone margin-related extension (Innermost Limit of Extension, or ILE). Commonly, the TTL can be approximated by the Apparent Taper Length (ATL), which is the distance between the TB and the escarpment crest (see text). To landward of the proximal margin lies the hinterland. The hinterland was, and remains, deformed by footwall uplift and margin related, long-wavelength, lithospheric-scale flexure controlled on the seaward end by the TB. The Hinterland Break in Slope (HBSL) marks the landward edge of the hinterland, and thus the rifted margin.*"]

In Fig. 3-5 it is difficult to locate exactly where Forsmark would be located on this cross-section, due to its cartoon nature. However, Redfield and Osmundsen (2014) included a map in their Electronic Supplement which shows the approximate location of Forsmark to be 45 km landward of the HBSL. This information was then transferred to the cross-section above. Their original map showing the trace of the HBSL is shown in Fig. 3-6.

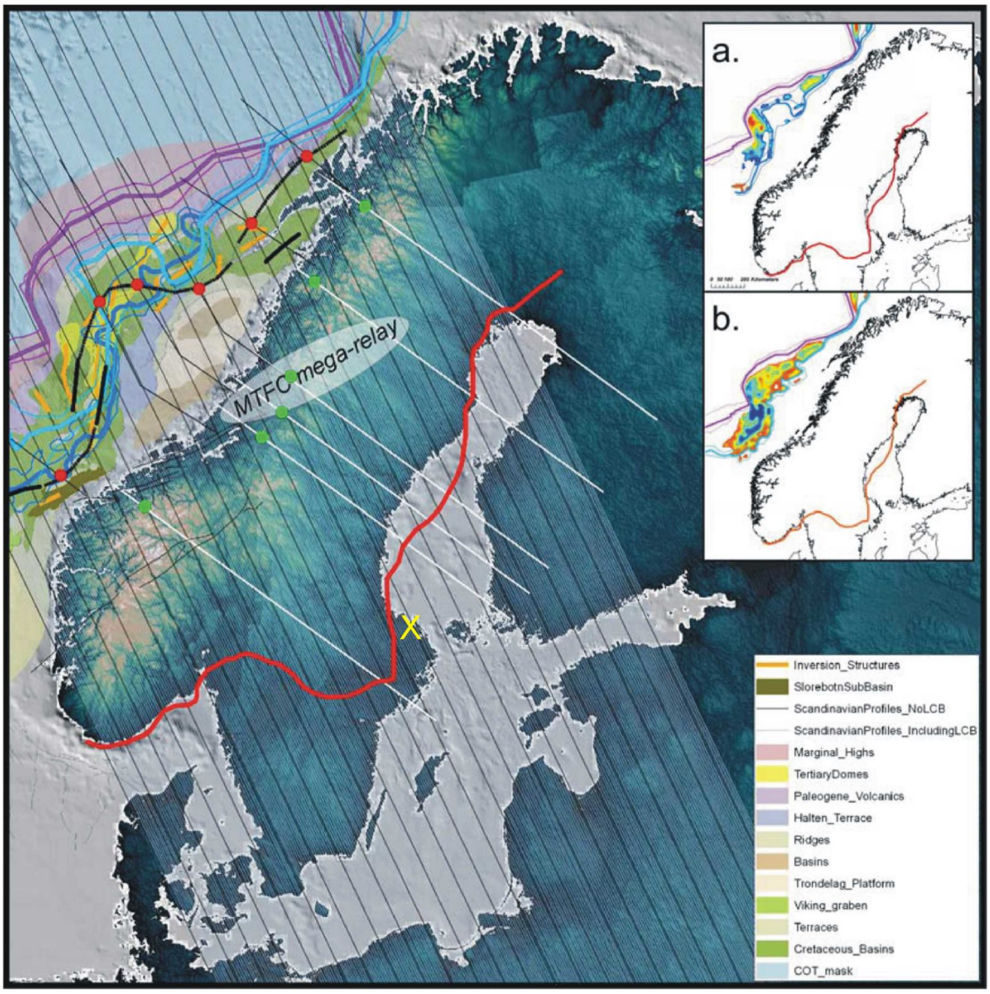

Figure 3-6. Location map of Forsmark (center of the yellow ”x”) with respect to the Hinterland Break in Slope (HBSL, solid red line). From Redfield and Osmundsen, 2014, Electronic Supplement, Figure ES-3. The HBSL marks the ”landward limit of the Scandinavian. rifted margin” (Redfield and Osmundsen, 2014, abstract). Forsmark lies roughly 45 km landward of the HBSL.*[Original caption of Redfield and Osmunsen, 2014, Electronic Supplement, Figure ES-3: ”Map representation of our 2011 and 2012 Scandinavian models. Thinnest white lines represent the location of individual profiles. Every tenth profile is shown as dark line. Inset maps show the thickness of continental crust (Osmundsen and Ebbing, 2008; Reynisson, 2010; Ebbing and Olesen, 2010) where all crust greater than 10 km has been filtered away. 2012 profiles are more COB-perpendicular. In inset (a) the Lower Crustal Bodies (LCBs) are included as "crust", whilst in inset (b) they are excluded. The Taper Break (heavy blue lines) is mapped as the first inboard instance of crust that has been reduced to 10 km thickness. The red line denotes the hinterland break-in-slope (HBSL), a pronounced topographic break in slope that is observed in Scandinavia’s hinterland on all 233 of our model’s cross sections. Also plotted are cross sections (heavy white) and Taper Break (heavy black) from Osmundsen and Redfield (2011). Red and green dots denote our 2011 TB and maximum elevations. Note that our 2011 Taper Break, drawn from interpreted geoseismic profiles (Faleide et al., 2008), is more inboard in the Lofoten and Tromsø region than that described by the gridded data cited above. Two Taper Breaks may plausibly exist, although they are not recoverable in the gridded data.”]*

Based on the data above, we conclude that Forsmark lies in the unextended part of the craton, similar to the Australian historic surface ruptures.

### 3.3.2. The issue of tectonic province boundaries

King (2019) concluded that all of Australia's historic surface-rupturing earthquakes occurred close to the boundaries of previously-defined Precambrian litho-structural provinces or domains. She wrote:

" *The Meckering, Calingiri, Cadoux, and Katanning events occurred in the Archean Yilgarn Craton within ~25 km of significant terrane boundaries... The Lake Muir event occurred in the Albany-Fraser Orogen, <15 km south of the south dipping terrane boundary with the Yilgarn Craton... The Marryat Creek, Pukatja and Petermann events occurred within the Mesoproterozoic Musgrave Block... within 0–10 km of major terrane boundaries. The Tennant Creek ruptures extend across the boundary of the Proterozoic Warramunga Province and Neoproterozoic–Cambrian Wiso Basin...".*

The implication is that, even in the unextended craton, faults are likely to be reactivated only near terrane boundaries.

How does this conclusion apply to Forsmark? Is it near previously-defined terrane boundaries within the craton? Torvela and Ehlers (2010) published a generalized geologic map of the Shield (Fig. 3-7a). The map shows Sweden's Bothnian coast is composed of five fault-bounded terranes (A through E) separated by NW-trending faults and shear zones. Forsmark lies on the boundary between terrane C to the north (the Ljusdal batholith, LB on Fig. 3-7a) and the amphibolite facies terrane D of similar age to the south. The fault separating terranes C and D is labeled as the Singö shear zone, which lies only a few km offshore of the Forsmark site. About the Singö shear zone, Torvela and Ehlers (2010, p.1134) say this:

*" During the Svecobaltic orogeny, much of the regional deformation partitioned into ductile crustal-scale shear zones throughout the Fennoscandian shield.......... Some of these shear zones follow crustal discontinuities that have been interpreted as terrane boundaries (e.g. 'Pori shear zone', Hassela shear zone, Singö shear zone...".*

In the same year Stephens et al. (2010) published a tectonic domain map of southern Sweden (Fig. 3-7b). In part "b" of that figure he defines the boundaries between terranes not as lines, bit as shear zones wide enough to define terranes of their own. For example, his tectonic domain 2 encompasses the Singö-Eckarfjärden-Forsmark shear zones, which straddle the elongated Forsmark "tectonic lens" that will host the repository.

From this perspective, the Forsmark site is within the same distances of major terrane boundaries (10-25 km) as the Australian earthquakes cited above. We interpret this as confirmation that future earthquakes near Forsmark are controlled by similar seismotectonic controls as the historic surface ruptures in Australia.

### 3.3.3. Historic seismicity of the north Atlantic margin

Redfield and Osmunsen (2014) compared the historic seismicity of the seaward and landward domains shown in Fig. 3-5. Specifically, they computed the Cumulative Seismic Moment (CSM) of historic seismicity for each zone. They observed that: (1) seismicity was concentrated on the boundaries between the domains (Fig. 3-8), and (2) seismicity on these boundary structures decreased rapidly from west to east (toward the craton). They state:

> *“The easternmost, least-energetic CSMw seismic belt (SB3) is located at the HBSL, where the tilted Scandinavian hinterland begins to merge with the interior lowlands. SB3 is roughly coincident with measureable increases in crustal thickness... and lithospheric stiffness..., as well as the crest of the post-glacial topographic dome... SB3 also roughly marks the western margin of Fennoscandia’s much older cratonic core). Although many of the earthquakes that comprise SB3 are small in moment.”*

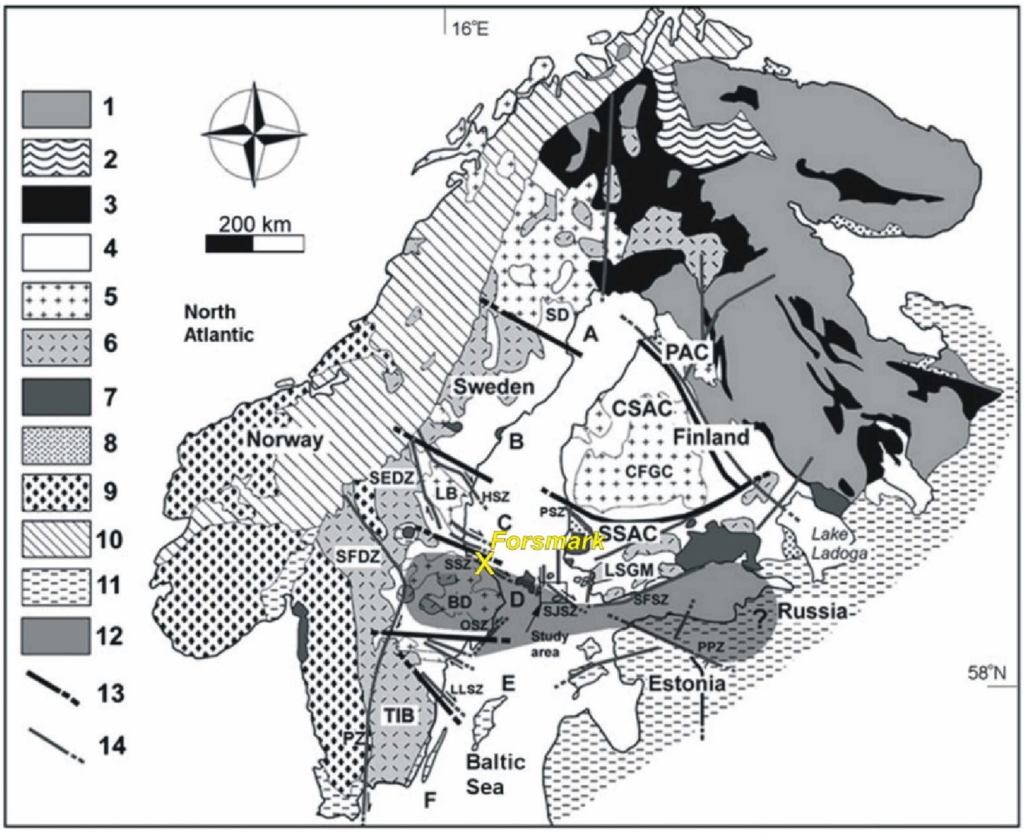

Figure. 3-7a. Generalised geological map of the Fennoscandian shield, from Torvela and Ehlers, 2010. Key to domains: 1-Archaean rocks, 3.2–2.5 Ga; 2-Lapland granulite belt, 2.2–1.9 Ga; 3-Karelian supracrustal rocks, 2.5–1.9 Ga; 4- Svecofennian supracrustal rocks, 2.0–1.85 Ga; 5-(Sveco)Fennian pre- and synorogenic magmatic rocks, 1.95–1.85 Ga; 6-Svecobaltic and Nordic granites and migmatites (previously called late-Svecofennian), 1.85–1.77 Ga; 7-Anorogenic rapakivi granites, 1.65–1.4 Ga; 8-Sandstones, Jotnian and younger, 1.5–0.57 Ga; 9-Sveconorwegian rocks, 1.25–0.9 Ga; 10-Caledonian rocks, 0.6–0.4 Ga; 11-Phanerozoic sedimentary cover, 0.57 Ga; 12-Mainly amphibolite facies terranes; 13-Domain borders; 14- Major Palaeoproterozoic deformation zones of the bedrock. LSGM, Late Svecofennian granite migmatite zone; PAC, primitive arc complex of central Finland; CSAC, Central Svecofennian arc complex; SSAC, southern Svecofennian arc complex; CFGC, Central Finland granitoid complex; LB, Ljusdal batholith; BD, Bergslagen district; SD, Skellefte district; TIB, trans-Scandinavian igneous belt; A through F, Palaeoproterozoic and Archaean bedrock domains in Sweden (partly from Sjo¨stro¨m and Bergman, 1998). Major shear zones: SFSZ, South Finland; SJSZ, Sottunga–Jurmo; PSZ, Pori; PPZ, Paldiski–Pskov; HSZ, Hassela; SEDZ, Storsjo¨n–Edsbyn deformation zone; SSZ, Singö; OSZ, Ornö; LLSZ, Loftahammar–Linköping; SFDZ, Sveconorwegian frontal deformation zone; PZ, Protogine zone..

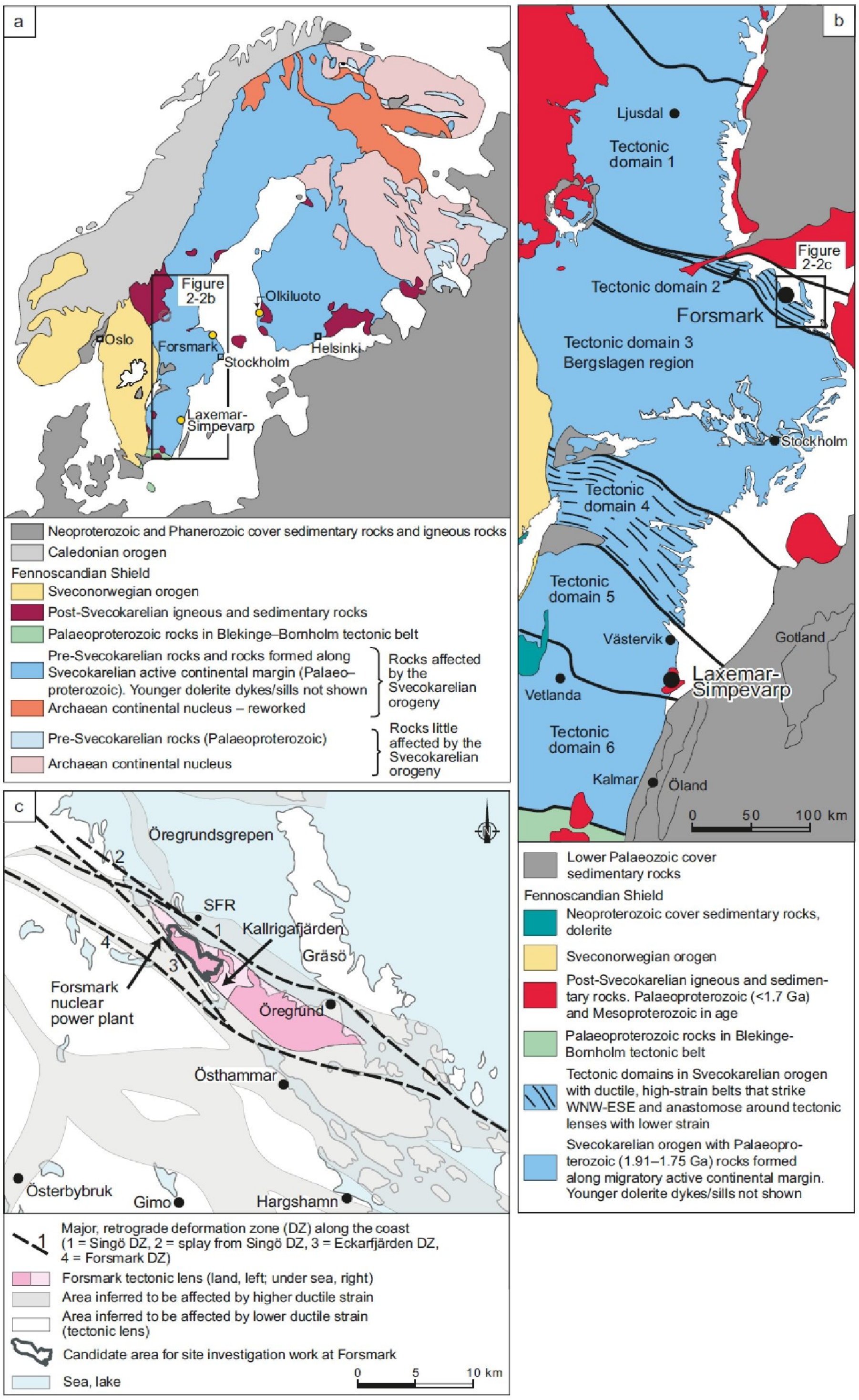

Figure. 3-7b. Regional geological setting of the Forsmark site. (a) Major tectonic units in the northern part of Europe. The locations of Forsmark, Laxemar-Simpevarp, and Olkiluoto in Finland also shown; (b) Svecokarelian tectonic domains and post-Svecokarelian rock units in the south-western part of the Fennoscandian Shield, south-eastern Sweden; (c) Inferred high-strain belts and tectonic lenses, including the Forsmark tectonic lens, in the area close to Forsmark, all situated along a coastal deformation belt. From Stephens et al. 2010.

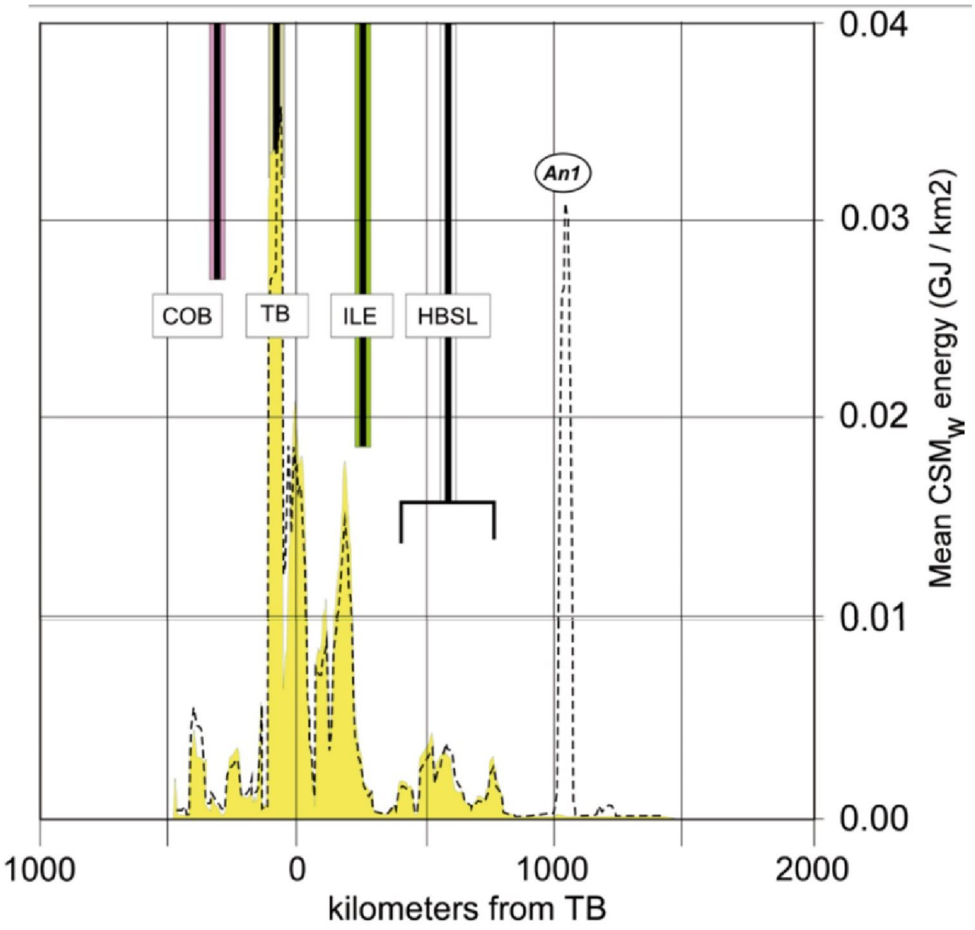

Figure 3-8. Cumulative Seismic Moment (CSMw) energy in GJ km-2. Mean CSMw peaks are interpreted to correlate to the benchmark boundaries of the extended margin: the Taper Break (TB); the Innermost Limit of Extension (ILE); and the Hinterland Break in Slope (HBSL; see Fig. 3-3). Sharp dashed peak at An1 illustrates a local spike caused by a spatially small cluster of relatively large earthquakes in southern Finland. COB – Continent Ocean Boundary. BØF – Bjørnøya Fan. SB1, SB2 and SB3 denote seismic belts discussed in the text of Redfield and Osmundsen, 2014.

Fig. 3-8 depicts the HBSL as a zone of seismicity rather than a narrow band. My interpretation based on the previous figures, is that at any one latitude the HBSL is narrow. But evidently amongst the 11 cross-profiles of Redfield and Omundsen (2014), its longitude varies somewhat between the profiles (note the curvature of the red line in Fig. 3-6). So the authors sought to represent that variance in Fig. 3-8 as a wider zone.

### 3.3.4. Comparison of driving forces

Both Forsmark and Australia occupy the interior of tectonic plates. Past studies of the driving force of intraplate seismicity point to ”ridge push” from the nearest oceanic spreading center as determining the stress state of SCRs. At Forsmark the mid-Atlantic Ridge spreading center lies 2145 km to the west. The site of historic surface ruptures in Western Australia lies 2063 km SW of the Southeast Indian Ridge spreading center. Thus, as far as distance from the origin of ridge push, the sites are equivalent.

However, the spreading rates at those mid-ocean ridges are different. At Iceland the mid-Atlantic Ridge is spreading east-west at 3.4 cm/yr, pushing Scandinavia eastward. On the SE Indian Ridge at 120°E latitude (Western Australia), the spreading rate is 7.5 cm/yr. This difference of 220% in spreading rate could explain why there have been larger historic earthquakes and surface ruptures in Western Australia than in Scandinavia.

SUMMARY: The above discussion suggests that Forsmark lies in a relatively aseismic structural domain east of the HBSL, in the intact, unextended craton. But within that domain, it lies very close to a lithologic terrane boundary (the Singö fault), and such boundaries have been observed to preferentially host historic surface-rupturing earthquakes, at least in the Australian craton. These similarities support a rather close analogy between the seismotectonic setting of Forsmark and that of historic surface ruptures in Australia, and a justification for using Australian displacement data on DFs in a comparison with the numerical model predictions.

### 3.3.5. Magnitudes of postglacial earthquakes in Scandinavia; endglacial ruptures

In this sub-section we describe which (if any) historic reverse surface ruptures are the best modern analogs to the 13 endglacial fault (EGF) scarps of Sweden. This discussion will be about principal (seismogenic) faults rather than about distributed faults, because no distributed faults have yet been identified in the Swedish ruptures. Using their fault scarp dimensions (length, height), estimates have been published about their moment magnitude, given some assumptions. These assumptions have long been used in Scandinavia, as follows.

ASSUMPTION 1-Each Swedish fault scarp preserved today was created in a single surface-rupturing earthquake. If true, then we can consider the length of today's scarp as a Surface Rupture Length (SRL), such as measured in modern field studies, and in databases such as SURE 1.0/ 2.0 and FDHI.

However, these (mainly) early Holocene scarps could also represent multiple, shorter fault reactivations that occurred along strike on an ancient shear zone, hundreds or thousands of years apart (see this report section 2.1.1). After the passage of 10 ka or more, erosion could have smoothed the component scarps so that their endpoints/ overlaps cannot be recognized as such. To date no rigorous tests of this single-event assumption have been performed. The most reliable test is to trench the fault scarps in multiple locations along strike, to confirm that every trench contains: (1) evidence of only a single event, and (2) that single event has the same age in every trench. This testing can understandably be expensive, as shown by hunt for segments/segment boundaries/sub-segments on the 300 km-long Wasatch fault zone, Utah, which involved more than 100 paleoseismic trenches spread over 40 years (McCalpin and Nishenko, 1996; DuRoss et al., 2016).

ASSUMPTION 2- At any given point on an EGF scarp, its height is the product of only a single paleoearthquake rupture. This is a long-standing assumption in Scandinavia, and if true, means that the EGF ruptures had larger single-event displacement than any historic earthquakes, by a large margin. For example, in the past ~125 years the largest average displacement on a reverse rupture anywhere in the world was 3.5 m (in the M8.02 Chon Kemin, Kyrgyzstan, earthquake of 1911; Arrowsmith et al., 2016). The largest 10 historic displacements are summarized in Table 3-3.

Table 3-3. List of the 10 largest historic reverse-fault surface ruptures (excluding subduction zones), listed by their average displacement.

| Rupture Name, Country, Year | Average Displacement (m) | Moment Magnitude |
|---|---|---|
| Chon Kemin, Kyrgyzstan, 1911 | 3.5 | 8.02 |
| Chi Chi, Taiwan, 1999 | 2.6 | 7.62 |
| Wenchuan, China, 2008 | 2.2 | 7.9 |
| Kaikoura, New Zealand, 2016 | 2.2 | 7.8 |
| Rikuu, Japan, 1896 | 2.1 | 7.2 |
| Changma, China, 1932 | 2.0 | 7.82 |
| El Asnam, Algeria, 1980 | 1.8 | 7.3 |
| Kashmir, Pakistan, 2005 | 1.5 | 7.6 |
| Tabas, Iran, 1978 | 1.5 | 7.4 |
| Bohol, Philippines, 2013 | 1.4 | 7.1 |

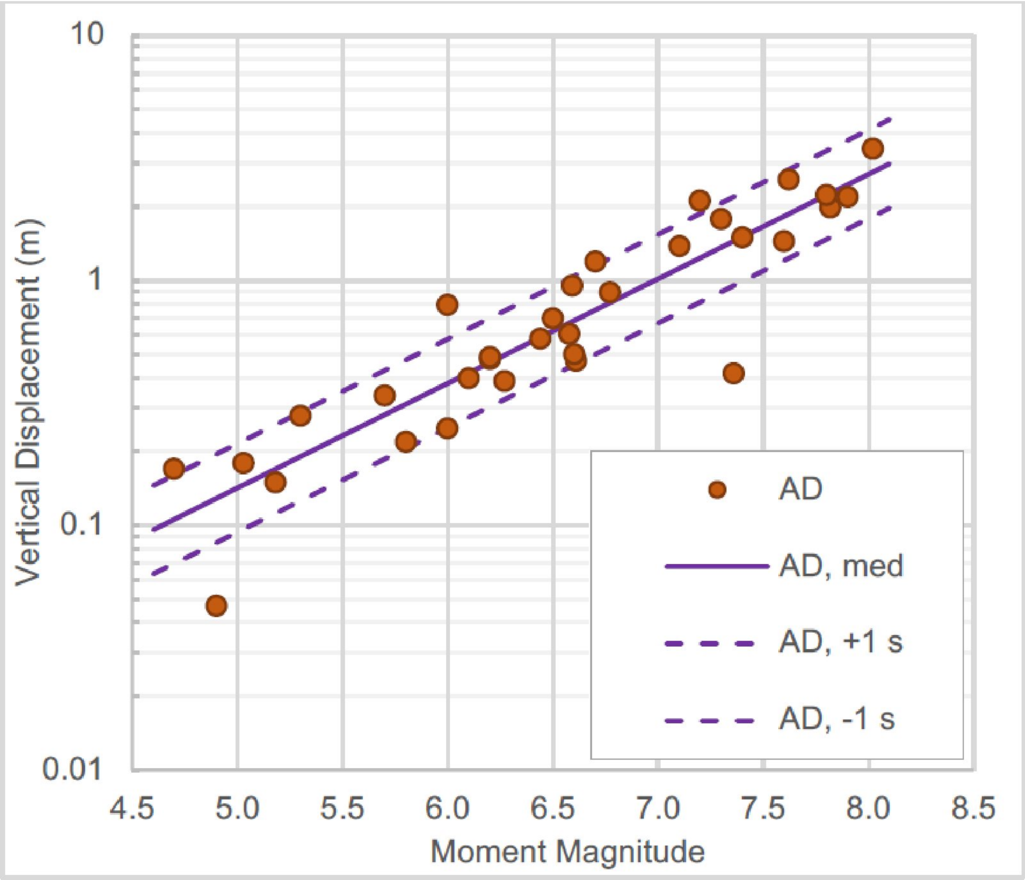

Figure 3-9. AD vs MW for worldwide data with preferred least-squares linear regression line (solid) and ± 1 standard error lines (dashed). The results of the initial fit to the 32 data points yields Log AD= -2.98 +0.427m, with sigma=0.18. The preferred and ± 1s lines show a reasonable fit, with residuals being approximately equally distributed above and below the average line across all magnitudes. From Moss et al., 2022, their Fig. 4.7.

Fig. 3-9 shows a plot of average vertical displacement (AD) as a function of earthquake moment magnitude (from Moss et al., 2022). The Chon Kemin rupture (M8, AD=3.5 m) defines the upper limit of the dataset, beyond which the regression is not supported by data. Graphs such as Fig. 3-9 can be used to predict earthquake magnitude from the average displacement (AD) of a prehistoric surface rupture. However, this popular technique does not work for Swedish postglacial fault scarps, because their average scarp heights are mostly larger than the AD values of any historic surface rupture (see Table 3-4). Note that 7 of the 13 ruptures in Table 3-4 have larger ”General heights” than any ruptures in the historic record. As a result, using the Moss et al. (2022) equation and believing Assumption 2 above, yields earthquake magnitude estimates of 8.1 to 9.02. Such earthquake magnitudes are found today only on major plate boundary faults, such as subduction zones.

The magnitude of Swedish EGF earthquakes can also be estimated by the length of the fault scarp and Assumption 1. As shown in Table 3-4, such length-based magnitudes are 1.5 to 2 magnitude units smaller than the displacement-based magnitudes.

The obvious solution to this discrepancy is that current EGF scarp heights result from multiple rupture events. Smith et al. (2022b) have documented that at least 4 of the 13 EGF ruptures have evidence for more than one event. They conclude: ”*While some of* *these ruptures occurred after the retreat of the Late Weichselian ice sheet, we hypothesize that some, perhaps most, of the displacement is not associated with the most recent deglaciation. Such results would be consistent with recent work in Finland, where stratigraphic investigations across fault scarps have indicated multiple ruptures, some of which are pre-Late Weichselian* (Mattila et al., 2019; Ojala et al., 2019)."

The preceding sections indicate that there have not been any historic SCR earthquakes worldwide that created scarps with average displacements >2 m. Reverse ruptures of that size have all been in plate boundary settings. So unfortunately, there do not seem to be any good historic analogs to the EGF ruptures.

ASSUMPTION 3- Swedish EGFs have long been assumed to be moderate-dip (40°-60°) reverse faults, similar to the example faults at Forsmark for which shear displacements were computed by SKB. For example, Stanfors and Ericsson 1993 state: "*The scarps are developed in strongly fractured and chemically weathered zones of presumed pre-Quaternary age. The results from the trenches suggest, at least at the surface, that the faults are reverse and dipping between 40-50° and the vertical.* "Malehmir et al. 2016 state*: ".... most glacially induced faults appear to be dominantly reverse, dipping between 50° and 60° (Juhlin et al., 2010; Juhlin and Lund, 2011; Ahmadi et al., 2015) and associated with zones of weakness in the bedrock (e.g. shear zones or at rock contacts)...." The geophysical results suggest a moderately (ca. 45° westward dip for the deformation zone)...".* Ojala et al. 2017 state in their Abstract: " *The fracture frequency and lithology of drill cores and fault geometry in the trench log indicate that the Riikonkumpu PGF dips to WNW with a dip angle of 40–45° at the Riikonkumpu site and close to 60° at the Riikonvaara site*." Abdi et al. (2015) imaged faults beneath the scarps of the Suasselka EGF and estimated their dips to be 35°and 45°.

Table 3-4. Summary of major glacially induced fault scarps in Sweden. Modified from Smith et al., 2022b, their Table 5.2.1. Bold magnitudes are larger than any known historic reverse rupture on land, globally.

| Fault | Discontinuous length (km) | Strike | Primary scarp aspect | General height (m) | Displ. Per Event (m)[1] | Maximum height (m) | Mag. Est. from SRL[2] | Mag. Est. from Displ. Per Event[3] | References |
|---|---|---|---|---|---|---|---|---|---|
| Bollnäs | 10 | N-S | E | 2– 4 | | 5 | 6.03 | **8.1** | Smith et al., 2014 |
| Burträsk | 45 | NE-SW | NW | 5– 10 | | 15 | 6.92 | **9.03** | Lagerbäck & Sundh, 2008 |
| Ismunden | 20 | NE-SW | SE | 3.5 | | 6 | 6.44 | **8.25** | Berglund & Dahlström, 2015 ; Mikko et al., 2015 |
| Lainio | 50 | NE-SW | NW | 10–20 | 2.6 | 30 | 6.98 | 7.95 | Lagerbäck & Sundh, 2008 |
| Laisvall | 11 | NE-SW | NW | 5 | | 5 | 6.09 | 7.91 | Mikko et al., 2015 |
| Lansjärv | 50 | NE-SW | SE | 5– 10 | | 20 | 6.98 | **9.03** | Lagerbäck, 1990 , 1992 |
| Lillsjöhögen | 6 | N-S | E | 1– 4 | | 8 | 5.73 | 7.91 | Berglund & Dahlström, 2015 ; Mikko et al., 2015 |
| Merasjärvi | 30 | NE-SW | NW | 10–15 | 5 (8)[4] | 20 | 6.68 | **8.62** | Lagerbäck & Sundh, 2008 ; Mikko et al., 2015 ; Smith |

| | | | | | | | | | |
|---|---|---|---|---|---|---|---|---|---|
| | | | | | | | | | et al., 2018a |
| Pärvie | 150 | NE-SW | NW | 5-10 | 2.5 | 35 | 7.6 to 8.25 | 7.92 | Lundqvist & Lagerbäck, 1976 ; Lagerbäck & Witschard, 1983 |
| Röjnoret | 60 | N-S | W | 5– 10 | | 10 | 7.09 | **9.03** | Lagerbäck & Sundh, 2008 |
| Sjaunja | 40 | N-S | E | 1– 2 | | 3 | 6.85 | 7.40 | Mikko et al., 2015 ; Smith et al., 2022b |
| Sorsele | 40 | NE-SW | SE | 1– 2 | | 2 | 6.85 | 7.40 | Ransed & Wahlroos, 2007 ; Mikko et al., 2015 ; Smith et al., 2022b |
| Suorsapakka | 17 | NE-SW | NW | 2– 4 | | 4 | 6.34 | **8.1** | Mikko et al., 2015 ; Smith et al., 2022b |

[1] from Smith et al., 2022b

[2] assuming the fault ruptures its entire length (i.e., no segments); M=1.36 log SRL + 4.67, Johnston, 1994b, for SCR surface ruptures

[3] Displacement per Event is taken from the average General scarp height, or from per-event displacement cited in published papers, such as Smith et al. 2021. M is calculated by the relationship log AD=a+bM (Moss et al., 2022; 32 Reverse events worldwide) where AD is average displacement, M is moment magnitude, a intercept= -2.98, and b=0.427.

[4] 5 m after late Weichselian (10 ka); 8 m after middle Weichselian (80 ka). From Smith et al., 2022a, p. 200

[5] cited by Lindblom et al., 2015, p. 1714. However, they also define three segments (North, 70 km long; Central, 45 km long; South, 40 km long) on the basis of instrumental seismicity. If these segments do rupture separately, the Johnston 1994b equation indicates earthquakes of M7.18, M6.92, and M6.85, respectively

However, some authors have disputed these moderate dips. For example, Arch Johnston of the USA (cited in Stanfors and Ericsson, 1993) observed: ”*The Pärvie and other faults where bedrock is exposed are very steep, within 10-15° of vertical. Such steep dips for thrust fault scarps are not known elsewhere in the world." (p. 3). He continued: " I don't believe the low-dip, shallow thrust "flakes" model of the PGFs is an open question. One look at the Pärvie exposed scarp or the vertical fault faces in the Molberget trenches can dismiss the shallow thrust model. Also, the length and fairly regular sinuosity of the PGFs, especially the Pärvie, argue against shallow dip. Also, I've seen no evidence on why the PGFs should be listric. I believe they extend deep in the crust, perhaps through the entire brittle upper crust. (The Pärvie may involve the lower crust as well.)" (p. 6).*

Ojala et al, 2019, trenched the Suasselkä Fault Zone (Retu trench) and found it to be steeply-dipping*: " What is important from the fault instability perspective is that both the gravel and till units are clearly offset and deformed at the fault ramp in the Retu trench.... The plunge of the cobbles in till unit 1 is progressively rotated from the more general horizontal to an almost vertical orientation when approaching the fault scarp.... The longest axes of cobbles in units 1 and 2 are almost vertical at the fault scarp and generally orientated concordant with the fault plane between 75° and 80°... ".*

The latest compilation of geophysically-imaged dips (Beckel et al., 2021) extends the confusion about EGF dips. For example, they say the Lansjarv EGF ”*follows a gently dipping, NNE-SSW-striking set of fractures zones, suggesting that most of the fault movements occurred as a result of reactivation of older structures.*” Yet on the same page, they refer to the Lansjarv as having ”a steep easterly dip” and show a cross-section of it with a dip of 73°, contradicting the previous sentence.

### 3.3.6. Magnitudes of postglacial faults in Scandinavia; interglacial ruptures

Based on historic global seismicity going back about 150 years, the largest earthquakes in ‘non-extended’ SCRs rarely exceed M6.1 or 6.2, with the upper limit in the high M5s. Thus interglacial earthquakes are smaller than even the smaller magnitudes estimated for endglacial earthquakes in Table 3-4. In the M5-6.5 range there are about 20 global historic SCR earthquakes which have been studied in some detail, including displacement measurements on both principal faults (PFs) and distributed faults (DFs). But these smaller interglacial surface ruptures are qualitatively different than the endglacial scarps of Scandinavia, which are relatively straight and have a similar map pattern to many M6-7.6 historic ruptures worldwide. Mid-magnitude historic surface ruptures in SCRs are more curved, irregular and fragmented than larger ruptures, as will be shown in the following section. Of the roughly 20 historic SCR ruptures in the M5-6.5 range, 11 have been in Australia. All of them have had very shallow focal depths, 10 km or less; some are only 1 km. These shallow focal depths are within the range of scenario earthquakes proposed in numerical models near the Forsmark repository, so it is important for our comparison to study their spatial pattern and displacements. In contrast, the longer and straighter Swedish EGFs, the closest of which lies 140 km NW of Forsmark (Böllnas), may represent deeper earthquakes that ruptured the whole crustal thickness, as suggested by Arvidsson (1996).

Table 3-5. SCR earthquakes from Klose and Seeber, 2007.

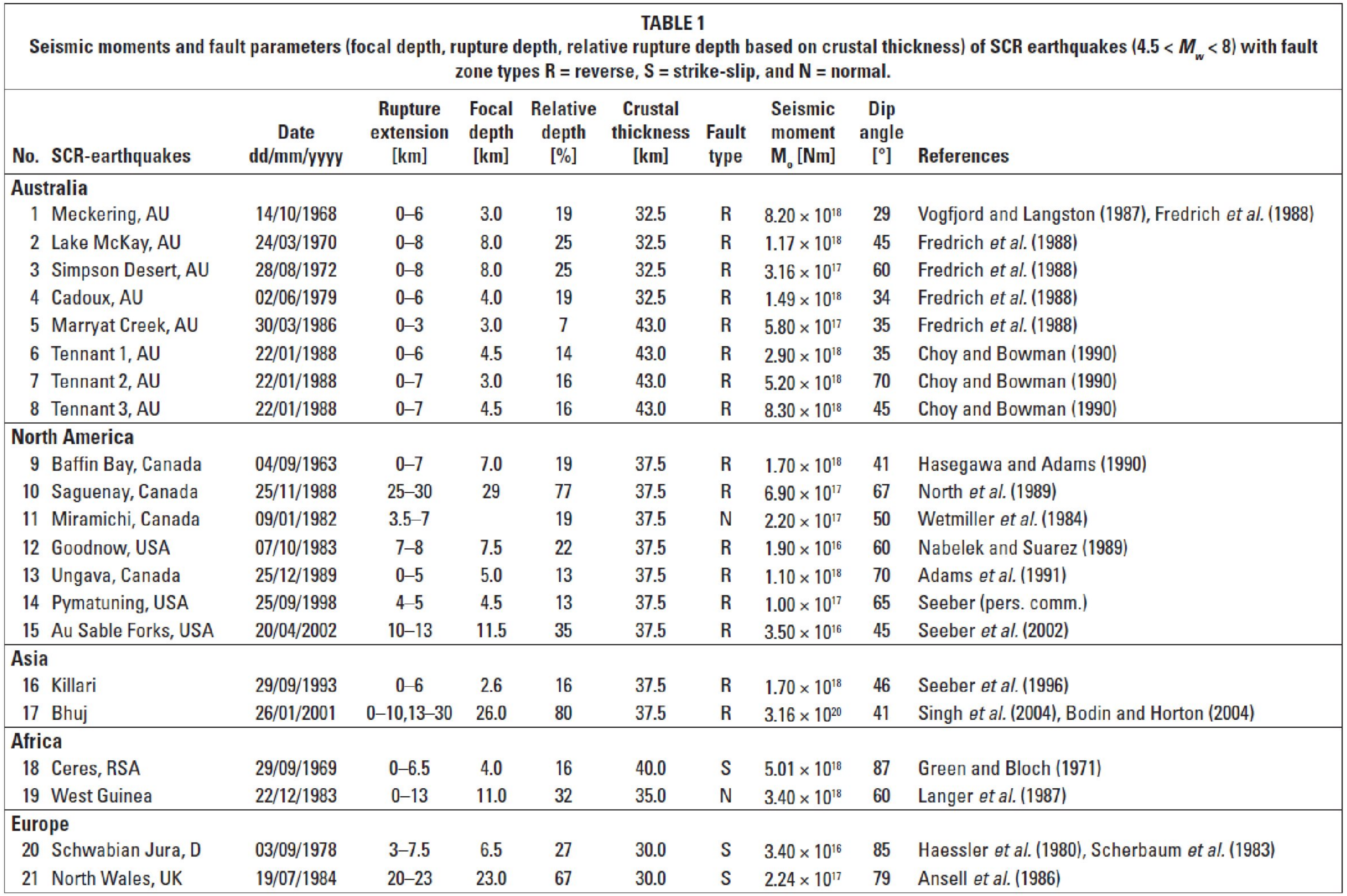

**TABLE 1**

**Seismic moments and fault parameters (focal depth, rupture depth, relative rupture depth based on crustal thickness) of SCR earthquakes ($4.5 < M_w < 8$) with fault zone types R = reverse, S = strike-slip, and N = normal.**

| No. | SCR-earthquakes | Date dd/mm/yyyy | Rupture extension [km] | Focal depth [km] | Relative depth [%] | Crustal thickness [km] | Fault type | Seismic moment $M_o$ [Nm] | Dip angle [°] | References |
|---|---|---|---|---|---|---|---|---|---|---|
| **Australia** | | | | | | | | | | |
| 1 | Meckering, AU | 14/10/1968 | 0–6 | 3.0 | 19 | 32.5 | R | $8.20 \times 10^{18}$ | 29 | Vogfjord and Langston (1987), Fredrich *et al.* (1988) |
| 2 | Lake McKay, AU | 24/03/1970 | 0–8 | 8.0 | 25 | 32.5 | R | $1.17 \times 10^{18}$ | 45 | Fredrich *et al.* (1988) |
| 3 | Simpson Desert, AU | 28/08/1972 | 0–8 | 8.0 | 25 | 32.5 | R | $3.16 \times 10^{17}$ | 60 | Fredrich *et al.* (1988) |
| 4 | Cadoux, AU | 02/06/1979 | 0–6 | 4.0 | 19 | 32.5 | R | $1.49 \times 10^{18}$ | 34 | Fredrich *et al.* (1988) |
| 5 | Marryat Creek, AU | 30/03/1986 | 0–3 | 3.0 | 7 | 43.0 | R | $5.80 \times 10^{17}$ | 35 | Fredrich *et al.* (1988) |
| 6 | Tennant 1, AU | 22/01/1988 | 0–6 | 4.5 | 14 | 43.0 | R | $2.90 \times 10^{18}$ | 35 | Choy and Bowman (1990) |
| 7 | Tennant 2, AU | 22/01/1988 | 0–7 | 3.0 | 16 | 43.0 | R | $5.20 \times 10^{18}$ | 70 | Choy and Bowman (1990) |
| 8 | Tennant 3, AU | 22/01/1988 | 0–7 | 4.5 | 16 | 43.0 | R | $8.30 \times 10^{18}$ | 45 | Choy and Bowman (1990) |
| **North America** | | | | | | | | | | |
| 9 | Baffin Bay, Canada | 04/09/1963 | 0–7 | 7.0 | 19 | 37.5 | R | $1.70 \times 10^{18}$ | 41 | Hasegawa and Adams (1990) |
| 10 | Saguenay, Canada | 25/11/1988 | 25–30 | 29 | 77 | 37.5 | R | $6.90 \times 10^{17}$ | 67 | North *et al.* (1989) |
| 11 | Miramichi, Canada | 09/01/1982 | 3.5–7 | | 19 | 37.5 | N | $2.20 \times 10^{17}$ | 50 | Wetmiller *et al.* (1984) |
| 12 | Goodnow, USA | 07/10/1983 | 7–8 | 7.5 | 22 | 37.5 | R | $1.90 \times 10^{16}$ | 60 | Nabelek and Suarez (1989) |
| 13 | Ungava, Canada | 25/12/1989 | 0–5 | 5.0 | 13 | 37.5 | R | $1.10 \times 10^{18}$ | 70 | Adams *et al.* (1991) |
| 14 | Pymatuning, USA | 25/09/1998 | 4–5 | 4.5 | 13 | 37.5 | R | $1.00 \times 10^{17}$ | 65 | Seeber (pers. comm.) |
| 15 | Au Sable Forks, USA | 20/04/2002 | 10–13 | 11.5 | 35 | 37.5 | R | $3.50 \times 10^{16}$ | 45 | Seeber *et al.* (2002) |
| **Asia** | | | | | | | | | | |
| 16 | Killari | 29/09/1993 | 0–6 | 2.6 | 16 | 37.5 | R | $1.70 \times 10^{18}$ | 46 | Seeber *et al.* (1996) |
| 17 | Bhuj | 26/01/2001 | 0–10,13–30 | 26.0 | 80 | 37.5 | R | $3.16 \times 10^{20}$ | 41 | Singh *et al.* (2004), Bodin and Horton (2004) |
| **Africa** | | | | | | | | | | |
| 18 | Ceres, RSA | 29/09/1969 | 0–6.5 | 4.0 | 16 | 40.0 | S | $5.01 \times 10^{18}$ | 87 | Green and Bloch (1971) |
| 19 | West Guinea | 22/12/1983 | 0–13 | 11.0 | 32 | 35.0 | N | $3.40 \times 10^{18}$ | 60 | Langer *et al.* (1987) |
| **Europe** | | | | | | | | | | |
| 20 | Schwabian Jura, D | 03/09/1978 | 3–7.5 | 6.5 | 27 | 30.0 | S | $3.40 \times 10^{16}$ | 85 | Haessler *et al.* (1980), Scherbaum *et al.* (1983) |
| 21 | North Wales, UK | 19/07/1984 | 20–23 | 23.0 | 67 | 30.0 | S | $2.24 \times 10^{17}$ | 79 | Ansell *et al.* (1986) |

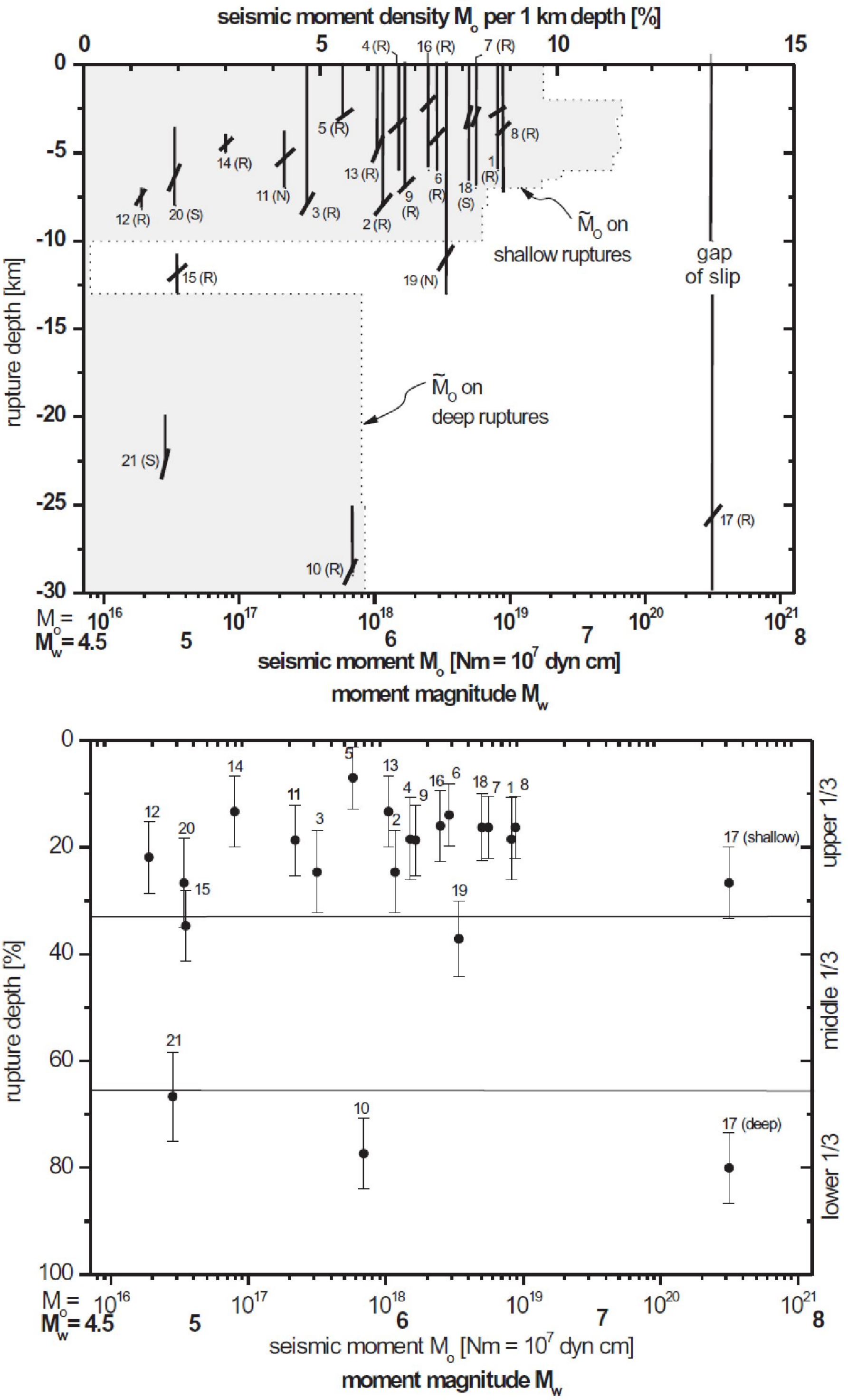

Fig. 3-10. (Top), relation between rupture extent (vertical lines), focal depths, and seismic moments of 21 SCR earthquakes. (Bottom), relation between focal depths and the local crustal thickness. From Klose and Seeber, 2007. Earthquake ID numbers on both figures correlate with those in Table 3-5.

Klose and Seeber (2007) made a worldwide compilation of well-constrained fault ruptures and focal depths of earthquakes in SCRs (Table 3-5), and concluded the 21 earthquakes had a bimodal depth distribution. Most of the earthquakes (16) ruptured only the upper 7.5 km of the crust (see Fig. 3-10), but the other five were widely scattered between 12 km and 29 km. Normalized by the crustal thickness at each site, 17 of the earthquakes occurred in the upper 30% of the local crustal thickness (Fig. 3-10). We propose that the shallow Australian rupture set, the best studied, can be used as analog to M5-6.5 interglacial ruptures in Sweden.

## 3.4. Description of historic surface ruptures in Australia

The following Introduction (in italics) is from Tamarah King's 2019 thesis on the subject:

"*In the 50 years between 1968 and 2018 Australia experienced eleven known surface rupturing earthquakes" (Table 3-6, Fig. 3-11). "Studies of Australian surface rupturing earthquakes have contributed to improvements in our collective understanding of intraplate earthquake behaviour, including rupture recurrence, in stable continental regions (SCR) (Calais et al., (2016); Clark et al., (2012); Crone et al., (2003), (1997); Quigley et al., (2010)) and empirically-derived scaling relationships for reverse earthquakes (Biasi and Wesnousky, (2016); Clark et al., (2014); Wells and Coppersmith, (1994); Wesnousky, (2008)). This paper reviews available published literature on historic surface ruptures" (Tables 3-6, 3-7). We re-evaluate and reconsider rupture and fault characteristics in light of new data (e.g., geophysical and geological) using modern analysis techniques (e.g., environmental seismic intensity scale (ESI-07) (Michetti et al., (2007))) and new or updated concepts in earthquake science since the time of publication (e.g., paleoseismology, SCR earthquake recurrence)."*

Table 3-6. Historic SCR earthquakes in Australia, analyzed by King ("This Paper" in table heading).

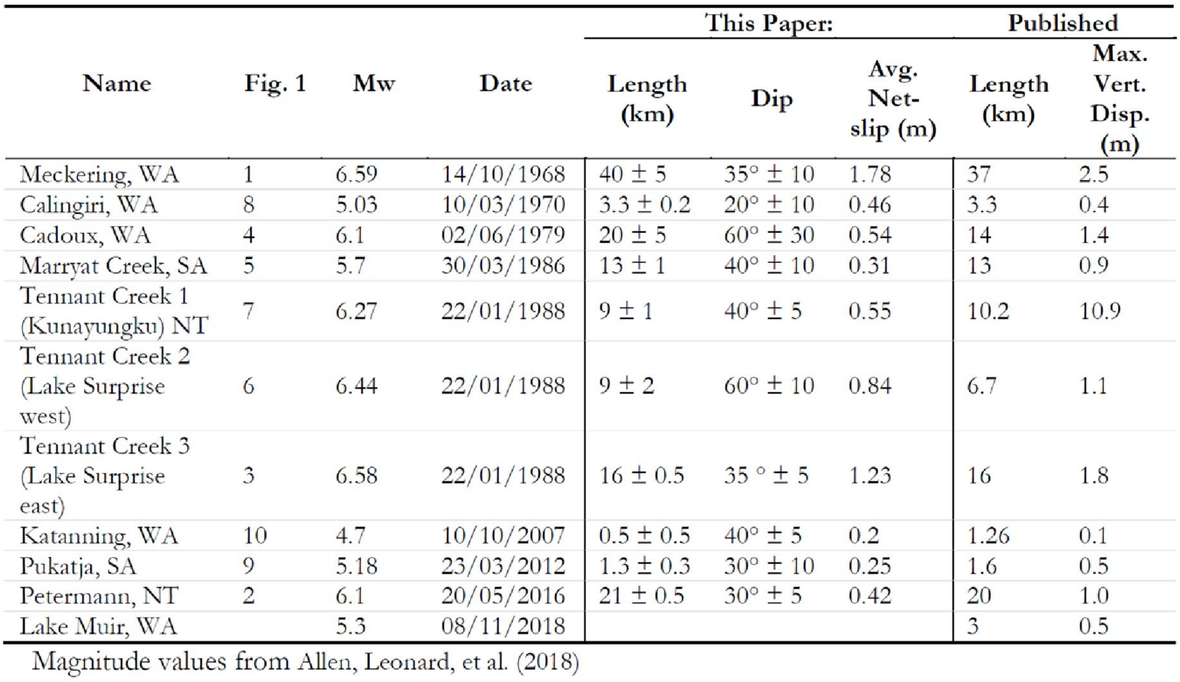

|  |  |  |  | This Paper: |  |  | Published |  |
|---|---|---|---|---|---|---|---|---|
| Name | Fig. 1 | Mw | Date | Length (km) | Dip | Avg. Net-slip (m) | Length (km) | Max. Vert. Disp. (m) |
| Meckering, WA | 1 | 6.59 | 14/10/1968 | 40 ± 5 | 35° ± 10 | 1.78 | 37 | 2.5 |
| Calingiri, WA | 8 | 5.03 | 10/03/1970 | 3.3 ± 0.2 | 20° ± 10 | 0.46 | 3.3 | 0.4 |
| Cadoux, WA | 4 | 6.1 | 02/06/1979 | 20 ± 5 | 60° ± 30 | 0.54 | 14 | 1.4 |
| Marryat Creek, SA | 5 | 5.7 | 30/03/1986 | 13 ± 1 | 40° ± 10 | 0.31 | 13 | 0.9 |
| Tennant Creek 1 (Kunayungku) NT | 7 | 6.27 | 22/01/1988 | 9 ± 1 | 40° ± 5 | 0.55 | 10.2 | 10.9 |
| Tennant Creek 2 (Lake Surprise west) | 6 | 6.44 | 22/01/1988 | 9 ± 2 | 60° ± 10 | 0.84 | 6.7 | 1.1 |
| Tennant Creek 3 (Lake Surprise east) | 3 | 6.58 | 22/01/1988 | 16 ± 0.5 | 35 ° ± 5 | 1.23 | 16 | 1.8 |
| Katanning, WA | 10 | 4.7 | 10/10/2007 | 0.5 ± 0.5 | 40° ± 5 | 0.2 | 1.26 | 0.1 |
| Pukatja, SA | 9 | 5.18 | 23/03/2012 | 1.3 ± 0.3 | 30° ± 10 | 0.25 | 1.6 | 0.5 |
| Petermann, NT | 2 | 6.1 | 20/05/2016 | 21 ± 0.5 | 30° ± 5 | 0.42 | 20 | 1.0 |
| Lake Muir, WA |  | 5.3 | 08/11/2018 |  |  |  | 3 | 0.5 |

Magnitude values from Allen, Leonard, et al. (2018)

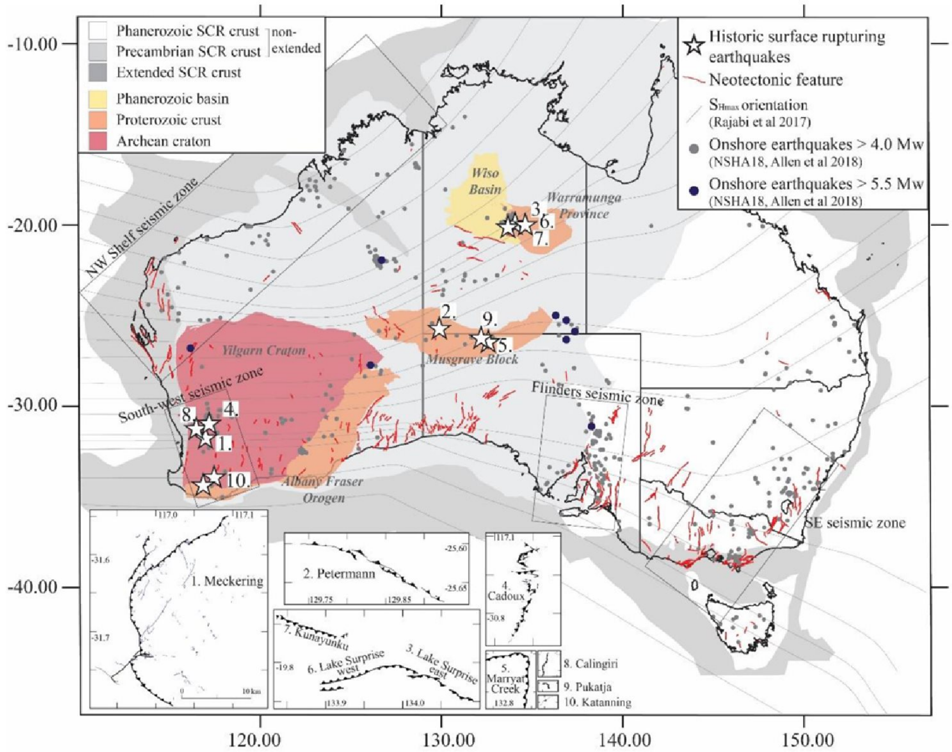

Figure 3-11. Map of Australia showing locations of historic surface rupturing events, continental scale crustal divisions (Leonard et al., (2014)), onshore historic seismology >4.0 (1840–2017) (Allen et al., (2018c)), simplified crustal stress trajectory map (Rajabi et al., (2017b)), GA neotectonic features database (Clark, (2012)), recognized seismic zones (Hillis et al., (2008); Leonard, (2008)) and specific crustal provinces relevant for surface rupture events (Raymond et al., (2018)). Small maps show individual surface ruptures at the same scale and ordered by rupture length (excluding 2018 Lake Muir). From King, 2019, her Fig. 5.1

Table 3-7. List of SCR ruptures in non-extended cratonic crust of Precambrian crystalline rocks. Bold text shows earthquakes with no identification of DFs or no displacement measurements on mapped DFs.

| Rupture No.[1] | Slip Sense | Year | Rupture event | Focal Depth (km) | Magnitude (Mw) | Analysed By[2] | Measured Displacements on DFs? |
|---|---|---|---|---|---|---|---|
| 5 | R | 1968 | Meckering, AUSTRALIA | 3 | 6.6 | FH | Y |
| 6 | R | 1970 | Calingiri, AUSTRALIA | 1 | 5.0 | FH, NR | Y |
| 8 | R | 1979 | Cadoux, AUSTRALIA | 4 | 6.1 | FH | Y |
| **11** | **R** | **1986** | **Marryat Creek, AUSTRALIA** | **3** | **5.8** | **NR** | **N** |

| | | | | | | | |
|---|---|---|---|---|---|---|---|
| **12** | **R** | **1988** | **Tennant Creek 1, AUSTRALIA** | **4.5** | **6.3** | **NR** | **N** |
| 12 | R | 1988 | Tennant Creek 2, AUSTRALIA | 3 | 6.4 | NR | Y |
| **12** | **R** | **1988** | **Tennant Creek 3, AUSTRALIA** | **4.5** | **6.6** | **NR** | **N** |
| 14 | R | 1993 | Killari, INDIA | 2.6 | 6.2 | NR | N?? |
| **-** | **R** | **2007** | **Katanning, AUSTRALIA** | **0.64** | **4.7** | **Dawson et al., 2008** | **N** |
| **18** | **R** | **2012** | **Pukatja, AUSTRALIA** | **11.4** | **5.4** | **This study** | **N** |
| 38 | R | 2016 | Petermann, AUSTRALIA | 3 | 6.1 | This study | Y |

[1] -rupture numbers from FDHI Flatfiles (Shapefiles of rupture traces and displacement measurement sites, with extensive attributing)

[2] FH, FHDI 2021; NR, Nurminen et al., 2020

### 3.4.1. Geologic setting of the historic ruptures

The Meckering, Calingiri, Cadoux, and Katanning events occurred in the Archean Yilgarn Craton within ~25 km of significant terrane boundaries (Fig. 3-11). The Lake Muir event occurred in the Albany-Fraser Orogen, <15 km south of the south dipping terrane boundary with the Yilgarn Craton. The Marryat Creek, Pukatja and Petermann events occurred within the Mesoproterozoic Musgrave Block within 0–10 km of major terrane boundaries. The Tennant Creek ruptures extend across the boundary of the Proterozoic Warramunga Province and Neoproterozoic–Cambrian Wiso Basin.

### AUSTRALIAN SCR EARTHQUAKES WITH SURFACE FAULTING (Fig. 3-12 shows Meckering rupture; other rupture maps and sections mentioned in text are found in Appendix A).

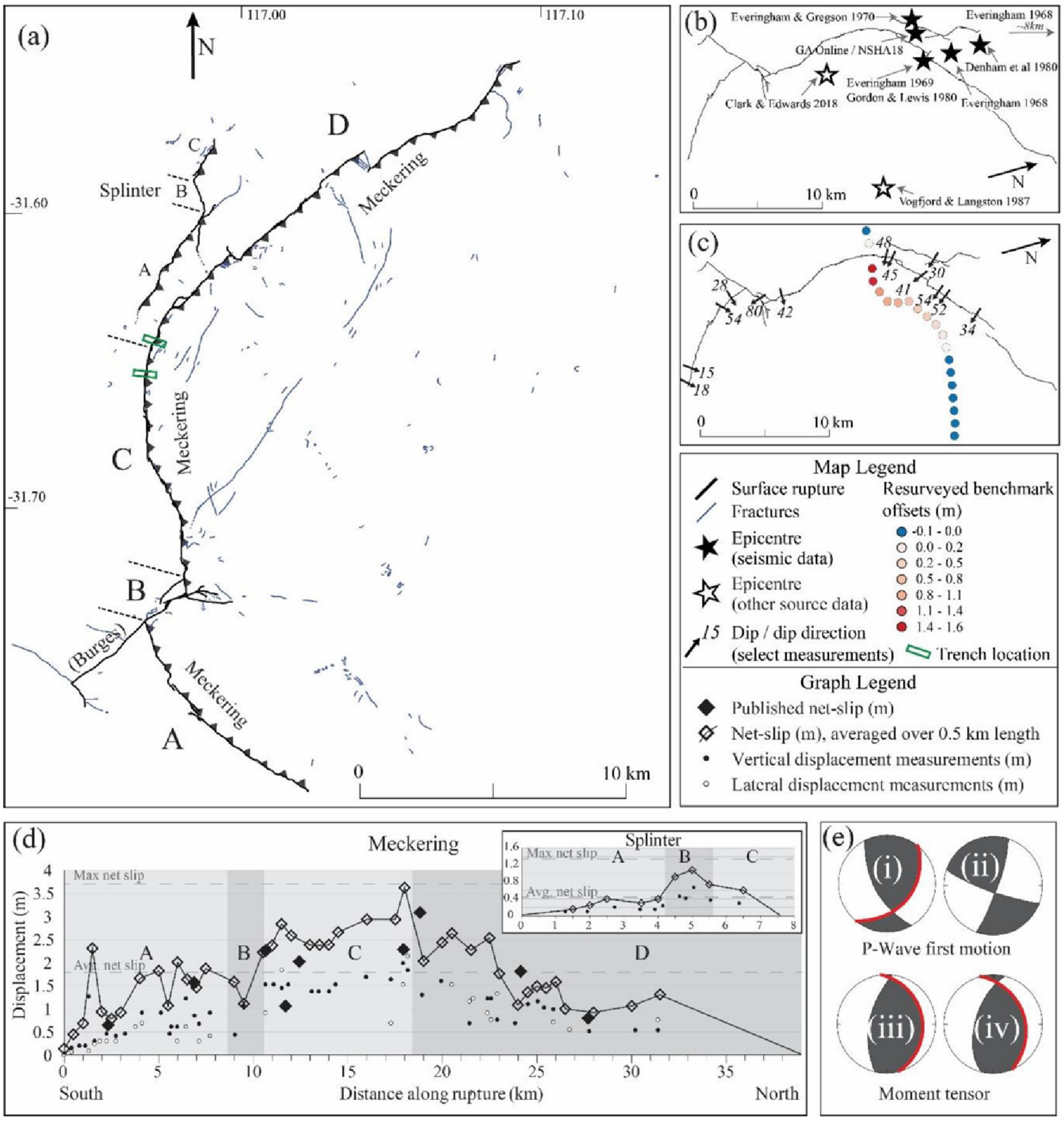

Figure 3-12. 1968 Mw 6.6 Meckering earthquake (a) rupture and fracture map of Meckering and Splinter scarps (Gordon and Lewis, (1980)) with faults labelled as per displacement graphs, trench location from Clark and Edwards (2018) (b) published epicenter locations, open stars show approximate locations of epicenters without published coordinates (c) selected dip measurements of scarp and displacement of resurveyed road bench marks (Gordon and Lewis, (1980)) (d) graphs of along-rupture vertical and lateral displacement measurements and net slip calculations (Gordon and Lewis, (1980)) and net slip calculated from available data averaged over 0.5 km increments (this study) (e)focal mechanisms (red line shows preferred plane from original publication) from (i) Fitch et al. (1973), (ii) Fitch et al. (1993) and Leonard et al. (2002), (iii) Fredrich et al. (1988), and (iv) Vogfjord and Langston (1987).

### 3.4.2. Long sympathetic distributed faults on the footwall of the PF, in Meckering and Tennant Creek 2 ruptures

In two of the five ruptures where displacements were measured on DFs (1968 Meckering, 1988 Tennant Creek 2), roughly half the measurements were made on long DFs that paralleled the PF on its footwall (Figs. 3-13a, b). At Meckering the footwall DF ("splinter fault") is 6.8 km long, lies 1.0 to 3.5 km from the PF, and projects to intersect with the PF at depth (Fig. 3-14). Splinter fault displacements at Meckering average ~34% of the PF displacements, which is a typical relationship. At Tennant Creek 2, the footwall DF lies 0.9-1.2 km from the PF and is 3.1 km long, but DF average displacement is essentially equal to PF displacement. It is unclear if the DF intersects the PF in the subsurface, because there are no dip measurements on the DF.

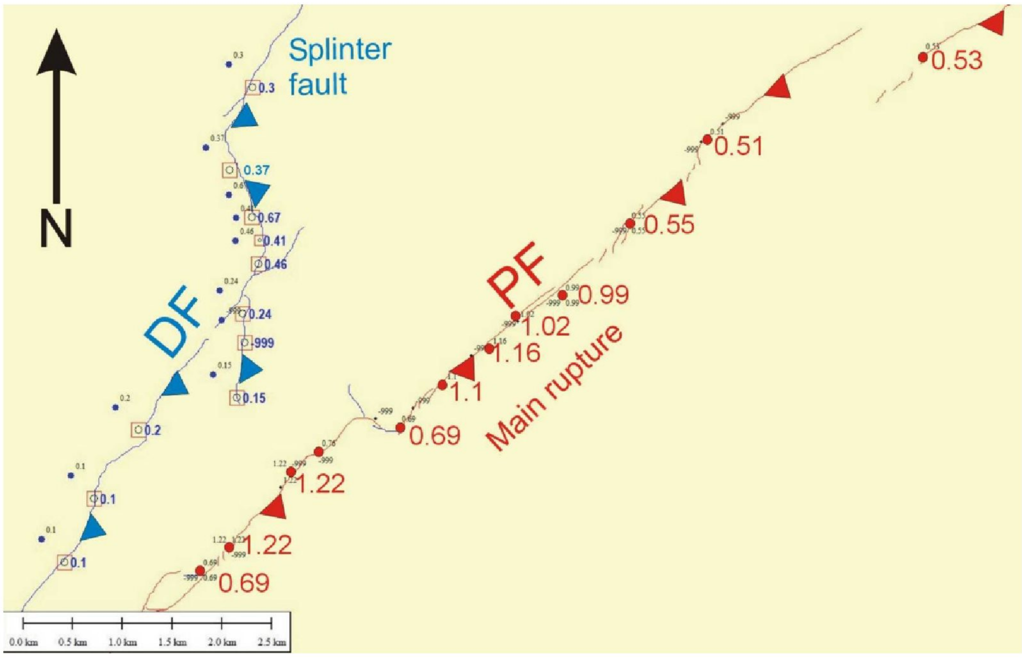

Figure 3-13a. Example 1 of a long distributed fault (blue line and numbers) that parallels the main (principal) rupture of the 1968 Meckering M6.59 earthquake (red line and numbers). Both reverse faults dip to the SE and are upthrown on that side. The DF lies 1.7 to 3 km from the PF, and had vertical displacements that average 0.3 m (range 0.1 to 0.67 m), compared to vertical displacements on the principal fault, which average 0.88 m (range 0.51 to 1.22 m). DF average displacement is 34% of PF average displacement.

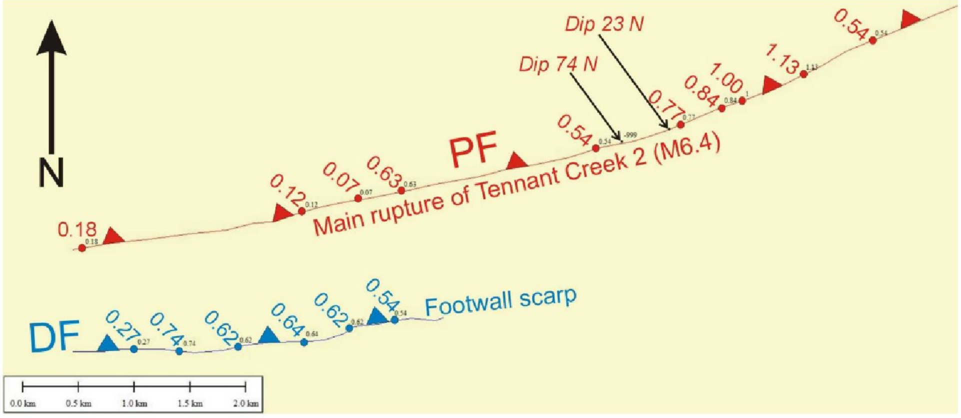

Figure 3-13b. Example 2 of a long distributed fault (blue line and numbers) that parallels the main (principal) rupture of the 1988 Tennant Creek 2 M6.4 earthquake (red line and numbers). Both reverse faults dip to the N and are upthrown on that side. The DF lies ~1 km from the PF, and had vertical displacements that average 0.57 m (range 0.27 to 0.74 m), compared to vertical displacements on the principal fault, which average 0.58 m (range 0.07 to 1.13 m). DF average displacement is ~100% of PF average displacement.

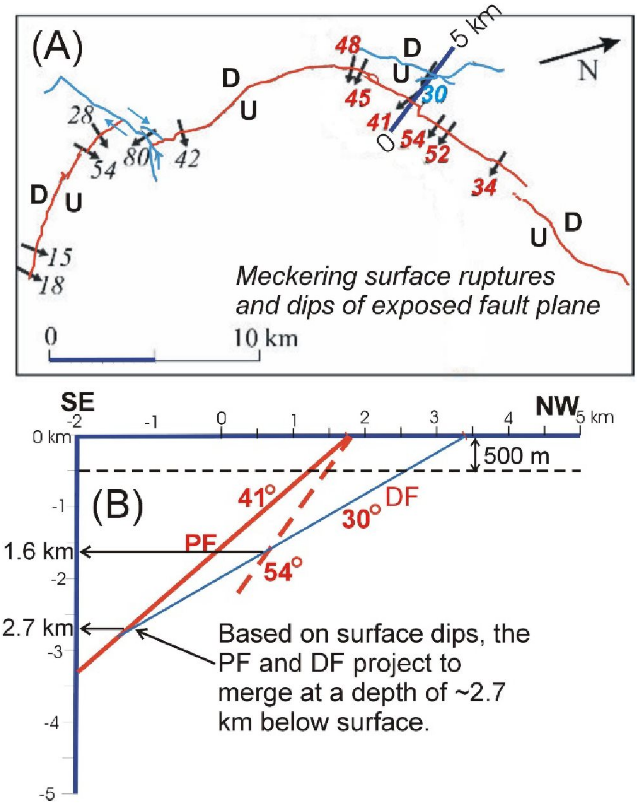

Based on surface dips, the PF and DF project to merge at a depth of ~2.7 km below surface.

Figure 3-14. Map (A) and cross-section (B) through the principal fault (PF, in red) and "Splinter" fault (DF, in blue) of the 1968 M6.6 Meckering, Australia surface rupture. Thick dark blue line on (A) shows the line of cross-section in (B). Note that North is to the upper right. Modified from King, 2019, her Fig. 5.3c. Thick red lines in (B) (solid and dashed) represent the PF with a 41° and 54° dip, respectively. Thin blue line in (B) represents the DF.

As shown in Fig. 3-14 (A), there is only one DF dip shown on the map (30°), and it is across strike from the lowest of the six PF dips (41°) measured opposite the DF. Assuming planar dips of 41°for the PF and 30° for the DF, they would intersect at a depth of 2.7 km below the surface. Four of the five dips measured elsewhere on the PF opposite the DF trace are steeper than 41°, and would result in shallower intersections if applied to the (B) cross-section. For example, assuming the steepest dip measured for the PF here (54°) would bring the intersection point with the DF up to 1.6 km below the surface. This is still much deeper than a typical repository depth (500 m), so should be handled as a distributed shear zone, independent from the PF, in any hazard model.

### 3.4.3. Other rupture complexities

The steepest dip on the main fault trace at Meckering is 80° in the southern 1/3 of the rupture, and is much steeper than all the other dips. This (blue in Fig. 3-14A) fault trace is perpendicular to the remainder of the main bow-shaped fault trace and forms a 1.7 km-wide stepover in the main trace (red). As shown by the blue arrows in Fig. 3-14A, this cross-fault appears to act as a transform fault between sections of the main reverse rupture, probably following a pre-existing, subvertical regional set of discontinuities (faults or joints). Note that the northern half of the Meckering principal rupture follows this same strike, as does the southern half of the Splinter fault. In contrast, the northern half of the Splinter fault contain a nearly-perpendicular bend that follows the same strike as the transform fault farther south. The simplest explanation of the overall rupture pattern is that it is controlled by two sets of discontinuities approximately at right angles to each other, one trending NE-SW (N half of main rupture; S half of Splinter fault; and transform fault), and the other trending NW-SE (southern half of main rupture; stepover in Splinter fault). This would explain the bow-shape of the main rupture, which changes direction nearly 90°in its center.

Dentith et al. (2009) perform a more in-depth structural assessment of the surface rupture, and conclude that the rupture follows three different structural trends in Precambrian rock; NE-SW, NW-SE, and N-S (Fig. 3-15a, b, and c). The latter trend contains the largest vertical displacements (up to 2 m; Fig. 3-15b) that are pure dip-slip, whereas the other two trends display smaller reverse-oblique slip with a right-lateral component in the north and a left-lateral component in the south (Fig. 3-15D).

Examination of all the other ruptures in Fig. 3-16 (and Appendix A) shows they all can be interpreted as reactivations of a small number of linear discontinuities. The PF of M5.7 Marryat Creek earthquake is also a bow-shaped rupture that bends through ~90°, while the PF at Pukatja (M5.4) bends through ~80°. The Calingiri M5.03 rupture zig-zags through three alternating 45° bends, whereas the Cadoux M6.1 rupture follows at least 3 or 4 different linear trends.

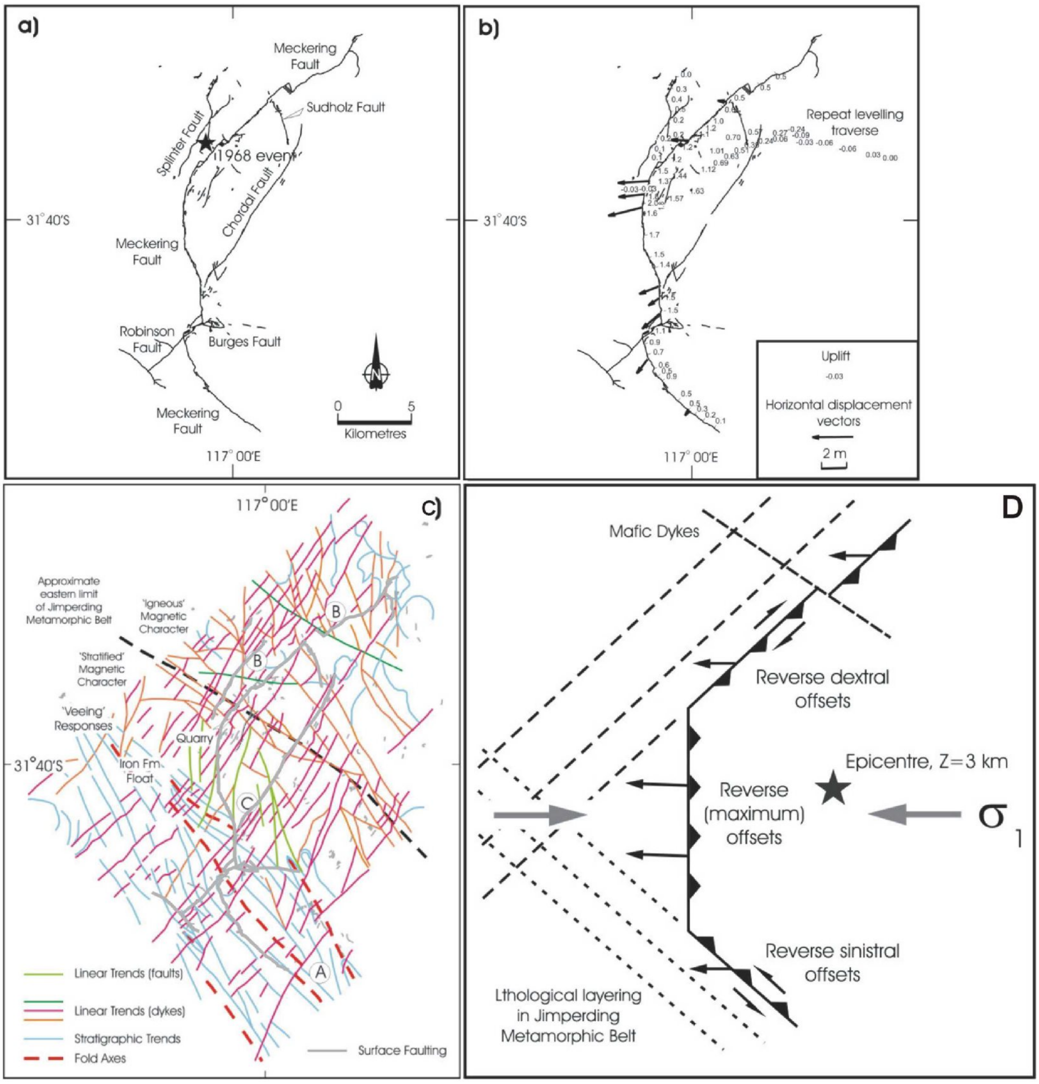

Figure 3-15. Maps showing effect of bedrock structural controls in the M6.6 Meckering surface rupture. (a) rupture traces and names; (b) rupture traces, their vertical component of displacement (= scarp height), in meters, and horizontal displacement vectors; (c) interpretation of aeromagnetic data, with main surface ruptures shown as thick gray lines; (D), interpreted geological controls that honor the preferred focal mechanism from teleseismic studies (pure westward thrusting on a N-S-striking nodal plane; Vogfjord and Langston, 1987; Fredrich et al., 1988).

Fig. 3-16 can highlight the importance of earthquake magnitude and focal depth in determining the surface rupture pattern. The two largest earthquakes (Meckering, Tennant Creek) were similar in magnitude and focal depth, and display the most continuous ruptures and the only instances of sympathetic footwall faulting. The Petermann and Cadoux ruptures have the same magnitude (6.1), but the Cadoux focus (5 km) was nearly twice as deep as the Petermann focus (3 km). The deeper Cadoux rupture has a more jagged, fragmented appearance than the Peterman, Tennant Creek, or Meckering. This suggests that the shallower the focus, the more continuous the rupture. The Pukatja M5.2 earthquake has an anomalously short rupture, much shorter than the smaller (M5.0) Calingiri earthquake. However, the Pukatja focus is much deeper (11.4 km) than the

Calingiri focus (1 km). This suggests that the deeper the focus, the more attenuation of displacement occurs upwards, yielding a shorter surface rupture.

The point of discussing these rupture complexities is to underscore how varied the surface rupture pattern can be, from slip on a single coseismic fault plane. Static and dynamic stress changes during rupture can trigger reactivation of fault planes other than the PF, some parallel to the coseismic plane, some perpendicular, and some oblique. This is easy to imagine as rupture propagates upward through Precambrian crystalline rocks that contain two or more pre-existing sets of weak discontinuities. Obviously, any predictive model of future surface faulting in such a geologic setting must be able to reproduce structurally-controlled complexities such as these, or at least allow for their occurrence statistically, perhaps as an output of multiple predictive realizations (e.g., Monte Carlo simulations). Conversely, a model that predicts DF displacements away from the PF as a simple function of distance measured perpendicular to PF strike, is likely to under-predict displacements in some areas and over-predict in others.

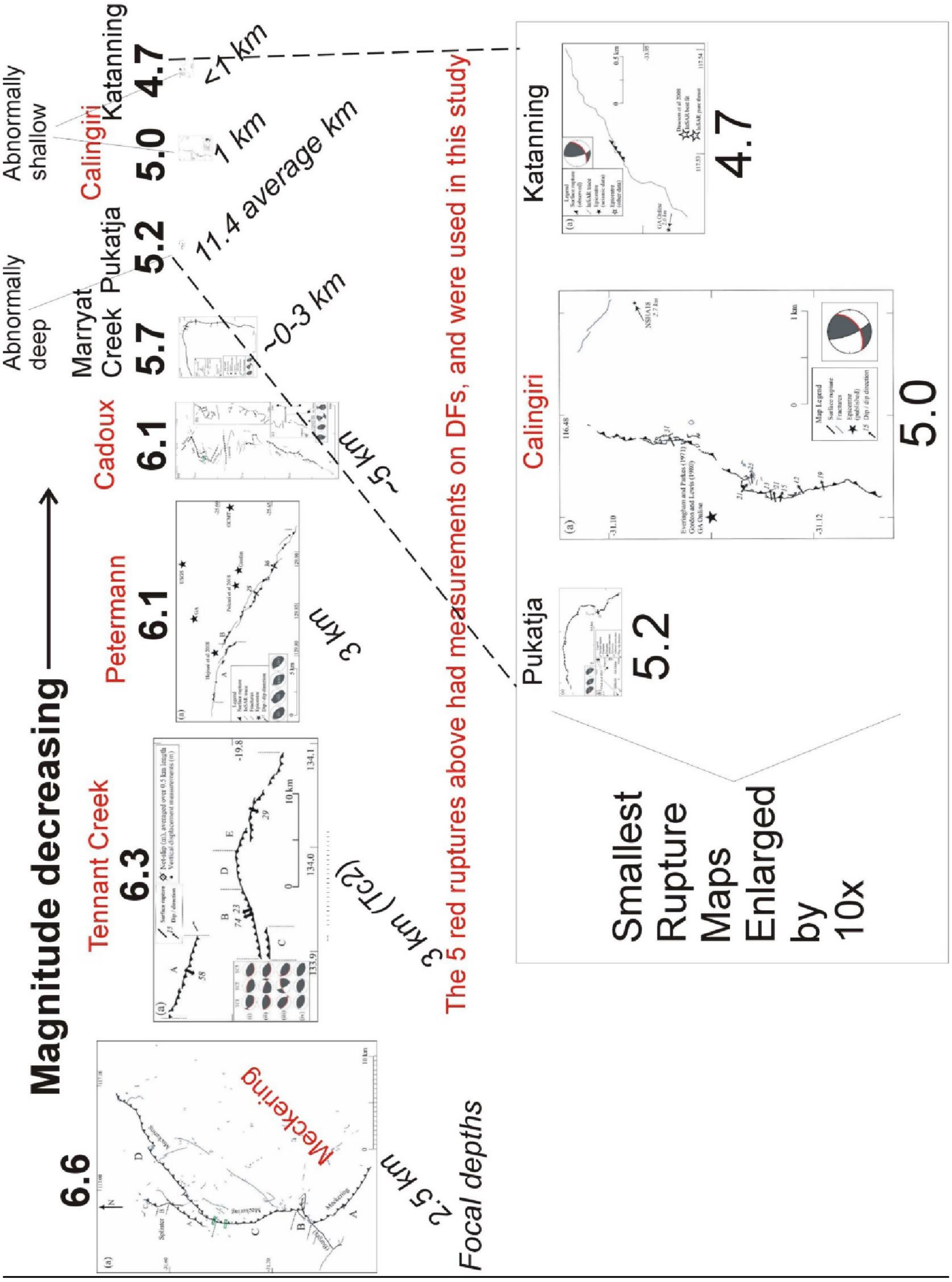

Figure 3-16. (Top/left), Maps of eight Australian historic surface ruptures, arranged in order of decreasing moment magnitude. (Bottom/right), the three smallest maps enlarged by 10x. See text for discussion of trends.

## 3.5. Probability of distributed faulting (DF) as a function of distance from the principal reverse fault (global datasets)

The occurrence probability[1] of DF as a function of distance from PF was first addressed by Youngs et al. (2003) for normal faults. They derived a logistic regression for Probability based on the independent variables ”r” (distance from PF) and ”m” (earthquake magnitude). Their single DF probability equation contained an additional term to account for whether DFs were on the FW or HW of the PF

$P= 2.06 + (-4.63) + 0.118m + (0.682h \ln(r + 3.32)$ Eq. 1 (cited in IAEA, 2021, p. 90).

A decade later Takao derived a similar equation for DFs in historic Japanese ruptures, without regard to FW or HW, as

$P = -3.839 + (-3.886) + (0.350m \ln(r + 0.200)$ Eq. 2 (cited in IAEA, 2021, p. 91)

Fig. 3-17 contrasts the results of these two equations for earthquakes of various magnitude classes. Given the range out to 25 km, almost all of these ”distributed ruptures” would now be classified as ”triggered ruptures.”

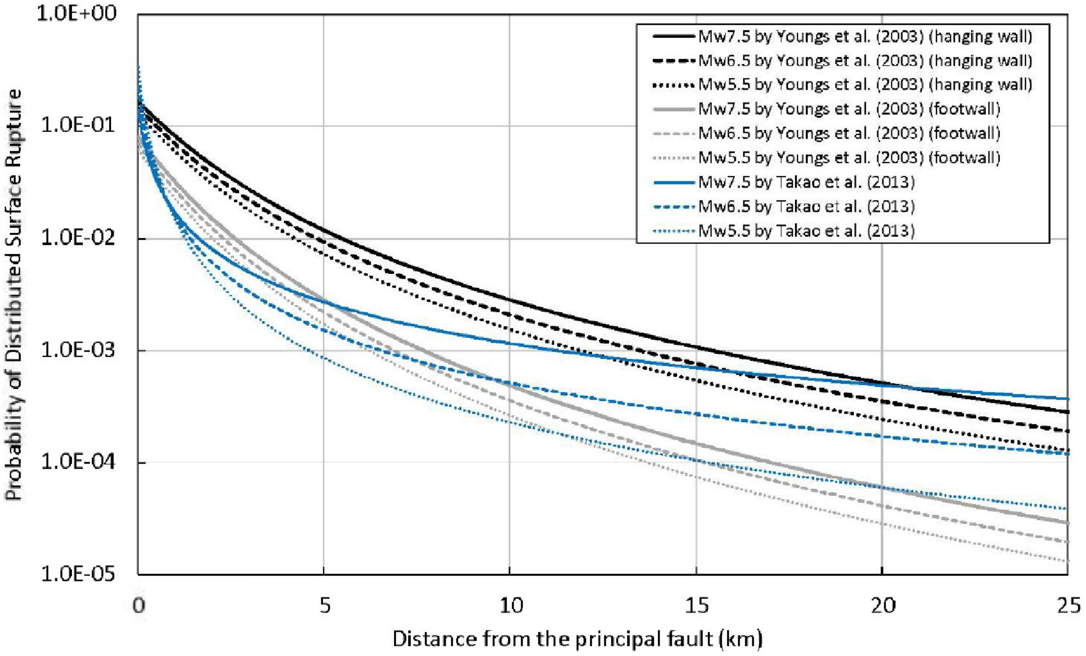

Figure 3-17. Probability of distributed surface rupture as a function of distance from PF, for various earthquake magnitude categories, from Youngs et al. (2003; normal faults only) and Takao et al. (2013; all fault types). Figure from IAEA, 2021, p. 92).

---

[1] In this section we use the term ”probabilities”, following the authors of the source publications. However the ”probabilities” described herein would more properly be termed frequencies of DF occurrence from limited data on surface ruptures. With the addition of future data these frequencies would change, indicating they represent only a sample, not the entire population.

In contrast, Petersen et al. (2011) used a power function equation to predict probability of strike-slip distributed ruptures within 2.5 km of the PF (Fig. 3-18). They considered any secondary faults >2.5 km from the PF to be ”triggered ruptures”.

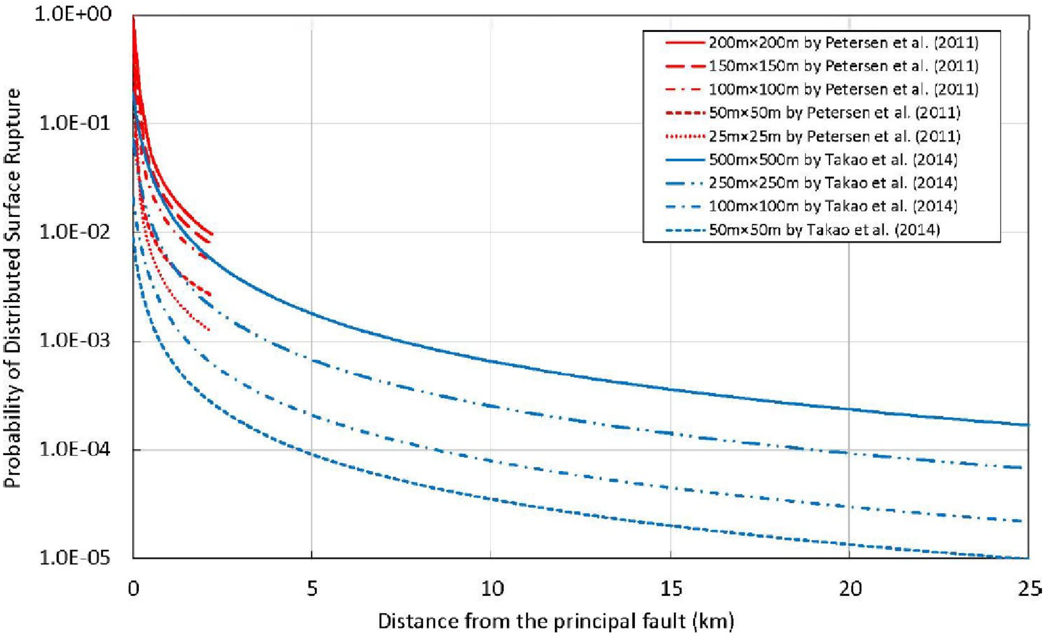

Figure 3-18. Probability of distributed surface rupture as a function of distance from PF, for various earthquake magnitude categories, from Petersen et al. (2011) and Takao et al. (2014).

These early estimates were based on a small database of DF measurements, so are now only of historic interest. Below we describe more recent papers based on greatly enlarged databases.

### 3.5.1. Probability of occurrence of DF as a function of distance to the PF; method of Nurminen et al., 2020

Nurminen et al. (2020) describe their method of computing the frequency of DFs encountered at various distances away from the PF (see Fig. 3-19): ” *The frequency–distance distributions of DFs is computed as the sum of slices intercepting at least a partial DF segment, normalized to the total number of the events. When the data of all earthquakes in the database are brought together, for each slice of distance r we can have a value ranging from 0 (none of the earthquakes has a rupture within the slice) to the total number of the events (all the earthquakes have at least a part of a DF segment intercepting the slice). This count is divided by the number of earthquakes to obtain the frequency.... Unlike the previous approaches utilizing gridding (Youngs et al., 2003; Petersen et al., 2011), the “slicing” method does not contain an assumption on the completeness of the database along the PF strike. We implicitly accept the very likely situation that not all the area is studied with the same precision in the field, as some parts can be hard if not impossible to reach. On the other hand, it is also likely that distributed rupturing does not occur homogenously along the PF strike due to the physical factors, such as subterranean structures and material distribution, and the mechanics of the process.*”

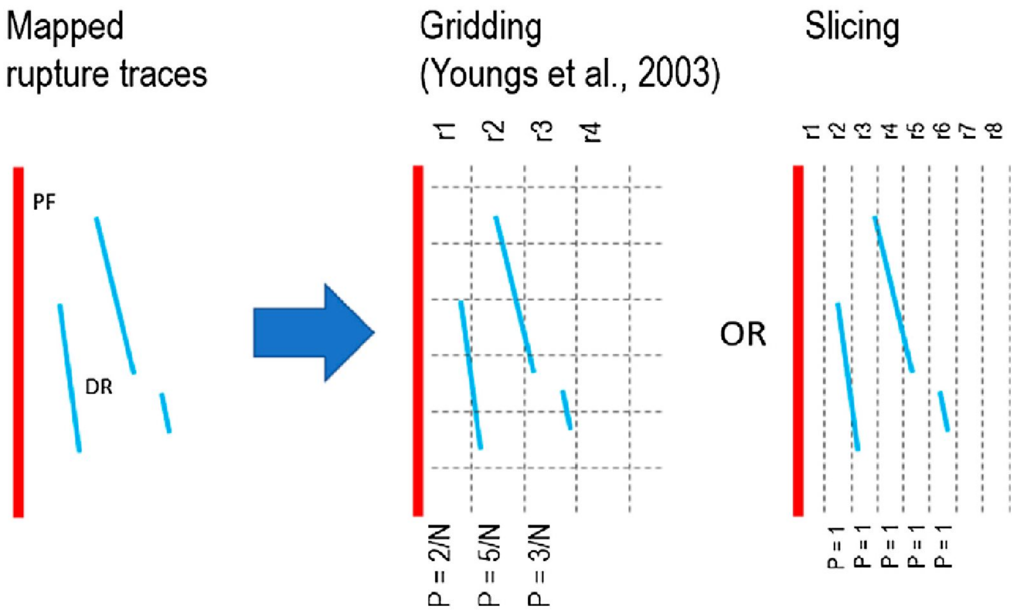

Figure 3-19. Map-view diagrams showing the difference between Youngs et al. (2003) method counting DFs in grid cells (”gridding”), as opposed to Nurminen’s method of counting DFs within fault-parallel slices or buffer zones (”slicing”). Red line, PF; thinner blue lines, DFs.

From the ”simple rupture” dataset, Nurminen et al.(2020) calculate probabilities of DFs occurring at various distances from the PF, using a multinomial logistic regression model with predictors X1 and X2, and the coefficient estimates, b1 and b2, for hanging wall and footwall (for coefficients, see Table 3-8). This practice follows Youngs et al. (2003) who proposed the first methodology for PFDHA.

Table 3-8. Empirical coefficients for Equation 4 of Nurminen et al. (2020).

| Coefficient | Footwall (FW) | Hanging Wall (HW) |
|---|---|---|
| Equation 4 | | |
| a | 8.5431 | 2.9179 |
| b1 | -1.5586 | -0.5566 |
| b2 | 0.0099 | 0.0030 |

Their predictive equation (Eq. 3) is:

$$\ln (Pf/(1-Pf)) = a + b1X1 + b2X2 \qquad \text{Eq. 3}$$

where:

-Pf is the probability of an outcome being in category “at least a partial rank 2 DR” with respect to the reference category of “no rank 2 DR,” and

-X1 and X2 are the earthquake magnitude and distance from the PF (in meters), respectively. –--empirical coefficients b1 and b2 are given in Table 3-8.

Their probability curves for three magnitudes (Mw 5.5, Mw 6.5, and Mw 7.5) are shown in Fig. 3-20.

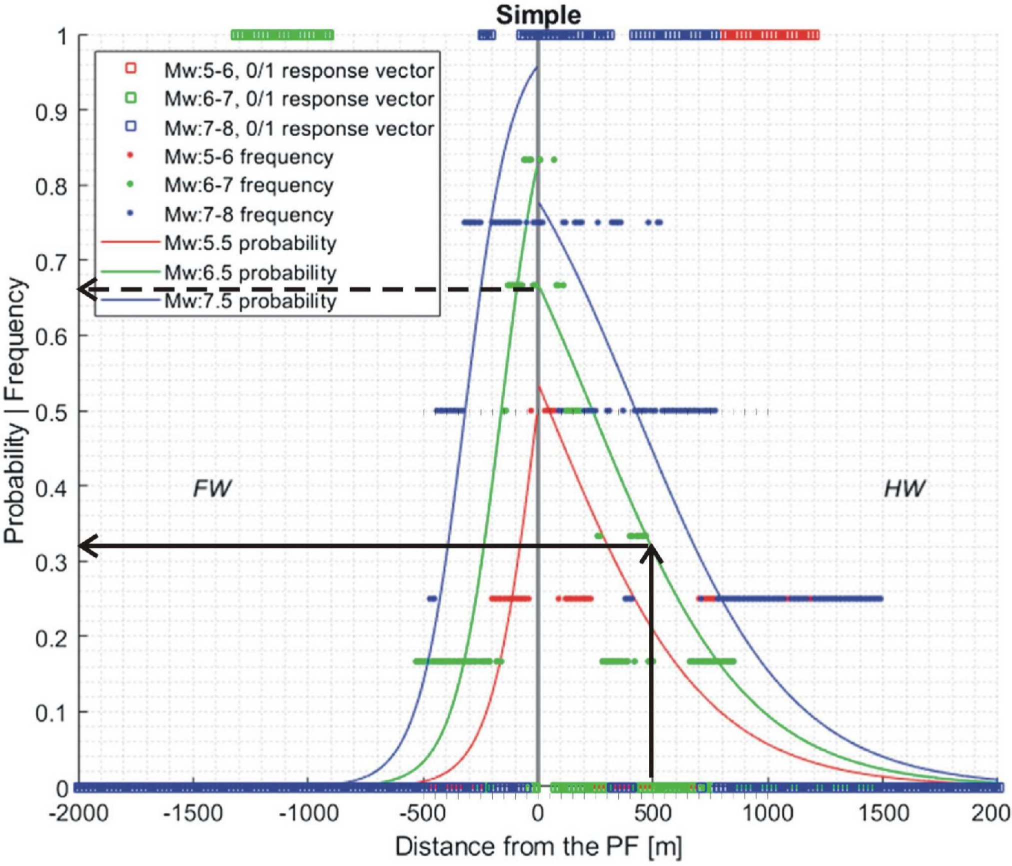

Figure 3-20. Probability of observing at least a partial DF as a function of distance from the principal fault. Curves on left half are for FW, those on right for HW. Black lines show example probability of having a DF on the HW in an M6.5 earthquake.

Interpreting the curves: We choose the M6.5 curve (green lines in Fig. 3-20) as our base case. On the FW, DFs are more abundant close to the PF, reaching an 82% probability of occurrence within ~10-20 m of the PF. With increasing distance away from the fault, probabilities of DFs drop rapidly, from 65% at a distance of 100 m, 42% at 200 m, 21% at 300 m, 9% at 400 m, and 3% at 500 m. On the HW, DFs are less common very close to the fault (66%) compared to the FW. However, DFs extend much farther away from the PF on the HW. For example, DFs have a probability of 3% at a distance of 1500 m from the PF, while on the FW that probability is found much closer to the PF (500 m). This asymmetry of wider DFs on the HW than FW affects both reverse and normal faults, as shown on Fig. 3-20. In reverse faulting the HW is forced to override the FW, often along a fault plane that flattens as it approaches the ground surface (McCalpin, 2009a, Figs. 5.21, 5.23, 5.24, 5.26, 5.29; McCalpin et al., 2020, Fig. 11). This creates secondary fault-bend folding in the HW (hanging-wall anticline), which in turn creates coseismic bending-moment ruptures(Fig. 3-4). In normal faults the origin of DFs on the HW is less obvious. Most normal surface faults steepen as they approach the ground surface and this ”fault refraction” creates thin vertical void slices in the HW, which collapse during shaking and create most of the simple DFs (McCalpin, 2009a, Chapter 3).

The probability of DFs increases with magnitude, as seen by the blue lines representing M7-8 earthquakes (M7.5 probability). Near the fault on the FW, probability of DFs is 96%, as opposed to 82% for M6.5s. The 3% probability band is shifted out to 700 m from the PF, compared to 500 m for M6.5. On the HW the difference is more extreme, with the 3% probability band shifted out to 1700 m.

### 3.5.2. Probability of occurrence of DF as a function of distance to the PF; method of Moss et al., 2022

Moss et al. (2022) likewise analyzed the SURE 2020 (which he calls SURE 1.0) database of surface ruptures. Like Nurminen et al. (2020) they used the slicing method to count DFs, but used much larger strips (100 and 500 m wide, unlike Nurminen’s 10 m wide). They state: ” *The data were also filtered to remove all deformations with the ranking of less than 2.0 which in the (Nurminen et al., 2021, 2022b) publications indicates principal deformations. We found no appreciable difference when rankings of 1.5 were filtered out or left in.*”

Like Nurminen et al. (2020), Moss et al. plotted the probability (frequency) of DFs in three magnitude ranges; M5-6, M6-7, and M7-8, and also for all magnitudes. Fig. 3-21 shows their frequency and cumulative frequency plot of DFs in 100 m-wide distance bins, for HW locations in M6-7 earthquakes. This is the same magnitude range as discussed in the previous section for M6.5 for frequency/probability. Their probability vs distance plot of SURE 1.0 data for magnitudes 7-8 can be found in Appendix B.

For the DFs in M6-7 earthquakes from the SURE 1.0 database, Moss et al. (2022) derive a cumulative distribution function (CDF) fitting the frequency data:

$$F(x)= a*\exp(b*x) + c*\exp(dx) \qquad \text{Eq. 4}$$

where:

X= distance of DF from PF

a=123.2

b= -7.639e-05

c= -127.1

d= -0.00135

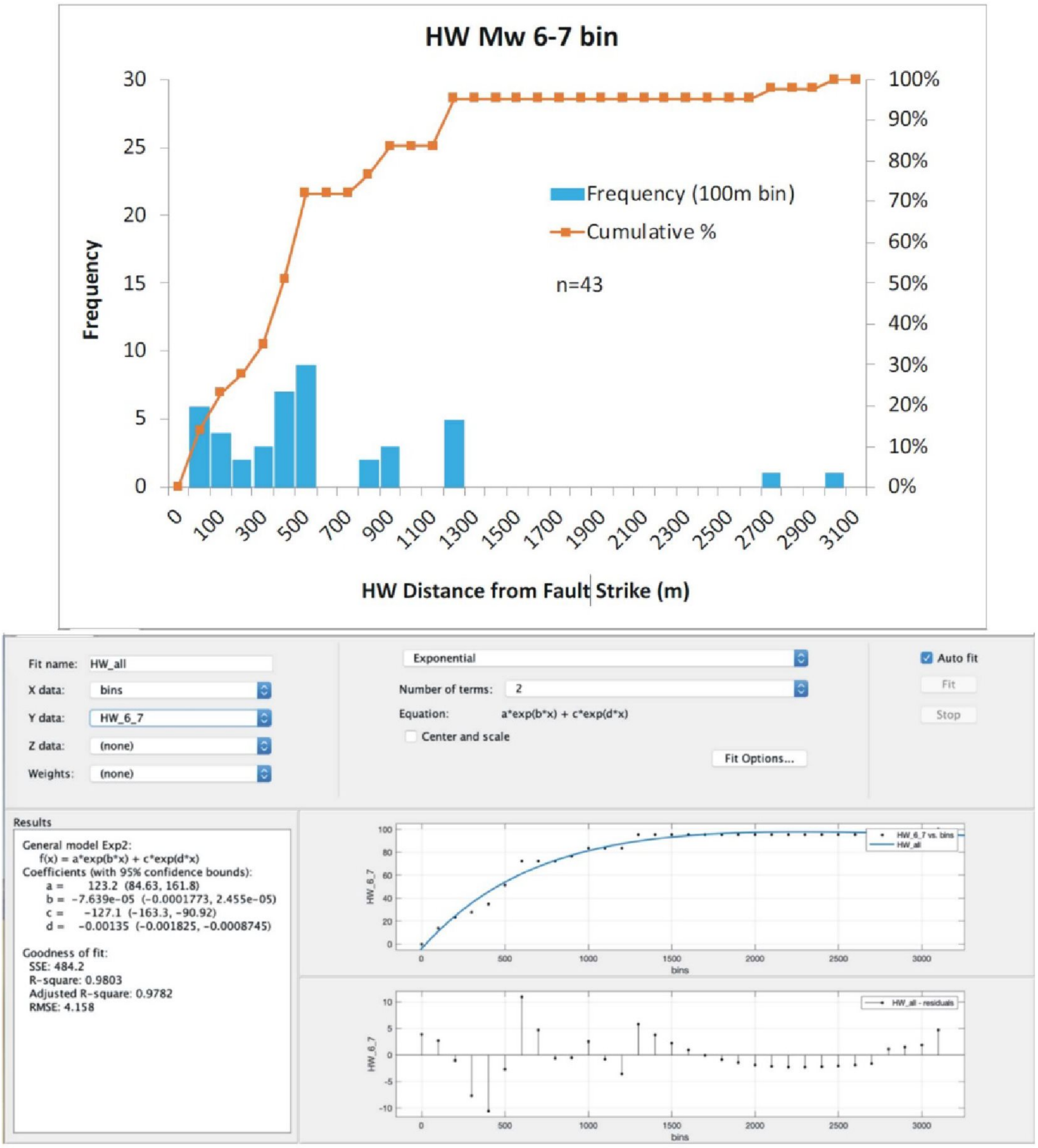

Fit name: HW_all
X data: bins
Y data: HW_6_7
Z data: (none)
Weights: (none)
Number of terms: 2
Equation: a*exp(b*x) + c*exp(d*x)
☐ Center and scale

```
General model Exp2:
    f(x) = a*exp(b*x) + c*exp(d*x)
Coefficients (with 95% confidence bounds):
     a =       123.2  (84.63, 161.8)
     b =  -7.639e-05  (-0.0001773, 2.455e-05)
     c =      -127.1  (-163.3, -90.92)
     d =    -0.00135  (-0.001825, -0.0008745)

Goodness of fit:
  SSE: 484.2
  R-square: 0.9803
  Adjusted R-square: 0.9782
  RMSE: 4.158
```

Figure 3-21. Frequency distribution (top) and CDF fitting (bottom) of the cumulative frequency data of DF versus distance from PF, on the HW of Mw 6-7 earthquakes in the SURE 1.0 database.

Note that this equation contains only a single independent variable (distance from the PF), unlike Nurminen's equation which contained two independent variables (distance to the PF, and earthquake magnitude). Because Moss et al. did not include a magnitude term in their probability equation, they had to generate different equations for M5-6, M6-7, and M78 earthquakes. The Moss equation has an r-squared of 0.98 and is plotted at the bottom of Fig. 3-21 as a blue line, with the cumulative frequency points as black dots. Test-solving this Equation for a distance of 500 m, we calculate a value for the cumulative distribution function to 53.9%..

After the larger FDHI dataset became available, Moss et al. (2022) created 12 plots of frequencies of DF as a function of distance from the PF, based on the FDHI dataset. Table 3-9 shows the figure numbers for graphs using various combinations of the independent variables (FW, HW, or both; magnitude range; and exponential DFs out to

3.5 km from the PF, versus all DFs [exponential and random] out to 15 km). Most of these Figures are in Appendices B and C; only illustrative examples are shown as Figures in this text.

Table 3-9. Index to figures in this report, of frequency of DF as a function of distance from the PF, based on the SURE 1.0 database (regular type) and the FDHI database (bold type).

| Moment Magnitude range | HW (Fig. number in text; Fig. number in Appendix B or C) | FW (Fig. number in text; Fig. number in Appendix B or C) |
|---|---|---|
| all | Freq. of DF vs. Dist. from PF; Fig. B-1 | Freq. of DF vs. Dist. from PF; Fig. B-5 |
| | **Freq. of DF vs. Dist. from PF; all DFs, (n=209), extends to 15 km; Fig. C-1** | **Freq. of DF vs. Dist. from PF; all DFs, (n=103), extends to 12.5 km; Fig. C-3** |
| | **Freq. of DF vs. Dist. from PF; exponential DFs, (n=172), extends to 3.5 km; Fig. C-2** | **Freq. of DF vs. Dist. from PF; exponential, (n=69), extends to 3.5 km; Fig. C-4** |
| M7-7.9 | Freq. of DF vs. Dist. from PF; Fig. B-2 | |
| | **Freq. of DF vs. Dist. from PF; exponential + random, (n=105), extends to 15 km; Fig. C-5** | **Freq. of DF vs. Dist. from PF; exponential + random, (n=53), extends to 12.5 km; Fig. C-10** |
| | **Freq. of DF vs. Dist. from PF; exponential DFs, (n=78), extends to 3.5 km; Fig. C-6** | **Freq. of DF vs. Dist. from PF; exponential, (n=18), extends to 3.5 km; Fig. C-11** |
| M6-6.9 | Freq. of DF vs. Dist. from PF; Fig. 3-23 and Fig. B-3 | |
| | **Freq. of DF vs. Dist. from PF; exponential + random; (n=97), extends to 15 km; Fig. C-7 and Fig.3-30** | **Freq. of DF vs. Dist. from PF; exponential, (n=51), extends to 3.5 km; Fig. C-12** |
| | **Freq. of DF vs. Dist. from PF; exponential DFs, (n=87), extends to 3.5 km; Fig. C-8 and Fig. 3-29** | Insufficient data |
| M5-5.9 | Freq. of DF vs. Dist. from PF; Fig. B-4 | |
| | **Freq. of DF vs. Dist. from PF; exponential DFs, (n=7), extends to 3.5 km; Fig. C-9** | Insufficient data |

Note the FDHI database of reverse events contained no random portion of displacements for the Mw 6.0-6.9 bin for foot wall. In addition, there were no foot wall distributed displacements measured for Mw less than 6.0.

An example of frequencies  of close-in DFs (or ”exponentially-distributed DFs” in the terminology of Moss et al. 2022) is shown in Fig. 3-22. These faults are closely associated with movement on the PF (Rank 2 DFs in the Nurminen scheme), may merge with the PF at shallow depths, and extend only ~2-3 km from the PF.

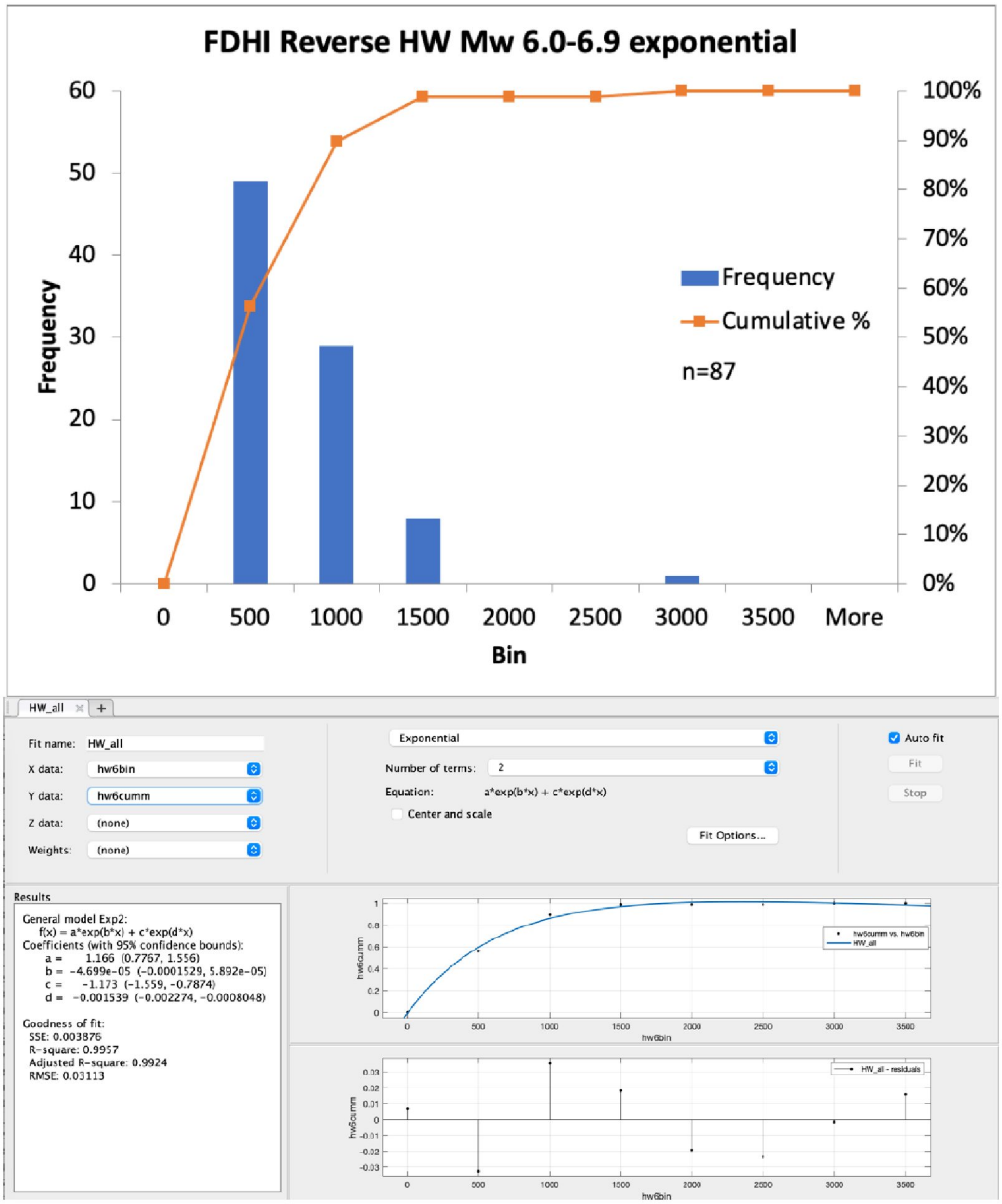

Fit name: HW_all
X data: hw6bin
Y data: hw6cumm
Z data: (none)
Weights: (none)

Exponential
Number of terms: 2
Equation: a*exp(b*x) + c*exp(d*x)
☐ Center and scale
☑ Auto fit

Results

```
General model Exp2:
    f(x) = a*exp(b*x) + c*exp(d*x)
Coefficients (with 95% confidence bounds):
      a =       1.166  (0.7767, 1.556)
      b =  -4.699e-05  (-0.0001529, 5.892e-05)
      c =      -1.173  (-1.559, -0.7874)
      d =   -0.001539  (-0.002274, -0.0008048)

Goodness of fit:
  SSE: 0.003876
  R-square: 0.9957
  Adjusted R-square: 0.9924
  RMSE: 0.03113
```

Figure 3-22. Frequency histogram and cumulative frequency data of DF on the HW, as a function of distance from the PF, for M6.0-6.9 earthquakes. This graph only covers the first 3.5 km away from the PF, where ”close-in” simple DFs are associated with movement on the PF, typically Rank 2 DFs in the Nurminen et al. scheme. Compare to Fig. 3-23 from SURE 1.0 data, which contains only 43 DFs, as opposed to the 87 data points here. The FDHI fit has an r-squared of 0.9957, versus the SURE 1.0 fit of 0.9803. Note also the large changes in coefficients a, b, c, and d in the two exponential equations.

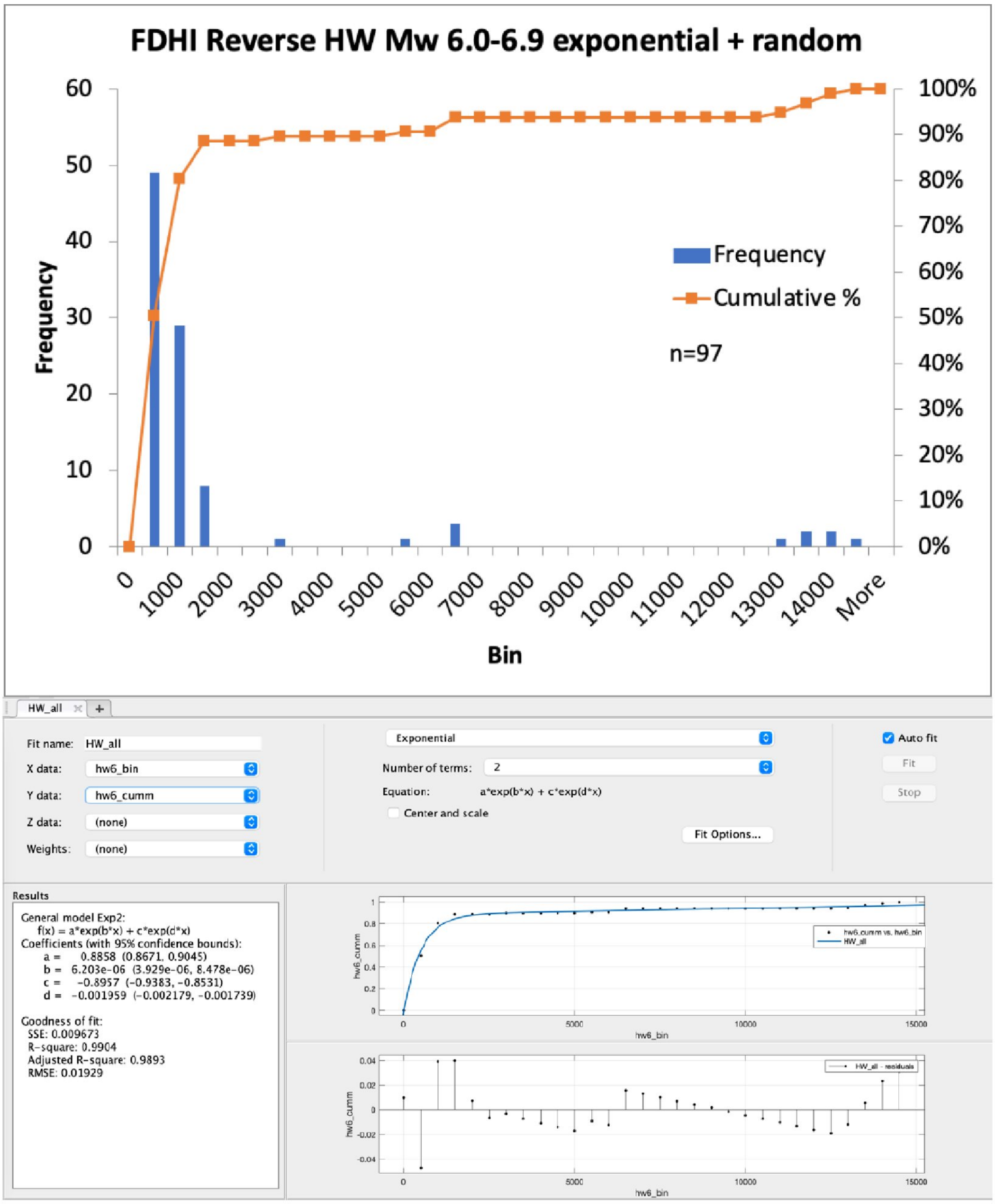

```
Fit name:   HW_all
X data:     hw6_bin
Y data:     hw6_cumm
Z data:     (none)
Weights:    (none)

Exponential
Number of terms:   2
Equation:          a*exp(b*x) + c*exp(d*x)
☐ Center and scale

☑ Auto fit
```

```
Results

General model Exp2:
    f(x) = a*exp(b*x) + c*exp(d*x)
Coefficients (with 95% confidence bounds):
      a =      0.8858  (0.8671, 0.9045)
      b =   6.203e-06  (3.929e-06, 8.478e-06)
      c =     -0.8957  (-0.9383, -0.8531)
      d =   -0.001959  (-0.002179, -0.001739)

Goodness of fit:
  SSE: 0.009673
  R-square: 0.9904
  Adjusted R-square: 0.9893
  RMSE: 0.01929
```

Figure 3-23. Frequency histogram and cumulative frequency data of DF on the HW, as a function of distance from the PF, for M6.0-6.9 earthquakes. This graph covers 15 km away from the PF, and includes both the ”close-in” simple DFs associated with movement on the PF (typically Rank 2), and complex DFs farther out (B-M, F-S, and Sy DFs of Nurminen). Note that ~89% of the DF distribution is 1500 m or less from the PF (simple DFs), whereas the remaining 11% represents complex DFs spread thinly out to a distance of 15 km. Compare to Fig. 3-21 from SURE 1.0 data, which contains only 43 DFs, as opposed to the 97 data points here.

## Summary of the Moss et al. 2022 equations.

One way to compare the 12 logistic regressions of Moss et al. 2022 (Appendix C) is to see how the 90th percentile frequency (~10% probability of exceedance) distance varies among different scenarios. All the Figures referred to are in Appendix C, and some are additionally used as examples in the text.

Table 3-10. Summary of the Moss et al. 2022 probability of DF relationships, using the FDHI dataset and the example of the DF to PF distance with only a 10% probability of exceedance. Cells in bold rectangle contrast probability distributions of DFs at three magnitude levels.

| Figure Number in Appendix C | Distance DF to PF; range analyzed (km) | DF on HW or FW? | Magnitude Range | Distance from DF to PF (km) at 10% probability of exceedance | No. of DFs | Remarks |
|---|---|---|---|---|---|---|
| C-1 | 0 to 15 | HW | 5.0-7.9 | 6.5 | 209 | Largest data set, includes all DFs (simple and complex reverse faulting) |
| C-2 | 0 to 3.5 | HW | 5.0-7.9 | 1.5 | 172 | 2nd-largest dataset, analyses only DFs within 3.5 km of PF |
| C-3 | 0 to 15 | FW | 5.0-7.9 | 12 | 103 | Sy DFs occur on FW far from PF |
| C-4 | 0 to 3.5 | FW | 5.0-7.9 | 1.5 | 69 | Within 3.5 km of PF, 10%PE is only 1.5 km; shows large difference between close-in, simple DFs and far-out complex DFs like Sy, B-M |
| C-5 | 0 to 15 | HW | 7.0-7.9 | 10 | 105 | As Magnitude decreases, the 10%PE distance overall decreases from 10 km to 3 km to 0.09 km. For the close-in DFs only, the 10%PE decreases from |
| C-6 | 0 to 3.5 | HW | 7.0-7.9 | 2.25 | 78 | |
| C-7 | 0 to 15 | HW | 6.0-6.9 | 3.0 | 97 | |
| C-8 | 0 to 3.5 | HW | 6.0-6.9 | 1.0 | 87 | |
| C-9 | 0.1 | HW | 5.0-5.9 | 0.09 | 7 | |

| | | | | | | |
|---|---|---|---|---|---|---|
| | | | | | | 2.25 km to 1.0 km to 0.09 km. |
| C-10 | 0 to 12.5 | FW | 7.0-7.9 | 12.25 | 53 | Compared to HW values, 10%PE distance on FW is slightly larger for M7-8 random, but smaller for M7-8 and M6-7 exponential. |
| C-11 | 0 to 3.5 | FW | 7.0-7.9 | 2.0 | 18 | |
| C-12 | 0 to 3.5 | FW | 6.0-6.9 | 1.5 | 51 | |

### 3.5.3. Width of the rupture zone; Method of Boncio et. al (2018)

Boncio et al (2018) analyzed the width of historic reverse-fault surface ruptures, measuring the width perpendicular to the PF from the DF farthest into the FW to the farthest into the HW. At the time of his compilation (2018) neither the SURE 2020 or FDHI surface-rupture databases existed, so he derived his data on distributed faulting directly from the published literature, with the help of Fiia Nurminen who had compiled much of the data for her MS thesis at Oulu Mining School.

Boncio et al. were the first to recognize the different types of DFs created by reverse ruptures, and correctly realized that the width of the rupture zone (WRZ) would depend on which categories (ranks) of DFs were used in the width measurement. Fig. 3-24 shows his raw data which separate different types of DFs. At the top (a), Boncio shows the width of DFs affected by ”complex ruptures” as described by Nurminen et al. 2020 and discussed earlier in Section 3. These include bending-moment ruptures (B-M, orange bars), flexural slip ruptures (F-S, red bars), sympathetic ruptures (Sy, green bars), and all the rank 2 DFs closer to the PF (blue bars). This graph shows that including B-M, F-S, and Sy DFs in the width measurement makes it very wide, from 2150 m into the FW and 2800 m in the HW. The Sy ruptures contribute most to this width, because they include sympathetic ruptures on faults that may (or may not) converge with the PF at depth, such as the Splinter fault on the Meckering rupture and the Footwall fault on the Tennant Creek rupture, which lie 1-3 km away from the PF.

The middle panel of Fig. 3-24 looks at a finer subdivision of DF types within a closer distance to the PF (from 550 m into the FW to 1550 m into the HW). These include all the faults labeled as ”Other types” in part (a) of the Figure.

The bottom panel (c) omits all the ”other types” of DFs and focuses on the five medium to large earthquakes that had the widest widths. Note that the gray bars are from the Tennant Creek 2 earthquake and its Footwall fault, which lies ~1 km from the PF. Boncio was not aware of the Meckering Splinter fault, which lies 3 km from its PF.

Boncio et al. then derived empirical cumulative probability distributions for his dataset. Like Nurminen et al. (2020), he created a ”simple thrust” subset of his reverse ruptures which did not contain complexities such as B-M, F-S, or Sy faults. He probably felt, like Nurminen, that simple ruptures made up the majority of past (and thus, likely future) ruptures, and would be a more realistic basis for predictions. His cumulative probability distributions and equations are shown for simple ruptures on Fig. 3-25; and for all ruptures (simple and complex) on Fig. 3-26. In Table 3-11 Boncio summarizes four percentiles for simple and all WRZs, plus the FW:HW ratio.

Table 3-11. Width of the rupture zone (WRZ) on the hanging wall (HW) and on the footwall (FW), and FW to HW ratio for: (a) "simple thrust" DFs (B-M, F-S and Sy excluded) and (b) all DFs.

| (a)Probability | WRZ HW | WRZ FW | Total WRZ | FW : HW |
|---|---|---|---|---|
| 90 % | 575 m | 265 m | 840 | 1 : 2.2 |
| 75 % | 260 m | 120 m | 380 m | 1 : 2.2 |
| 50 % | 80 m | 45 m | 125 m | 1 : 1.8 |
| 35 %[b] | 40 m | 20 m | 60 m | 1 : 2 |

| (b) Probability | WRZ HW | WRZ FW | Total WRZ | FW : HW |
|---|---|---|---|---|
| 90 % | 1100 m | 720 m | 1820 m | 1 : 1.5 |
| 75 % | 640 m | 330 m | 970 m | 1 : 1.9 |
| 50 % | 260 m | 125 m | 385 m | 1 : 2.1 |
| 35 %[c] | 130 m | 65 m | 195 m | 1 : 2 |

[a] Probabilities refer to cumulative distribution functions of Boncio et al (2018), this report Figs. 3-25 (Table a) and 3-26 (Table b).

[b] Corresponding to a sharp drop of data in the histograms of Boncio et al (2018) Fig. 4, close to the PF.

[c] Calculated for comparison with "simple thrust" database, but not corresponding to particular drops of data in the histograms of Fig. 5.

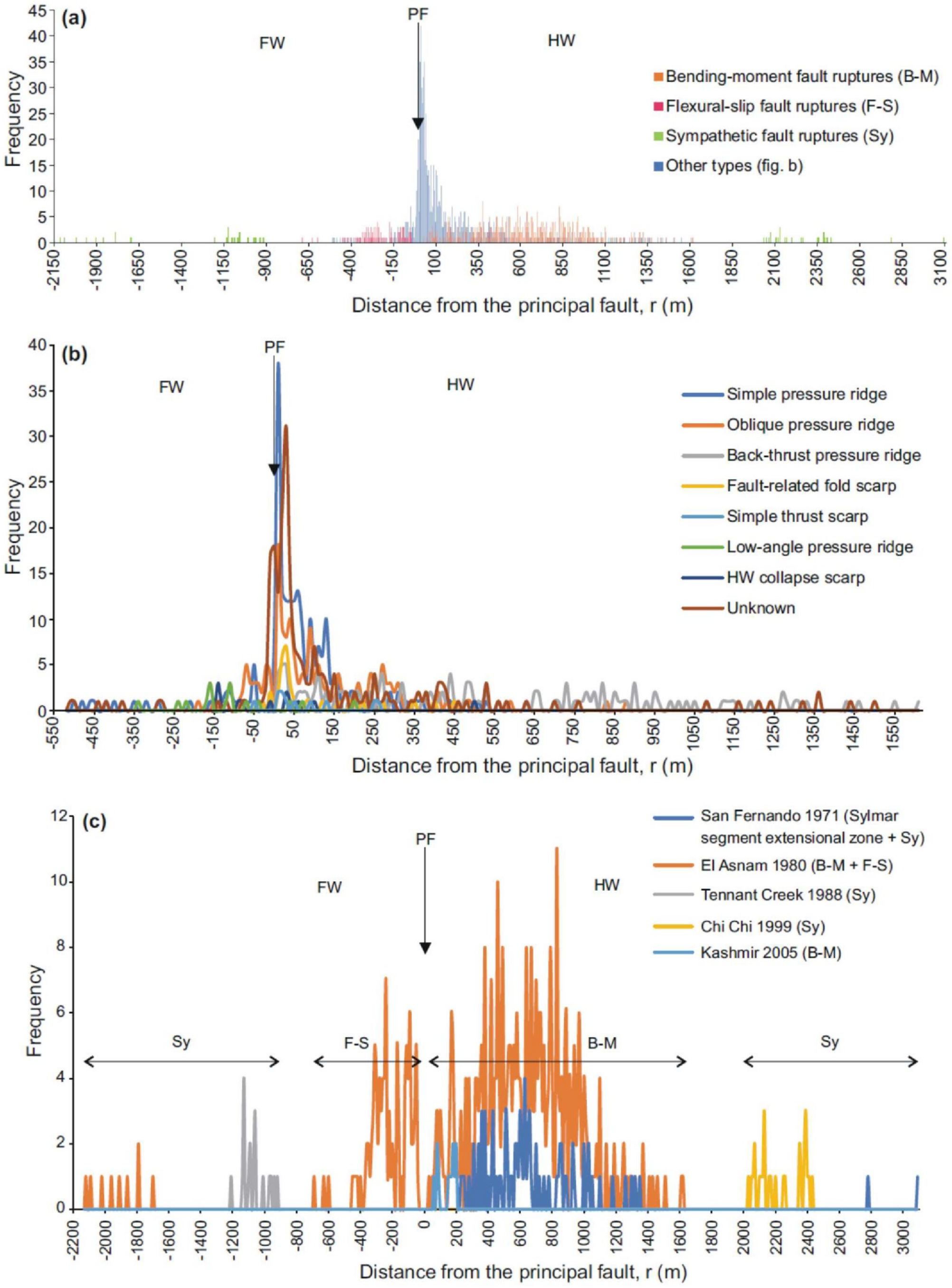

Figure 3-24. Frequency histograms for DFs as a function of distance ”r”. (a) complex DFs; (b) all simple DFs; (c) complex DFs from five selected ruptures. From Boncio et al. (2018).

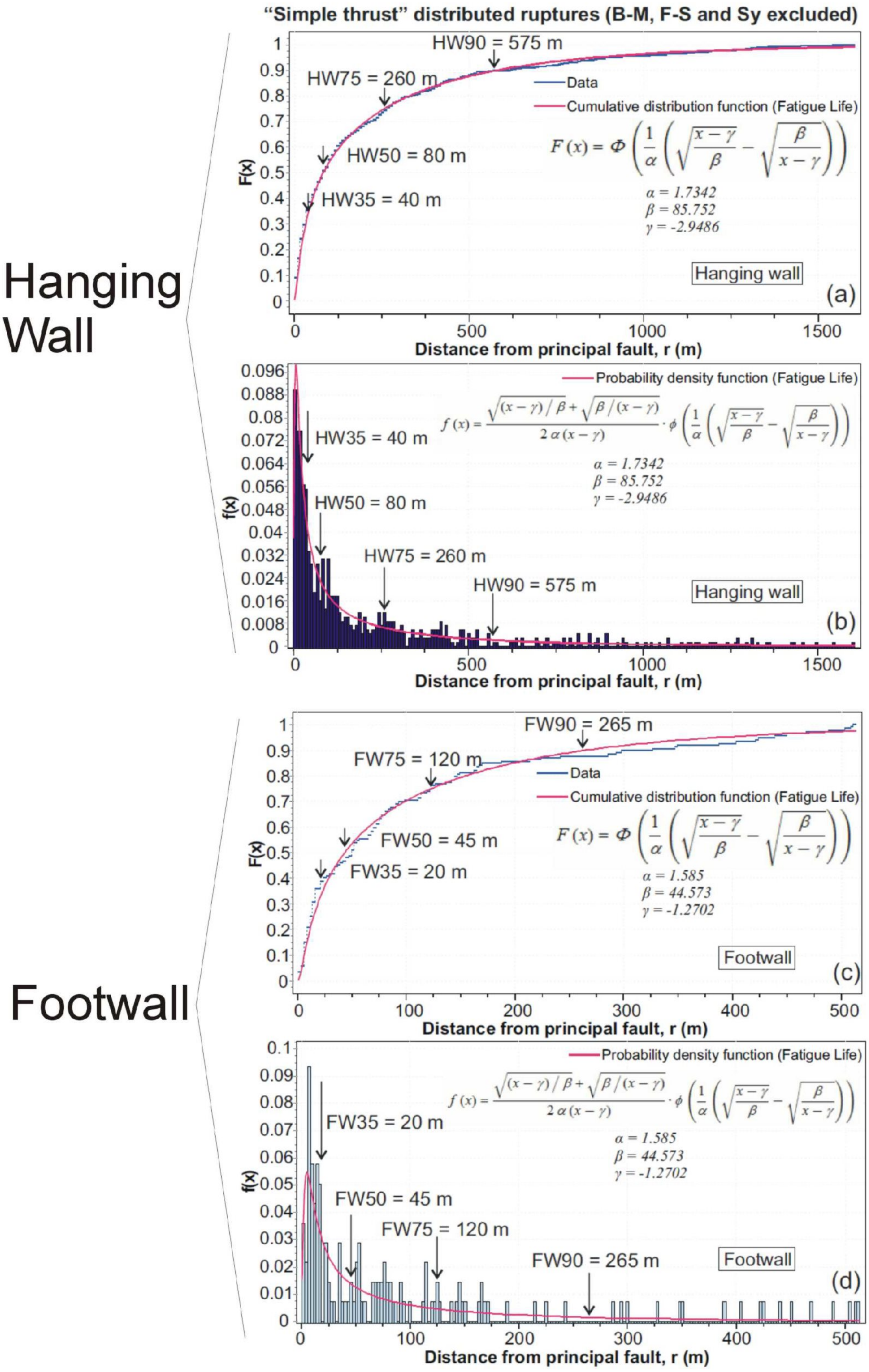

Figure 3-25. Probability density functions for simple DFs as a function of distance from the PF. HW DFs are tabulated within 1500 m of the PF, whereas HW DFs are tabulated only within 500 m of the PF. (a) cumulative distribution function (CDF), HW; (b) probability distribution function (PDF), HW; (c), CDF, FW; (d) PDF, FW. From Boncio et al., 2018.

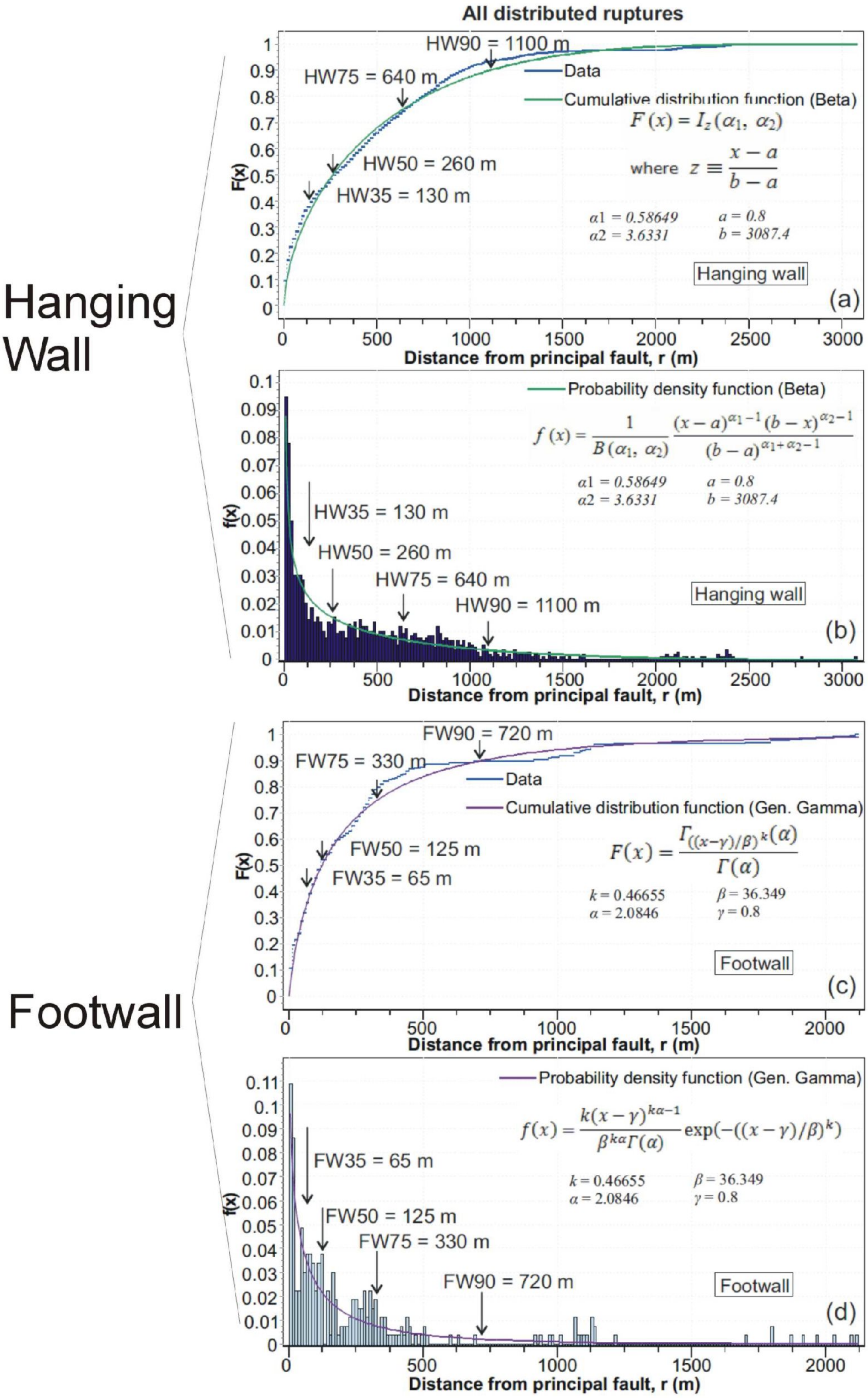

Figure 3-26. Probability density functions for ALL DFs as a function of distance from the PF. HW DFs are tabulated within 3000 m of the PF, whereas HW DFs are tabulated only within 2125 m of the PF. (a) cumulative distribution function (CDF), HW; (b) probability distribution function (PDF), HW; (c), CDF, FW; (d) PDF, FW. From Boncio et al., 2018.

At this point we should note that Boncio's analysis of DF probability data is based only on a single independent variable (r, the distance from DF to PF) and does not include a second term for earthquake magnitude. Boncio et al. (2018) address the effect of magnitude on WRZ in this way: *"In order to analyse the potential relationships between WRZ and the earthquake size, in [his] Fig. 6 the total WRZ (WRZ tot= WRZ hanging wall + WRZ footwall) is plotted against Mw..."* (our Fig. 3-27).

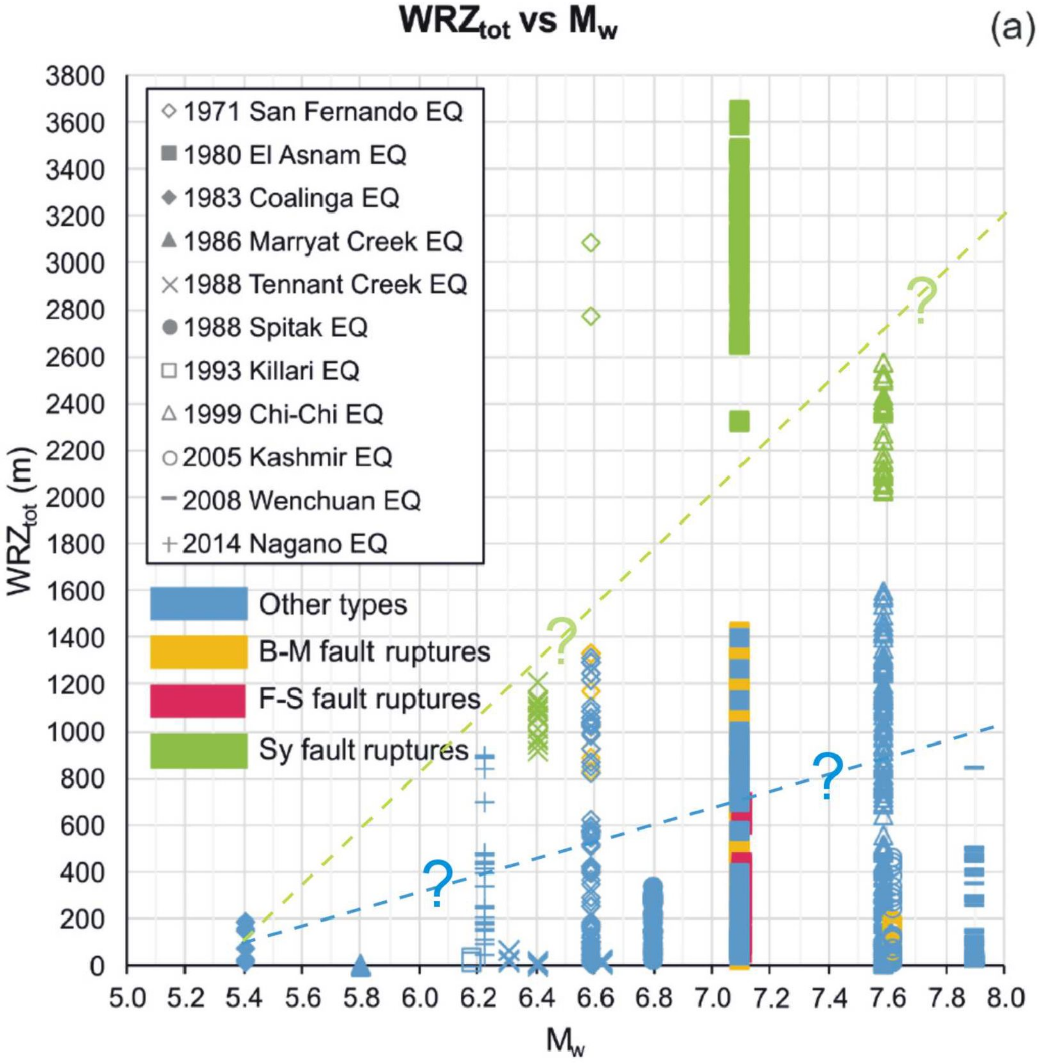

Figure 3-27. Diagram plotting the total WRZ (WRZtot= WRZ hanging wall + WRZ footwall) against earthquake magnitude (Mw), modified from Boncio et al. (2018). Dashed colored lines added by the author, as fit-by-eye trend lines for Sy DF ruptures (green) and all other rupture types (blue+yellow+red).

Boncio mentions that in Fig. 3-27 *"....a positive relation between the total WRZ and Mw is clear, particularly if sympathetic (Sy) fault ruptures are not considered. In fact, Sy data appear detached from the other data, suggesting that their occurrence is only partially dependent on the magnitude of the mainshock. They also depend on the structural features of the area, such as (1) whether or not an active, favourably oriented fault is present, and (2) its distance from the main seismogenic source."* This is a critical observation because, in our five Australian SCR ruptures analyzed in detail, two of the five contain Sy ruptures. So such ruptures might be characteristic of SCR ruptures in Precambrian cratons.

Boncio et al. (2018) admit that their study had a practical aim, to use the WRZ values for hazard assessment and mitigation.

### 3.5.4. How to use the DF probability-with-distance data to support regulations and/or design

The Nurminen et al. (2020) and Moss et al. (2022) papers did not address using their DF probability data for seismic hazard assessment. In contrast, Boncio et al. (2018) devote 2.5 pages of their paper to ”Comparison with Italian guidelines and implications for fault zoning during seismic microzonation.” They say their data *”can support the evaluation and mitigation of SFRH* [surface fault rupture hazard]*”*. By this they mean specifically, the process of zoning areas around active faults in which detailed hazard studies must be performed by law, such as in California’s Alquist-Priolo Earthquake Fault Zoning Act (e.g. Bryant and Hart, 2007). They do not address using their DF data for engineering design, because they analyzed only probabilities of DF occurring, rather than displacements on the DFs, which would of course be required for design. Nevertheless, Boncio et al. (2018) do make some remarks on the limitation of the DF database that would influence engineering design.

1-The first question they pose is: ”which set of data between “simple thrust” DRs [Fig. 3-25, Table 3-11a] and all DRs [Fig. 3-26, Table 3-11b] is the most appropriate to be used for sizing the fault zones.” They suggest using the results from “simple thrust” DFs in most cases, but omitting the outlier points beyond the 90th percentile. They suggest reserving the use of ”all DFs” data for areas with poor geologic knowledge.

2-They recognize that *”some secondary faults connected with the PF can be sufficiently large to have their own geologic and geomorphic signature, and can be recognized before the earthquake. Most likely, close to the surface these structures behave similarly to the PF, with their own DRs. Faults with these characteristics should have their own zone, unless they are included in the PF zone.”* These comments would apply to sympathetic DFs (Sy of Nurminen and Ross), such as the Splinter fault on the Meckering rupture and the Footwall fault on the Tennant Creek rupture.

3-They also point out: ”*Using Sy fault ruptures for shaping zones of fault rupture hazard would imply distributing the hazard within areas that can be very large... [see Figs. 3-25 and 3-26]. ...The size of the resulting zone would depend mostly on the structural setting of the analysed areas (presence or not of the fault, distance from the seismogenic source) rather than the mechanics which controls distributed faulting in response to principal faulting.”*

## 3.6. Displacement on distributed faults as a function of distance from the principal reverse fault (global datasets)

Displacement on DFs as a function of distance from PF was first addressed by Youngs et al. (2003) for normal faults. They derived an exponential function of DF displacement with increasing distance from the PF (their ”r”), for both HW and FW. Because the normal fault earthquakes in their dataset spanned a wide range of magnitudes (and thus, areal extent of PF and DF), they could not simply use absolute displacement values. Instead they ”normalized” all measured DF displacement values (their ”d”) by the size of the maximum displacement (MD) on the PF in each earthquake. This normalization removed the effect of their earthquakes being of different sizes.

Their best-fit equations were (also cited in IAEA, 2021, p. 97):

$d/MD= 0.35e-0.091r$ for the HW, and Eq. 5

$d/MD= 0.16e-0.137r$ for the FW Eq. 6

where:

d= displacement on the DF (meters)

MD= maximum displacement on the PF (meters)

R= distance from DF to PF (km)

A decade later Takao et al (2013) derived a similar equation for DFs in historic Japanese ruptures (all slip senses), normalizing DF displacements by both MD and AD. His exponential fit to empirical data (aggregating FW and HW DFs) yielded these two equations:

Their best-fit equations were (also cited in IAEA, 2021, p. 98):

$d/MD= 0.55e-0.17r$ , and Eq. 7

$d/AD= 1.9e-0.17r$ Eq. 8

where:

d= displacement on the DF (meters)

MD= maximum displacement on the PF (meters)

AD= average displacement on the PF (meters)

R= distance from DF to PF (km)

Graphs of the Youngs et al. (2003) and Takao et al. (2013) equations for DFs within 20 km of the PF are shown in Figs.3-28 (for d/MD) and Fig. 3-29 (for d/AD).

Additionally, Takao et al. (2013, 2014) derived an exponential fit to a mix of field data and experimental calculations, as (also cited in IAEA, 2021, p. 98):

$d/AD= 1.6e-0.20r$ Eq. 9

where:

d= displacement on the DF (meters)

AD= average displacement on the PF (meters)

R= distance from DF to PF (km)

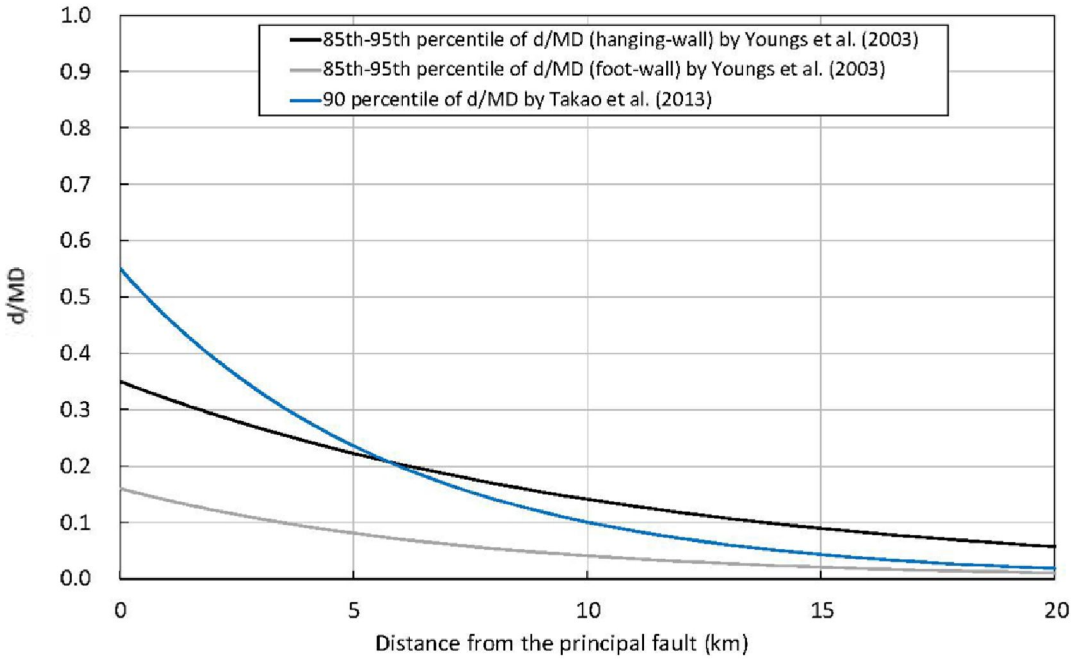

Figure 3-28. Graphs of d/MD for as a function of distance ”r” for Normal faults, from Youngs et al., 2003) and Takao et al. (2013).

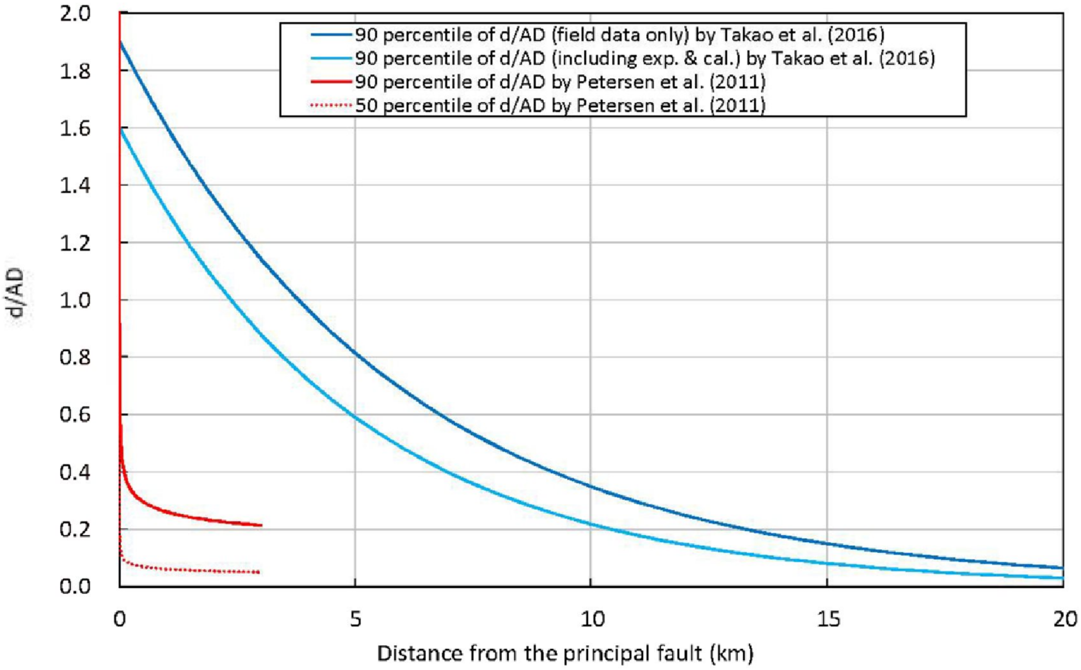

Figure 3-29. Graphs of d/AD for as a function of distance ”r” for Normal faults, from Takao et al. (2016, all slip senses) and Petersen et al., 2011 (strike-slip only). Peterson et al. consider secondary faults more than 3 km from the PF to be triggered faults, not DFs.

The Youngs and Takao method has one weakness, in that it normalizes displacement on DFs by the maximum displacement on the PF (MD). MD is an outlier value in the distribution of displacement along strike, by definition. Sometimes MD is fractionally larger than most of the other displacements along the length of the rupture, but sometimes it is much larger than even the 2nd-largest displacement, much less average displacement (AD). In other words, it is an outlier. The MD outlier may have resulted from a unique local site condition not representative of the rest of the rupture, or it might even represent a measurement error. By normalizing ”d” by ”MD”, Youngs and Takao were betting that the MD value in every rupture was a reliable, stable predictor of the typical slip on the fault plane, but did no detailed research to assure this was true. In 2003 (Youngs) it was considered valid to normalize ”d” by MD, but by 2013 (Takao) it was realized that AD was a more reliable, stable parameter for normalization.

### 3.6.1. Method of Nurminen et al., 2020

Nurminen et al. (2022) compiled a larger and more modern dataset of reverse faults than available to Takao et al. 2013, as part of the SURE 2020 (also called SURE 1.0) database (Table 3-12).

Table 3-12. Dataset of reverse surface ruptures analyzed by Nurminen et al. (2020), derived from the SURE 2020 database. MDv= maximum surface displacement, vertical component; MDn, maximum surface displacement, net slip. The five events in bright yellow (counting Tennant Creek as one event) occurred in ‘non-extended’ SCRs similar to Forsmark. Event in light grey occurred in the Indian craton, but no DF displacements were measured.

| EARTHQUAKE | DATE (yyyymmdd) | Moment Magnitude | Sense of Slip | SRL (km) | MDv (m) | MDn (m) | Types of DF |
|---|---|---|---|---|---|---|---|
| Calingiri, Australia | 19700310 | 5.0 | RL-L | 3.3 | 0.4 | 1.2 | 2 |
| San Fernando, CA, United States | 19710209 | 6.6 | R-LL | 16 | 0.76 | 2.5 | 2, 1.5, 21, 3 |
| El Asnam, Algeria | 19801010 | 7.1 | R | 31 | 5.0 | 6.5 | 2, 21 |
| Coalinga (Nunez), CA, United States | 19830611 | 5.4 | R | 3.3 | 0.50 | 1.0 | 2 |
| Marryat Creek, Australia | 19860330 | 5.8 | R-LL | 13 | 0.9 | 1.1 | 2 |
| Tennant Creek, Australia | 19880122 (event1) | 6.3 | R | 10.2 | 1.20 | 2.84 | 2 |
|  | (event 2) | 6.4 | R-LL | 6.7 | 1.10 | 2.60 | 2, 3 |
|  | (event 3) | 6.6 | R | 16 | 1.77 | 2.50 | 2 |

| | | | | | | | |
|---|---|---|---|---|---|---|---|
| Spitak, Armenia | 19881207 | 6.8 | R-RL | 25 | 1.6 | 2 | 2 |
| Killari, India | 19930929 | 6.2 | R | 5.5 | 0.6 | 1.2 | 2 |
| Chi, Taiwan | 19990920 | 7.6 | R-LL | 72 | 9.8 | 11.65 | 2 |
| Kashmir, Pakistan | 20051008 | 7.6 | R | 70 | 3.40 | 7.05 | 2 |
| Wenchuan, China | 20080512 | 7.9 | R-RL | 312 | 6.9 | 13.0 | 2 |
| Pukatja, Australia | 20120323 | 5.4 | R | 1.6 | 0.5 | 1.0 | 2 |
| Nagano, Japan | 20141122 | 6.2 | R | 9.34 | 0.8 | 1.60 | 2 |
| Petermann, Australia | 20160520 | 6.1 | R-LL | 20 | 0.9 | 1.9 | 2 |
| Le Teil, France | 20191111 | 4.9 | R | 5 | 0.23 | 0.33 | 2 |

Nurminen et al. (2020) had to deal with several practical issues in relating DF displacement to distance from the PF. They state: *” In situ [DF] measurements were performed and reported in different ways from one study to another. The field conditions (visibility, accessibility, presence of displaced, and matching features) impact on the possibility to measure the displacement, and the available slip components might not be uniform. In some, but not all cases, it is possible to derive all the slip components from available data. However, this is not always possible, and therefore some blanks remain in the database. For example, the net displacement (ND), which represents the best the total deformation caused by the earthquake, can be calculated as a vector sum of the vertical displacement (VD) and the two horizontal slip components (fault-parallel, and fault-normal slip), or obtained by utilizing the fault dip angle if not all the vectors are known. Fault attitude (strike, slip) is usually well documented along the PF, but the DR can have different orientations with respect to the PF, and the assumptions of dip angles cannot be justified especially if not reported for the DR trace in consideration. Thus, obtaining rigorous ND based on reproducible mathematical methods is not equally correct when it comes to DR, as the DR slip parameters are rarely reported with a high level of detail.”*

Nurminen et al. intuited that DF displacements would be controlled by their distance from the PF (s in the equation below) and by earthquake size. Earthquake size could simply be represented by the moment magnitude (m), but if that value were applied to the entire length of the PF, it would ignore the increase in PF slip towards the center of the PF and decrease towards the ends. Perhaps they also noticed that DFs seemed to have larger displacements where displacements on the PF were larger. Because PF displacements are larger in the center of a rupture and decrease to zero at the ends, this implies that DF vary likewise along strike. Thus, they did not want to normalize their ”d” data by a single PF displacement such as MD or AD, but instead wanted to relate ”d” to the PF displacement closest to the DF measurement site (see below). Their final equation includes both earthquake magnitude (m) and displacement on the PF (DN) as independent variables.

In a perfect world, every measured DF displacement would have a corresponding measured PF displacement directly opposite it. In practice, DF displacement points tend to fall (randomly) between displacement measurements on the PF. Nurminen et al. therefore decided to ’interpolate’ what the PF displacement should be (DN in Fig. 3-30) directly opposite the DF displacement point (ps), based on the two closest measurements on the PF (VD1 and VD2 in Fig. 3-30).

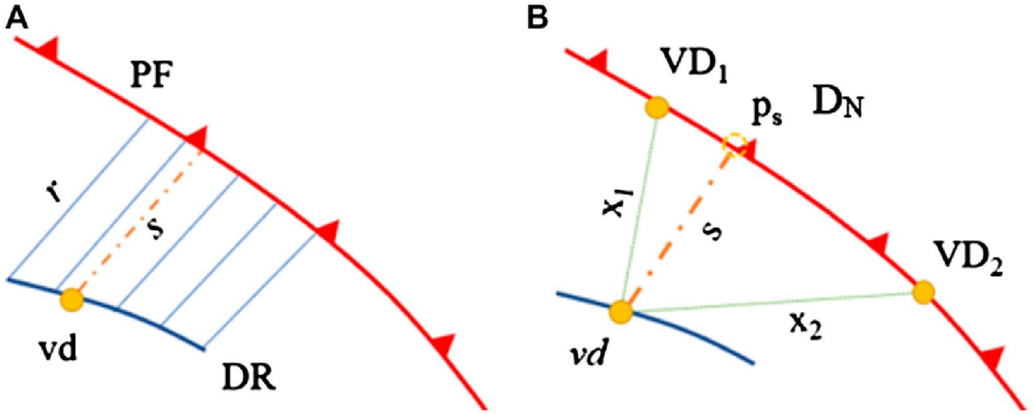

Figure 3-30. Measurements obtained from the georeferenced maps and displacement data of each earthquake in the dataset distinguishing the principal fault (PF, red line) and distributed ruptures (DR, thick blue line). (A) vd, vertical displacement at a point on the DR. (B) VD, vertical displacement at a point on the PF; Point ps is the nearest point on the PF to the vd point. DN (normalized VD) on the PF at ps is interpolated according to the following equation:

$$D_N=(VD_1x_{2+}\ VD2_2x_1/(x1+x2)m \qquad \text{Eq. 10}$$

Once they solved the problem of how to calculate DN, Nurminen et al. performed multiple regression of the dependent variable Y (measured vertical displacement on the DF) to: the distance from the PF (s); the interpolated vertical displacement on the PF (DN); and the earthquake magnitude (m), as seen below:

$$\ln(Y) = a + b1(\ln(s)) + c1(\ln(DN)) + d1(m) \qquad \text{Eq. 11}$$

where:

Y= median expectation (50 percentile) of vd (the vertical component of DF displacement), in meters

s= closest distance of DF displacement measurement to the PF (in meters)

DN= interpolated vertical displacement on the PF closest to the measured DF displacement point

M= earthquake moment magnitude

The best-fit multiple regression equation had the following empirical coefficients (Table 3-13), with residual standard deviations of 0.88 on the FW and 0.91 on the HW.

TABLE 3-13.| Coefficients for Equation 11 (Nurminen et al. ,2020) from her data set of “simple ruptures.”

| Coefficient | Footwall (FW) | Hanging Wall (HW) |
|---|---|---|
| Equation 6 | | |
| a | -5.1043 | -4.2549 |
| b1 | -0.6483 | -0.1514 |
| c1 | 0.1983 | 0.4404 |
| d1 | 0.9461 | 0.5711 |
| Std | 0.8812 | 0.9129 |

Std= residual standard deviation

Fig. 3-31 shows correlations between Y and s, DN, and m. In row A (HW data only) one can see a very weak-to-indistinguishable negative correlation between ”vd” and ”s”; a very good positive correlation is between ”vd” and ”DN”; and a slightly weaker positive correlation between ”vd” and ”m”. These trends are reflected in the HW coefficients [Table 3-13] for those respective parameters in Equation 6 (-0.1514 for ”s”; 0.4404 for DN; and 0.5711 for ”m”). The coefficients imply that the correlation of ”vd” with ”m” (earthquake magnitude) is actually a bit stronger than with ”DN” (displacement on the PF opposite the DF).

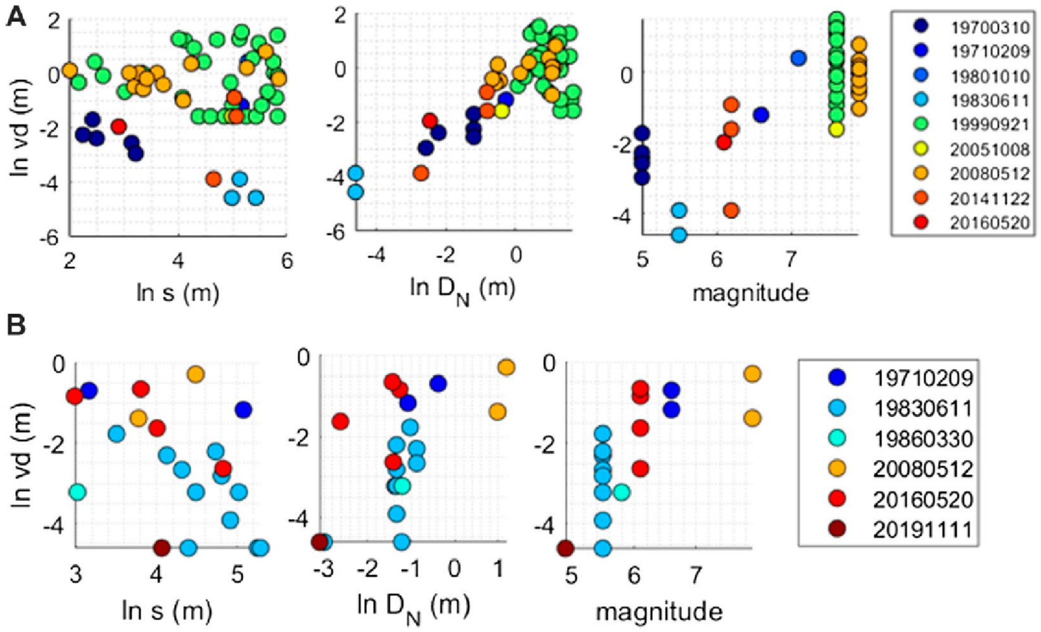

Figure 3-31. Bivariate plots of ln vd (vertical DF displacement) as a function of three independent variables (ln s, where ”s” is distance from DF measurement point to closest point on PF; ln DN, where DN is vertical displacement on the PF at that closest point; and m, earthquake magnitude. Row A, data from HW; row B, data from FW. From Nurminen et al, 2020.

In Row B (FW data only) one can see a moderately strong negative correlation between ”vd” and ”s”; a weak positive correlation is between ”vd” and ”DN”; and a moderately strong positive correlation between ”vd” and ”m”. These trends are reflected in the FW coefficients [Table 3-13] for those respective parameters in Equation 6 (-0.6483 for ”s”; 0.1983 for DN; and 0.9461 for ”m”. The coefficients imply that the correlation of ”vd” with ”m” is actually a bit stronger than with ”DN”.

## 3.6.2. Method of Moss et al., 2022

Moss et al. (2022) is the most recent quantitative analysis of surface rupture, which covers principal and distributed faults, and their probabilities and displacements. Like Youngs et al. (2003) and Takao et al. (2013, 2014, 2016), Moss analyses field measurements of d, normalized to MD or AD, as a function of distance from DF to PF (”r”, in meters). Figs. 3-32 (HW) and 3-33 (FW) compare the d/MD ratio for all three slip senses of ruptures (normal, red line; strike slip, yellow line; and reverse+strike slip from Japan; blue line).

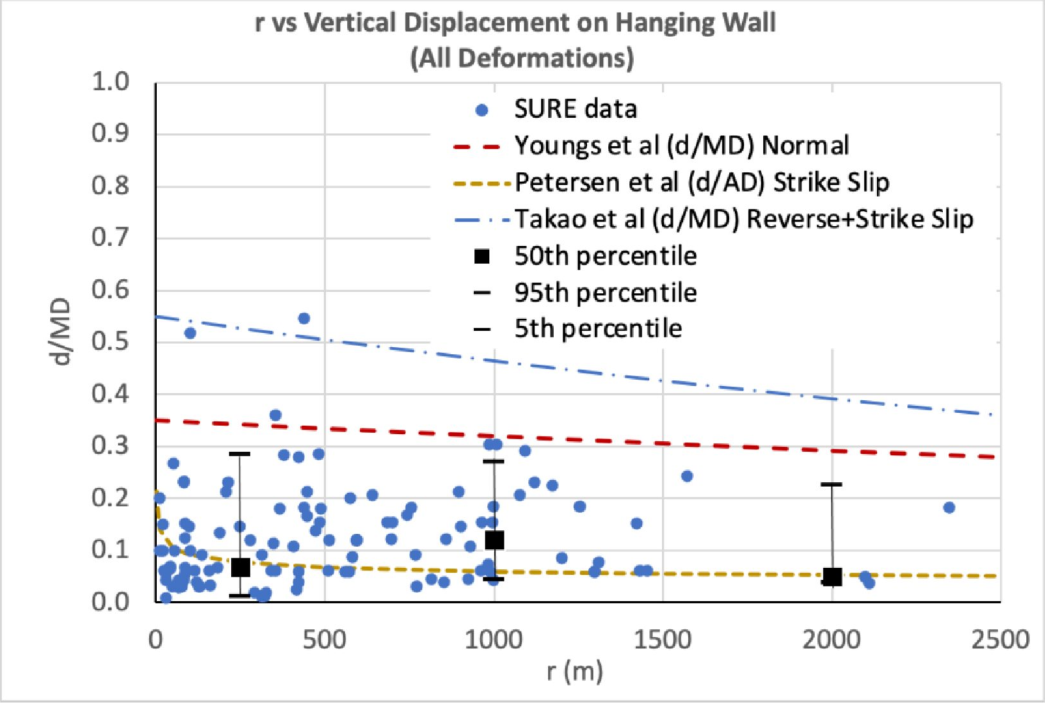

Figure 3-32. Ratio of d/MD for DFs on the HW, as a function of distance from the PF (0-2500 m). From IAEA, 2021, p. 56. Data from SURE 2020 (SURE 1.0).

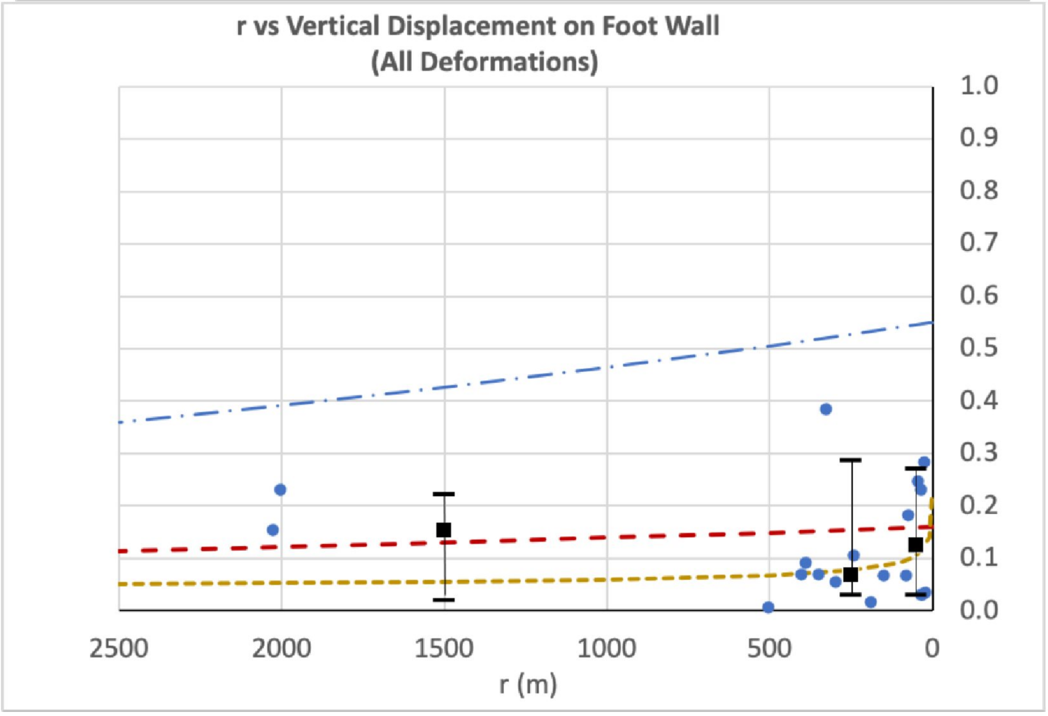

Figure 3-33. Ratio of d/MD for DFs on the FW, as a function of distance from the PF (0-2500 m). From IAEA, 2021, p. 56. Data from SURE 2020 (SURE 1.0).

During the preparation of the Moss et al. 2022 study, the new FDHI surface rupture database became available. The FDHI database contained 20 Reverse ruptures in contrast to SURE 1.0 (only 6 events). Analysis of the larger FDHI database showed something not seen in the SURE 1.0 database. Moss et al. 2022 recognize an *exponentially* decreasing group of DFs within a few km of the PF, followed by a random group that can reach tens of kilometers from the PF (this is the same approach Moss et al. used for analyzing *occurrence probability* of DF ruptures, see Table 3-9 and Figs. 3-22 and -23). The exponential group agrees with analytical solutions (such as Takao et al.) as well as with prior SURE 1.0 data, whereas the random group of DFs represents complex ruptures containing higher-Rank DFs, such as the sympathetic faults in the Meckering and Tennant Creek ruptures discussed previously (these complex ruptures were not contained in SURE 1.0). After examining the events that contribute to the random group of the distributed displacements (Wenchuan, Kaikoura, and Rikuu), Moss et al. (2022) concluded these far displacements can be attributed sympathetic and/or conjugate faults and therefore are controlled by a different physical process than the close-in, Rank 2 simple DFs that flank the PF.

Thus Moss et al. (2022) separated the data and provided distributions that fit both phenomena;

a) A single fault trace where the mechanics of distributed displacements can be conceptualized similar to the analytical solution presented above (this would be simple distributed faulting as defined by Nurminen et al, 2020, mostly Rank 2)

or

b) A complex fault system where distributed displacements may occur at larger distances due to sympathetic release on adjacent or nearby faults (this would be complex distributed faulting as defined by Nurminen et al, 2020, including Rank 1.5 (primary DFs); Rank 21 (B-M faults); Rank 22 (F-S faults), and Rank 3).

Moss et al. (2022) wished to derive an equation of the form:

$d/MD= C1e-C2\ r$ Eq. 12

where:

d= displacement on the DF (meters)

MD= maximum displacement on the PF (meters)

R= distance from DF to PF (km)

C1, C1= empirical constants

This is the same form of equation described in Section 3.6 that was used on the older data sets of Youngs et al. (2003) and Takao et al. (2013, 2014, 2016). However, Moss et al. 2022 had access to the newer, larger FDHI database, so wished to perform a more rigorous analysis. This analysis would have to address two outstanding issues:

(1) the importance of correctly characterizing the MD and AD values in each rupture, because they would be used as the normalizing value for DF displacements ”d” or ”vd”, and
(2) how to incorporate the two DF distributions recognized in their probability of faulting analysis of Section 3-5 (the close-in, simple DFs, with exponential decay away from the PF, versus the farther-out, complex DFs of higher rank, of a random nature).

To address the first issue, Moss et al. (2022) re-computed all the MD and AD values for reverse faults. To address the second issue, they produced separate regression equations for DFs depending on whether they represented the close-in, simple, ”exponential” DFs, or farther-out, complex, random DFs.

Moss 2022 Equations fit to the hanging wall DF displacements are:

For $r\ from$ 0 $km\ to$ 5.5 $km$:

$d/MD$= 0.58 $*$ ($-$0.17 $*$ $r$) Eq. 12

For $r$ > 5.5 $km$:

$d/MD$= 0.22 Eq. 13

Equations fit the foot wall DFs are:

For $r\ from$ 0$km\ to$ 6.5$km$:

$d/MD$= 0.58 $*$ ($-$0.26 $*$ $r$) Eq. 14

For $r$ > 6.5 $km$:

$d/MD$= 0.09 Eq. 15

Where d=vertical displacement on the DF (m)

MD= maximum displacement on the PF (m)

r= distance from DF to PF (km)

Note that within the closer distance intervals, the equations are exponential, and in the farther distances, they are linear. Figs. 3-34 and 3-35 show their solutions, compared to curves from earlier publications.

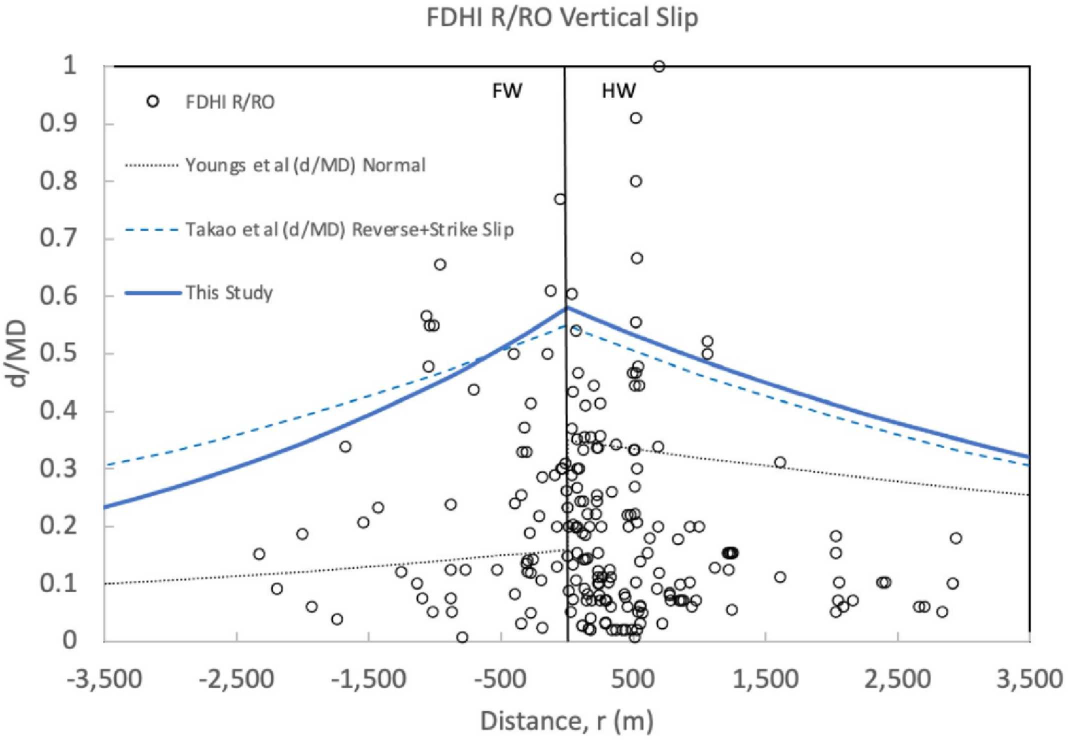

Figure 3-41. Plot of near fault (<3km) d/MD footwall and hanging wall FDHI data showing relationships from prior studies (dashed lines) and recommendations from Moss et al., 2022 (solid blue line). From Moss et al., 2022, their Fig. 5.31.

One odd thing to note is that Moss et al. (2022) never identify the ruptures they used to create their empirical equations for distributed displacement. So, although they show roughly 150 distributed displacement points on Figs. 3-41 and 3-42, there is no way to re-create their equations without knowing which ruptures they based the equations on.

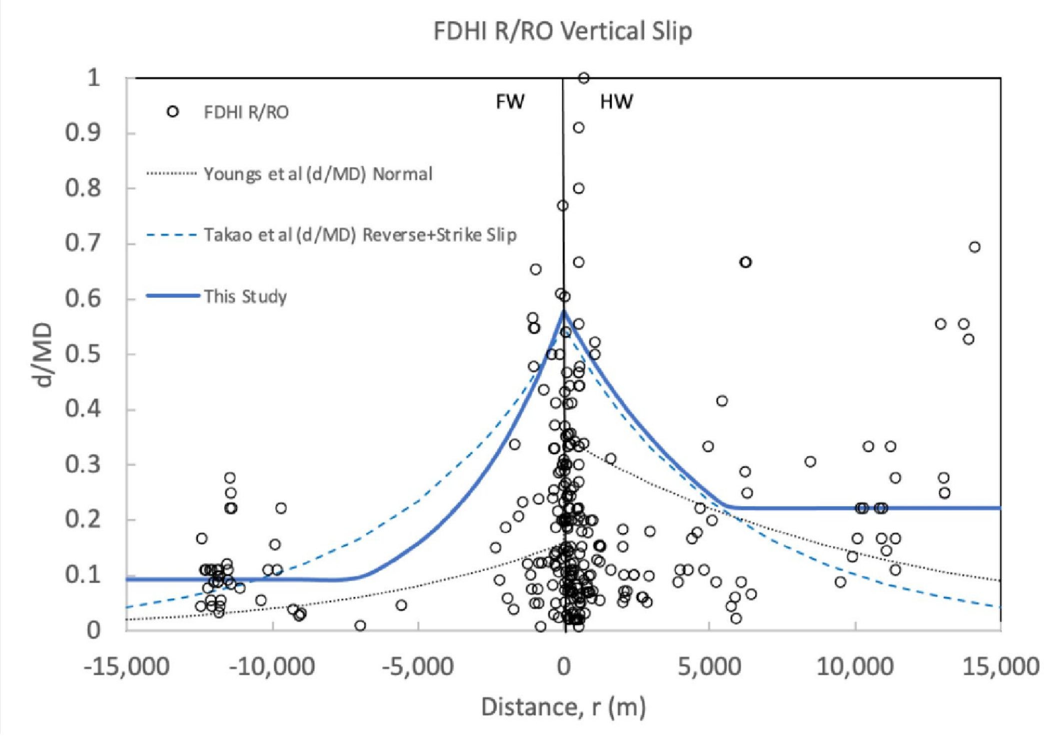

Figure 3-42. Plot of all d/MD footwall and hanging wall FDHI data showing relationships from prior studies (dashed lines) and recommendations from Moss e al. 2022 (solid blue line).

The recommended curves of Moss et al. (2022; solid blue lines in Figs. 3-34 and -35) are a composite of the exponential portion and the random portion. The exponential portion is fit to the 95th percentile of the FDHI data (Fig. 3-34) and the random portion to the 50th percentile of the FDHI data (Fig. 3-35). As can be observed, the exponential portion is quite similar to that suggested by Takao et al. (2014).

## 3.7. Revised regressions using only rupture data from stable continental regions

The two prior sections on probability of DF as a function of ”r” (Sec. 3.5) and displacement of DF as a function of ”r”, used whole data sets of reverse faults. To limit the datasets for more specific hazard applications, separate equations were derived for reverse faults in different earthquake magnitude classes. However, no quantitative analysis was made for a subset of reverse ruptures defined by geological setting. Many previous studies had remarked on how reverse ruptures in Stable Continental Regions (SCRs) produced abnormally long and complex ruptures for their relatively modest magnitudes, as compared to the more abundant reverse ruptures in active fold-thrust zones related to plate boundaries (Clark, King, Crone and Machette, etc.). The exact reason for this discrepancy is unknown.

For comparing historic empirical rupture data with Forsmark shear displacement estimates from numerical models, we would prefer to use only empirical data from an SCR seismotectonic and geologic setting like Forsmark. Accordingly we created a subset of reverse ruptures in SCRs based on the SCR earthquakes contained in the FDHI database (see Sec. 3.4). We identified five ruptures, all in Australia, where measurements were made both on the PF and DF (Table 3-14).

Table 3-14. Number of displacement measurements made on the five Australian SCR ruptures.

| **EQ** | **TOTAL No. of Displ. Meas.** | **No. of PF Meas.** | **No. of DF Meas.** | **No. of DF Meas. of Type/Rank** | | |
|---|---|---|---|---|---|---|
| | | | | **PDF/1.5** | **DF/2** | **DF/21, 22, 3** |
| Meckering | 96 | 81 | 15 | 0 | 5 | 10 |
| Calingiri | 41 | 35 | 6 | 0 | 6 | 0 |
| Cadoux | 54 | 38 | 16 | 4 | 12 | 0 |
| Tennant Creek | 64 | 58 | 6 | 0 | 0 | 6 |
| Petermann | 104 | 99 | 13 | 0 | 13 | 0 |
| TOTALS | 359 | 311 | 56 | 4 | 36 | 16 |

Of the 56 DF measurements in Table 3-14, 33 were on the FW and 23 on the HW. Obviously this data subset is much smaller than the overall FDHI reverse rupture dataset (60 events; Table 3.1). The five earthquakes are even a subset of nine historic Australian ruptures, because in only five of those events were displacements measured both on the PF and DFs. We extracted the FDHI measurements for the five events and divided their DF displacements into FW and HW.

We then downloaded the files ”FDHI Project Database Report Rev3 – All Appendices. Zip” from: http://www.risksciences.ucla.edu/girs-reports/2021/08

The unzipped Appendices contain ”zipped Flatfiles” that unzip to GIS Shapefiles containing the worldwide mapped rupture trace vectors (A06_FDHI_FLATFILE_RUPTURES_rev2.shp) and all the displacement measurement points (A05_FDHI_FLATFILE_MEASUREMENTS_rev2,shp). The latter point set contains extensive attribute values.

For the five Australian ruptures we opened the two files in Global Mapper v22 GIS and manually re-measured all the parameters required by the Nurminen et al. (2020) Equation 6 (Y, s, DN, m) for all DF measurement points on the five SCR ruptures. During this process we identified numerous discrepancies between displacement measurements in the Measurements flatfile, and rupture vector polylines in the Rupture flatfile. These included misregistration errors in the rupture Shapefiles between the measurement point locations and the rupture traces, and discovering that ”distance to rupture” in the Measurement flatfile was not the distance between the DF and PF, as we originally assumed. Instead, the ”distance to rupture” field lists only the distance between the DF measurement point and the nearest mapped rupture. One might think this field would contain only zeroes, since displacement measurements could only be measured on a fault trace. It turned out that the ”distance to rupture” value simply represented the GIS misregistration between the DF measurement point and the location of the mapped DF trace on which the measurement was made. We fixed those errors and updated our Excel versions of the measurement Flatfiles (Table 3-15, 3-16).

| eq_name | magnitude | RUP_ID[1] | DF-PF dist (s)[2] | depth_km[3] | vs_central[4] | recom_net (m)[5] | Dn[6] | ln Y[7] | ln s | ln Dn | d1*m[8] |
|---|---|---|---|---|---|---|---|---|---|---|---|
| Meckering | 6.59 | 64 | 1207 | 10 | 0.1 | 0.1 | 1.33 | 0.285179 | 6.234799 | 0.285179 | 6.234799 |
| Meckering | 6.59 | 64 | 822 | 10 | 0.1 | 0.1 | 1.33 | 0.285179 | 6.234799 | 0.285179 | 6.234799 |
| Meckering | 6.59 | 63 | 848 | 10 | 0.15 | 0.15 | 0.76 | -0.27444 | 6.234799 | -0.27444 | 6.234799 |
| Meckering | 6.59 | 60 | 1275 | 10 | 0.15 | 0.15 | 1.038 | 0.037296 | 6.234799 | 0.037296 | 6.234799 |
| Meckering | 6.59 | 64 | 1276 | 10 | 0.2 | 0.2 | 1.22 | 0.198851 | 6.234799 | 0.198851 | 6.234799 |
| Meckering | 6.59 | 60 | 1413 | 10 | 0.24 | 0.24 | 1.038 | 0.037296 | 6.234799 | 0.037296 | 6.234799 |

Table 3-15. Parameters for DFs on the FW of five Australian SCR ruptures. Red values were used to derive a Nurminen-style multiple regression of ln Y (dependent variable) as a function of ln s, ln Dn, and m (independent variables), for this SCR subset of FW measurements. The Nurminen equation is lnY=a+(b1*ln(s))+(c1*ln(Dn))+(d1*m) (Eq. 11 of this paper). Using the multiple regression function in Microsoft Excel, we derived the intercept ”a” and coefficients b1, c1, and d1 for this small data subset.

| eq_name | magnitude | RUP_ID[1] | DF-PF dist (s)[2] | depth_km[3] | vs_central[4] | recom_net (m)[5] | Dn[6] | ln Y[7] | ln s | ln Dn | d1*m[8] |
|---|---|---|---|---|---|---|---|---|---|---|---|
| Meckering | 6.59 | 60 | 3241 | 10 | 0.3 | 0.3 | 1.09 | 0.086178 | 6.234799 | 0.086178 | 6.234799 |
| Meckering | 6.59 | 60 | 2753 | 10 | 0.37 | 0.37 | 1.13 | 0.122218 | 6.234799 | 0.122218 | 6.234799 |
| Meckering | 6.59 | 60 | 2109 | 10 | 0.41 | 0.41 | 1.452 | 0.372942 | 6.234799 | 0.372942 | 6.234799 |
| Meckering | 6.59 | 35 | 85 | 10 | 0.43 | 0.43 | 1.11 | 0.10436 | 6.234799 | 0.10436 | 6.234799 |
| Meckering | 6.59 | 60 | 2033 | 10 | 0.46 | 0.46 | 1.262 | 0.232698 | 6.234799 | 0.232698 | 6.234799 |
| Meckering | 6.59 | 60 | 2321 | 10 | 0.67 | 0.67 | 1.452 | 0.372942 | 6.234799 | 0.372942 | 6.234799 |
| Meckering | 6.59 | 58 | 114 | 10 | -999 | 0.41 | 1.07 | 0.067659 | 6.234799 | 0.067659 | 6.234799 |
| Meckering | 6.59 | 51 | 208 | 10 | -999 | 1.52 | 1.51 | 0.41211 | 6.234799 | 0.41211 | 6.234799 |
| Cadoux | 6.1 | 6 | 347 | 15 | 0.2 | 0.2 | 0.392 | -0.93649 | 5.77121 | -0.93649 | 5.77121 |
| Cadoux | 6.1 | 17 | 144 | 15 | 0.4 | 0.4 | 0.426 | -0.85332 | 5.77121 | -0.85332 | 5.77121 |

| eq_name | magnitude | RUP_ID[1] | DF-PF dist (s)[2] | depth_km[3] | vs_central[4] | recom_net (m)[5] | Dn[6] | ln Y[7] | ln s | ln Dn | d1*m[8] |
|---|---|---|---|---|---|---|---|---|---|---|---|
| TennantCr2 | 6.44 | 2 | 966 | 4 | 0.27 | 0.27 | 0.159 | -1.83885 | 6.092884 | -1.83885 | 6.092884 |
| TennantCr2 | 6.44 | 2 | 1025 | 4 | 0.74 | 0.74 | 0.154 | -1.8708 | 6.092884 | -1.8708 | 6.092884 |
| TennantCr2 | 6.44 | 2 | 1046 | 4 | 0.62 | 0.62 | 0.147 | -1.91732 | 6.092884 | -1.91732 | 6.092884 |
| TennantCr2 | 6.44 | 2 | 1106 | 4 | 0.64 | 0.64 | 0.142 | -1.95193 | 6.092884 | -1.95193 | 6.092884 |
| TennantCr2 | 6.44 | 2 | 1115 | 4 | 0.62 | 0.62 | 0.095 | -2.35388 | 6.092884 | -2.35388 | 6.092884 |
| TennantCr2 | 6.44 | 2 | 1114 | 4 | 0.54 | 0.54 | 0.345 | -1.06421 | 6.092884 | -1.06421 | 6.092884 |
| Petermann | 6 | 117 | 82 | -999 | 0.103 | 0.103 | 0.466 | -0.76357 | 5.6766 | -0.76357 | 5.6766 |
| Petermann | 6 | 121 | 142 | -999 | 0.112 | 0.112 | 0.48 | -0.73397 | 5.6766 | -0.73397 | 5.6766 |
| Petermann | 6 | 125 | 220 | -999 | 0.122 | 0.122 | 0.491 | -0.71131 | 5.6766 | -0.71131 | 5.6766 |
| Petermann | 6 | 217 | 280 | -999 | 0.08 | 0.08 | 0.51 | -0.67334 | 5.6766 | -0.67334 | 5.6766 |
| Petermann | 6 | 170 | 343 | -999 | 0.082 | 0.082 | 0.539 | -0.61804 | 5.6766 | -0.61804 | 5.6766 |

| eq_name | magnitude | RUP_ID[1] | DF-PF dist (s)[2] | depth_km[3] | vs_central[4] | recom_net (m)[5] | Dn[6] | ln Y[7] | ln s | ln Dn | d1*m[8] |
|---|---|---|---|---|---|---|---|---|---|---|---|
| Petermann | 6 | 170 | 368 | -999 | 0.092 | 0.092 | 0.548 | -0.60148 | 5.6766 | -0.60148 | 5.6766 |
| Petermann | 6 | 158 | 46 | -999 | 0.52 | 0.52 | 0.241 | -1.42296 | 5.6766 | -1.42296 | 5.6766 |
| Petermann | 6 | 92 | 363 | -999 | 0.127 | 0.127 | 0.566 | -0.56916 | 5.6766 | -0.56916 | 5.6766 |
| Petermann | 6 | 47 | 369 | -999 | 0.095 | 0.095 | 0.556 | -0.58699 | 5.6766 | -0.58699 | 5.6766 |
| Petermann | 6 | 73 | 100 | -999 | 0.072 | 0.072 | 0.246 | -1.40242 | 5.6766 | -1.40242 | 5.6766 |
| Petermann | 6 | 49 | 25 | -999 |  | 0.059 | 0.195 | -1.63476 | 5.6766 | -1.63476 | 5.6766 |

[1] rupture ID number in the FDHI database

[2] closest distance of the DF from the PF (meters)

[3] focal depth (km)

[4] vs_central= vertical component of displacement at the DF measurement point

[5] recom_net-= the FDHI compiler's ”recommended net slip vector for analysis”. Following the procedure of Nurminen et al. 2020, we manually re-measured and calculated DN in GIS from the recomm_net values of the closest two points on the PF to the DF

[6] Dn= inferred recom_net displacement on the PF opposite the DF measurement point, interpolated from the two field-measured PF displacements flanking the perpendicular to the DF point (method of Nurminen et al., 2020)

| eq_name | magnitude | RUP_ID[1] | DF-PF dist (s)[2] | depth_km[3] | vs_central[4] | recom_net (m)[5] | Dn[6] | ln Y[7] | ln s | ln Dn | d1*m[8] |
|---|---|---|---|---|---|---|---|---|---|---|---|
| Meckering | 6.59 | 35 | 71 | 10 | 1.07 | 1.07 | 1.17 | 0.067659 | 4.26268 | 0.157004 | 3.763549 |
| Calingiri | 5.03 | 37 | 24 | -999 | 0.051 | 0.051 | 0.076 | -2.97593 | 3.178054 | -2.57702 | 2.872633 |
| Calingiri | 5.03 | 56 | 55 | -999 | 0.076 | 0.076 | 0.302 | -2.57702 | 4.007333 | -1.19733 | 2.872633 |
| Calingiri | 5.03 | 45 | 22 | -999 | 0.076 | 0.076 | 0.076 | -2.57702 | 3.091042 | -2.57702 | 2.872633 |
| Calingiri | 5.03 | 44 | 101 | -999 | 0.102 | 0.102 | 0.302 | -2.28278 | 4.615121 | -1.19733 | 2.872633 |
| Calingiri | 5.03 | 44 | 116 | -999 | 0.178 | 0.178 | 0.302 | -1.72597 | 4.75359 | -1.19733 | 2.872633 |

Table 3-16. Parameters for DFs on the HW of five Australian SCR ruptures. Red values were used to derive a Nurminen-style multiple regression of ln Y (dependent variable) as a function of ln s, ln Dn, and m (independent variables), for this SCR subset of FW measurements. The Nurminen equation is $\ln Y = a + (b1 * \ln(s)) + (c1 * \ln(Dn)) + (d1 * m)$ (Eq. 11 of this paper). Using the multiple regression function in Microsoft Excel, we derived the intercept ”a” and coefficients b1, c1, and d1 for this small data subset.

| eq_name | magnitude | RUP_ID[1] | DF-PF dist (s)[2] | depth_km[3] | vs_central[4] | recom_net (m)[5] | Dn[6] | ln Y[7] | ln s | ln Dn | d1*m[8] |
|---|---|---|---|---|---|---|---|---|---|---|---|
| Calingiri | 5.03 | 21 | 11.8 | -999 | 0.089 | 0.089 | 0.122 | -2.41912 | 2.4681 | -2.10373 | 2.872633 |
| Cadoux | 6.1 | 37 | 173 | 15 | 0.15 | 0.15 | 0.31 | -1.89712 | 5.153292 | -1.17118 | 3.48371 |
| Cadoux | 6.1 | 37 | 246 | 15 | -999 | 0.15 | 0.319 | -1.89712 | 5.505332 | -1.14256 | 3.48371 |
| Cadoux | 6.1 | 36 | 750 | 15 | -999 | 0.1 | 0.329 | -2.30259 | 6.620073 | -1.1117 | 3.48371 |
| Cadoux | 6.1 | 18 | 506 | 15 | 0.25 | 0.25 | 0.4 | -1.38629 | 6.226537 | -0.91629 | 3.48371 |
| Cadoux | 6.1 | 8 | 230 | 15 | 0.2 | 0.2 | 1.167 | -1.60944 | 5.438079 | 0.154436 | 3.48371 |
| Cadoux | 6.1 | 10 | 307 | 15 | -999 | 0.15 | 1.307 | -1.89712 | 5.726848 | 0.267734 | 3.48371 |
| Cadoux | 6.1 | 9 | 516 | 15 | -999 | 0.3 | 1.212 | -1.20397 | 6.246107 | 0.192272 | 3.48371 |
| Cadoux | 6.1 | 9 | 162 | 15 | 0.1 | 0.1 | 1.34 | -2.30259 | 5.087596 | 0.29267 | 3.48371 |
| Cadoux | 6.1 | 22 | 1097 | 15 | -999 | 0.2 | 0.2 | -1.60944 | 7.000334 | -1.60944 | 3.48371 |
| Cadoux | 6.1 | 23 | 1021 | 15 | -999 | 0.02 | 0.35 | -3.91202 | 6.928538 | -1.04982 | 3.48371 |

| eq_name | magnitude | RUP_ID[1] | DF-PF dist (s)[2] | depth_km[3] | vs_central[4] | recom_net (m)[5] | Dn[6] | ln Y[7] | ln s | ln Dn | d1*m[8] |
|---|---|---|---|---|---|---|---|---|---|---|---|
| Cadoux | 6.1 | 46 | 354 | 15 | -999 | 0.1 | 0.28 | -2.30259 | 5.869297 | -1.27297 | 3.48371 |
| Cadoux | 6.1 | 46 | 398 | 15 | 0.1 | 0.1 | 0.28 | -2.30259 | 5.986452 | -1.27297 | 3.48371 |
| Cadoux | 6.1 | 46 | 524 | 15 | 0.18 | 0.18 | 0.28 | -1.7148 | 6.261492 | -1.27297 | 3.48371 |
| Cadoux | 6.1 | 46 | 578 | 15 | -999 | 0.19 | 0.28 | -1.66073 | 6.359574 | -1.27297 | 3.48371 |
| Petermann | 6 | 215 | 95 | -999 | 0.056 | 0.056 | 0.27 | -2.8824 | 4.553877 | -1.30933 | 3.4266 |
| Petermann | 6 | 67 | 35 | -999 | 0.172 | 0.172 | 0.277 | -1.76026 | 3.555348 | -1.28374 | 5.6766 |

Footnotes are the same as in previous Table.

### 3.7.1. Results of the multiple regression on the SCR datasets

Tables 3-15 and 3-16 show the results of the multiple regression of DF displacements, for FW and HW data points, respectively.

The best-fit equation (Eq. 16) is shown in bold below table 3-17.

Table 3-17. Results of multiple regression of DF displacement on HW for five Australian SCR ruptures.

SUMMARY OUTPUT

multiple regression of ln Y (displ on DF) as a function of ln s, ln Dn, and m

for 5 Aussie earthquakes (Meckering, Calingiri, Cadoux, Tennant Creek, and Petermann)

**HW ONLY!**

| *Regression Statistics* | |
|---|---|
| Multiple R | 0.5655 |
| R Square | 0.3198 |
| Adjusted R Square | 0.2124 |
| Standard Error | 0.6707 |
| Observations | 23 |

ANOVA

| | *df* | *SS* | *MS* | *F* | *Significance F* |
|---|---|---|---|---|---|
| Regression | 3 | 4.020978 | 1.3403 | 2.978 | 0.057388 |
| Residual | 19 | 8.549400 | 0.4499 | | |
| Total | 22 | 12.57037 | | | |

| | *Coefficients* | *Standard Error* | *t Stat* | *P-value* | *Lower 95%* | *Upper 95%* | *Lower 95.0%* | *Upper 95.0%* |
|---|---|---|---|---|---|---|---|---|
| Intercept | -4.3070 | 2.359416 | -1.8254 | 0.083 | -9.24535 | 0.631276 | -9.2453 | 0.63127 |
| X Variable 1 (s) | -0.1852 | 0.147929 | -1.2519 | 0.225 | -0.49482 | 0.124414 | -0.4948 | 0.12441 |
| X Variable 2 (Dn) | 0.3434 | 0.221745 | 1.5489 | 0.137 | -0.12065 | 0.807585 | -0.1206 | 0.80758 |
| X Variable 3 (m) | 0.6138 | 0.438067 | 1.4011 | 0.177 | -0.30306 | 1.530703 | -0.3030 | 1.53070 |

HW displacement On DFs

$$\ln Y= -4.31 + (-0.185*(\ln s)) + (0.343*(\ln Dn)) + (0.614*m) \qquad \text{Eq. 16}$$

Table 3-18. Results of multiple regression of DF displacement on FW for five Australian SCR ruptures.

The best-fit equation (Eq. 17) is shown in bold below table 3-18.

SUMMARY OUTPUT

multiple regression of ln Y (displ on DF) as a function of ln s, ln Dn, and m

for 5 Aussie earthquakes (Meckering, Calingiri, Cadoux, Tennant Creek, and Petermann)

**FW ONLY!**

| *Regression Statistics* | |
|---|---|
| Multiple R | 0.6626927 |
| R Square | 0.4391617 |
| Adjusted R Square | 0.3811439 |
| Standard Error | 0.6718967 |
| Observations | 33 |

ANOVA

| | *df* | *SS* | *MS* | *F* | *Significance F* |
|---|---|---|---|---|---|
| Regression | 3 | 10.25155 | 3.417 | 7.56 | 0.0006 |
| Residual | 29 | 13.09191 | 0.451 | | |
| Total | 32 | 23.34347 | | | |

| | *Coefficients* | *Standard Error* | *t Stat* | *P-value* | *Lower 95%* | *Upper 95%* | *Lower 95.0%* | *Upper 95.0%* |
|---|---|---|---|---|---|---|---|---|
| Intercept | -17.5972 | 3.663586 | -4.803 | 4.38 E-05 | -25.09 | -10.1 | -25.09 | -10.10 |
| X Variable 1 (s) | -0.08306 | 0.126165 | -0.658 | 0.51 | -0.341 | 0.174 | -0.341 | 0.1749 |
| X Variable 2 (Dn) | -0.3998 | 0.163040 | -2.452 | 0.02 | -0.733 | -0.066 | -0.733 | -0.066 |
| X Variable 3 (m) | 2.59156 | 0.642125 | 4.035 | 3.63 E-04 | 1.2782 | 3.904 | 1.2782 | 3.9048 |

FW displacement On DFs

**ln Y= -17.6 + (-0.083*(ln s)) + (-4*(ln Dn)) + (2.592*m) Eq. 17**

### 3.7.2. Comparing DF equations from the Nurminen et al (2020) simple rupture dataset to that for the SCR dataset (this report)

Looking at the DF regression intercept (a) and three coefficients b1, c1, and d1 on the HW, Nurminen's 2020 values (Table 3-19, 2nd column) from a large dataset look very similar to those of the much smaller SCR rupture subset (Table 3-19, 3rd column). The relatively minor difference in coefficients suggest that the independent variables s, DN, and m are imposing similar controls on DF displacements, presumably following similar physical processes. The largest difference is in standard deviation, which is larger for our smaller dataset. That variability is easy to understand when looking at the highly variable rupture patterns in our five Australian earthquakes (Appendix A).

However, the same is not true of the FW coefficients. First, the ”a” intercept value for the SCR ruptures is nearly three times smaller than that for Nurminen's simple ruptures. With the intercept so low, this would tend to make SCR DF displacements smaller than those on simpler ruptures, if the regression line has the same slope for SCR and simple cases.

TABLE 3-19. Comparing the Coefficients in Equation 11 (Nurminen et al., 2020, from her data set of “simple ruptures”), to Coefficients from the subset of five SCR ruptures (Equations 16 and 17).

| **Coefficients** | Nurminen simple ruptures, Hanging Wall (HW) | SCR subset, Hanging Wall (HW) | Nurminen simple ruptures, Footwall (FW) | SCR subset, Hanging Wall (FW) |
|---|---|---|---|---|
| **a** | -4.2549 | -4.3070 | -5.1043 | -17.5973 |
| **b1** | -0.1514 | -0.1852 | -0.6483 | -0.0831 |
| **c1** | 0.4404 | 0.3435 | 0.1983 | -0.3999 |
| **d1** | 0.5711 | 0.6138 | 0.9461 | 2.5916 |
| **std** | 0.9129 | 0.6708 | 0.8812 | 0.6719 |

Second, coefficient b1 for SCR ruptures is much smaller (about 1/8th the size) than b1 for Nurminen's simple ruptures. Coefficient b1 indicates the strength of correlation between the DF displacement and the distance from DF to PF. In Nurminen's simple rupture dataset, this coefficient was strongly negative, indicating that DF displacement decreases rapidly with distance from the PF. In contrast, the near-zero coefficient for SCR ruptures indicates that DF displacement is basically independent of distance to the PF. This is probably a result of two of the five SCR ruptures (Meckering, Tennant Creek 2) having long sympathetic DFs on their footwalls. At Meckering the DF displacements 2-4 km away from the PF were still ~30% as large as the PF displacements, whereas at Tennant Creek 2, the DF displacements 1 km from the PF were mainly larger than displacements on the PF!

Third, coefficient c1 for SCR ruptures has the opposite sign from c1 for Nurminen's ruptures. Coefficient c1 indicates the strength of correlation between the DF displacement and DN (the closest PF displacement). A negative value for c1 indicates an inverse relationship between DF displacement and PF displacement; in other words, large DF displacements occur opposite small PF displacements. This counter-intuitive result comes directly from the ”footwall fault” at Tennant Creek 2.

Finally, coefficient d1 for SCR ruptures is roughly 2.5 times larger than for simple ruptures. Coefficient d1 indicates the strength of correlation between the DF displacement and earthquake magnitude. Over the magnitude range of our five SCR ruptures (5.0-6.6), magnitude was the strongest control over DF displacement, whereas distance from the PF (s) and displacement on the PF (DN) were only weak controls.

Starting with a low intercept value and having weak control from DF-PF distance and DN on the PF, almost the entire value of DF (slope of the regression line) is determined by earthquake magnitude. In small earthquakes like M5.0, DFs displacements are small, almost regardless of distance to the PF or displacement on the PF. In larger earthquakes (M6.6), DFs are larger, but not necessarily influenced by displacements on the PF. This is because in two of five SCR events, the earthquake ruptured on two separate, parallel faults across strike, classified as DFs. That classification made all of their displacement measurements fall into the DF category.

Given the strong effect of the two multi-fault Australian ruptures (Meckering, Tennant Creek 2) on 5 SCR empirical equations, one might ask why they were not omitted, or why two separate equations were not derived (one with all 5 events, and one that omitted Meckering and Tennant Creek 2). The reason is this: Meckering and Tennant Creek 2 suggest that the SKB modelling assumption of slip on a single mapped fault is too simplistic, compared to observed historic ruptures. Based on Australian evidence, in 40% of cases coseismic slip on a fault resulted in large coseismic slip on a nearby, parallel fault. The displacement on the parallel fault at Tennant Creek 2 was as large or larger than slip on the principal fault. This pattern is unlike most cases of distributed faulting (which decreases predictably away from the PF), and more resembles “triggered faulting.”

To my knowledge, none of SKB’s scenario outputs result in such a pattern of displacement on “target fractures.” What this implies to me is: (1) SKB was unaware that two historic SCR reverse faults had slipped with such a pattern, and (2) they did not consider it in devising the 3D PF geometry in their scenarios. Their scenarios place all the coseismic slip on a single PF fault plane, making them essentially 2D models. This is the simplest model. But the Meckering and Tennant Creek ruptures indicate that the PF rupture is not always restricted to a single fault plane along strike, but displacement can jump onto a nearby, parallel fault. Thus, if any of SKB’s scenario faults were close to a nearby parallel fault (within 1-3 km), then the possibility of PF displacement jumping from one fault to the next along strike should be considered.

## 3.8. How to predict the distance and displacement of distributed faulting at repository depth (500 Meters)?

DF probabilities and displacements predicted by the Nurminen, Moss, and our SCR datasets are based on surface distances. How should we adjust our probability and displacement values for various surface distances, to a depth of 500 m below the surface? This is actually two questions: would the location of the subsurface DFs be the same (relative to the PF) as at the surface, and would the displacement on the DF be the same?

### 3.8.1. Position of the DFs at -500 m at Forsmark.

Our easiest option would be to assume that all fractures reactivated by future Forsmark earthquakes have a strike and dip identical to the scenario Principal fault plane. Under this assumption, relative horizontal distances between the PF fault plane and reactivated DFs would not change, regardless of the depth they were measured at. The relative distances (actually, the entire coordinate system) would simply shift horizontally toward the PF fault plane with increasing depth, along the PF fault dip; but relative distances between PF and DF would remain as they were at the surface. This assumption has two advantages. First, it is supported by fracture mechanics. SKB assumed certain faults (their scenario faults) were optimally oriented to slip and generate earthquakes in future stress fields. It would logically follow that the fractures most likely to be reactivated would be those with the same 3D orientation as the PF. Second, the assumption permits us to use the DF-to-PF surface distances from the Australian ruptures as a proxy for the same distances at 500 m depth at Forsmark. That, in turn, allows us to use the probability and displacement equations of Nurminen and Moss.

However, the one thing that we do not know about the Australian DF rupture dataset, is whether all the measured DFs occurred on structures with the same 3D orientation as the PF fault plane. Very few DF displacement measurement points in the five Australian ruptures recorded the dip of the DF. In the cases that did (Meckering ”splinter” fault), the DF had a strike very similar to the PF and dipped in the same direction, but not at exactly the same dip angle (the Meckering splinter fault dipped more gently than the PF, and thus intersected it in the subsurface ~2.5 km below ground surface; see Fig. 3-18).

Olesen et al. (2021, p.203) cite a similar situation in Norway with EGF fault traces. They state: ”*The MFS [Maze Fault System] is located within the regional ~4 km-wide MSSZ [Mierojavr-Sviaerholt Shear Zone]. The dips of the western and eastern segments of the MFS within the SFC [Stouragurra Fault Complex] as read from the migrated seismic section are 48° and 59°, respectively. The dip increases to 52° and 65° after correcting for oblique crossing. The two postglacial fault segments seem to merge at a depth of ~500 m.”* Radiocarbon dates from a trench on the Maze fault indicate the most recent displacement occurred about 600 years ago (Olesen et al., 2018).

For the purpose of comparing empirical DFs to the SKB predicted shear fractures, we will assume that all DFs strike and dip parallel to the PF, and thus the DF-to-PF distances used in the Nurminen and Moss equations can also be used at a depth of 500 m at Forsmark. Assuming anything else leads to unconstrained dips and thus unpredictable locations for DFs relative to PF, leaving us in a wilderness of non-unique solutions based on no data.

### 3.8.2. Predicting displacement at -500 m at Forsmark

The Nurminen and Moss equations for DF displacement as a function of distance to the PF are based on surface data. How might those displacements change at a depth of 500 m? We can envision two possible options for relating subsurface displacements to surface displacements.

1. Option 1: assume that the along-dip slip gradient between 500 m depth and the surface is negligible, so displacements at -500 m will be identical to surface displacements.
2. Option 2: use slip gradients from the published literature to adjust surface displacements to a predicted value at -500 m.

a. - use surface (along-strike) slip gradients measured on historic surface ruptures
b. - use subsurface (3D) slip gradients shown in slip distribution diagrams for historic reverse surface ruptures, inverted from either InSAR data or teleseismic data.

Although using Option 1 is a tempting choice, there is enough published slip gradient information on M5-7 reverse earthquakes to show that slip gradients, even in the upper 500 m, are non-zero. The problem is, finding slip distribution diagrams from the correct historic analog earthquakes, similar to scenario earthquakes in numerical models.

*Surface Slip Gradients*: Shaw (2011) analyzed 20 surface rupturing earthquakes to define typical gradients of surface slip along strike. All 20 plots of surface displacement along strike were dominated by high-frequency variations of unknown origin (the so-called ”sawtooth curve” of displacement; McCalpin, 2009b, p. 15). Shaw concluded this ”noise” included measurement error, local effects caused by thickness and rheology of surface deposits, and unknown factors. However, seven of his ruptures showed coherent slip gradients based on five or more adjacent measurement points (Fig. 3-36), including two SCR ruptures in Australia (1988 Tennant Creek 3 M6.6; 1986 Marryat Creek, M5.9). Slip gradient is measured as change in slip/distance over which the change occurs, which can either be cited in m/km, or as m/m (dimensionless number). In fact it can be treated as a strain, such as a change in length/length. All of the coherent rupture sections yielded slip gradients in the range of $1x10^{-4}$ to $9x10^{-4}$.

Shaw then plotted the coherent slip gradients against their length (Fig. 3-37a) and their earthquake magnitude (Fig. 3-37b). There is no apparent correlation in either case. Shaw remarked: *” In both cases, importantly, there is a lack of any obvious trend. That is, coherent surface-slip strain values appear to be independent of length scale and also independent of event magnitude.”* The implication is that surface slip gradients are limited by some type of physical restraint within the faulting process itself, which prevents fault-plane slip from changing too rapidly in space.

*Subsurface Slip Gradients*: Seismologists use two methods to deduce the 2-D pattern of slip distribution on fault planes of large historic earthquakes. The older method inverts teleseismic recordings to reconstruct the spatial pattern of slip on the fault plane (e.g. Hartzell and Heaton, 1983). The more recent method is to measure the spatial field of coseismic deformation with InSAR, and then invert that field (e.g. Atzori et al., 2009). For historic surface ruptures in unextended SCRs, we have located several studies that compute subsurface slip distributions using the older or more recent methods.

The first case is the 2016 M6.1 Petermann, Australia earthquake, where Polcari et al., (2018) reconstructed the slip distribution from InSAR data. As shown in Fig. 3-38A, the Petermann fault plane dips about 40°NE based on its surface outcrop and hypocentral of ~3 km. Movement was reverse with a smaller left-lateral component. On the fault plane (white area in B), slip vectors were reconstructed for 0.5x0.5 km cells, shaded as to their net slip vector in pink (slip class 1, 0.3-0.6m) through red (slip class 5, 1.5-1.8m). In part B the small green numbers indicate the variability in slip classes along the emergent edge of the rupture plane. Compared to the region of highest slip (class 5) on the plane, displacement at the surface has decreased to an average of class 3, a decrease of 0.6 m in a distance of 1.1 km. This equates to a downward-increasing slip gradient of $5.5x10^{-4}$ in the upper 1 km of the fault plane.

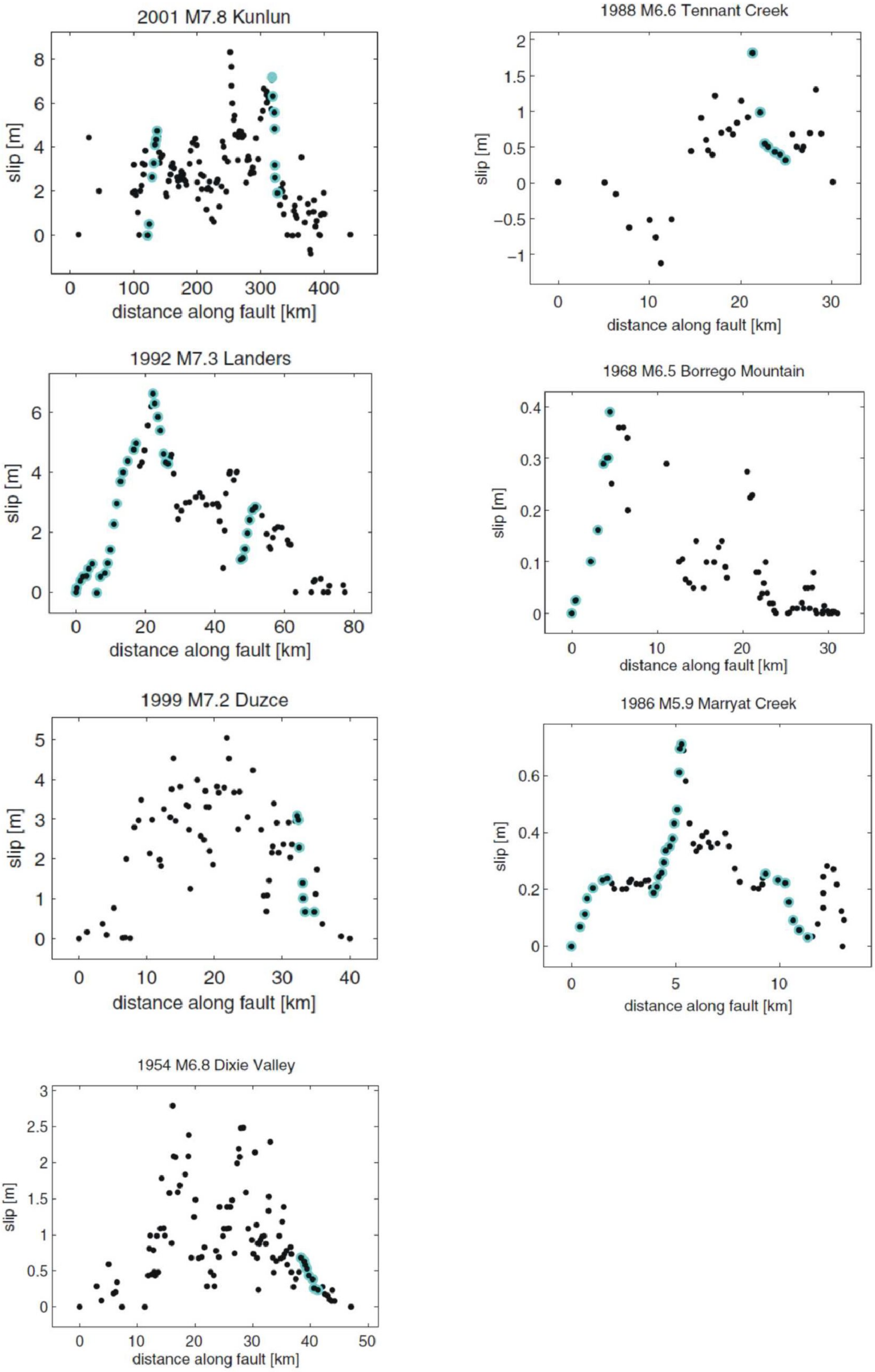

Figure 3-36. Along-strike surface slip gradients (blue dots) recognized by Shaw (2011) in historic surface ruptures. Ruptures are arranged in decreasing magnitude from upper left.

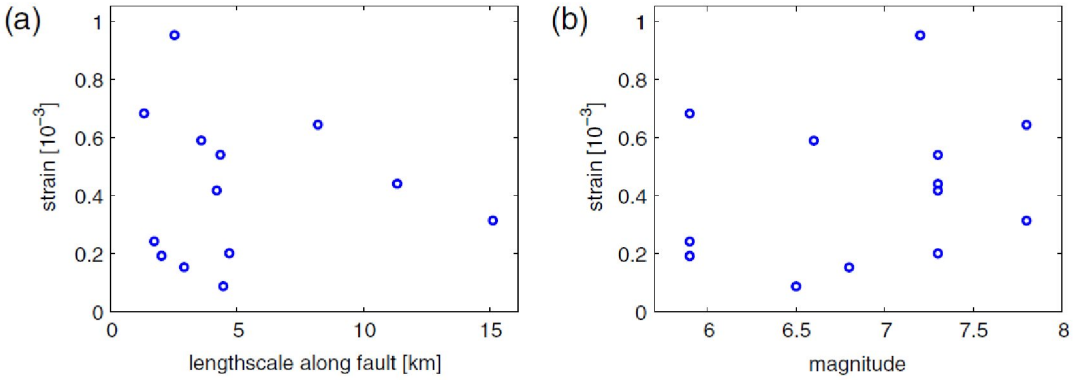

Figure 3-37. Coherent slip gradients (or strains) in 13 coherent sections of strike-slip ruptures. (a) slip gradients as a function of length; (b) slip gradients as a function of magnitude. Shaw (2011) concluded there was significant trend in either plot.

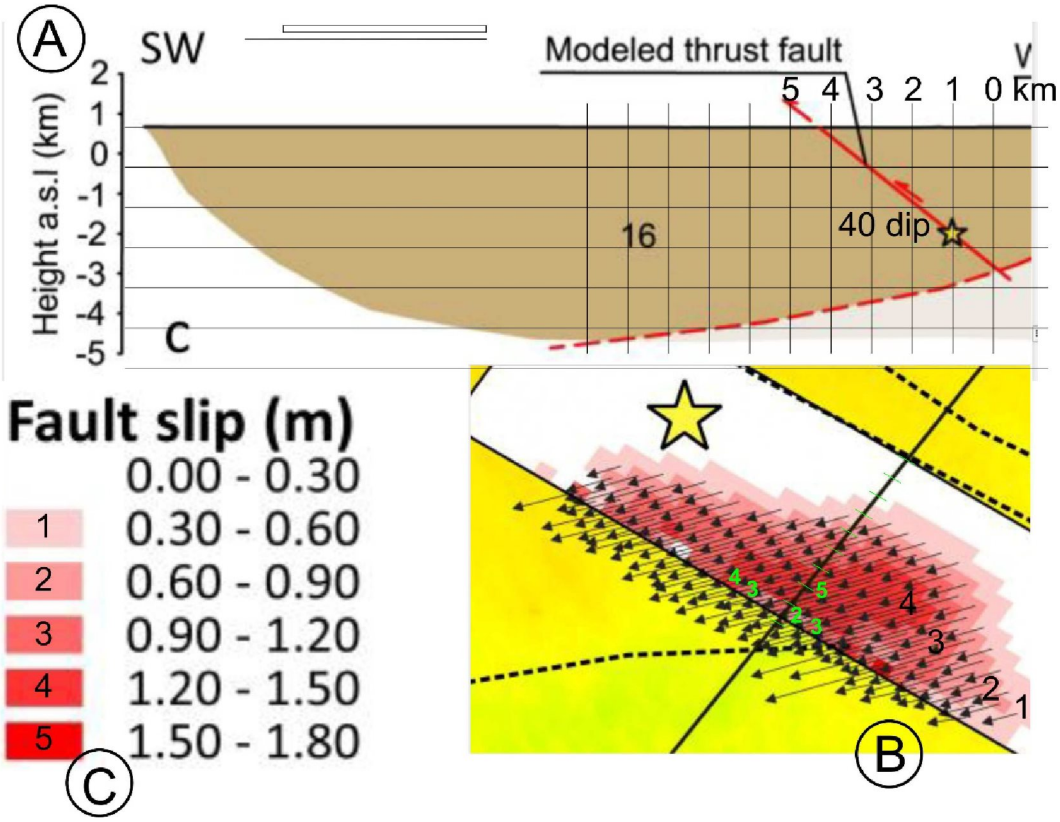

Figure 3-38. Slip distribution on the M6.1 Petermann fault plane; see text for discussion.

Another Australian example of lower magnitude is the 2007 M4.7 Katanning earthquake, where the slip distribution was also calculated from InSAR data (Dawson et al., 2008). The Katanning rupture was extremely shallow, extending only from ~640 m below the surface to the surface. As shown in Fig. 3-39a, the surface rupture was only about 1 km long, although the geodetic uplift along the fault was ~3 km long. Fig. 3-39a, c, and d show slip distribution on the fault plane, with maximum slip of ~0.8 m at a depth of 0.5 km (red pixels). From that point upward slip decreases in an irregular manner (as at

Petermann), with surface slips in the range of 0.4-0.5 m. That represents an average slip gradient of 0.35 m in 0.5 km, or 0.7 m/km, equivalent to a downward-increasing (dimensionless) slip gradient of $7x10^{-4}$.

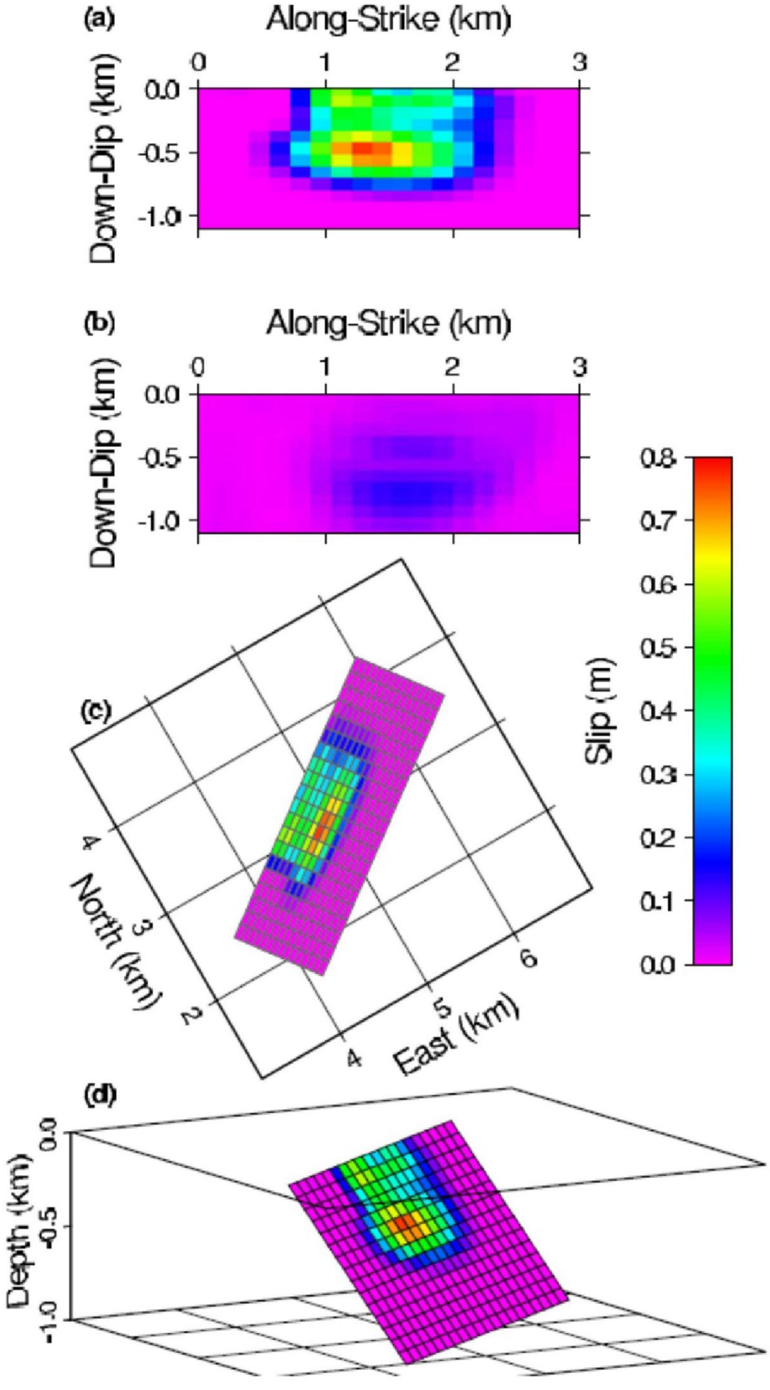

Figure 3-39. Slip distribution model for the M4.7 Katanning earthquake, from Dawson et al. (2008).

Slip gradients have been cited by other authors for SCR reverse ruptures such as the 1993 Killari (Latur, India) M6.2 event, where Silpa and Earnest (2021) derived a rather coarse-resolution along-dip slip gradient of 1.4x10$^{-4}$. Numerous authors have studied slip distributions in subduction megathrust earthquakes, which are also reverse faults. Sun et al. (2017) calculated a slip gradient of 5 m/40 km= 1.25x10$^{-4}$. Benz (2018) similarly cited a slip gradient of 0.15m/1 km= 1.5x 10$^{-4}$. Yue et al. (2013) cite what they call a large slip gradient of 0.25 m/km, in contrast with the updip slip gradient of ~0.1 m/km" (a range of 1.0x 10$^{-4}$ to 2.5x 10$^{-4}$) for an M7.6 earthquake in a subduction zone.

Overall the dip-direction slip gradients cited above cluster in the range 1.0x10$^{-4}$ to 7x10$^{-4}$, almost exactly the same range as slip gradients measured from along-strike surface displacements. Despite what Shaw (2011) concluded about surface slip gradients, these subsurface slip gradients seem to correlate with the magnitude of the earthquake (Fig. 3-40). However, given small number of observations, this apparent inverse correlation may be a coincidence. The author is unaware of any published paper that specifically addresses this topic.

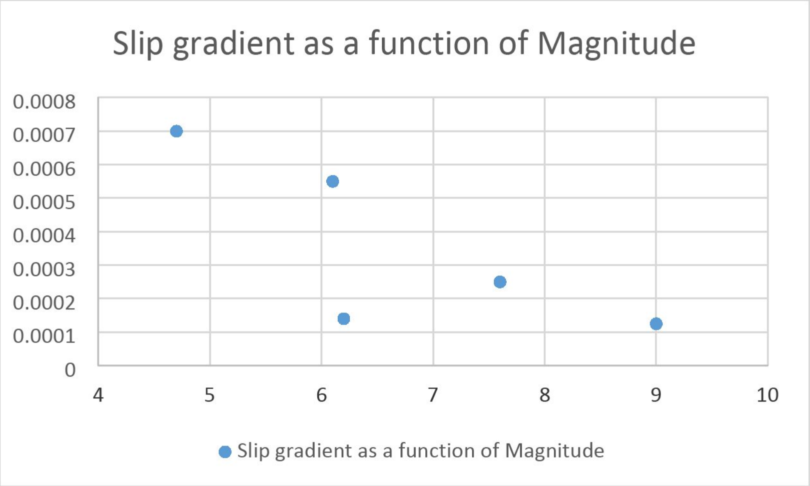

Figure 3-40. Maximum subsurface slip gradients, measured in the dip direction, in our example reverse earthquakes. There does appear to be an inverse correlation, such that maximum slip gradients can be larger on small fault ruptures but smaller on very large fault ruptures.

How should we use these slip gradients to correct surface DF displacements to those at -500 m? For example, if we applied a downdip slip increase of 0.15 m/km (0.00015) from the surface to a depth of 500 m, that would result in a 0.075 m (7.5 cm) increase in displacement at 500 m, compared to the surface displacement. That 7.5 cm is larger than the displacement threshold assumed for canister failure. In other words, even if a DF displacement were zero at the surface, it would be more than the threshold displacement at -500 m. And this is using the low end of slip gradient values.

The fact is, all the slip gradient data we have is on coseismic Principal faults; we have no actual data on Distributed faults. And since most DFs do not generate their own seismic energy, we cannot use teleseismic data to invert for their slip distributions. The area of DFs is within the elastic deformation area imaged by InSAR, so the inversion technique there has already assigned the cumulative off-fault vertical deformation to elastic crustal deformation by the PF. So there is would be nothing left to assign to DFs at any rate without violating the inversion model assumptions.

IN SUMMARY: It does not seem justifiable at this time to adjust DF displacements at the surface to any depths (such as -500 m), due to lack of any empirical subsurface data on DFs. Simply assuming that slip gradients on DFs are the same as on PFs has no support from the published literature. It does not seem likely we will ever be able to measure such subsurface displacements on DFs. However, we may be able to make some type of comparison between observed DFs at the surface, and the 3DEC models. If it were possible for the 3DEC models to calculate shear displacements on fractures at the ground surface, rather than at a depth of 500 m. Then we could compare those 3DEC surface displacements to the empirical data sets.

# 4. The geologic approach to predicting distributed faulting for strike-slip faults

As shown in Section 3.1.2 (Table 3-1, Fig. 3-3), the largest faults affecting Forsmark are vertical faults, which are most likely to be reactivated as strike-slip faults in both the present stress field and glacial stress fields. Therefore, it is most appropriate to use global historic strike-slip surface ruptures, in calculating the probability and displacement on DFs.

## 4.1. Worldwide database of strike-slip surface ruptures

There is now a good database of global strike-slip surface ruptures, numbering 35 events in the FDHI dataset (Table 4-1, modified from Sarmiento et al., 2021).

Table 4-1. Chronological list of the 35 strike-slip surface ruptures in the FDHI database. The eight events in bold were used by Petersen et al., 2011 to analyze distributed faulting. Shaded gray events occurred after occurred after Petersen et al.'s manuscript was submitted.

| EQ_ID | Name | Region | Date | Style[1] | Magnitude, Type[2] |
|---|---|---|---|---|---|
| 28 | Imperial1940 | California | 5/19/1940 | SS | 6.95, Mw |
| 75 | YeniceGonen | Turkey | 3/18/1953 | SS | 7.3, Mw |
| 53 | SanMiguel | Mexico | 2/9/1956 | SS | 6.8, Ms |
| 29 | Parkfield1966 | California | 6/28/1966 | SS | 6.19, Mw |
| **6** | **Borrego** | **California** | **4/9/1968** | **SS** | **6.63, Mw** |
| 61 | IzuPeninsula | Japan | 5/8/1974 | SS | 6.5, Ms |
| 32 | GalwayLake | California | 6/1/1975 | SS | 5.2, ML |
| 62 | IzuOshima | Japan | 1/14/1978 | SS | 6.6, Mwc |
| 70 | HomesteadValley | California | 3/15/1979 | SS | 5.2, ML |
| **7** | **Imperial1979** | **California** | **10/15/1979** | **SS** | **6.53, Mw** |
| 36 | ChalfantValley | California | 7/21/1986 | SS | 6.19, Mw |
| 57 | ElmoreRanch | California | 11/24/1987 | SS | 6.22, Mw |
| **8** | **SuperstitionHills** | **California** | **11/24/1987** | **SS** | **6.54, Mw** |
| 55 | Luzon | Philippines | 7/16/1990 | SS | 7.7, Mwc |
| **1** | **Landers** | **California** | **6/28/1992** | **SS** | **7.28, Mw** |
| **9** | **Kobe** | **Japan** | **1/16/1995** | **SS** | **6.9, Mw** |

|  |  |  |  |  |  |
|---|---|---|---|---|---|
| 65 | Neftegorsk | Russia | 5/27/1995 | SS | 7.0, Mwc |
| 37 | Zirkuh | Iran | 5/10/1997 | SS | 7.2, Mw |
| **5** | **Izmit_Kocaeli** | **Turkey** | **8/17/1999** | **SS** | **7.51, Mw** |
| **2** | **HectorMine** | **California** | **10/16/1999** | **SS** | **7.13, Mw** |
| **11** | **Duzce** | **Turkey** | **11/12/1999** | **SS** | **7.14, Mw** |
| 67 | Kunlun_Kokoxili | Northern Tibet | 11/14/2001 | SS | 7.8, Mwc |
| 10 | Denali | Alaska | 11/3/2002 | SS | 7.9, Mw |
| 22 | Parkfield2004 | California | 9/28/2004 | SS | 6.0, Mw |
| 14 | Yushu | China | 4/13/2010 | SS | 6.9, Mwc |
| 58 | Pisayambo | Ecuador | 3/26/2010 | SS | 5.0, Mw |
| 21 | Darfield | New Zealand | 9/3/2010 | SS | 7.0, Mw |
| 4 | Balochistan | Pakistan | 9/24/2013 | SS | 7.7, Mw |
| 54 | Yutian | China | 2/12/2014 | SS | 6.9, Mw |
| 13 | Napa | California | 8/24/2014 | SS | 6.0, Mw |
| 17 | Kumamoto | Japan | 4/15/2016 | SS | 7, Mww |
| 15 | Hualien | Taiwan | 2/6/2018 | SS | 6.4, Mw |
| 71 | Palu | Indonesia | 9/28/2018 | SS | 7.5, Mww |
| 42 | Ridgecrest1 | California | 7/4/2019 | SS | 6.4, Mw |
| 43 | Ridgecrest2 | California | 7/6/2019 | SS | 7.1, Mw |

[1] Style of faulting abbreviations: SS = Strike-Slip; NML = Normal; RV = Reverse; OBL = Oblique

[2] Magnitude types from USGS (2021): Mw = moment magnitude, details not reported; Mwc = moment magnitude based on centroid moment tensor inversion of long-period surface waves; Mww = moment magnitude based on centroid moment tensor inversion of W-phase; mB = bodywave magnitude; ML = local magnitude; Ms = surface-wave magnitude; U = unspecified

Unfortunately, the only quantitative analysis of strike-slip rupture probabilities and displacements is that of Petersen et al. (2011), now 12 years old. Eleven of the ruptures in Table 4-1 occurred after Petersen et al.'s manuscript was submitted, which means they could only include the 24 older earthquakes in their database. But of that number, Petersen et al. analysed only eight ruptures (1/3 of the total), bold text in Table 4-1). Why did they not analyze the other 2/3 of the pre-2010 surface ruptures?

On page 809 of their published paper, Petersen et al. (2011) state: *” These [n=8] earthquake ruptures were selected for our analysis because large-scale, detailed rupture maps are available as well as a dense sampling of displacement measurements both along the rupture as well as along other faults that ruptured during the earthquake. A number of other historical strike-slip earthquake ruptures [n=16] were not included in this analysis due to a lack of detailed slip measurements or a lack of detailed mapping along the length of the rupture.”*

For some of the ”missing” 16 ruptures, the lack of detailed displacement measurements is understandable, especially for those older than 1968. In the 1970s there were five ruptures (3 in California, two in Japan), but only the largest of the California ruptures (1979) was mapped in satisfactory detail for Petersen. After 1979 about half the global ruptures (n=14) had detailed published maps (Table 4-2). In California maps of the low-magnitude-6 earthquakes were either not detailed enough, or they had few to no displacement measurements on distributed faults. Only in ruptures >M6.5 were measurements detailed enough to satisfy Petersen et al.’s criteria. For ruptures outside California, only 38% of ruptures were mapped in enough detail for inclusion in Petersen et al.’s paper, and these were of M6.9 and larger. Some very large ruptures (M7.7, Pakistan; M7.8, northern Tibet; M7.9, Alaska) failed to meet Petersen’s criteria, due to their remote locations which restricted the post-rupture reconnaissance parties, and in Tibet and Alaska, the rupture was obscured by snow on the ground.

Table 4-2. Location and magnitude of the 20 strike-slip surface ruptures between 1968 and 2009 (from Table 4-1).

| **RUPTURES** | **California** | | **Non-California** | |
|---|---|---|---|---|
| Total Ruptures | 11 | Mw- Name | 9 | Mw- Name |
| Detailed Maps,<br>Many Displacement Measurements | 5 (50%) | 6.54-Borrego<br>6.5-Imperial<br>6.5-Superstition<br>7.28-Landers<br>7.13-Hector | 3 (38%) | 6.9-Kobe<br>7.51-Izmit<br>7.14-Duzce |
| No Detailed Map, or Not Enough Measurements | 6 (50%) | 5.2-Galway<br>5.2-Homestead<br>6.19-Chalfont<br>6.22-Elmore<br>6.0-Napa<br>6.0-Parkfield | 6 (62%) | 6.5-Izu<br>7.7-Luzon<br>7.0-Neftogarsk<br>7.2-Zirkuh<br>7.8-Kunlun<br>7.9-Denali |

So surprisingly, even though there were more strike-slip ruptures in the FDHI database (35) than reverse ruptures (25), the percentage used in analytical studies is lower for strike slip (8/20, or 40%) than for reverse ruptures (80%). This situation could potentially be remedied if all 11 post-2010 strike-slip ruptures had detailed maps with lots of displacement measurements. In that case, those maps could be digitized and a Nurminen-style or Moss-style analysis could be made on them.

However, there are two drawbacks to performing such work in the present study. First, it would take many months of work (basically a PhD project) to update the Petersen et al. (2011) paper to 2023, involving more than doubling the number of ruptures in the dataset (this is based on the time consumed updating the Australian reverse-fault ruptures). Second, it is hard to justify such work in this present report, because none of the ruptures (the eight from Petersen and the 11 new ruptures) occurred in a geologic setting like Forsmark. The 19 ruptures occurred either at plate boundaries or at the boundaries of known (defined) microplates. Earlier in Section 3 we justified manually updating the FDHI and Nurminen analysis of reverse faults in SCRs, because Australia is a very close SCR analog to Sweden. That same justification cannot be made for the strike-slip ruptures, either the ones analyzed by Petersen et al. (2011), or the post-2009 ruptures that could be added.

Therefore, our analysis will use the eight-rupture dataset of Petersen et al. (2011), in which they analyzed trends in probabilities and displacements of distributed faults.

Strike-slip Principal faults typically have vertical dips (Fig. 4-1). Because of this dip, the fault traces may extend for many km without a change in strike, even when crossing moderately rugged topography. The fault trace looks like it was carved by a knife. The main complexities in principal fault traces are stepovers (Fig. 4-1) and changes of strike. Stepovers and changes of strike are either transtensional or transpressional, and thus generate most of the secondary faulting associated with strike-slip ruptures. In contrast, if the fault maintains a constant strike, secondary ruptures will be limited to simple DRs (Rank 2) which die off exponentially away from the principal fault.

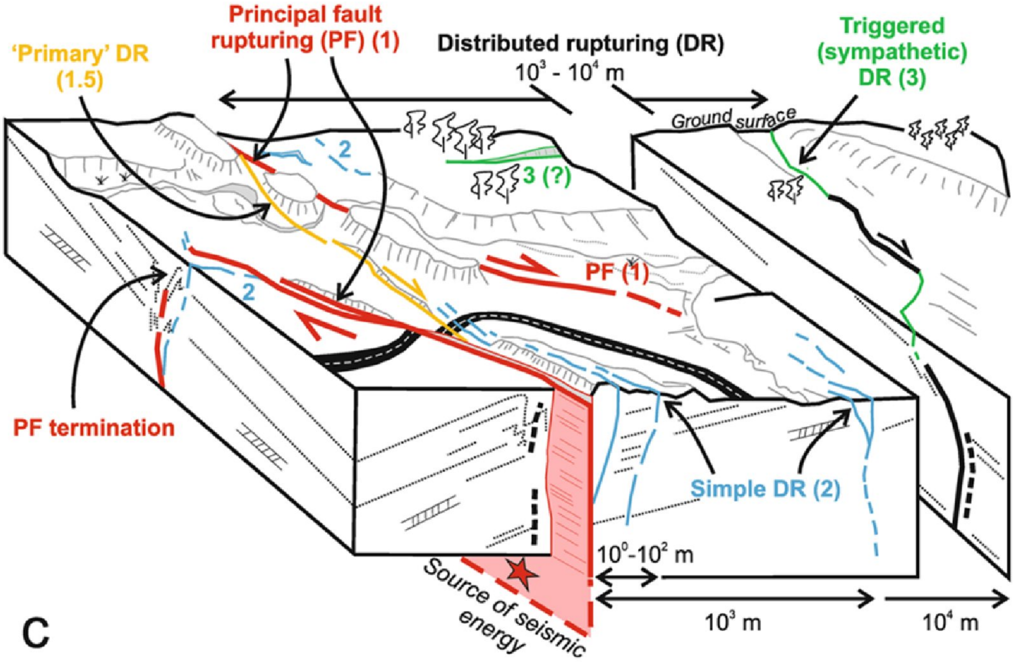

Figure 4-1. From Nurminen et al. (2022). Idealized diagram of a principal strike slip fault (red), flanked by secondary faults. Orange, primary DRs; blue, simple DRs; green sympathetic DRs. The red right-lateral fault makes a right step, which places the stepover area in fault-parallel extension (a transtensional stepover).

## 4.2. Is the crustal setting of Forsmark Similar to that of California?

The short answer is, no. If anything, the setting of Forsmark (non-extended Precambrian craton) is the tectonic opposite of California and other plate boundaries. Most SCRs are in a state of tectonic compression, so strike-slip surface ruptures are very rare in SCRs. The only compilation of historic strike-slip earthquakes in SCRs is that of Leonard (2014; see our Table 4-3). His 10 earthquakes range from M2.6 to 6.45, but only four created surface ruptures.

Table 4-3. Historic strike-slip earthquakes in nonextended Stable Continental Regions (SCRs). Listed from largest magnitude to smallest. Modified from Leonard, 2014.

M0 Range (N·m × 1016)

| Date (yyyy/ mm/ dd) | Event | Type | $\mathbf{M_W}$ | $M_0$ (N·m × $10^{16}$) | Mini-mum | Maxi-mum | References |
|---|---|---|---|---|---|---|---|
| 1939/07/22 | Ghana, Africa | SS | **6.45** | 590 | 209 | 16630 | *Kutu et al., 2013*; en-echelon fissure zone 20 km long; with left-lateral |
| 1983/12/22 | Guinea, Africa | N/SS | **6.29** | 339 | 240 | 479 | *Dorbath et al, 1984*; 10 km-long zone of cracks and en-echelon faults; max. dextral slip 10 cm; max. vert. displ. 15 cm<br>*Langer et al., 1985*; 9.4 km-long rupture, max. dextral slip 13 cm; max. vert displ 5-7 cm |
| 1967/12/10 | Koyna India | SS | **6.27** | 320 | 180 | 460 | *Modak et al., 2022*; 4 km-long, en-echelon fissure zone; max. Vert displ. 5- |
| 2011/11/06 | Oklahoma 2, United | SS | **5.7** | 45 | 32 | 63 | *Grandin et al., 2017*; NSR, but InSAR shows 3 cm |
| 1966/10/09 | Sudan, Africa | SS | **5.64** | 36 | 8.1 | 144 | *Warage, 2007*; Zone of tension gashes up to 4 cm wide, 8 km long |
| 2008/04/18 | Mt. Carmel, | SS | **5.23** | 8.8 | 7.0 | 17 | NSR |
| 2011/11/05 | Oklahoma 1, United | SS | **5.0** | 4 | 2.8 | 5.6 | NSR |
| 2011/11/08 | Oklahoma 3, United | SS | **5.0** | 4 | 2.8 | 5.6 | NSR |
| 2010/02/09 | Siheung, | SS | **3.14** | 0.0065 | 0.0046 | 0.009 | NSR |
| 2004/08/07 | Siheung, | SS | **2.62** | 0.00107 | 0.0009 | 0.0015 | NSR |

NSR- No Surface Rupture

The M6.45, 6.29, 6.27, and 5.64 earthquakes created surface rupture zones composed of ”en-echelon fissures or tension gashes”, interspersed with small faults with strike-slip and vertical displacements. Unfortunately, the published rupture maps are poor and few displacement measurements were made during the immediate post-earthquake reconnaissance. Given the small displacements and open fissures, it is unlikely these surface ruptures have been preserved. The ruptures range in age from 84 years, 57 years, 56 years, and 40 years. This means the only data we will ever have on these surface ruptures are those collected by the initial reconnaissance studies. It is understandable that FDHI and SURE 2.0 did not include these ruptures in their databases.

## 4.3. Probability of distributed faulting (DF) as a function of distance from the principal strike-slip fault (global datasets)

Petersen et al. (2011) used the grid cell approach to counting the presence/absence of DFs at various distances from the PF, following Youngs et al. (2003), rather than using the slice method of Nurminen et al. (2020) or Moss (2022). They also examined the effect of grid cell size on the ’probability’ of rupture in their cells. They state: *” We examined the probability of ground rupture in areas off of the principal fault of 25 m×25 m, 50 m×50 m, 75 m×75 m, 100 m×100 m, and 200 m×200 m.”* It might have been more precise for them to say they ”measured the frequencies” rather than they ”examined the probabilities.”

They assumed that DF occurrence as a function of distance from the PF was a power function, such as:

*”*$Ln(P) = a(z) \ln (r) + b(z)$ *Eq. 18*

*where a(z) and b(z) are regression coefficients and are functions of grid size, and r is fault distance. These parameters are listed in [our Table 4-4] for the five grid sizes investigated in this study.”*

Table 4-4. Probability of distributed fault rupture for different cell sizes (see Eq. 20). Table 4 from Petersen et al. (2011).

| Cell size (m2) | a(z) | b(z) | std. deviation |
|---|---|---|---|
| 25x25 | -1.1470 | 2.1046 | 1.2508 |
| 50x50 | -0.9000 | 0.9866 | 1.1470 |
| 100x100 | -1.0114 | 2.5572 | 1.0917 |
| 150x150 | -1.0934 | 3.5526 | 1.0188 |
| 200x200 | -1.1538 | 4.2342 | 1.0177 |

Note that their only independent variable affecting ”d” is ”r”, the distance away from the PF. There is no term for earthquake magnitude in their equation.

Example calculation: Given that r=300 m, and cell size is 100x100 m, what is the probability of having a DF at that distance?

$Ln(P) = a(z) \ln (r) + b(z)$ Eq. 18

Where(P) is probability of having a DF at the given distance ”r”?

[a] $Ln(P) = -1.0114 * \ln (300m) + 2.5572$

[b] $Ln(P) = -1.0114 * 5.70 + 2.5572$

[c] $Ln(P) = -5.765 + 2.5572$

[d] Ln(P)= -3.2078

[e] (P)= e-3.2078

[f] (P)= 0.040

The equation indicates that the probability of having a DF 300 m away from the PF is 4%, regardless of the magnitude of the earthquake. That conclusion certainly contradicts all other studies (e.g., Youngs et al., 2003; Nurminen et al., 2020; and Moss et al, 2022). Petersen et al. (p. 818) explain their results in this way: *"The probability of surface displacements is high for sites very close to the fault. However, this frequency drops off quickly. The displacement data indicate that most displacements occur on or within a few hundred meters of the principal fault. Contrary to the results of Youngs et al. (2003), we found no magnitude dependence for this probability."*

I personally have little confidence in this conclusion, and venture to guess that if the other 11 post-2009 strike-slip ruptures were added to Petersen's database, the larger dataset would reveal that probability of rupture is indeed affected by earthquake magnitude.

We can also calculate DF rupture probabilities at closer distances to the PF (100 m, 200 m) using Eq. 18, see below:

[a] Ln(P)= -1.0114* ln (200m) + 2.5572

[b] Ln(P)= -1.0114* 5.3 + 2.5572

[c] Ln(P)= -5.3604 + 2.5572

[d] Ln(P)= -2.8032

[e] (P)= e-2.8032

[f] (P)= 0.061

[a] Ln(P)= -1.0114* ln (100m) + 2.5572

[b] Ln(P)= -1.0114* 4.6 + 2.5572

[c] Ln(P)= -4.6577 + 2.5572

[d] Ln(P)= -2.1005

[e] (P)= e-2.1005

[f] (P)= 0.122

As expected, probability of DF increases closer to the PF, being 4% at 300 m, 6% at 200 m, and 12% at 100 m. However, Petersen et al. warn: *" This power function, however, does not extrapolate well in areas within a few hundred meters of the fault. Therefore, for areas close to the [principal] fault (near field), rupture probability is linearly interpolated using the rupture probability (p0) on the [principal] fault and the first two off-fault rupture probability measurements (p1 at a distance of r1 for the first point and p2 at a distance of r2 for the second point)."*

The equation they use for probability of faulting on the PF is:

$P[sr \neq 0 \mid m] = e(a+bm) / (1+e(a+bm))$ Eq. 19

Where:

m= moment magnitude

a= -12.51

b= 2.053

### 4.3.1. Comparison of (P) using the ln(P) equation, versus a linear interpolation

First, let us assume we have an M6.5 surface rupture. Solving Equation 19 for m=6.5 and with the coefficients of Petersen et al. (2011), we derive the probability of faulting on the PF= 0.7. Thus the probabilities at 100 m and 200 m distances can be linearly interpolated between the P(PF) and the P(r=300 m). This yields a ”probability gradient” of 0.66/300 m, or 0.0022/m. The interpolated probabilities of DF faulting at 100 and 200 m can be compared with the probabilities calculated with Equation 18 (Table 4-5).

Table 4-5. Comparison of probabilities of DF computed by Eq. 18, to those computed by a linear interpolation between P(PF) and P(r=300 m).

| Distance from PF (r) | Prob. of DR From ln(P) equation (Eq. Xx) | Prob. of DR from Linear Interpolation between P(PF), P(r1), and P(r2) |
|---|---|---|
| 0 (at PF) | 0.7 | 0.7 |
| 100 m | 0.122 | 0.48 |
| 200 m | 0.061 | 0.26 |
| 300 m | 0.040 | 0.04 |

Table 4-5 shows much higher probabilities of DF faulting at 200 m and 100 m than does Eq. 18. In Eq. 18, almost all the probability increase occurs between 100 m from the PF and the PF (from 0.122 to 0.7). When we transition from Eq. 18 to a linear interpolation at 300 m from the PF, the probability increase is spread out over 300 m, instead of being ”telescoped” into the interval r=0 and r=100m. Unfortunately, Petersen et al. (2011) do not say exactly where this transition should occur. They just say it should be ”*for areas close to the [principal] fault”* (Petersen et al., 2011, p. 819). In the example above I chose to make the transition at 300 m, but do not know if that is what Petersen et al. would consider ”close to.”

## 4.4. Displacement on distributed faults as a function of distance (r) from the principal strike-slip fault (global datasets)

### 4.4.1. Distributed-fault displacements (d) as a natural log function of "m" and "r"

Petersen et al. (2011) derived two regression equations of displacements on distributed strike-slip faults. Their first regression was on observed "d" values (DF displacement; rendered as ln d) as a function of independent variables "m" (earthquake magnitude) and "r" (distance from the primary fault, rendered as ln r). This is very similar to what Nurminen did with three independent variables (her "s", "DN", and "m"). On page 818-819 Petersen states:

*"We performed regression analysis on the off-fault displacements and found a weak correlation with magnitude (m) and distance (r, in meters) from the rupture. Figure 7 [our Fig. 4-2] shows the off-fault displacement data and regression lines for M 6.5 to 7.5 events."*

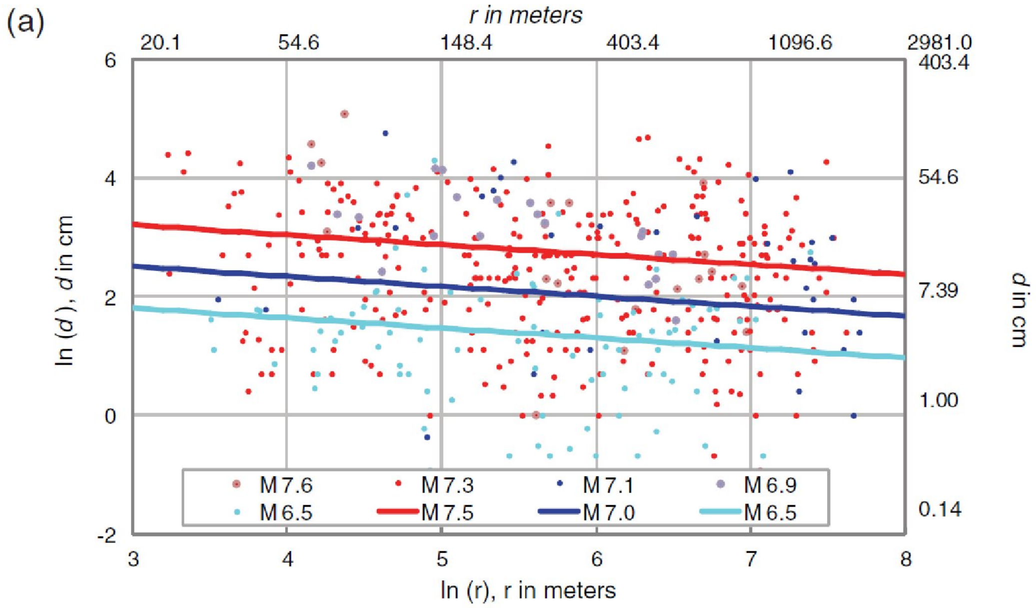

Figure 4-2. Distributed-fault displacement data and (a) regression displacements color-coded by magnitude with bilinear regression lines for M 6.5 to 7.5. From Petersen et al., 2011, their Fig. 7a.

They continue: *"Statistical analysis on distributed-fault displacement data shows that the relationship between d and r is best described by a power function: d=arb. The regression is performed on its transformed form (i.e., both d and r are in ln terms by taking the natural log on both sides of the equation). Adding a linear dependence of m, we obtain:*

$$\ln(d) = 1.4016m - 0.1671\ln[r] - 6.7001 \qquad \text{Eq. 20}$$

*Where: d is in centimeters and r is in meters. This regression has a standard deviation of 1.1193 in ln units. The standard error for the slope of ln [r] is 0.0476. Based on the rule of thumb (i.e., if a coefficient estimate is more than 2 standard errors away from zero,* *then it is statistically significant; Gelman and Hill, 2007), the distance term is significant although the correlation is rather weak.*"

The coefficients in the above equation indicate that the major control on "d" is earthquake magnitude (m), rather than distance from the principal fault [r]. This is understandable due to the ambiguity in measuring "r" where there are multiple, parallel traces of the principal fault, such as in stepovers. Despite this fact, we have no choice but to use the Equation 20 to calculate "d" to compare with the predicted "d" from the numerical methods on vertical faults.

### 4.4.2. Normalized distributed-fault displacements as a power function of "r"

In the manner of Moss et al. (2022) described for reverse ruptures, Petersen et al. relate a normalized measure of "d" as $d/D_{ave}$, when regressing it against the independent variable "r" (distance to the PF). [Remember, they do not think "d" is affected by earthquake magnitude]. They state (p. 818*)" "Again, using a power function, the off-fault displacement normalized by the average displacement for a given earthquake is found to be:*

$\ln(d/D_{ave}) = -0.1826 \ln[r] - 1.5471$ *Eq. 21*

*Where: r is in meters. This regression has a standard deviation of 1.1388 in ln units, and standard error for the slope is 0.0483. Figure 7b [our Fig. 4-3] shows the normalized off-fault displacements along with the regression curve and its uncertainties."*

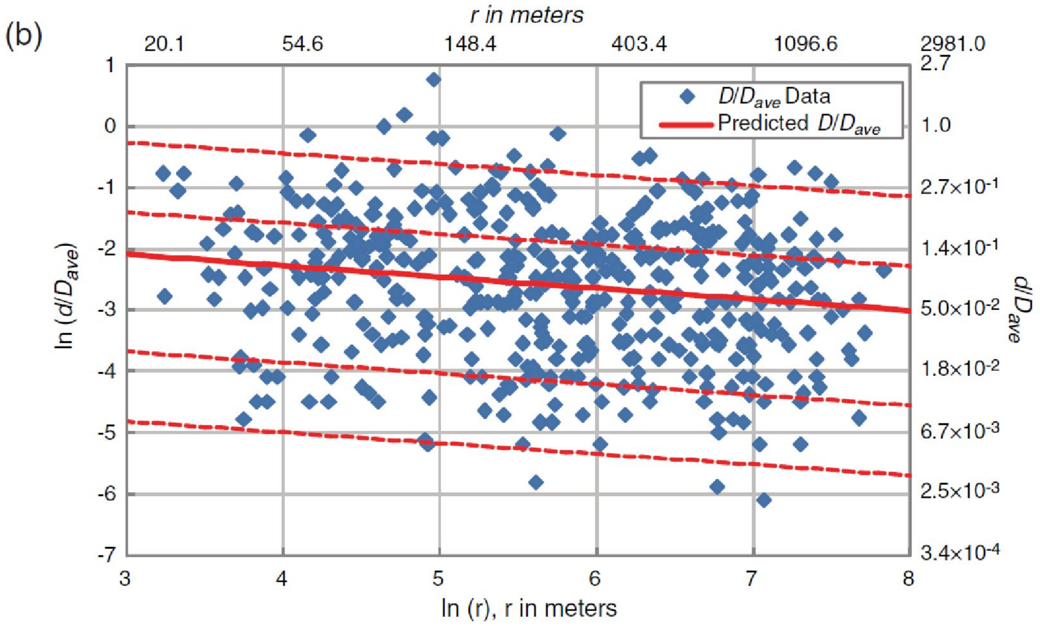

Figure 4-3. Distributed-fault normalized displacement data ($d/D_{ave}$) with bilinear regression line and uncertainties (±1 and ±2 standard deviations). From Petersen et al., 2011, their Fig. 7b.

However, both Petersen et al. (2011) and Moss et al. (2022) have introduced a source of error in the way they calculated $D_{ave}$. $D_{ave}$ should be the average of all the displacement measurements along the Principal fault. But rather than using the displacement measurements from each rupture to compute its own unique, area-weighted $D_{ave}$ (and they had the data to do that; see McCalpin, 2009b, p. 617-618), they instead 'compute' $D_{ave}$

from earthquake magnitude, using an empirical equation which contains considerable uncertainty. They explain this unnecessary procedure below:

*"To calculate the average on-fault displacements, $D_{ave}$, which is needed for the normalized regressions, we have applied the Wells and Coppersmith (1994) equation for strike-slip faults. They derived the formula*

*$log10(D_{ave}) = a + bm \pm \varepsilon$;* *Eq. 22*

*where $D_{ave}$ is in meters; a is -6:32; b is 0.90; and ε, the standard deviation in log10 units, is 0.28. This analysis analyzed displacements from earthquakes with M 5.6 to 8.1. The average displacement data that we used in this study are consistent with the Wells and Coppersmith (1994) data and their strike-slip regression equation."*

This procedure would not have compromised their results, if the above empirical equation had a standard deviation of zero. But as they state, it has a standard deviation of 0.28 log units of $D_{ave}$. So by introducing a $D_{ave}$ value they know contains error, they introduce a major source of error into their quantity $d/D_{ave}$. And this error is then propagated through every prediction of "d" as a function of ln "r".

Below is an example calculation of "d" given a specified value of "r" and $D_{ave}$:

Given the Borrego Mountain earthquake with $D_{ave}$= 18 cm; if r=200 m, then ln r= 5.3

Solving for d requires the six steps below (from Eq. 21)

[a] ln $(d/D_{ave})$= -0.1826 ln [r] – 1.5471 (yields the mean/median value of $d/D_{ave}$)

[b] ln $(d/D_{ave})$= -0.1826*5.3 – 1.5471

[c] ln $(d/D_{ave})$= -0.9678 – 1.5471

[d] ln $(d/D_{ave})$= -2.515

[e] $d/D_{ave}$= e-2.515= 0.081

[f] given that $D_{ave}$= 18 cm, then:

d= $D_{ave}$*0.081= 18 cm * 0.081= 1.46 cm.

This is the mean value of displacement.

However, if one wishes to know a more conservative measure of induced displacement such as the mean+2σ value for $d/D_{ave}$, at the same distance r=200 m, we have to use the mean+2σ intercept value (+0.3) of Petersen's equation

[ln $(d/D_{ave})$= -0.1826 ln [r] +0.3], which reduces to:

[a] ln $(d/D_{ave})$= -0.1826 ln [200] +0.3]

[b] ln $(d/D_{ave})$= -0.1826*5.3 +0.3

[c] ln $(d/D_{ave})$= -0.9678 +0.3

[d] ln $(d/D_{ave})$= -0.6678

[e] $d/D_{ave}$= e-0.6678= 0.513

[f] given that $D_{ave}$= 18 cm, then:

d= $D_{ave}$*0.513= 18 cm+0.513= 9.23 cm

In this example case, the predicted mean of "d" at 200 m from the Principal fault is 1.46 cm, but the predicted mean+2σ value of "d" at the same distance is 9.23 cm, or a factor of 632% larger. Note that the lower number is well below the 5 cm threshold for displacement on target fractures, while the higher number is 185% of the threshold displacement.

I personally think the large size of the standard deviation results from how Petersen et al. got their estimate of $D_{ave}$, as explained above. If the real, area-weighted $D_{ave}$ had been measured for each surface rupture, I suspect the standard deviation would be cut in half.

So it can be seen that the present published strike-slip data for PFDHA is not quite up to the standard needed for design, compared to the state of reverse and normal faults. This situation could be partly remedied in several ways: (1) adding the 11 post-2009 strike-slip ruptures to Petersen's strike-slip rupture dataset; (2) for the $d/D_{ave}$ method, calculating the true, geometrically-weighted $D_{ave}$ for each rupture; and (3) deriving a Nurminen style three-factor equation for "d". This includes calculating DN for every DF measurement point.

## 4.5. How to Predict the distance and Displacement of Distributed Faulting at a Depth of 500 m?

We follow the same general procedure for strike-slip PFs as for reverse PFs (Section 3.8).

### 4.5.1. Position of the DFs at -500 m at Forsmark.

As before, our easiest option is to assume all fractures reactivated by future Forsmark earthquakes have a strike and dip identical to the scenario Principal fault plane (i.e., vertical). Under this assumption, horizontal distances between the PF fault plane and reactivated DFs would not change, regardless of the depth they were measured at. This assumption has two advantages. First, it is supported by fracture mechanics. SKB assumed certain faults (their scenario faults) were optimally oriented to slip and generate earthquakes in future stress fields. It would logically follow that the fractures most likely to be reactivated would be those with the same 3D orientation as the PF. Second, the assumption permits us to use the DF-to-PF surface distances from the Australian ruptures as a proxy for the same distances at 500 m depth at Forsmark. That, in turn, allows us to use the probability and displacement equations of Nurminen and Moss.

For the purpose of comparing empirical DFs to predicted shear fractures from numerical models, we will assume that all DFs strike and dip parallel to the PF, and thus the DF-to-PF distances used in the Nurminen and Moss equations can also be used at a depth of 500 m at Forsmark. Assuming anything else leads to unconstrained dips and thus unpredictable locations for DFs relative to PF, leaving us in a wilderness of non-unique solutions based on no data.

### 4.5.2. Predicting displacement at -500 m at Forsmark

The Nurminen and Moss equations for DF displacement as a function of distance to the PF are based on surface data. How might those displacements change at a depth of 500 m? We can envision two possible options for relating subsurface displacements to surface displacements.

1. Option 1: assume that the dip-direction slip gradient between 500 m depth and the surface is negligible, so displacements at -500 m will be identical to surface displacements.
2. Option 2: use slip gradients from the published literature to adjust surface displacements to a predicted value at -500 m.
    a. use surface (along-strike) slip gradients measured on historic strike-slip surface ruptures as a proxy for dip-direction slip gradients.
    b. use subsurface (3D) slip gradients shown in slip distribution diagrams for historic strike-slip surface ruptures, inverted from either InSAR data or teleseismic data

Although using Option 1 is a tempting choice, there is enough published slip gradient information on M5-7 strike-slip earthquakes to show that slip gradients, even in the upper 500 m, are non-zero. The problem is finding slip distribution diagrams from the correct historic analog earthquakes, similar to scenario earthquakes in numerical models.

*Surface Slip Gradients*: Shaw (2011) analyzed 20 surface rupturing earthquakes to define typical gradients of surface slip along strike (previously described in Section 3.8.2). All 20 plots of surface displacement along strike were dominated by high-frequency variations of unknown origin (the so-called ”sawtooth curve” of displacement; McCalpin, 2009b, p. 15). Shaw concluded this ”noise” included measurement error, local effects caused by thickness and rheology of surface deposits, and unknown factors. However, seven of his ruptures showed coherent slip gradients based on five or more adjacent measurement points (Fig. 3-38), of which five are strike-slip events. Slip gradient is measured as change in slip/distance over which the change occurs, which can either be cited in m/km, or as m/m (dimensionless number). In fact it can be treated as a strain, such as a change in length/length. All of the coherent rupture sections yielded slip gradients in the range of $1x10^{-4}$ to $9x10^{-4}$.

Shaw then plotted the coherent slip gradients against their length (Fig. 3-39a) and their earthquake magnitude (Fig. 3-39b). There is no apparent correlation in either case. Shaw remarked: *”In both cases, importantly, there is a lack of any obvious trend. That is, coherent surface-slip strain values appear to be independent of length scale and also independent of event magnitude.”* The implication is that surface slip gradients are limited by some type of physical restraint within the faulting process itself, which prevents fault-plane slip from changing too rapidly in space.

*Subsurface Slip Gradients*: Seismologists use two methods to deduce the 2-D pattern of slip distribution on fault planes of large historic earthquakes. The older method inverts teleseismic recordings to reconstruct the spatial pattern of slip on the fault plane (e.g. Hartzell and Heaton, 1983). The more recent method is to measure the spatial field of coseismic deformation with InSAR, and then invert that field (e.g. Atzori et al., 2009). For historic surface ruptures not at plate boundaries, we have located several studies that compute subsurface slip distributions using the older or more recent methods.

Chen et al. (2021) used the InSAR coseismic deformation field from the 2021 M7.3 Maduo, China earthquake to invert to a subsurface strike-slip distribution (Fig. 4-4). We measured the two highest-appearing, dip-parallel slip gradients between a shallow slip maximum and the ground surface. On the left the dip-slip gradient is 1.4 m/6 km; on the right the gradient is 2 m/6 km. These slip gradients reduce to $2.33x10^{-4}$ and $3.33x\text{-}10^{-4}$, respectively.

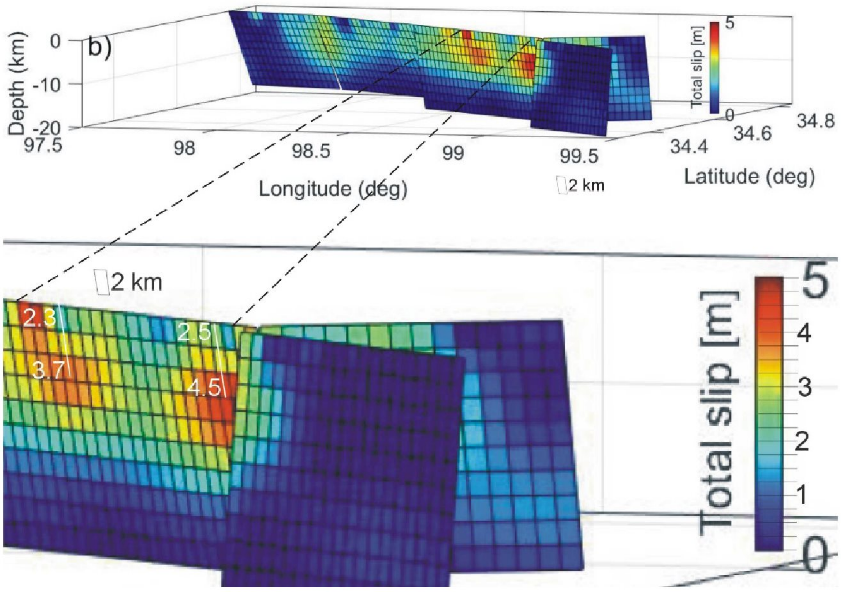

Figure 4-4. Estimated coseismic slip along the Maduo fault strike. Top, original Fig. 5b from Chen et al., 2021. Bottom, enlarged part of slip distribution showing two high dip-slip gradients (white lines). White numbers are average strike-slip displacement in each cell; cells are 2 km high.

Pedersen et al. (2003) analyzed a pair of smaller (M6.5) earthquakes from Iceland, perhaps more representative of earthquake scenarios at Forsmark.

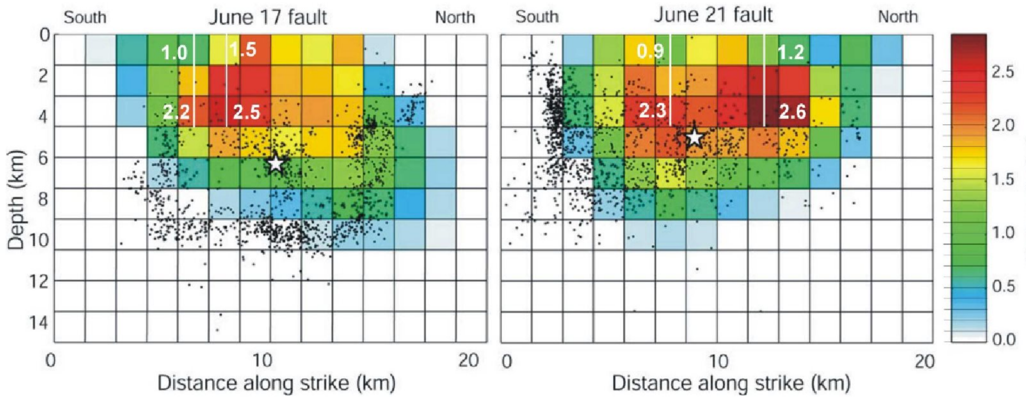

Figure 4-5. Estimated coseismic slip along the M6.5 South Iceland Seismic Zone ruptures. Left, the June 17 earthquake, from Pedersen et al., 2003, their Fig. 4. Right, the June 21 earthquake. Dip-slip gradients (vertical white lines) in strike-slip. White numbers are average strike-slip displacement in each cell; cells are 1.5 km square.

The largest slip gradients in the June 17 event, measured between largest slip cells and the surface, were 1.0 to 1.2 m/km (2.22 to $2.67\text{x}10^{-4}$). In the June 21 event the largest slip gradient was 1.4 m/km, or $3.11\text{x}10^{-4}$.

Overall the dip-direction slip gradients cited above cluster in the range $2.2\text{x}10^{-4}$ to $3.11\text{x}10^{-4}$, almost exactly the same range as slip gradients measured from along-strike surface displacements. Unlike for reverse faults, dip-direction slip gradients do not seem to correlate with the magnitude of the strike-slip earthquake (Fig. 4-6).

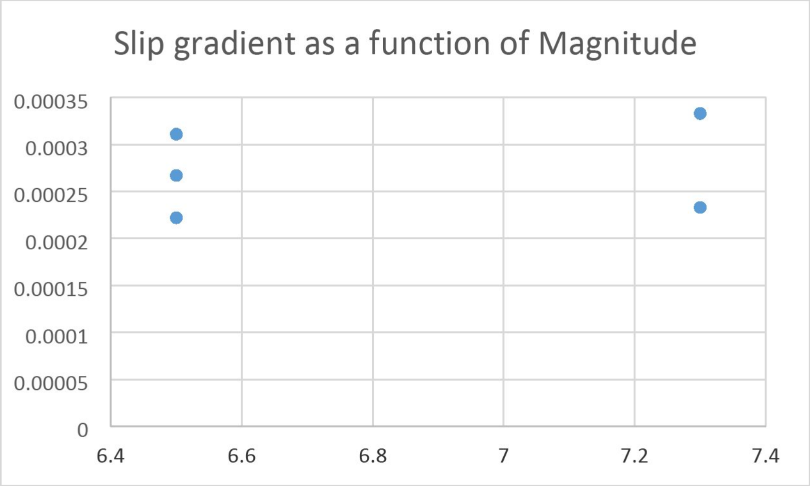

Figure 4-6. Maximum slip gradients in our example strike-slip fault planes, measured in the dip direction, as a function of earthquake magnitude. No trend is apparent; variance within each earthquake is larger than variance between earthquakes.

How should we use these slip gradients to correct surface DF displacements to those at -500 m? For example, if we applied a downdip slip increase of 0.15 m/km from the surface to a depth of 500 m, that would result in a 0.075 m (7.5 cm) increase in displacement at 500 m, compared to the surface displacement. That 7.5 cm is larger than the displacement threshold assumed for canister failure. In other words, even if a DF displacement were zero at the surface, it would be more than the threshold displacement at -500 m. And this is using the low end of slip gradient values.

The fact is, all the slip gradient data we have is on coseismic principal faults; we have no data on distributed faults. And since most DFs do not generate their own seismic energy, we cannot use teleseismic data to invert for their slip distributions. The area of DFs is within the elastic deformation area imaged by InSAR, so the inversion technique there has already assigned the cumulative off-fault vertical deformation to elastic crustal deformation by the PF. So there would be nothing left to assign to DFs at any rate without violating the inversion model assumptions.

IN SUMMARY: It does not seem justifiable at this time to adjust DF displacements at the surface to any depths such as -500 m, due to lack of any empirical subsurface data on DFs. For the reasons described above, it does not seem likely we will ever be able to measure such subsurface displacements. However, we may be able to make some type of comparison between observed DFs at the surface, and the 3DEC models. If it were possible for the 3DEC models to calculate shear displacements on fractures at the ground surface, rather than at a depth of 500 m, then we could compare those 3DEC surface displacements to the empirical data sets.

# 5. Comparison of empirical df displacements with numerical analysis displacements

This section answers a simple question: do potential earthquake-induced shear displacements on fractures in the Forsmark repository, calculated by SKB and SSM, match displacements calculated by the PFDHA method used by seismologists and earthquake engineers? McCalpin recommended this comparison in 2013 (McCalpin, 2013), because the ”rock mechanics” method used by SKB and SSM was very difference than that used by seismic hazard analysts. The standard method of calculating permanent, off-fault, surface displacements during future earthquakes is the Probabilistic Fault Displacement Hazard Analysis (PFDHA), and is recommended for use by the International Atomic Energy Agency (IAEA, 2021. IAEA (2021, their Section 3.3.4) says this about the use of numerical models in PFDHA:

*”Ideal models to fill the gaps due to the lack of data are physics-based models that take into account the following elements: (1) geometry of finite fault rupture; (2) physical rupture criteria to break the free-surface; (3) three-dimensional (3-D) stress field; and (4) geological and site conditions. These physics-based models can be constrained with available information of the area of interest; in particular, of primary importance, are the geometrical fault complexity ...and the 3-D stress field. The level of detail of the fault geometry depends on the needs and sensitivity of the results [Aochi and Ulrich, 2015]. The stress field is particularly essential when considering non-elastic off-fault deformation and fault networks with different fault orientations and depths [Aochi et al., 2005; Durand et al., 2017]. All these features are relevant for fault displacement prediction.*

*As described in [IAEA Sections 3.1 and 3.3.1], due to data limitation the different components of PFDHA use empirical probability distribution models based in global data set (also limited) to estimate fault displacement. Nevertheless, earthquake processes are not consistent with such ergodic assumption, as demonstrated by some researchers using the largely increased ground motion database over the last decade.... The use of site-specific non-ergodic models can have a large effect on seismic hazard estimates.... Therefore, in the context of site-specific PFDHA, the physics-based numerical simulations, capturing details of the site of interest for fault displacement prediction, can complement the empirical models and available data to improve the representation of the site of study and to be consistent with the non-ergodic process of natural earthquakes.”*

## 5.1. Numerical methods used to predict fracture shear displacements during earthquakes at Forsmark

Prediction of off-fault fracture displacements were based on some form of finite-element model, as published by SKB in its own report series, and papers in the peer-reviewed journals. This includes later publications by non-SKB consultants such as Lei and Loew, 2021. In contrast, SSM commissioned consulting that used a Particle Flow Code approach (Yoon et al., 2014; Yoon and Zang, 2019). Both sets of reports were reviewed herein and used for the comparison between numerical and empirical predictions of ”d”.

### 5.1.1. DF displacement (d) as a function of DF length (L)

Both numerical approaches assume that induced fracture displacement is positively correlated with fracture length. Let us examine the displacement/length ratios in historic surface ruptures in Australia to see if that relationship holds true for actual ruptures.

The most critical decision in this process is to determine if the FDHI classification of rupture traces into Principal versus Distributed is correct, First, if a rupture trace with a large displacement was classified by FDHI as Distributed, when it was actually principal, that large Principal displacement would mistakenly be designated as a DF. Such a mis-classification would lead to overestimation of true DF displacements. Second, some DFs are expressed as separate rupture segments that are on-strike, separated by gaps. My assumption is that these DF segments are underlain by a single reactivated fracture, with a length (L) equal to at least the cumulative length of the segments.

As can be seen in Figs. 5-1 to 5-3, the displacement/length ratios in Australian distributed ruptures generally do not show that displacement increases with length. In Fig. 5-1 (Cadoux rupture, 16 DF displacement points, R2=0.38) and in Fig. 5-2 (Petermann rupture, 13 DF displacement points, R2=0.05), displacement decreases with increasing rupture length.

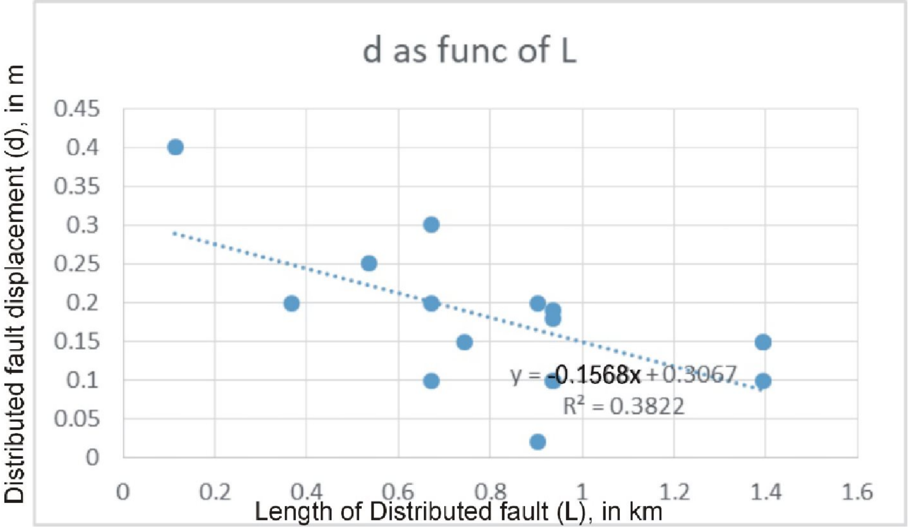

Figure 5-1. DF displacement (d, in m) as a function of length of DF rupture strand (L, in km) for 16 DF measurement points on the 1979 M6.1Cadoux, Australia, rupture.

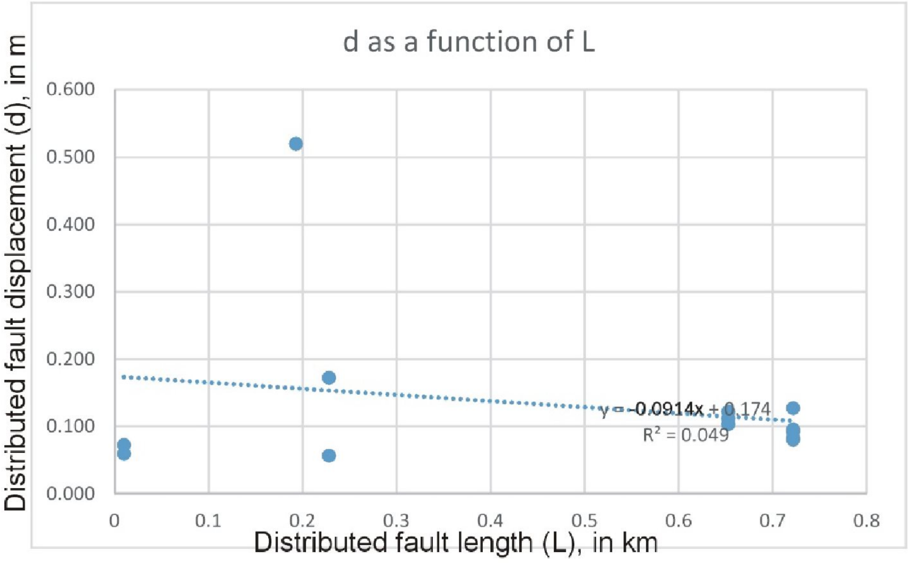

Figure 5-2. DF displacement (d, in m) as a function of length of DF rupture strand (L, in km) for 13 DF measurement points on the 2016 M6.0 Petermann, Australia, rupture.

In contrast, the smaller Calingiri rupture (M5.03, with six DF displacement points) shows a positive correlation between DF rupture length and DF displacement, with an R2=0.25 (Fig. 5-3).

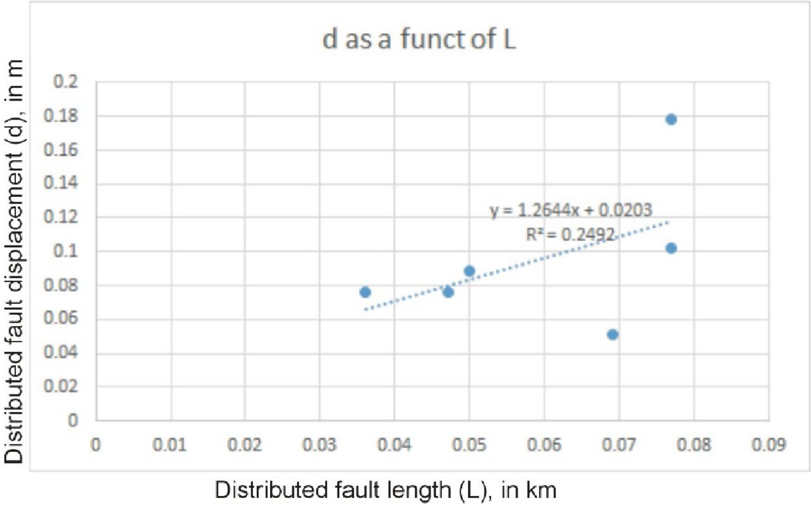

Figure 5-3. DF displacement (d, in m) as a function of length of DF rupture strand (L, in km) for six DF measurement points on the 1970 M5.03 Calingiri, Australia, rupture.

The other two ruptures in the analyzed Australian dataset (Meckering and Tennant Creek) have very few DF displacement measurements outside of long, sympathetic DFs. In the Meckering surface rupture, the footwall ”splinter fault” has its own slip gradient along strike, similar to a triangular distribution (Fig. 3-12). The maximum displacement (0.67 m) compares to the maximum PF displacement opposite the splinter fault of ~1.2 m. In other words, dmax/DPF= 0.56.

The Tennant Creek rupture has no measured DF displacements except on the long footwall fault, and of those six DF measurements, five have even larger displacements than on the PF. The footwall fault has its own boxlike slip gradient along strike (Fig. A-4d, center inset).

SUMMARY: In historic reverse ruptures worldwide (Sec. 3.6) and in Australia (Sec. 3.7.1), DF displacement decreases with increasing distance (s) from the PF (an inverse relationship). The latter can be shown by equations for the hanging wall and footwall, respectively:

$$\ln Y= -4.31 + (-0.185*(\ln s)) + (0.343*(\ln Dn)) + (0.614*m) \qquad \text{Eq. 23-HW}$$

$$\ln Y= -17.6 + (-0.083*(\ln s)) + (-4*(\ln Dn)) + (2.592*m) \qquad \text{Eq. 24-FW}$$

Note that the regression coefficient for distance (ln “s”) is negative in both cases, indicating an inverse relationship between distributed displacement (Y) and distance from the PF (s).

Both SKB (3DEC) and Yoon and Zang (PFC) codes assume that induced shear fracturing is controlled by the length of the fracture (a positive correlation), and it doesn’t make any difference how far away the fracture is from the activated fault. We showed in Figs. 5-1 through 5-3 that DF displacements in two of three well-studied SCR ruptures decreased as a function of fracture length. So we then combined the DF displacement measurements (d) from the Calingiri, Cadoux, and Petermann ruptures (n=35) and regressed them as a group against fracture length (L). Fig. 5-4 shows that, in the grouped dataset, d still has an inverse relationship with L.

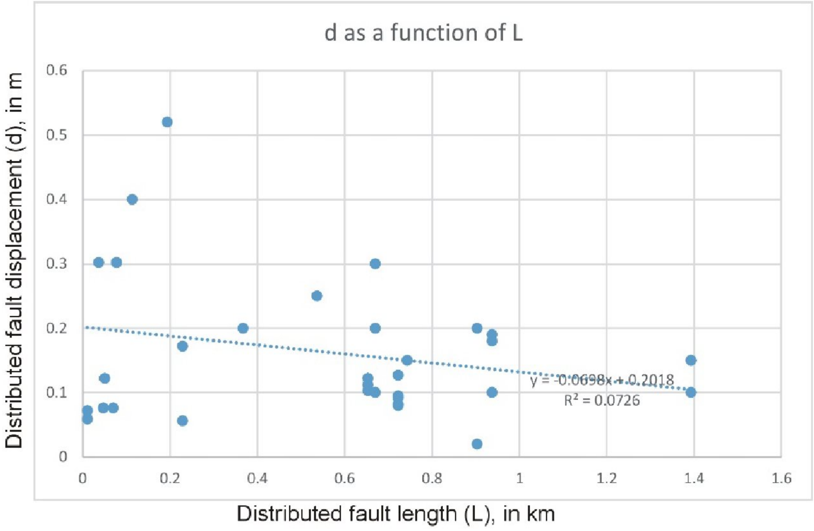

Figure 5-4. DF displacement (d, in m) as a function of length of DF rupture strand (L, in km) for 35 DF measurement points on the Calingiri, Cadoux, and Petermann, Australia, ruptures.

Granted, the R2 value of the regression is not high (0.0726). The inverse regression line is mainly controlled by the six points with highest displacement (>0.25 m). If we eliminated these six points the regression line might switch to positive, and the R2 value would certainly increase. However, these six large displacements are the least likely to be in error, because it is easier to measure them in the field, and they would have caught the eye of the field geologists on-site. The most likely displacement points to be in error are the smaller ones. And trimming off all the displacements <0.1 m would lead to a stronger inverse relationship, rather than a positive relationship.

So there does not seem to be any empirical data from DFs supporting a positive relationship between ”d” and ”L”, which apparently underlies the basis of the numerical methods. There is, however, a large body of empirical observations of ”d” on DFs decreasing with increasing distance from the Principal fault, a trend also predicted by the numerical methods.

## 5.2. 3DEC displacements of SKB

The SKB Report TR-19-19 (Hökmark et al., 2019) summarizes 3DEC earthquake simulations made for Forsmark, in which ”secondary off-fault fracture displacements” were computed using numerical models.

They state (p. 11*): ”There is, however, the theoretical possibility that also modestly sized fractures could slip in response to dynamic and quasi static stress effects of an earthquake occurring on a nearby or distant fault. Since such secondary, seismically induced, fracture shear displacements would be powered and controlled by complicated combinations of stress wave effects and stress redistribution effects rather than by the type of stresses powering the seismic events considered by Wells and Coppersmith (1994), there is no way of using the empirical data shown in Figure 1-3 to obtain lower area bounds to fractures that potentially could slip by 50 mm or more in response to a nearby earthquake. Since there does not seem, at the present time, to exist any systematic compilation of empirical data relevant to this issue, estimates of secondary off-fault fracture displacements for different types of earthquakes will have to be based on results of numerical simulations...............In this overview, the results of the many attempts made, both in the past with very schematic input assumptions and more recently with input assumptions based on Forsmark and Olkiluoto site data, to set bounds to seismically induced secondary displacements are compiled.”*

Numerical analysis of earthquake-induced shear displacements on preexisting fractures and faults was initially published in a peer-reviewed journal by Fälth et al. (2015). It modeled how dynamic, coseismic stress changes around an active fault would theoretically induce secondary faulting on pre-existing fractures and faults. Secondary faulting was modeled with the software 3Dimensional Distinct Element Code (3DEC). A later independent analysis of secondary faulting at Forsmark was recently published by Lei and Loew (2021). In their abstract, Lei and Loew state: *”During the assessment period of up to one million years for the KBS-3 repository, one large earthquake (at most two) having a moment magnitude ≥5 within a 5 km radius around the repository may be expected... Such an earthquake is considered to be probably triggered by post-glacial processes that destabilise some of the fault zones around the repository. Based on the established site descriptive model of SKB, most fault zones at Forsmark are steeply dipping (80°-90°) and are therefore anticipated to be stable under the present-day/post-glacial reverse faulting stress regimes. However, a few gently dipping (20°-30°) reverse fault zones, e.g. a shallow fault zone called ZFMA2... may potentially be reactivated by post-glacial activities, producing large earthquakes threatening the integrity of deposition holes and waste canisters.”*

In response to their analysis, Fälth et al. (2021) published a Comment in the same journal, to which Lei and Loew (2022) posted a Reply.

## 5.2.1 Local area, low-angle fault: M5.6 earthquake on fault ZFMA2 (from Fälth et al., 2015)

Several publications have identified low-angle fault ZFMA2 as the most likely fault to be reactivated near the repository under both present-day stresses and endglacial stresses (Fälth et al., 2015; Lei and Loew, 2021; see Fig. 5-5). The latter state: *”ZFMA2 has a strike of N80°E, dip angle of 24°, maximum depth of 1.1 km, surface trace length of 4.2 km, and a maximum rupture area of 12 km2. According to the previous rupture modelling results in the literature, ZFMA2 tends to accommodate a maximum earthquake moment magnitude of Mw ≈ 5.6 .... with the corresponding seismic moment M0 calculated as 3.1 × 1017 N m... Thus, we may estimate the average shear displacement ΔU on this seismogenic fault to be ~0.92 m.....”*. Importantly, the repository tunnels at -550-550 m will lie in the footwall of ZFMA2.

On page 146 Fälth et al. (2015) admit to some controversy over the coseismic displacement on ZFMA2: *”The model generates an Mw 5.6 end-glacial earthquake with average and maximum slip of 0.97 and 1.7 m, respectively. We find that the maximum slip is large compared to data for typical crustal earthquakes of similar moment magnitude. Regressions published by Wells and Coppersmith (1994) and Leonard (2010), for instance, suggest that the maximum slip predicted by our model would correspond rather to an Mw 6.9 event. The regressions also imply that the 12* $km^2$ *rupture area in the model is small relative to the resulting moment magnitude, which typically should be around Mw 5.1. We also note that the maximum slip is found at the surface. Both the relatively large slip and the slip distribution can be attributed mainly to two features of the model...”*.

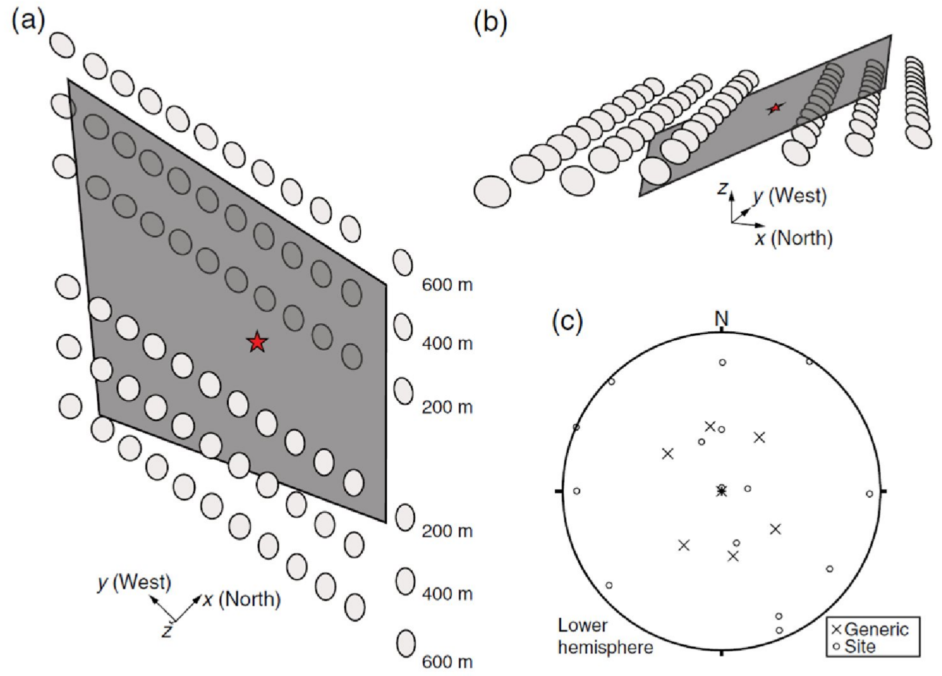

Figure 5-5. (a) View from above showing the ZFMA2 zone (dark gray) surrounded by circular target fractures at three different distances on both footwall side and hanging-wall side. (b) The same as in (a) but view from the northeast. The red star indicates the hypocenter. (c) Pole plot showing the orientations of the target fracture sets. There are 7 generic sets and 15 sets based on site investigation data. From Fälth et al., 2015.

Fälth et al. (2015) justify using these discordant rupture area/ displacement/Magnitude as follows:

*"...Both the relatively large slip and the slip distribution can be attributed mainly to two features of the model. First, we lock in all the glacially induced stresses prior to the earthquake, and thus do not allow any aseismic release of this additional strain energy. Close to the ground surface, where the stability of the gently dipping deformation zone will be significantly reduced long before the stabilizing ice load has disappeared completely, this is probably not realistic. This means that we are likely to overestimate the strain energy available at shallow depths at the time of maximum instability, that is, the point of time assumed for end-glacial earthquakes in our analyses. Second, we apply a low residual strength uniformly over the entire fault plane, which leads to an almost complete stress drop. For this shallow event, the average stress drop is about 10 MPa, and the ratio between the average stress drop and the average initial fault shear stress is 0.95."*

This explanation is based on legacy observations that displacements on endglacial fault scarps in northern Fennoscandia were abnormally large, both in a single rupture event, and compared to the length of the fault scarps. See discussion in Sec. 3.3.5, compare Table 3-3 to Table 3-4.

On page 147 they state: *" The event we simulate here, with large fault slip relative to the rupture area, should be regarded as a limiting case that aims at producing upper bound estimates rather than best estimates of secondary fracture displacements."*

For the M5.6 earthquake, Fälth et al. (2015) predict the displacement induced on the series of 300 m-diameter target fractures, on both the FW and HW of ZFMA2 (Fig. 5-6). Because the repository will lie on the FW, that is the first comparison we make with empirical distributed fault displacements.

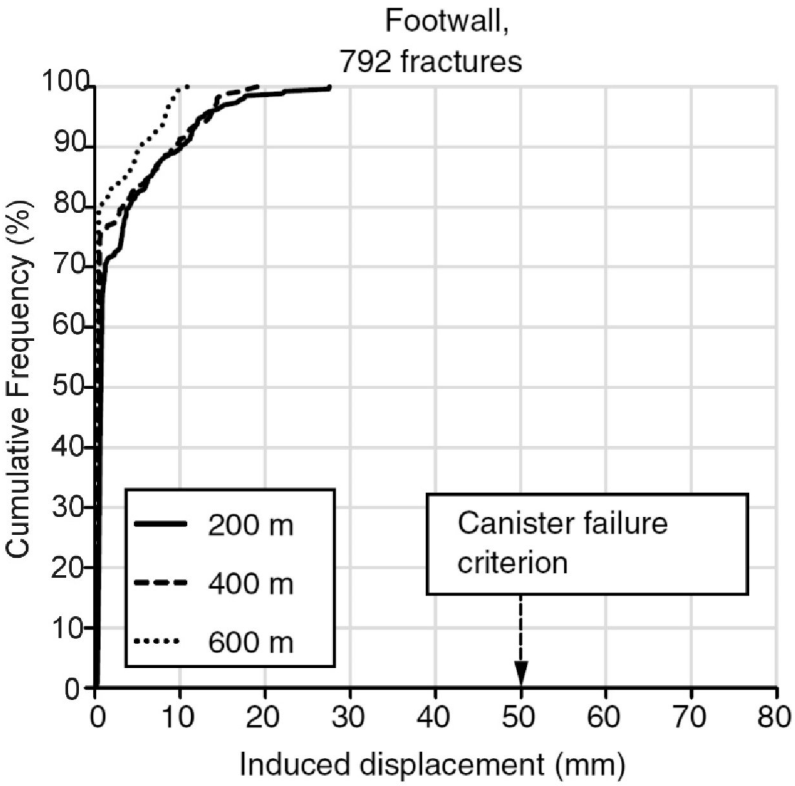

Figure 5-6. "Cumulative distribution of target fracture displacements for three fault-fracture distances, Induced by an Mw5.6 end-glacial earthquake with average and maximum slip of 0.97 and 1.7 m, respectively. No fracture displacement on the footwall side exceeds the canister failure criterion." Figure and caption from Fälth et al., 2015.

Fälth et al. (2015) measured their fault-to-fracture distance ("r") on horizontal planes in the subsurface, the same way empirical distances are measured on the ground surface from principal-to-distributed faults ("s").

#### 5.2.1.1 Nurminen et al. 2020 Method:

We calculated FW distributed fault displacements by the method of Nurminen et al. (2020), for a reverse fault, with M=5.6 earthquake, $D_{maximun}$ ($D_{max}$)=1.7 m, $D_{average}$ ($D_{avg}$)=0.97 m (Fälth's 2015 values), at distances of 200 m, 400 m, 600 m from the fault. At 200 m with $D_{avg}$ on the entire fault plane, median displacement was 0.0389 m (38.9 mm); with $D_{max}$ on the entire fault plane, median displacement was 0.0435 m (43.5 mm). See spreadsheet in Appendix D1. At 400 m with $D_{avg}$ on the whole fault plane, median displacement was 0.0248 m (24.8 mm); with $D_{max}$ on the entire fault plane, median displacement was 0.0277 m (27.7 mm). At 600 m with $D_{avg}$ on the whole fault plane, median displacement was 0.0191 m (19.1 mm); with $D_{max}$ on the entire fault plane, median displacement was 0.0213 m (21.3 mm). All of these values are smaller than the canister failure criterion, but are merely median values; higher-percentile values could easily exceed 50 mm.

The above median displacements are almost certainly overestimates for two reasons. First, because the principal fault displacements used are larger than normal for the stated rupture area and M5.6 magnitude, compared to historic earthquake data (e.g., Wells and Coppersmith, 1994; Moss et al., 2022). Second, some scenarios use $D_{max}$ as an input, but

$D_{max}$ cannot occur over the entire area of the fault plane. The subsurface slip maps in Sec. 3.8.2, "Subsurface slip gradients" clearly show that $D_{max}$ is restricted to a small area of the fault plane.

We then computed the Wells and Coppersmith (1994) $D_{avg}$ and $D_{max}$ for an M5.6 historic earthquake, resulting in median values of $D_{avg}$= 0.22 m and $D_{max}$= 0.61 m. We then re-calculated "d' values (triangles in Fig. 5-8) using 0.22 m and 0.61 m as DN in Nurminen's equation based on all simple ruptures (Appendix D2). Finally, we performed the same calculations using the Wells and Coppersmith (1994) D values and the SCR subset of Nurminen's equation, as derived in this study (Appendix D3; see also Sec. 3.7 2, and Table 3-19). This gave us six sets of estimates for "d" at each distance, by varying the parameters described above (Fig. 5.8).

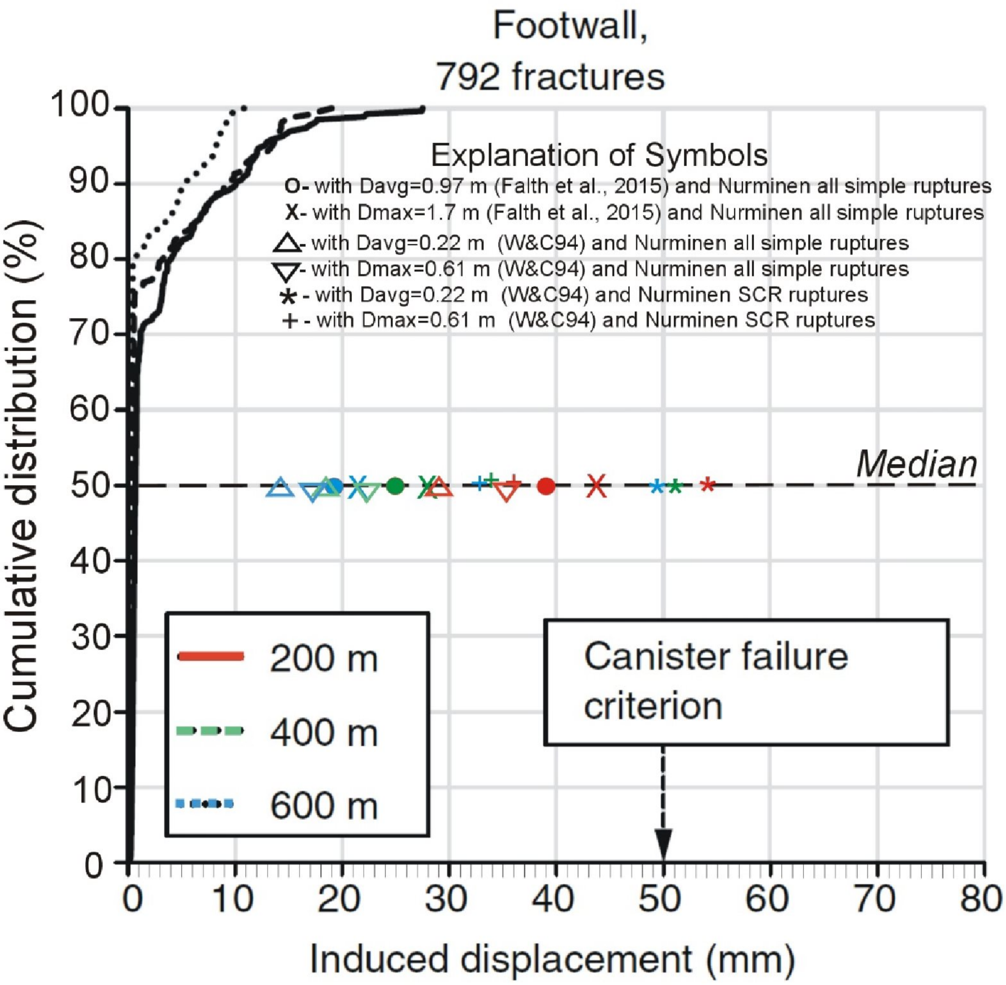

Figure 5-8. Comparison of induced fracture displacements (d) on the FW predicted by Fälth et al. (2015, upper left, three black cumulative curves), with median values of (d) predicted by Nurminen et al. (2020) for earthquakes of the same magnitude, $D_{avg}$, and $D_{max}$ ("d" values are colored symbols on the 50%-ile line; shapes represent different scenarios, colors correspond to the three distances at lower left).

Please note that in all 18 realizations in Fig. 5-8 (six scenarios times three distances), the median displacement predicted by the Nurminen equation is much larger than the median value predicted by Fälth et al. (2019), which is in the range of ~1mm. Two realizations have a median value greater than 50 mm (both using the SCR dataset, Appendix D3).

To approximate the cumulative distribution function of ”d” for each of the 18 realizations, we computed five values of ”d” for each realization in Appendix D, i.e. median-2σ, median-1σ, median, median+1σ, and median+2σ. We use the FW sigma value for ln(Y) given by Nurminen et al. (2020), of 0.8812 ln units for Scenarios 1-4 (Appendices D1 and D2), and the value of 0.6179 for our SCR-derived subset of data (Scenarios 5 and 6, Appendix D3). The CDF for each of the 6 scenarios are shown in Figs. 5-10a through 5-10g.

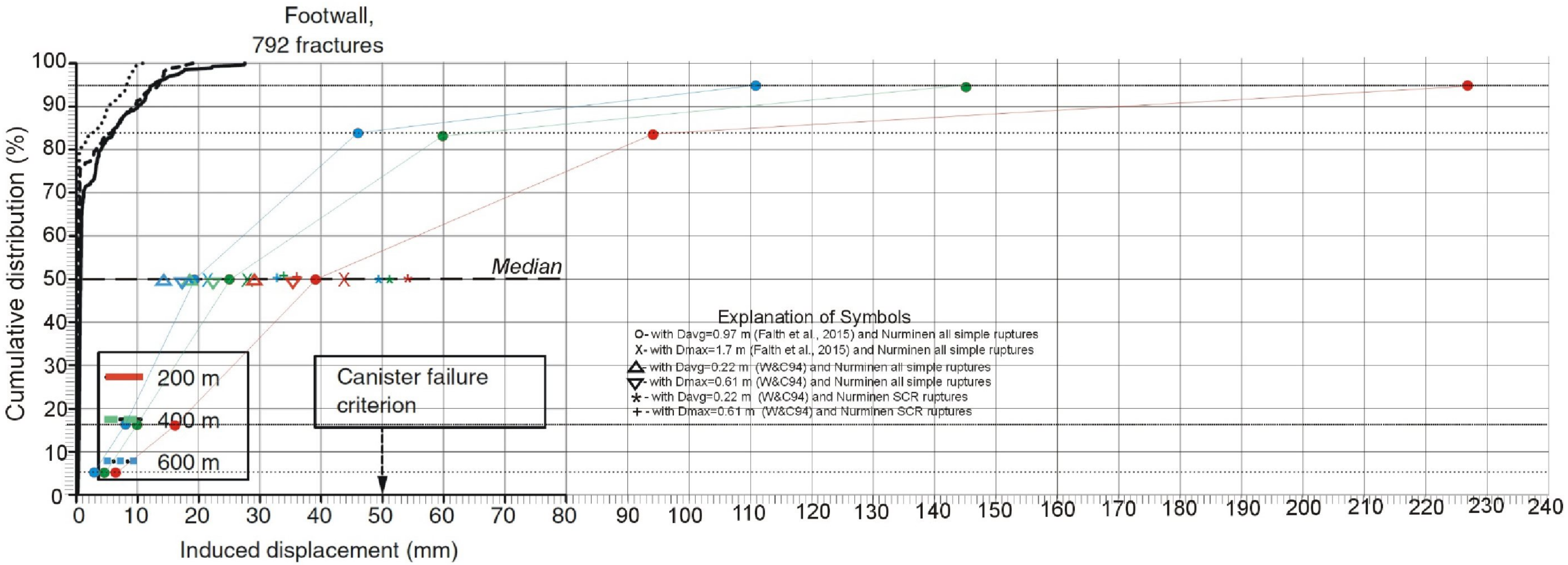

Figure 5-10a. Cumulative distribution (CD) of induced displacement (d) in Scenario 1 (top line in Explanation), with computations from Equation 6 of Nurminen et al., 2020. DN= $D_{avg}$ of Fälth et al., 2015= 0.97 m. Color of CD line represents distance between Distributed fault and Principal fault, red=200 m; green= 400 m; blue= 600 m. Leftmost 1/3 of figure is from Fälth et al., 2015 and contains their cumulative curves from 3DEC. Calculations are in Appendix D1, top rows

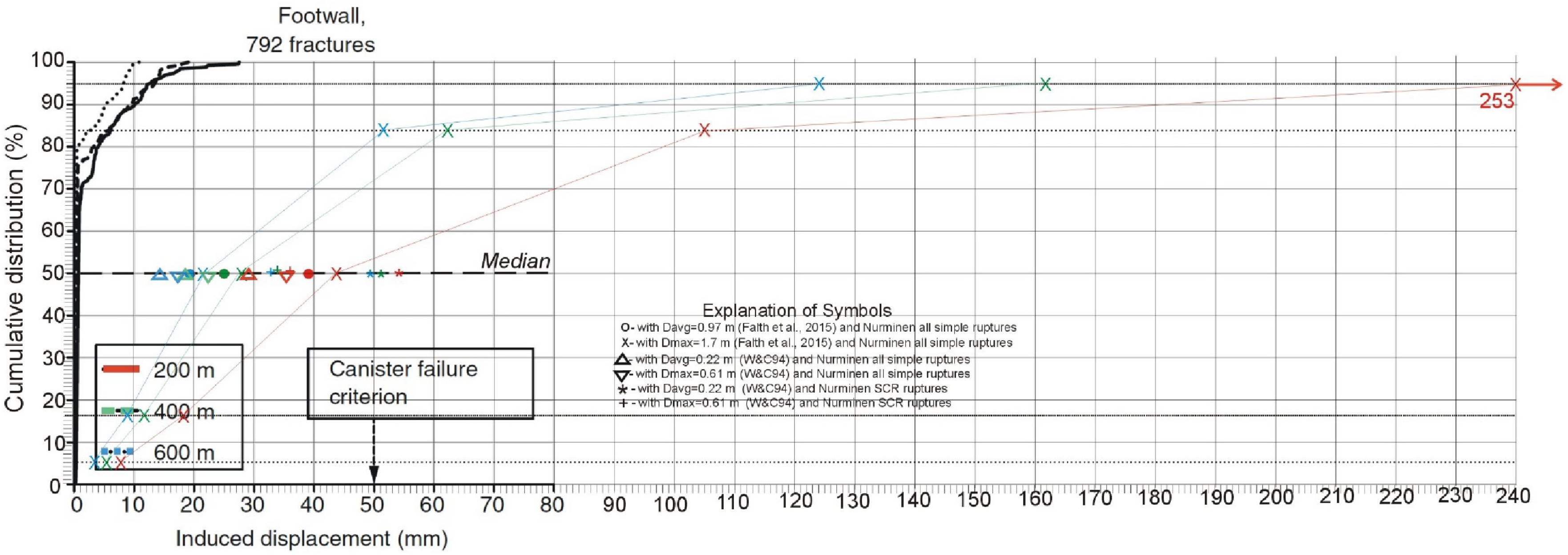

Figure 5-10b. Cumulative distribution of induced displacement (d) in Scenario 2 (second from top in Explanation), with computations from Equation 6 of Nurminen et al., 2020. DN= $D_{max}$ of Fälth et al., 2015= 1.7 m. Color of CD line represents distance between Distributed fault and Principal fault, red=200 m; green= 400 m; blue= 600 m. Leftmost 1/3 of figure is from Fälth et al., 2015 and contains their cumulative curves from 3DEC. Calculations are in Appendix D1, bottom rows.

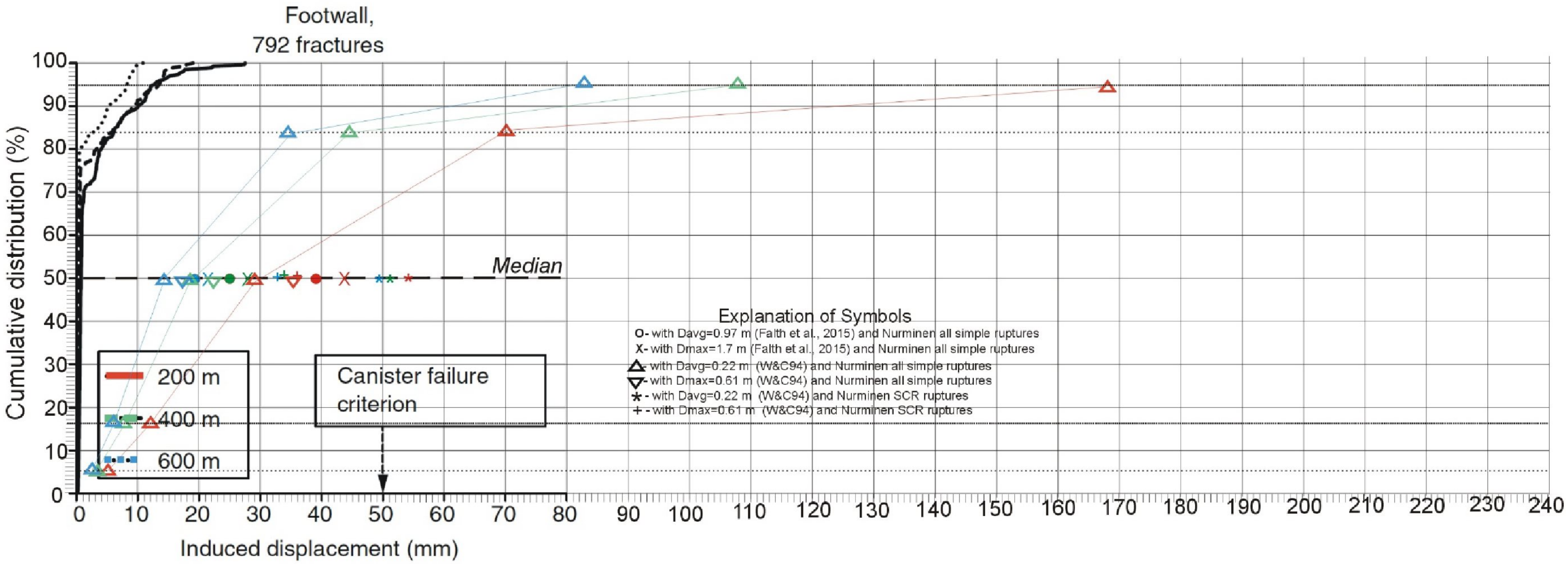

Figure 5-10c. Cumulative distribution of induced displacement (d) in Scenario 3 (third from top in Explanation), with computations from Equation 6 of Nurminen et al., 2020. DN= $D_{avg}$ of wells and Coppersmith 1994 for M5.6 = 0.22 m. Color of CD line represents distance between Distributed fault and Principal fault, red=200 m; green= 400 m; blue= 600 m. Leftmost 1/3 of figure is from Fälth et al., 2015 and contains their cumulative curves from 3DEC. Calculations are in Appendix D2, top rows.

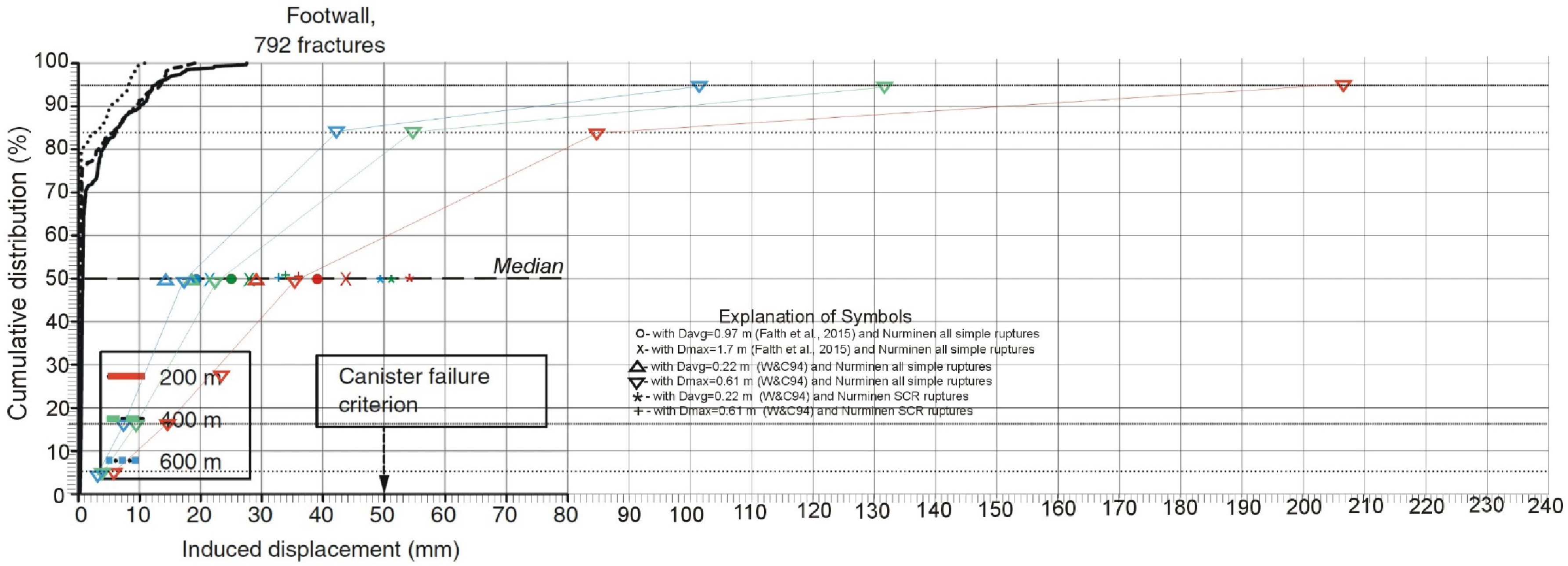

Figure 5-10d. Cumulative distribution of induced displacement (d) in Scenario 4 (fourth from top in Explanation), with computations from Equation 6 of Nurminen et al., 2020. DN= $D_{max}$ of Wells and Coppersmith 1994 for M5.6= 0.61 m. Color of CD line represents distance between Distributed fault and Principal fault, red=200 m; green= 400 m; blue= 600 m. Leftmost 1/3 of figure is from Fälth et al., 2015 and contains their cumulative curves from 3DEC. Calculations are in Appendix D2, bottom rows.

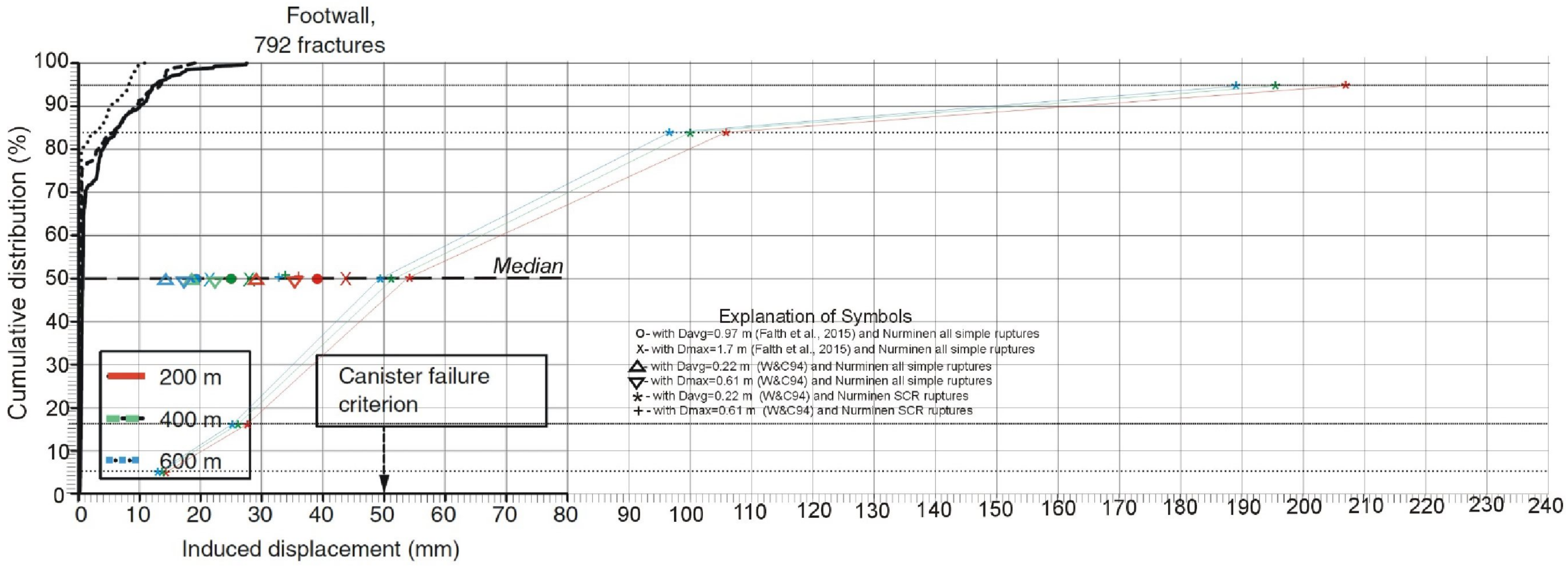

Figure 5-10e. Cumulative distribution of induced displacement (d) in Scenario 5 (fifth from top in Explanation), with computations from Equation 6 of Nurminen et al., 2020, but with coefficients from Australian SCR events only [ln Y= -17.6 + (-0.083*(ln s)) + (-4*(ln Dn)) + (2.592*m)], standard error of ln Y= 0.6719. DN= $D_{avg}$ of Wells and Coppersmith 1994 for M5.6= 0.22 m. Color of CD line represents distance between Distributed fault and Principal fault, red=200 m; green= 400 m; blue= 600 m. Leftmost 1/3 of figure is from Fälth et al., 2015 and contains their cumulative curves from 3DEC. Calculations are in Appendix D3, top rows.

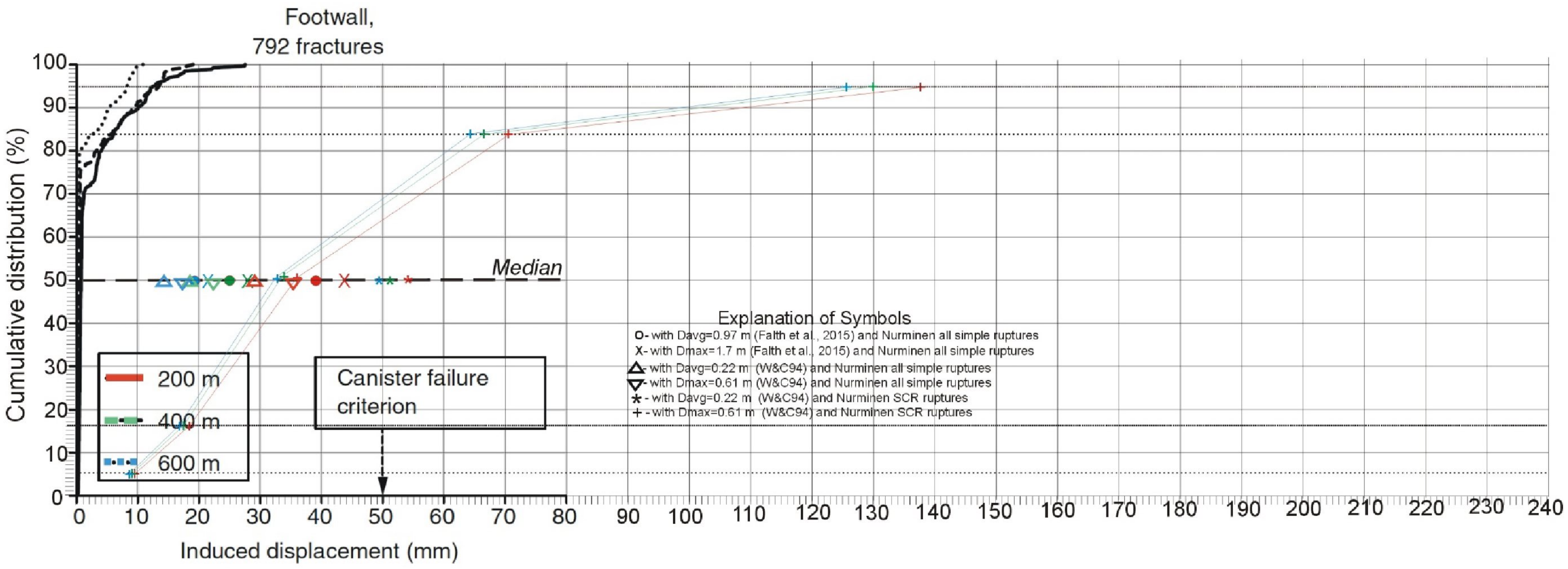

Figure 5-10f. Cumulative distribution of induced displacement (d) in Scenario 6 (bottom line in Explanation), with computations from Equation 6 of Nurminen et al., 2020, but with coefficients from Australian SCR events only. [ln Y= -17.6 + (-0.083*(ln s)) + (-4*(ln Dn)) + (2.592*m)], standard error of ln Y= 0.6719. DN= $D_{max}$ of Wells and Coppersmith 1994 for M5.6= 0.61 m. Color of CD line represents distance between Distributed fault and Principal fault, red=200 m; green= 400 m; blue= 600 m. Leftmost 1/3 of figure is from Fälth et al., 2015 and contains their cumulative curves from 3DEC. Calculations are in Appendix D3, bottom rows.

We summarize the distributed displacement estimates shown in the preceding six figures, in Table 5-1.

Table 5-1. Estimates of distributed induced displacement (”d”, rounded to nearest mm) for a given Scenario (M5.6, varying $D_{avg}$ and $D_{max}$, or empirical equation) and PF-to-DF distances of 200, 400, and 600 m. Values of ”d” in red exceed the 50 mm canister criterion. Values in blue indicate spatial probability of DF faulting at the given distance.

| | DISTANCE | 200 m | Spatial Prob. | 400 m | Spatial Prob. | 600 m | Spatial Prob. |
|---|---|---|---|---|---|---|---|
| SCEN-ARIO | %-iles | ”d”, mm | | ”d”, mm | | ”d” | |
| 1 | 50 | 39 | 0.12 | 24 | 0.02 | 19 | <0.002 |
| | 84 | 94 | | 60 | | 46 | |
| | 95 | 227 | | 144 | | 111 | |
| 2 | 50 | 44 | | 28 | | 21 | |
| | 84 | 105 | | 67 | | 52 | |
| | 95 | 253 | | 162 | | 124 | |
| 3 | 50 | 29 | | 19 | | 14 | |
| | 84 | 70 | | 46 | | 34 | |
| | 95 | 169 | | 108 | | 83 | |
| 4 | 50 | 36 | | 23 | | 17 | |
| | 84 | 86 | | 55 | | 42 | |
| | 95 | 207 | | 132 | | 101 | |
| 5 | 50 | 54 | | 51 | | 49 | |
| | 84 | 106 | | 100 | | 97 | |
| | 95 | 207 | | 195 | | 189 | |
| 6 | 50 | 36 | | 34 | | 33 | |
| | 84 | 70 | | 66 | | 64 | |
| | 95 | 138 | | 130 | | 126 | |

Considering the median (50%-ile) values predicted for ”d”, all scenarios except number 5 yield displacements smaller than the 50 mm canister failure criterion. Scenario 5 values barely exceed 50 mm. But when we consider the mean+1σ predicted values of ”d” (the six 84%-ile rows), 14 of the 18 exceed 50 mm. This includes all six values at 200 m distance; five of six values at 400 m distance; and three of six values at 600 m. Looking at the six mean+2σ values of predicted ”d” (95%-ile rows), they all exceed 50 mm regardless of distance.

Although there are a lot of red numbers in Table 1, one should realize that the associated probability of these displacements occurring is very low. According to Pizza et al. (2023), the probability of M5.6 ruptures having any principal faulting at all is 0.06 (Fig. 5-11a). And if principal faulting does occur, then probability of distributed faulting 200 m from the PF is 0.12; at 400 m, 0.02; and at 600 m, <0.002 (Fig. 5-11b, from Nurminen et al., 2020).

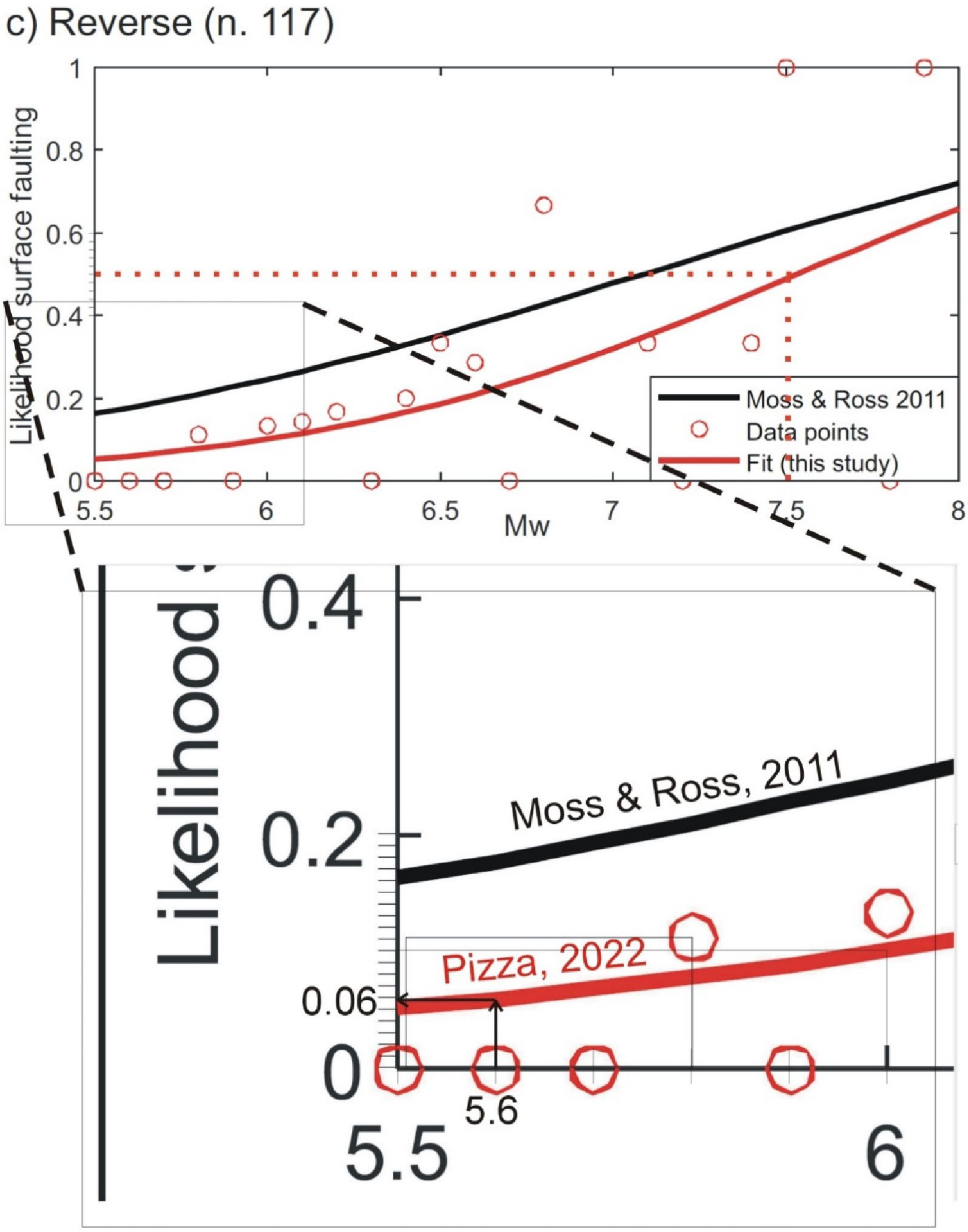

Figure 5-11a. Top, probability of principal surface rupture given earthquake magnitude, for reverse faults. Black line, original probability curve of Moss and Ross, 2011; redline and circles, updated curve and data points from Pizza et al. (2023). Red dotted line shows the probability of surface rupture does not even reach 50% until earthquake magnitude rises to M7.5. The update includes many new M5-6 earthquakes that had no surface rupture at all, which lowered the whole probability curve compared to that of Moss and Ross, 2011. Bottom, enlargement showing probability of faulting for M5.6 equals 0.06.

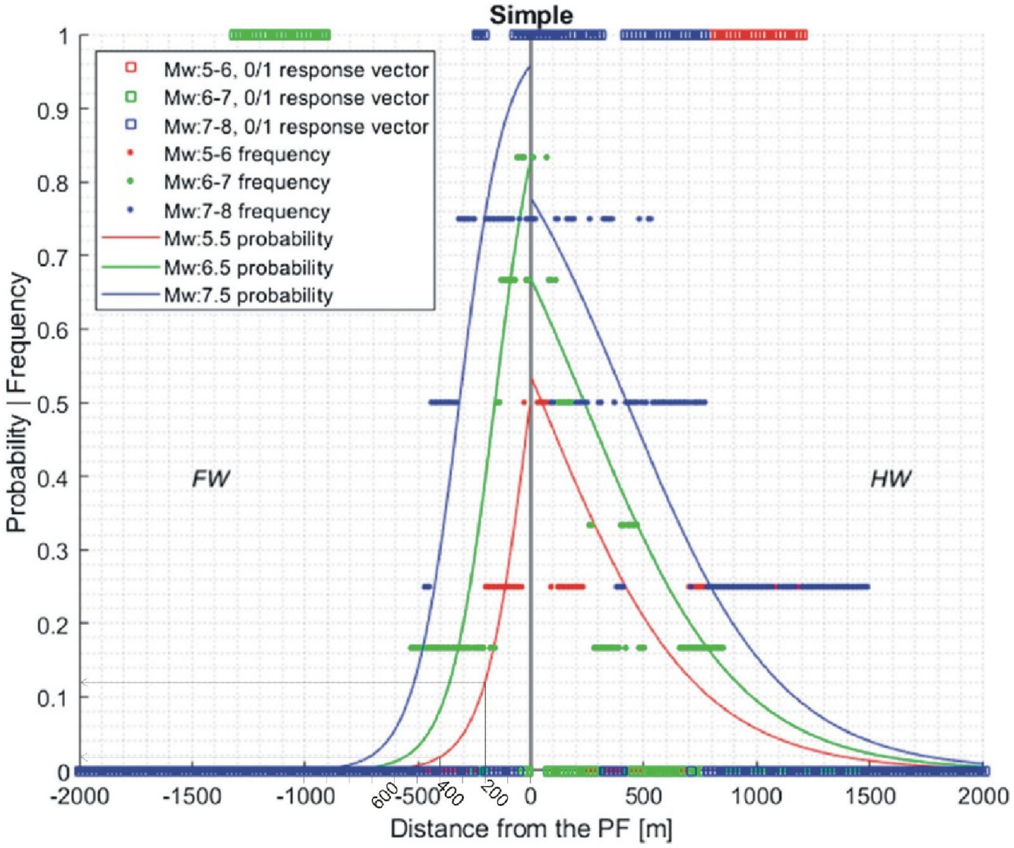

Figure 5-11b. Probability of distributed faulting (given principal faulting) as a function of earthquake magnitude class and distance from the PF (zero point on the horizontal axis). For an M5.5 earthquake (red line), probability of DF 200 m into the hanging wall (thin black lines and labels at lower left) is 0.12; at 400 m, 0.02; at 600 m, <0.002. Modified from Nurminen et al., 2020.

For example, the annual probability of a given scenario earthquake exceeding the displacements ”d” shown in Table 5-1 consists of:

(Step 1)-the annual probability of an M>5 earthquake occurring within a 5 km radius around the repository (~1x10$^{-6}$) ; see Table 2-1 on p. 24, from Table 10-14 in SKB TR-11-01;

*Multiplied times*

(Step 2)-the probability that the earthquake will occur on fault ZFMA2, and not on another of the 30 faults within the 5 km radius (~0.0333);

*Multiplied times*

(Step 3)- The probability that fault ZFMA2 will have Principal surface rupture, given a magnitude of 5.6 (0.06 according to Pizza et al., 2023) (our Fig. 5-11a)

*Multiplied times*

(Step 4)-given Principal rupture, the probability of having distributed faulting at the specified distance from ZFMA2 (0.12 at 200 m; 0.02 at 400 m; <0,002 at 60 m; see Fig. 5-11b);

*Multiplied times*

(Step 5)-the probability of the distributed fault displacement being larger than a given amount (as defined by the Cumulative Distribution Function, or CDF, of ”d” from the Nurminen equation; Table 5-1).

As an example, the cumulative probability of having a displacement at 400 m distance from ZFMA2 greater than 46 mm (Table 5-1, Scenario 3, 84%-ile, at 400 m) would be (working backwards from Step 5 to Step 1 above):

0.16* 0.02* 0.06* 0.0333* $1x10^{-6}$, or ~6.4x10-12. Or 6 chances in 1,000,000,000,000.

For comparison, we also calculated six DF displacement scenarios in a Scenario 3 realization for the HW of ZFMA2. Given $D_{avg}$=0.22 m, at 200 m from the PF, median ”d” would be 0.0789 m (78.9 mm); at 400 m from the PF would be 0.0709 m (70.9 mm); and at 600 m from the PF would be 0.0666 m (66.6 mm). The corresponding numbers for the FW were (Table 5-1) 29, 19, and 14 mm, respectively. Thus, median distributed displacements on the HW are predicted to be ~275% to 475% of those on the FW, and in Scenario 3, they all exceed the 50 mm canister criterion. If the median (50%-ile) “d” value in any scenario exceeds the criterion at 600 m, it is obvious that “d” at closer distances or or higher %-iles will even further exceed the criterion. The clear implication: it is a good thing the repository is not on the HW of fault ZFMA2.

#### 5.2.1.2 Distributed fault displacement for M5.6 reverse event calculated by the method of Moss et al., 2022:

As described in Sec. 3.6.2, the Moss et al. (2022) Equations fit to the footwall DF displacements are:

For $r\ from\ 0km\ to\ 6.5km$: the 95%-ile value of “d” is computed from:

$d/MD$= $0.58 * (-0.26 * r)$ Eq. 14

For $r > 6.5\ km$: the 50%-ile value of “d” is computed from:

$d/MD$= 0.09 Eq. 15

Where: d=displacement on the DF (m)

r= distance from DF to PF, in km

MD= maximum displacement of PF (m)

In Eq. 14 there is only a single independent variable (”r”, the distance from PF to DF). The effect of varying earthquake magnitude could be considered to be covered by normalization of ”d” by $D_{max}$. Please note that Eqs. 14 and 15 yield the 95%-ile of d/MD, not the median (50%-ile).

Unfortunately, the FDHI database used by Moss did not contain any measurements of DF displacements on the FW of ruptures in the M5-6 range. That means that Eq. 14 is based entirely on FW data points from M>6 ruptures. Thus, in using Moss's equation in the following analysis, we are extrapolating the equation beyond the range of his data.

First, we compute the d/MD ratio for distances of 200, 400, and 600 m from the PF, using Eq. 14 above. This yields d/MD ratios of 0.55, 0.52, and 0.50, respectively. In other words, "d" at those distances is roughly half of MD. The MD value given for ZFMA2 by Fälth et al. (2015) is 1.7 m. Thus "d" at 200 m, 400 m, and 600 m from the PF would be 0.94 m, 0.89 m, and 0.84 m, respectively (Appendix E, rows 10-12). This is a huge number compared to the 0.05 m "canister failure criterion."

As a more reasonable check, we perform the same procedure with an empirical estimate of MD from Moss et al. (2022) for an M5.6 earthquake. Their equation for "complete reverse ruptures" is $\text{Log10MD}= -2.5 + 0.415\text{Mag}$ Eq. 23

Using Mag=5.6 in this equation, we see that median MD for an M5.6 earthquake=0.67 m, less than half the value chosen by Fälth et al. (2015). We then apply the same d/MD ratios as in the computation above for distances of 200, 400, and 600 m from the PF (i.e., d/MD ratios of 0.56, 0.54, and 0.52, respectively). The "d" values at those distances are then computed to be 0.37 m, 0.35 m, and 0.33 m, respectively (Appendix E, rows 1-2).

The two sets of values described above are shown on Fig. 5-12. Note that these values of 330 to 370 mm are larger than even the highest 95%-ile values from the Nurminen equation in Secs. 5.1.2.1 (253 mm) and 5.2.1.2 (189 mm), as shown in Table 5-1.

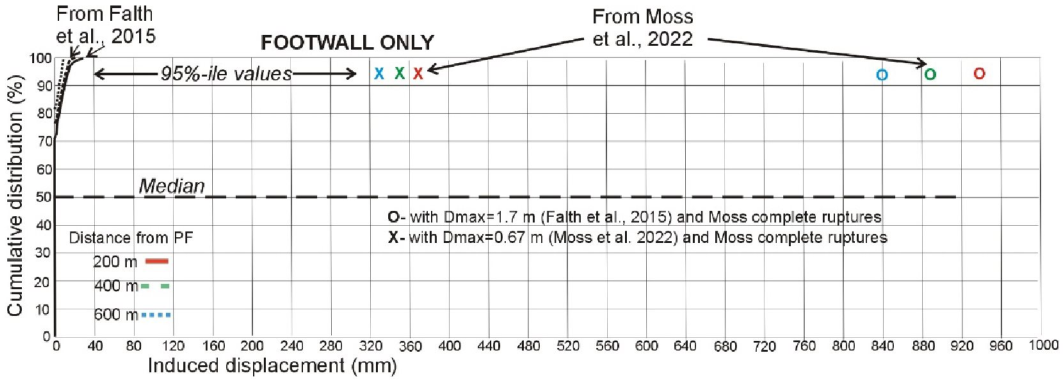

Figure 5-12. Comparison of induced fracture displacements (d) predicted by Fälth et al. (2015, upper left, three cumulative curves), with 95%-ile values of (d) predicted by Moss et al. (2022) for an earthquake of M5.6 and two values of $D_{max}$ ("d" values are colored symbols on the 95%-ile line).

The Moss values of "d" computed from $D_{max}$ (Fig. 5-12, 325-365 mm, 840-940 mm) are 200% to 450% larger than the 95%-ile Nurminen predictions for equivalent scenarios (Scenario 2, 124-253 mm; Scenario 4, 189-207 mm). As previously mentioned, $D_{max}$ on any surface rupture is usually an isolated, outlier value, and a poor choice for representing the type of uniform slip on a fault plane, such as was modeled by Fälth et al. (2015). Fälth et al. (2015) even realize this (p. 146) when they state: *" Regressions published by Wells and Coppersmith (1994) and Leonard (2010), for instance, suggest that the maximum slip* *predicted by our model would correspond rather to an Mw 6.9 event."* In other words, their $D_{max}$ would be appropriate for an earthquake 1.3 magnitude units larger than M5.6

If we do not wish "d" to exceed 0.05 m, then given even the lower value of $D_{max}$=0.67 m, d/MD cannot exceed 0.07. By varying "r" in Moss's Eq. 14 by trial and error (Appendix E, rows 4-9), we find that d/MD=0.07 will occur at r~7.8 km from the activated fault. In other words, the 95%-ile of "d" will exceed 0.05 m at all distances less than 7.8 km from fault ZFMA2. However, Moss et al. (2022) do not suggest using this equation more than 6.5 km from the PF.

Fig. 3-41 shows a graphical depiction of the Moss et al. (2022) recommended d/MD curve that defines the 95%-ile bound of values within 3.5 km of the Principal fault. Note that on the FW at distances of 200, 400, and 600 m from the fault (right half of Figure), the 95%-ile empirical bound to d/MD points is drawn slightly above 0.5, so distributed displacement "d" is slightly more than 50% of MD.

Likewise, Fig. 3-42 shows how Moss et al. (2022) changed their 95%-ile bounding curve (solid blue line) on the FW from a natural log function to a constant-value of d/MD= 0.09. The way they have drawn this curve, one could never reach a distance at which d/MD= 0.07, which is where "d" would finally fall below 0.05 m for an M5.6 earthquake. I suspect Moss did not anticipate that this curve would ever be used for design. Clearly there are problems with its use, compared to the Nurminen equation.

One might ask, why did Moss et al.(2022) even publish this equation? First, I don't think Moss ever compared his estimates of "d" against Nurminen, for the same suite of input parameters. So he didn't know how discordant his values were. Second, he may not have wanted to do extra work needed to compute $D_{avg}$ so he could normalize by that parameter. However, for most (if not all) of the ruptures in his data set AD is already known(see his Table 4.1; San Fernando, 1971, 0.47 m; El Asnam, 1980, 1.8 m; Spitak, 1988, 0.9 m; Chi-Chi, 1999, 2.6 m; Kashmir, 2005, 1.5 m; Wenchuan, 2008, 2.2 m). So he could have normalized by $D_{avg}$.

### 5.2.2 Triggered displacement from a 70°-dipping hypothetical fault (Fälth et al., 2008; SKB Report TR-08-11)

In an earlier simulation, Fälth et al. (2010) computed induced fracture displacements for M5.5, M6.2, and M7.5 earthquakes at distances of 200, 600, 1000, and 1500 m from a hypothetical 70°-dipping fault. We input the same magnitudes and distances into the Nurminen displacement equation, but had to assume a displacement on the activated fault. Fälth et al. mentioned only "maximum displacement" in their analysis, but their activated values were too large, given the magnitudes. For example in their Table 5-1, the M5.3-5.6 had maximum slips of 0.71 to 1.4 m. In contrast, Moss et al. (2022) show that for known reverse-fault ruptures, M5.5 events have a maximum surface slip of 0.61. Fälth's M6.2 earthquakes were assumed to have a maximum slip of 2.9 m, compared to historical observations where the typical value is 1.2 m. Fälth's M7.5 earthquakes were assumed that have a maximum slip of 10 m, compared to an empirical value of 4.1 m. So we had no confidence in Fälth's values when comparing to empirical data sets. We did not want to overestimate $D_{max}$ on the activated fault, because that would lead to an overestimate of distributed displacement when plugged into the Nurminen equation. Instead, we used the $D_{max}$ values of Moss et al. (2002); for M5.5, Dmax= 0.61 m; for M 6.2, 1.2 m; and for M7.5, 4.1 m.

#### 5.2.2.1 Method of Nurminen et al, 2020

Despite using these lower $D_{max}$ values, the outputs of the Nurminen equation yielded much higher fracture shear displacements that shown by Fälth et al. (2010). The difference between predicted displacements increased greatly with increasing magnitude (calculations in Appendix F). For example, in Fig. 5-13 our displacement-with-distance curve for M5.5 earthquakes (blue) overlaps Fälth's curve for M7.5 earthquakes. Our curve for M6.2 earthquakes (green) yields values of displacement about twice as large as our M5.5 curve, far exceeding Fälth's values for M6.2 shear displacements. And our curve for M7.5 earthquakes is larger still, yielding displacement values (d) seven to eight times larger than our M6.2 curve. This is not unexpected, due to the structure of the Nurminen equation. Nurminen's strongest coefficient for an independent variable is d1=0.9461, applied to earthquake magnitude. Compared to that, coefficients for the other independent variables are smaller, and are applied to a natural log function of distance (s) and PF displacement (DN).

The magnitude scale itself is logarithmic, with seismograph displacements increasing 10x with each magnitude unit. Therefore, an M7.5 earthquake moves the ground 100 times more than (at a given distance) than an M5.5 earthquake. Thus, we were not surprised to see the great increase in fracture displacements as scenario magnitude increased.

What is surprising is that Fälth's displacement curves do not share this logarithmic spacing, but seem almost to increase linearly as magnitude increases. Having experienced an M5.5 earthquake (I was standing on the fault) and an M7.1 earthquake (sleeping in bed 115 km away), I appreciate the logarithmic nature of the magnitude scale. The shaking from 115 km away was stronger.

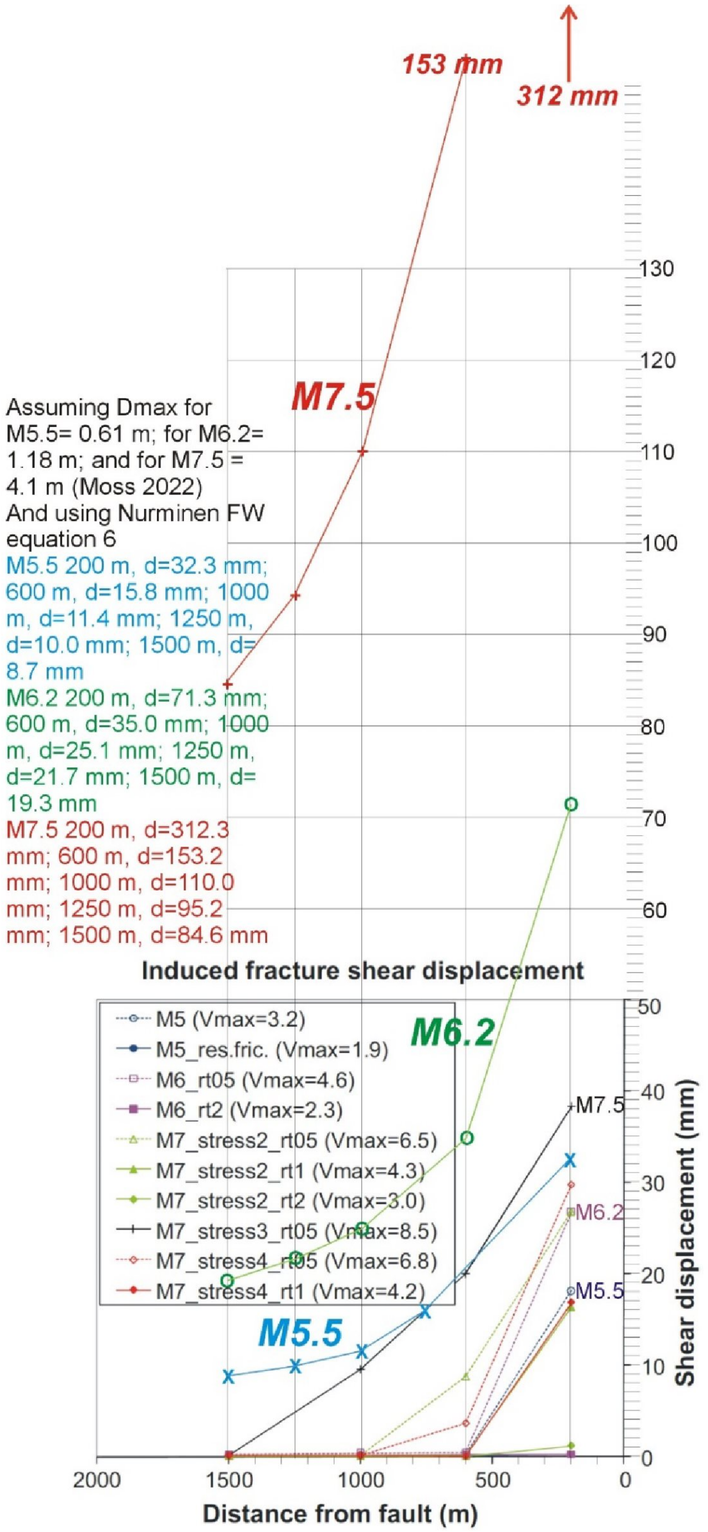

Assuming Dmax for M5.5= 0.61 m; for M6.2= 1.18 m; and for M7.5 = 4.1 m (Moss 2022) And using Nurminen FW equation 6

M5.5 200 m, d=32.3 mm; 600 m, d=15.8 mm; 1000 m, d=11.4 mm; 1250 m, d=10.0 mm; 1500 m, d= 8.7 mm

M6.2 200 m, d=71.3 mm; 600 m, d=35.0 mm; 1000 m, d=25.1 mm; 1250 m, d=21.7 mm; 1500 m, d= 19.3 mm

M7.5 200 m, d=312.3 mm; 600 m, d=153.2 mm; 1000 m, d=110.0 mm; 1250 m, d=95.2 mm; 1500 m, d=84.6 mm

Figure 5-13. Comparison of Fälth et al. (2010) shear displacements (lower 1/3 of figure, points connected by dotted lines) to distributed displacements from the Nurminen equation (the 3 thin colored lines with large labels).

#### 5.2.2.2 Method of Moss et al, 2022

Just as in Sec. 5.2.1.2, we used the method of Moss et al. (2022) to calculate d/MD as a function of ”r” (Step 1), then calculated MD as a function of Magnitude (Step 2), then multiplied (d/MD) * MD to derive ”d” (see Appendix G). For the M5.5 earthquake (MD=0.41 m), distributed displacements at the 95%-ile level remained above 5 cm (0.05 m) until a distance of >7 km. Compared to the Nurminen median displacement prediction at a distance of 1 km (11 mm, Fig. 5-13), the Moss method predicted a 95%-ile displacement of 273 mm. For M=6.2, the Nurminen median displacement prediction at a distance of 1 km is 25 mm (Fig. 5-13), while the Moss method predicted a 95%-ile displacement of 528 mm. For M=7.5, the Nurminen median displacement prediction at a distance of 1 km is 110 mm (Fig. 5-13), while the Moss method predicted a 95%-ile displacement of 2257 mm. This great divergence between the Nurminen median and the Moss 95%-ile values was observed in previous sections, and emphasizes the long ”tail” of the CDFs at low probabilities/high displacements.

### 5.2.3 Summary of 3DEC displacements versus empirical displacements

For the case of local area, low-angle faults (like ZFMA2, M5.6), our induced displacement values are all larger than the Fälth et al. (2015) values. Fälth’s median displacement value at a distance of 200 m was 5 mm. In six scenarios using Nurminen’s 2020 equation and $D_{avg}$ values as DN, median (50%-ile) displacements at 200 m distance ranged from 29 mm to 54 mm, or 580% to 1080% of Fälth’s values. At higher %-iles our displacement values grew even larger than Fälth’s. We also ran two simulations (same magnitude and distances as above) with the new Moss et al. (2022) equation for distributed displacements during reverse ruptures, which predicts $d/D_{max}$ at various distances. Compared to Fälth’s 5 mm predicted at 200 m, the Moss equations predicted displacements of 370 mm at the same distance (7400% larger). Fälth et al. (2010) predicted shears on target fractures at distances of 200, 600, 1000, and 1500 m from a hypothetical activated fault dipping 70° and magnitudes of M5.5, 6.2, and 7.5. We calculated the same displacements using the FDHI database and empirical equation of Nurminen. Again, the Nurminen displacement curve for an M5.5 event predicted displacements >200% of Fälth’s. For an M6.2 event, a similar ratio was observed. For an M7.5 event, Nurminen’s displacements were 450% to 800% of Fälth’s.

## 5.3 Particle Flow Code 3D v4 (PFC3D 4)

The earliest use of PFC for Forsmark was in 2014 (Yoon et al, SSM Report 2014-59). A later report followed in 2019 (Yoon and Zang, 2019, SSM Report 2019-15). During the comparison below we only compare our empirical data with Yoon’s calculations done for present-day stress state scenarios. In that way we avoid complications from comparing different stress states (e.g., glacial forebulge and endglacial GIA rebound).

### 5.3.1 Yoon and Zang 2019. – activated low-angle reverse faults

Yoon and Zang also analyzed target fracture displacements in response to activated faults such as ZFMA2 and ZFMA3. Fig. 5-14a shows the geometry of a model in which ZFMA3 is activated by an M5.76 earthquake with 0.47 m uniform displacement. The induced fracture slips from this earthquake were calculated at 56 target fracture positions (Fig. 14b). The resulting fracture displacements are color-coded.

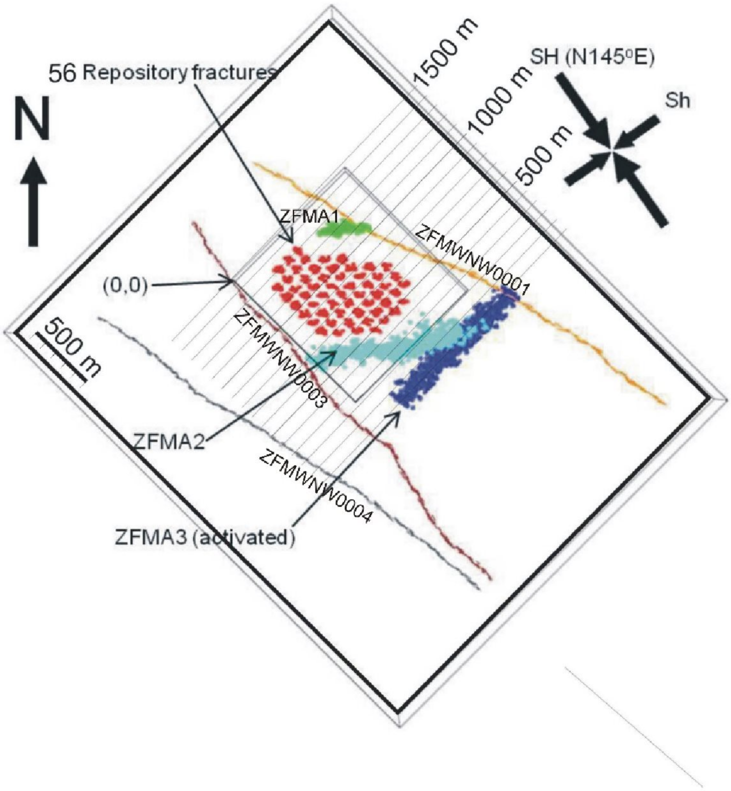

Figure 5-14a. Top view of the reference model with ZFMA3 (dark blue trace), other named faults, and 56 uniformly spaced fractures (red) at the depth of the repository (-500 m). Other faults shown are favorably oriented for slip by activation under present day reverse faulting in-situ stress condition. 100 m-wide buffer zones from the edge of ZFMA3 are shown. Modified from Yoon and Zang, 2019.

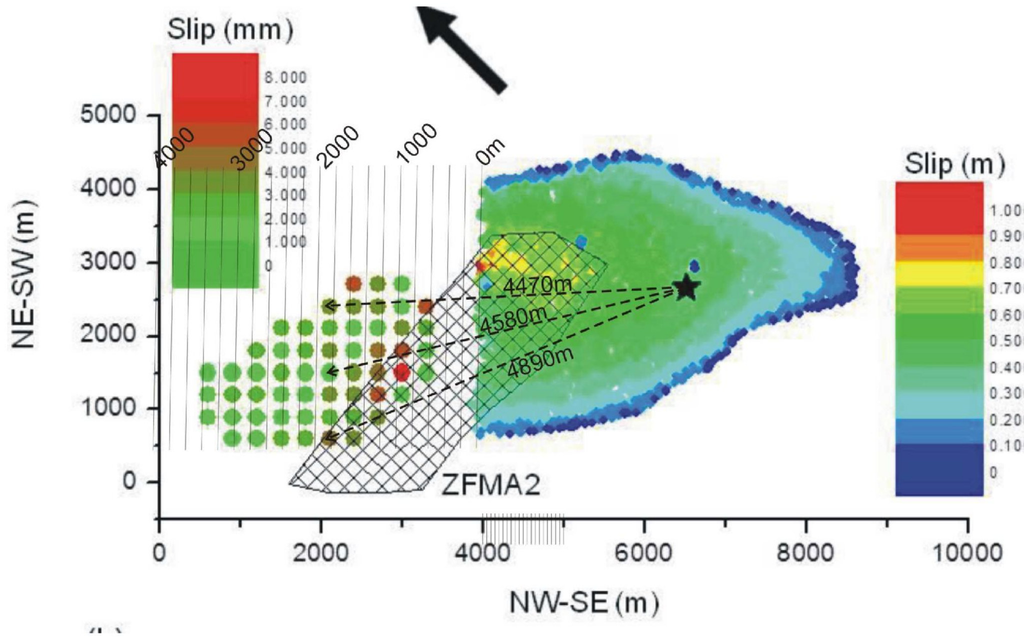

Figure 5-14b. ZFMA3 Map showing the difference between distances measured by Yoon and Zang (2019; three dashed lines) and those measured in PFDHA (thin lines parallel to fault edge, 0-4000 m).

Yoon and Zang measured their distances from a point (rupture source center) to the fracture of interest (for example, the three black dashed lines). In PFDHA distance is always measured horizontally from the Principal fault plane to the distributed faults (e.g., on Fig. 5-14b, thin vertical black lines, spaced 200 m apart). In the above example we choose three fractures (colored circles) of interest, all at a distance of 1900 m from edge of the activated fault plane. The corresponding distances measured from the rupture source point (Yoon and Zang's method) vary from 4470 m to 4890 m.

In generating input numbers for the Nurminen and Moss equations, we use 1900 m as the distance to the three fractures. Yoon et al assign those three fractures colors ranging from light green (1-2 mm slip) to darker green (2-3 mm slip) to olive green (3-4 mm slip).

Using the Nurminen equation for M5.76, $D_{avg}$=0.47 m, distance= 1900 m, we derive the following target fracture displacements ("d") and accompanying %-iles:

| %-iles on CDF | "d" (mm) |
|---|---|
| 5%-ile (mean-2σ) | 1.6 |
| 16%-ile (mean-1σ) | 3.8 |
| 50%-ile (mean) | 9.1 |
| 84%-ile (mean+1σ) | 22.0 |
| 95%-ile (mean+2σ) | 53.1 |

Yoon and Zang's predicted values of 1-4 mm are covered by our 5%-ile and 16%-ile values. Our mean value of 9.1 mm would correspond to a red dot on Fig. 13b, but all of those are located closer to the fault (800-1000 m). From our >mean values, you can see the asymmetric nature of the CDF, with a long tail toward the higher displacements.

We also calculate "d" values with the method of Moss et al. (2022), wherein: d/MD (95%-ile)= 0.58 * exp (-0.26*r)

Given MD=0.47m, r= 1.9 km, then d/MD=0.354. Because MD=0.47, the 95%-ile value of "d"=0.1663 m, or 166 mm. Note this is three times larger than the 95%-ile of "d" from the Nurminen equation (53.1 mm).

Yoon and Zang (2019) also calculated the induced displacement on other recognized DZs (faults rather than simple fractures, see Fig. 5-13a). In the example below, they activate fault ZFMA2 under present stress conditions with an M5.5 earthquake and uniform displacement D=0.32 m. That earthquake then triggers slip on the other named faults, large enough to generate its own earthquakes. This is a different process (triggered faulting) than inducing distributed faulting on a smooth fracture. Table 5-2 shows Yoon and Zang's displacements compared to empirical distributed displacements by the methods of Nurminen (2020) and Ross (2022)

Table 5-2. Activated slip on fault ZFMA2 and predicted induced slip on known nearby faults. Modified from Yoon and Zang, 2019, their Table 8-4. The grayed marking of the Moss values indicate low confidence.

| **Activation** | **Deform. Zone** | **Slip (m)** | **Mag.Mw** | **Distance from ZFMA2 (m)** | **"d" from Nurminen equation (m)** | **"d" from Moss Equation (m)** |
|---|---|---|---|---|---|---|
| Primary | ZFMA2 | 0.32 | 5.5 | n/a | | |
| Secondary | ZFMA1 | 0.08 | 4.32 | 850 | 0.0111 | 0.1488 |
| | ZFMA3 | 0.08 | 4.27 | 1150 | 0.0091 | 0.1376 |
| | ZFMWN-W0003 Eckarfjärden Fault | 0.02 | 4.03 | 600 | 0.0139 | 0.1588 |
| | ZFMWN-W0001 Singö Fault | 0.03 | 4.15 | 1770 | 0.0069 | 0.1171 |
| | ZFMWN-W0004 Forsmark Fault | 0.02 | 4.02 | 1100 | 0.0094 | 0.1394 |

All Nurminen's "d"s are much lower than Yoon and Zang (2019) except for Eckarfjärden, which is slightly smaller. There is no pattern here, probably because I chose midpoint distances on faults that ran perpendicular to ZFMA2 (like ZFMWNW0003, Eckarfjärden; ZFMWNW0001, Singö Fault; and ZFMWNW0004, Forsmark. And Yoon and Zang (2019) didn't. Actually ZFMA1, ZFMA2, and ZFMA3 strike perpendicular to the other three faults and intersect them. So obviously at their intersection r=0.

As in previous cases, "d" values from the Moss et al. (2022) equation are an order of magnitude larger than those of the Nurminen equation. This occurs because Moss used a smaller database of reverse faults (n=6) than did Nurminen (n=20), so there were zero distributed fault measurements on the FW of M5-6 earthquakes. Therefore, he derived his equation for "all magnitudes", meaning from the following ruptures (Table 3):

Table 5-3. Ruptures used by Moss et al. (2022) to create their regression of d/MD as a function of "r".

| Name | Magnitude | MD |
|---|---|---|
| Wenchuan | 7.9 | 6.0 |
| Chi-Chi | 7.62 | 9.8 |
| Kashmir | 7.6 | 7.1 |
| El Asnam | 7.3 | 5.0 |
| Spitak | 6.77 | 1.6 |
| San Fernando | 6.61 | 1.0 |
| Mean | 7.3 | 5.1 |
| Sigma | 0.5 | 3.35 |

Note that the ruptures Moss derived his equation from were an average of 1.8 magnitude units larger than the Yoon and Zang (2019). Scenario (M5.5); the smallest event (San Fernando) was still 1.1 magnitude units above M5.5. For displacement, the mean $D_{max}$ was 5.1 m, compared to 0.32 m in the Yoon et al. scenario. So to apply his empirical equation to a small M5.5 earthquake, it had to be projected more than an order of magnitude below his dataset. In addition, Moss used an outlier parameter ($D_{max}$, or MD) to normalize his "d" measurements, which then had to be compared to Yoon and Zang (2019) uniform displacement. For these reason, we grayed out the Moss values in Table 5-2, indicating we have little confidence in them.

## 5.3.2 Yoon and Zang, 2019– activated vertical strike-slip faults

Yoon and Zang (2019) made a series of simulations in which a large fault was activated, and induced displacements occurred on similar-size and smaller named faults, rather than fractures. Table 5-4 gives an example of an earthquake on the Singö fault, and predicted induced slips on other nearby faults. We assume that the Mw6.05 earthquake on the Singö fault will be a strike-slip event (see Sec. 3.1.2), so we use the two empirical equations of Petersen et al. (2011) to predict distributed displacements.

Petersen's first equation is:

$$\mathrm{Ln}(d) = 1.4016m - 0.1671\,\ln[r] - 6.7991 \qquad \text{Eq. 20}$$

with $\sigma$ of (ln d)= 1.1193

Using the values for m and r in Table 5-4, we calculate median values for “d” and put them in the last column of Table 5-2. All of the “d” values computed from this equation (Table 5-4, column 6) are smaller than Yoon and Zang’s estimates (Table 5-4, column 3), with the difference becoming larger closer to the Singö fault. This shows that Petersen’s regression line has a very low slope with respect to distance “r”, as can be seen by the very low coefficient (0.1671) in the equation above; in contrast, the coefficient applied to magnitude (m) is nearly 10 times as large.

Table 5-4. Activated slip on the Singö fault and predicted induced slip on known nearby faults. Modified from Yoon and Zang, 2019, their Table 8-1.

| ACTIV-ATION | DEFORM. ZONE | SLIP (m) | Mag.Mw | Distance from Singö Fault (m) | “d” from Petersen’s equation (m) |
|---|---|---|---|---|---|
| Primary | ZFMWNW0001<br>Singö Fault | 0.72 | 6.05 | n/a | |
| Seconda | ZFMA1 | 0.11 | 4.42 | *120 avg* | *0.0241* |
| | ZFMA2 | 0.12 | 4.23 | *785 avg* | *0.0176* |
| | ZFMA3 | 0.06 | 4.18 | *600 avg* | *0.0184* |
| | ZFMWNW0003<br>Eckarfjärden Fau | 0.03 | 4.15 | 905 | 0.0172 |
| | ZFMWNW0004<br>Forsmark Fault | 0.02 | 4.02 | 1525 | 0.0158 |

The discrepancy in “d” may also exist partly from the geometry of secondary faults with respect to the Singö fault. The Eckarfjärden and Forsmark faults are basically parallel to the Singö fault, which is the typical geometry the Petersen et al. dataset was based on. In contrast, the ZFMA faults are all highly oblique to the Singö fault, such that they start at their intersection with the Singö (r=0), and extend away at an angle of roughly 45°, as far as the Eckarfjärden and Forsmark faults (r= 3350 to 5250 m). Yoon and Zang (2019) did not say exactly where on the ZFMA faults they made their calculations. For my prediction using Petersen’s equations, I chose a rough midpoint on each fault between the Singö and the other two long faults, near the geographic center of the proposed repository. But if Yoon and Zang picked a point closer to the Singö fault, that would explain why their induced slip predictions are larger than mine.

Petersen’s second equation predicts a normalized version of d, as $d/D_{avg}$:

$$\mathrm{Ln}(d/D_{avg}) = -0.1826 \ln[r] - 1.5471 \qquad \text{Eq. 21}$$

with $\sigma$ of $(\ln d/D_{avg}) = 1.1388$

Using the values for r, and 0.72 m for $D_{avg}$ on the Singö fault, we calculate median values for "$d/D_{avg}$" and "d", and put them in column 6 and 7 of Table 5-5.

Table 5-5. Activated slip on the Singö fault (Row 1) and predicted induced slip on known nearby faults. Modified from Yoon and Zang, 2019, their Table 8-1.

| ACTIVATION | DEFORM. ZONE | SLIP (m) | Mag Mw | Distance from Sin Fault (m) | "$d/D_{avg}$" from Petersen's 2nd equation | "d" (m) |
|---|---|---|---|---|---|---|
| Primary | ZFMWNW000<br>Singö Fault | 0.72 | 6.05 | n/a | | |
| Secondar | ZFMA1 | 0.11 | 4.42 | *120 avg* | *0.075124* | *0.0639* |
| | ZFMA2 | 0.12 | 4.23 | *785 avg* | *0.054328* | *0.0454* |
| | ZFMA3 | 0.06 | 4.18 | *600 avg* | *0.052432* | *0.0477* |
| | ZFMWNW000<br>Eckarfjärden Fault | 0.03 | 4.15 | 905 | 0.048354 | 0.0442 |
| | ZFMWNW000<br>Forsmark Faul | 0.02 | 4.02 | 1525 | 0.054544 | 0.0402 |

The "d" values computed from the Petersen equation 21 (Table 5-5, column 7) are both larger and smaller than Yoon and Zang's estimates (Table 5-5, column 3). Close to the Singö fault, Petersen's predicted "d" is ~50% of Yoon and Zang's value. But by 600 m away from the Singö, his values are essentially the same. By 1525 m away from the Singö, Petersen's "d" is 100% larger than Yoon and Zang's.

How realistic is this scenario of an M6.05 earthquake on the Singö fault occurring in the next 100 kyr? At present the Singö fault is entirely submerged east of Forsmark, so it is not possible to determine whether there are postglacial fault scarps on it. If such scarps did exist on the seafloor, this would be a realistic scenario. However, realize that the probability of an M6.05 strike-slip earthquake rupturing to the surface is only 0.1 (see Fig. 5-11a), so the lack of such a scarp on the Singö is hardly definitive. In the absence of definitive evidence on the Singö, we can look at its two "sister" faults west of the repository (the Eckarfjärden and Forsmark fault zones). The Singö fault zone is very similar in orientation, age, and deformation style to those two faults. Both the Eckarfjärden and Forsmark zones are on-land for their entire length, but neither displays postglacial fault scarps, to the level of detection of lidar-based reconnaissance of Öhrling et al. (2018) and Öhrling and Smith (2020). The truth is, it is very difficult to prove that an M6 strike-slip earthquake did not occur on a fault, 10,000 years after the fact. However, no clear indications of earthquake related activity have been observed in the

Quaternary stratigraphy in the Forsmark area (Lagerbäck and Sundh, 2008, and references therein).

### 5.3.3 Yoon et al. 2014- activated vertical strike-slip faults

In the 2014 report to SSM, Yoon et al. 2014 provided 11 graphs of predicted displacement on target fractures as a function of the length of the fracture (Figs. 53, 57, 60, 64, 67, 70, 73, 76, 78, 90. 94). All these graphs show a very wide range of predicted displacements for fractures of the same length. For example, Fig. 5-15 shows that predicted displacement on the smallest fractures (~110 m long) ranges over four orders of magnitude. ($10^{-1}$ m to $10^{-5}$ m).

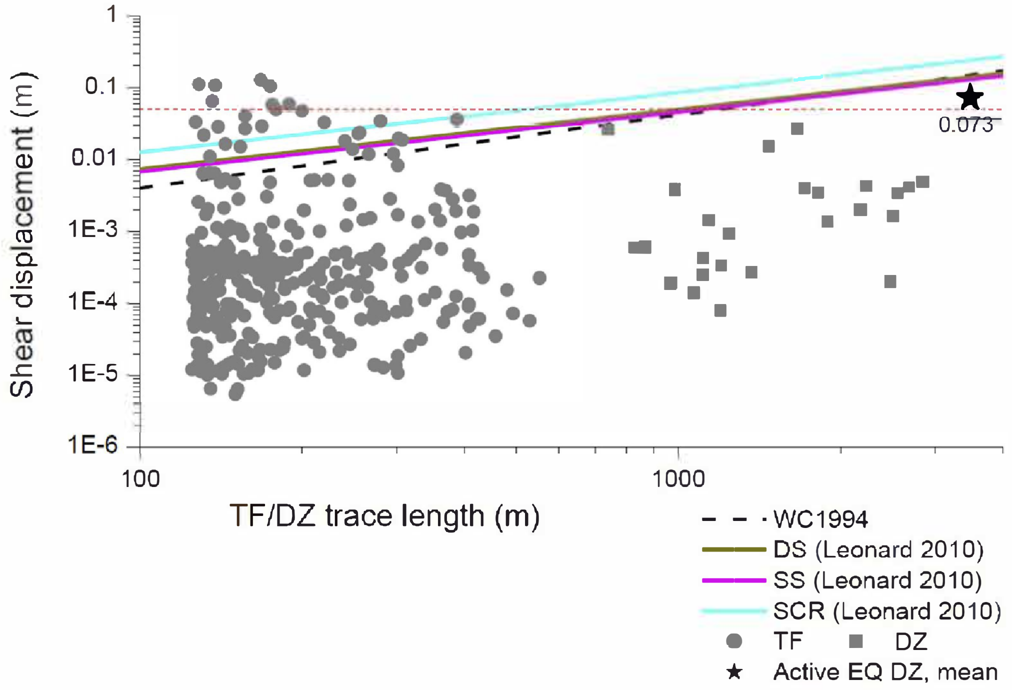

Figure 5-15. Shear displacement of the target fractures (TF) and deformation zones (DZ) with respect to length, due to earthquake at zone ZFMWNW0809A with realization DFN03h and comparison with empirical regressions (their Figure A3-18).

In contrast, according to the colored trend lines of displacement and length, displacement varies less than one order of magnitude over the whole range of fracture lengths (100 to 4000 m). This indicates that fracture length is a very, very weak control on predicted displacement. They state on page 62: *"Data points of TFs and DZs, in general, show no clear trend in the plot of [fracture] length versus displacement"*. This same statement could be made for all 11 of their graphs. So if length of fracture is not the main control on fracture displacement, what is?

If Yoon et al. (2014) had read any of the PFDHA papers published prior to 2014 (Youngs et al., 2003 for normal faults; Petersen et al., 2011 for strike-slip faults; and Moss and

Ross, 2011, for reverse faults), they would have noticed that those papers (and even Fälth et al., 2010, p. 3) made a different assumption. That assumption, based on hundreds of historic surface ruptures, is that the major control on displacement on secondary faults is distance to the seismogenic (activated) fault. Not on the length of the secondary fault/fracture.

Actually, Yoon et al. (2014) noticed this trend in their data, even without knowing of the PFDHA papers cited above. On page 62 they state: *"in general, the greater the distance from the earthquake hypocentre, the smaller the displacement of the joint segments consisting the TFs and DZs….In general, shear displacement of smooth joints decreases as the distance from the earthquake hypocentre increases."* But having made this observation, they did not do anything with it.

Yoon et al. (2014) made a parallel series of map figures (Figs. 52, 56 (powered shear force), 59, 63, 66, 69, 72, 75, 77, 89, 93) showing the displacement class of all repository fractures in map view. There is no explanation of the fracture colors on any of these maps. However, from their statement on page 64 *"TFs within the repository footprint undergo shear displacement larger than 1 mm"* we can infer the brown color (Fig. 5-16) represents shear displacements between $10^{-3}$ m and $10^{-2}$ m.

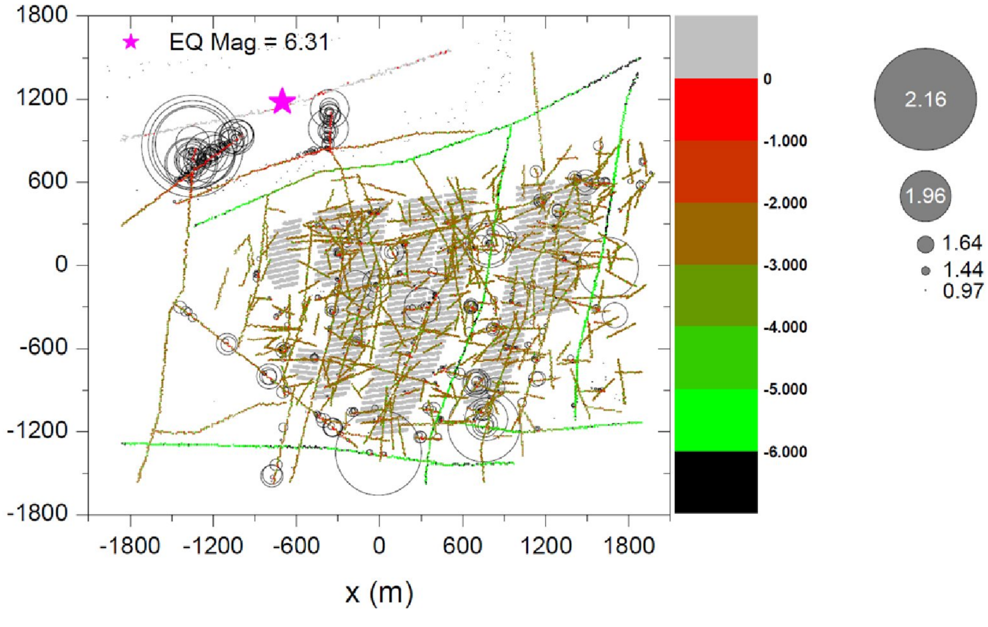

Figure 5-16. Spatial distribution of the induced seismic events and median shear displacement of smooth joints of the TFs and DZs, due to an M6.31 earthquake at zone ZFMWNW0001 (Singö fault) with realization DFN03h (Yoon et al., 2014, their Fig. 56).

The repository fractures in Fig. 5-16 range from 800 m from the Singö fault to 2800 m away. Over this 2000 m range target Yoon et al. show fracture displacements to remain between $10^{-3}$ m and $10^{-2}$ m (1 mm to 1 cm).

By comparison, we can input the same parameters into Petersen et al.'s 2011 equation:

$\ln d = 1.4016\, m - 0.1671 \ln [r] - 6.7991$ Eq. 20

Where: m=6.31, d is in centimeters and r is in meters. This regression has a standard deviation of 1.1193 in ln units.

For the closest fracture distance [r] of 800 m away from the PF, the equation yields: d=2.67 cm= 0.0267 m

For a distance [r] of 2800 m away from the PF, d= 2.05 cm= 0.0205 m.

Both of these displacements are larger than the range $10^{-2}$ to $10^{-3}$ m (1 cm to 0.1 cm) predicted in Fig. 5-14, but smaller than the fracture shear threshold (5 cm).

### 5.3.4 Summary of PFC displacements versus empirical displacements

For the case of local area, low-angle faults (like ZFMA2, M5.76, D=0.47 m), our induced fracture displacement values are all larger than the Yoon values. Yoon's median displacement values at a distance of 1900 m was 1 to 4 mm. For the same input variables using Nurminen's 2020 equation, median (50%-ile) displacements at 1900 m distance were 9.1 mm (+13 mm/-5.3 mm). We also ran two simulations (same magnitude and distances) with the new Moss et al. (2022) equation for distributed displacements during reverse ruptures, which predicts $d/D_{max}$ at various distances. Compared to Yoons's (median?) 5 mm predicted at 1900 m, the Moss equations predicted (95%-ile) displacements of 166 mm at the same distance, roughly three times the Nurminen 95%-ile value. Yoon and Zang (2019) predicted shears on other named deformation zones at distances of 600 to 1770 m from a hypothetical M5.5 event on ZFMA3, with D=0.32 m. Their "d" values ranged from 20 to 80 mm. Our values from empirical equations ranged from 9 to 14 mm (Nurminen) and 117 to 158 mm (Moss), thus bracketing the Yoon values.

Yoon and Zang also simulated an M6.05 earthquake on the regional, vertical Singö fault (D=0.72 m) and calculated induced displacements on the Eckarfjärden, Forsmark, and three ZFMA faults ranging from 20 to 120 mm. We calculated the distributed displacements from the Petersen et al. (2011) equations for strike-slip faults. Petersen equation 20 predicts "d" based on magnitude and distance, with values ranging from 15 to 24 mm, just overlapping the lower part of the Yoon range. Petersen equation 21 predicts "d/MD" as a function of distance, with values ranging from 40 to 64 mm, which lies in the center of Yoon's range.

The closest correspondence of any empirically-predicted "d" values with numerically-predicted "d" values appears to be in this last case above, where "d" was being predicted on pre-existing deformation zones (DZs). Where "d" was predicted on smooth fractures, the empirical predictions were always larger to much larger than the numerical "d" values. This suggests that the distributed faults mapped in post-earthquake reconnaissance in the field may have mostly been the result of reactivating pre-existing shear zones, rather than smooth fractures. If that is the case, it is improper to use the present empirical equations to predict shear on smooth target fractures, but only shear on other DZs.

# 6. Discussion

The goal of Sections 3-5 of this report was to compare numerically-predicted target fracture displacements, induced by future earthquakes on faults in or near the Forsmark repository, to observed distributed faults worldwide caused by same-size historic earthquakes in SCR tectonic settings. This comparison of predicted versus observed displacements is complicated because the underlying data sets and analysis methods are so different. In the numerical model scenarios (SKB and Yoon), the geometry and characteristics of the principal (coseismic) fault (PF) and target fractures are well known, because they have been mapped at the surface and in tunnels and boreholes. The magnitude and slip of the earthquakes on the PF are assumed by the modelers, sometimes with pairs of values incompatible with historic earthquakes. The output values of displacement are dominantly for simple, “clean” target fractures, of 150 m radius (300 m max. length), at the repository depth (500 m).

In the database of historic surface faulting, the geometry of the PF is well known, because: (1) the surface rupture trace was mapped after the event, and (2) the subsurface geometry was defined from location of the focus and the aftershock cloud. However, only the surface trace location is known for the DFs, almost all of which had to break through a layer of alluvium/colluvium/regolith to reach the surface; the bedrock is not visible. Accordingly, we do not know the characteristics of the geologic structure underlying the surface DF trace in bedrock; whether it is a simple “clean” fracture, a thin fault zone of small displacement, or a thick shear zone of large displacement. The displacement values could only be measured at the surface, not at a depth of 500 m.

Additionally, most DFs in SCR ruptures are longer than 300 m max length of modeled target fractures. For example, on the Meckering rupture PF scarps had a cumulative length of 38.3 km, whereas DF scarps totalled 20.7 km (FDHI data). The DF/PF length ratio is 0.54. Of the 26 mapped DFs, 13 are shorter than 300 m. However, the underlying fracture/fault in bedrock may have been longer than the surface scarp (it cannot have been shorter). Unfortunately, none of the 12 DF displacement measurements at Meckering were on scarps <300 m long. Instead, they were made on DF scarps 0.8 to 4 km long, much longer than the 300 m target fractures modeled by SKB.

On the Cadoux rupture PF scarps had a cumulative length of 15.7 km, whereas DF scarps totalled 8.2 km. The DF/PF length ratio is 0.52, nearly identical to Meckering, even though the rupture pattern looks very different. Of the 30 mapped DFs, 19 are shorter than 300 m. Of the 18 DF displacement measurements made at Cadoux, only 5 were on scarps <300 m long. The remaining DF measurements were on longer scarps 0.3 to 0.9 km long, longer than the modeled 300 m target fractures.

The disparities between the input data for the numerical model versus for empirical database should be kept in mind when interpreting the comparison graphs of displacement in Sections 5.2 and 5.3.

# 7. Conclusions and recommendations

## 7.1. Conclusions on stationarity of seismicity in Sweden

In Sec. 2 we described the geological and seismological setting of Fennoscandia. Scandinavian publications over the past 8 years (cited previously) and my interpretation thereof, seem to support the spatial stationarity of seismicity between the present and ~57ka (end of the middle Weichselian). It has been known since the 1980s that instrumental and historic seismicity clustered around PGFs. Newly-discovered PGFs have not changed that pattern. It now appears that PGFs have been active in the same locations over >50 kyrs.

## 7.2. Conclusions on distributed faulting versus induced shear on target fractures

In Sec. 3 we described current methods of PFDHA and suggested that the best analog for past and future surface ruptures in Fennoscandia would be historic reverse-fault ruptures in the non-extended Stable Continental Region of Australia. A set of five Australian ruptures had been mapped and measured in enough detail (i.e., displacements on Principal and Distributed faults) that we could extract a multivariate regression equation from them for Distributed displacement. However, in two of the five ruptures up to half distributed displacements were from long, anomalous footwall secondary faults, and this somewhat skewed the regression equations. Therefore, when comparing empirical versus numerical displacements on reverse surface ruptures, we used equations from both global datasets (Nurminen et al., 2020; Moss et al., 2022), and from our own SCR subset.

Midway through preparation of the report we realized that many of the numerical scenario displacements on target fractures had been made for principal faulting on long faults such as the Singö. These faults are vertical and cannot host reverse-faulting, but can accommodate strike-slip faulting in a compressional regime. Therefore in Sec. 4 we used the appropriate equations from Petersen et al. (2011) to estimate distributed displacements. [These 12 year-old equations are in need of an update. One has been submitted for publication as of Feb. 10, 2023].

The formal comparison of distributed fault displacements calculated empirically versus numerically composes Sec. 5. For both reverse ruptures and strike-slip ruptures, empirically-predicted displacements are larger to much larger than 3DEC displacements on target fractures. This same situation exists to a lesser extent to PFC code-predicted displacements, some of which are slightly smaller or larger than empirically-predicted values. However, the best match between empirical and numerical predictions comes where the PFC code predicts induced displacements on other deformation zones (DZs), rather than on smooth target fractures.

This suggests that the distributed faults mapped in post-earthquake reconnaissance in the field may have been mostly the result of reactivating pre-existing deformation zones, rather than smooth fractures. If that is the case, it would be improper to use the present empirical equations to predict shear on smooth target fractures, but only shear on other DZs.

In other words, we now suspectthat the empirical displacements are measuring one phenomenon (reactivation of relatively long preexisting fault zones and shear zones) and the numerical displacements measuring another phenomenon (reactivation of relatively short simple, clean fractures). In that case this report cannot invalidate the SKB and PFC predicted displacements on clean fractures. The message to the paleoseismologists who study historic surface ruptures, should be to ascertain what type of bedrock structures inderlie the kilometers of DFs in historic ruptures. Where regolith is thin, this could be done by trenching, and where thicker, possibly by geophysics.

## 7.3. Recommendations

In priority order:

Issue 1-Establish exactly how PFC modeling of induced displacement on other DZs (which matches empirical displacements) differs from PFC modeling of induced displacement on smooth target fractures (which underestimates empirical displacements). Is it because the DZs were assigned different geotechnical properties than the smooth joints in the PFC model? And if not that, what causes the difference?

Issue 2-Having answered Issue 1, can 3DEC modeling be similarly reconfigured to output induced displacements on DZs more in line with empirical displacements?

Issue 3-When additional PGFs are mapped in Sweden using lidar, investigators should look for possible DFs associated with the main PGF scarp. If trenching is performed, on the PGF scarp, consider also trenching the possible DF scarps. Some care should be taken: (1) lengthen the trenches away from the PF scarp to look for evidence of DFs which might have been obscured by weathering and erosion, and (2) document the type of bedrock structure that underlies any DFs. The more surface rupture data we can obtain from the Fennoscandian SCR, the less we will have to rely on analogs from other SCRs (such as Australia), which possibly might not be appropriate for use in Fennoscandia.

# References

Abdi, A, Heinonen, S., Juhlin, C., and Karinen, T., 2015, Constraints on the geometry of the Suasselka post-glacial fault, northern Finland, based on reflection seismic imaging. Tectonophys. 649: 130-138.

Adams, J., Wetmiller, R.J., Hasegawa, H. and Drysdale, J. ,1991, The first surface faulting from a historical intraplate earthquake in North America, Nature, 352, 617–619.

American Nuclear Society Standards Committee Working Group ANS-2.30 (ANSI-ANS-2.30-2015), 2015, Criteria for assessing tectonic surface fault rupture and deformation at nuclear facilities, American Nuclear Society, La Grange Park, Illinois, available at: https://webstore.ansi.org/standards/ansi/ansians302015 (last accessed May 2021).

Arrowsmith, R., Crosby, C.J., Korzhenkov, A.M., Mamyrov, E., Povolotskaya, I., Guralnik, B., and Landgraf, A., 2016, Surface rupture of the 1911 Kebin (Chon-Kemin) earthquake, northern Tien Shan, Kyrgyzstan, *in* Landgraf, A. et al. (eds.), Seismicity, Fault Rupture, and Earthquake Hazards in Slowly Deforming Regions. Geol. Soc. London., Spec. Pub. 432: 233-253.

Arvidsson, R., 1996, Fennoscandian earthquakes; whole crustal rupturing related to postglacial rebound. Science 274: 744-746.

Baize, S., Nurminen, F., Sarmiento, A., Dawson, T., Takao, M., Scotti, O., Azuma, T., Boncio, P., Champenois, J., Cinti, F.R., Civico, R., Costa, C., Guerrieri, L., Marti, E., McCalpin, J., Okumura, K., and Villamor, P., 2020, A worldwide and unified database of surface ruptures (SURE) for fault displacement hazard analyses. Seismol. Res. Lett., 91(1):499-520.

Beckel, S., Juhlin, C., Malehmir, A. and Ahmadi, O., 2021, Imaging and characterizing of glacially induced faults using applied geophysics, *in* Steffen, H., Olesen, O. and Sutinen, R. (eds.), 2022, Glacially-Triggered Faulting: Cambridge Univ. Press, Cambridge, UK, p. 118-132.

Benz, N.J., 2018, New slip and stress distributions hold implications for the next great earthquake in Cascadia. M.S. thesis, Univ. Of Missouri- Columbia, July 2018, 76 p.

Berglund, M. and Dahlström, N., 2015, Postglacial fault scarps in Jämtland, central Sweden. GFF, 137, 339–343, doi.org/10.1080/11035897.2015.1036361.

Boncio, P., Liberi, F., Caldarella, M, and Nurminen, F.-A., 2018, Width of surface rupture zone for thrust earthquakes: implications for earthquake fault zoning. Nat. Hazards Earth Syst. Sci., 18, 241–256, 2018. https://doi.org/10.5194/nhess-18-241-2018

Bryant, W. A. and Hart, E. W., 2007, Fault-Rupture Hazard Zones in California, Alquist-Priolo Earthquake Fault Zoning Act With Index to Earthquake Fault Zones Maps, Calif. Geol. Surv., Sacramento, CA, Spec. Pub. 42, Interim Revision 2007, 41 pp., 2007.

Calais, E., Camelbeeck, T., Stein, S., Liu, M. and Craig, T.J., 2016, A new paradigm for large earthquakes in stable continental plate interiors. Geophysical Research Letters, 43(20).

Caskey, S.J., Wesnousky, S.G., Zhang, P., and Slemmons, D.B., 1996, Surface faulting of the 1954 Fairview Peak (MS 7.2) and Dixie Valley (MS 6.8) earthquakes, central Nevada. Bull. Seismol. Soc. Am. 86(3): 761-787.

Chapman, N., Stephansson, O., Lanaro, F. and Sonnerfelt, L, 2014, Workshop on seismic hazard at Forsmark, Main Review Phase. Technical Note 2014:22, ISSN: 2000-0456, available at www.stralsakerhetsmyndigheten.se, 21 p.

Chen, H., Qu, C., Zhou, D., Ma, C. and Shan, X, 2021, Rupture kinematics and coseismic slip model of the 2021 Mw 7.3 Maduo (China) earthquake; Implications for the seismic hazard of the Kunlun fault. Remote Sensing, 13, 3327, https://www.mdpi.com/2072-4292/13/16/3327

Coppersmith, K.J., 1994, Introduction, Chapter 1, *In* Johnston, A.C., Coppersmith, K.J., Kanter, L.R. and Cornell, C.A. (editors), The Earthquakes of Stable Continental Regions. Volume 1: Assessment of Large Earthquake Potential, Chapter 1, pp. 1-1 to 1-10, Electric Power Research Institute, EPRI Report TR-102261-V1, Palo Alto, California, USA.

Coppersmith, K.J. and others, 2012, Technical Report: Central and Eastern United States Seismic Source Characterization for

Nuclear Facilities. EPRI, Palo Alto, CA, U.S. DOE, and U.S. NRC.

Danciu, L., Nanden, S., Reyes, C., Basili, R., Weatherill, G., Beauval, C., Rovida, A., Villanova, S., Sesetyan, K., Bard, P-Y., Cotton, F., Weimer, S., and Giardini, D, 2021, The 2020 update of the European Seismic Hazard Model; Model overview. EFEHR Technical Report 001, v1.0.0, https://doi.org/10.12686/a15

Dawson, J., Cummins, P., Tregoning, P. and Leonard, M., 2008, Shallow intraplate earthquakes in Western Australia observed by interferometric synthetic aperture radar. Jour. Geophys. Res. 113, B11408, doi:10.1029/2008JB005807.

Dentith, M., Clark, D. and Featherstone, W., 2009, Aeromagnetic mapping of Precambrian geological structures that controlled the 1968 Meckering earthquake (Ms 6.8): Implications for intraplate seismicity in Western Australia. Tectonophys. 475(3-4): 544-553.

Dorbath, C., Dorbath, L., Gaulon, R., George, T., Mourgue, P., Ramdani, M., Robineau, B. and Tadili, B., 1984, Seismotectonics of the Guinean earthquake of December 22, 1983. Geophys. Res. Lett. 11(10): 971-974.

DuRoss, C.B., Personius, S.F., Crone, A.J., Olig, S.S., Hylland, M.D., Lund, W.R. and Schwartz, D.P., 2016, Fault segmentation; New concepts from the Wasatch fault zone, Utah, USA. Jour. Geophys. Res. 121:1131-1157.

DuRoss, C.B. and 46 others, 2020, Surface displacement distributions for the July 2019 Ridgecrest, California, earthquake ruptures. Bull. Seismol. Soc. Amer., 110(4): 1400-1418.

FDHI (15 authors), 2021, Fault Displacement Hazard Initiative Database: Natural Hazards Risk & Resiliency Research Center, B. John Garrick Institute for the Risk Sciences, Report GIRS-2021-08, University of California, Los Angeles, DOI: 10.34948/N36P48, 94 p. plus Supplemental data files.

Fälth, B., Hökmark, H. and Munier, R., 2010, Effects of large earthquakes on a KBS-3 repository; Evaluation of modelling results and their implications for layout and design: SKB Technical Report TR-08-11, 171 p.

Fälth, B., Hökmark, H., Lund, B., Mai, P.M., Roberts, R. and Munier, R., 2015, Simulating earthquake rupture and off-fault fracture response; Application to the safety assessment of the Swedish nuclear waste repository: Bull. Seismol. Soc. Amer. 105(1), 134-151.

Fälth, B., Lonnqvist, M. and Hökmark, H., 2019, Coseismic secondary fracture displacements under different stress conditions: Posiva Oy, Posiva Working Report 2019-10, Eurajoki, Finland.

Fälth, B., Grigull, S., Galing, J., Ivars, D.M. and Wagner, F., 2022, Comment on ”Modelling coseismic displacements of fracture systems in crystalline rock during large earthquakes: Implications for the safety of nuclear waste repositories”, as published by Lei and Loew (2021) in IJRMMS 138, 104590. International Journal of Rock Mechanics & Mining Sciences 150, 105013.

Ferrario, M. F., and F. Livio, 2021, Conditional probability of distributed surface rupturing during normal-faulting earthquakes: Solid Earth 12, 1197–1209, doi: 10.5194/se-12-1197-2021.

Figueiredo, P.M. and 14 others, 2022, The Mw 5.1, 9 August 2020, Sparta earthquake, North Carolina: The first documented seismic surface rupture in the eastern United States. GSA Today 32(3-4): 4-11.

Fletcher, J.M. et al., 2014, Assembly of a large earthquake from a complex fault system: Surface rupture kinematics of the 4 April 2010 El Mayor-Cucapah (Mexico) Mw 7.2 earthquake. Geosphere 10(4): 797-827.

Fredrich, J.T., McCaffrey, R. and Denham, D., 1988, Source parameters of seven large Australian earthquakes determined by body waveform inversion. Geophysical Journal of the Royal Astronomical Society, 95, 1-13.

Gelman, A., and J. Hill, 2007, Data Analysis Using Regression and Multilevel/Hierarchical Models, Cambridge University Press, New York.

Green, R.A. and Bommer, J.J., 2019, What is the smallest earthquake magnitude that needs to be considered in assessing liquefaction hazard? Earthquake Spectra 35(3): 1441-1464.

Grunthal, G., 1999, Seismic hazard assessment for Central, North, and Northwest Europe. Annali di Geofisica 42(6): 999-1011.

Harry, D.L. and 17 others, 2020, Evolution of the southwest Australia rifted continental margin during breakup of East Gondwana: Results from the International Ocean Discovery Program Expedition 369. Geochem. Geophys. Geosys. 21, e2020GC009144, https://doi.org/10.1029/2020GC009144

Hartzell, S.H. and Heaton, T.H., 1983, Inversion of strong ground motion and teleseismic waveform data for the fault rupture history of the 1979 Imperial Valley, California, earthquake. Bull. Seismol. Soc. Amer. 73(6): 1553-1583.

Hökmark, H., Fälth, B., Lönnqvist, M. and Munier, R., 2019, Earthquake simulations performed to assess the long-term safety of a KBS-3 repository; Overview and evaluation of results produced after SR-Site. SKB TR-19-19, Sept. 2019, Svensk Kärnbränslehantering AB, 105 p.

IAEA, 2019, Site evaluation for nuclear installations: IAEA Safety Standards Series No. SSR-1, IAEA, Vienna, Austria.

IAEA, 2021, An introduction to probabilistic fault displacement hazard analysis in site evaluation for existing nuclear installations: IAEA TECDOC-1987, Vienna, Austria, 131 p.

IAEA, 2022, Seismic hazards in site evaluation for nuclear installations: no. DS507, Rev. 1, Safety Guide SSG-9, IAEA, Vienna, Austria, 78 p.

Johnson, M. D., Fredin, O., Ojala, A. E. K. and Peterson, G., 2015, Unraveling Scandinavian geomorphology: the LiDAR revolution. GFF, 137, 245–251, doi.org/11035897.1111410.

Johnston, A.C., Coppersmith, K.J., Kanter, L.R. and Cornell, C.A. (editors), 1994a, The Earthquakes of Stable Continental Regions. Volume 1: Assessment of Large Earthquake Potential, chapter 4, pp. 4-1 to 4-103, Electric Power Research Institute, EPRI Rpt. TR-102261, Palo Alto, CA.

Johnston, A. C., 1994b, Seismotectonic interpretations and conclusions from the stable continental region seismicity database, *in* A. C. Johnston, K. J. Coppersmith, L. R. Kanter, and C. A. Cornell (editors), The Earthquakes of Stable Continental Regions. Volume 1: Assessment of Large Earthquake Potential, chapter 4, pp. 4-1-4-103, Electric Power Research Institute, EPRI Rpt. TR-102261, Palo Alto, CA.

Juhlin, C., Lund B (2011) Reflection seismic studies over the Burträsk fault, Skellefteå, Sweden. Solid Earth 2:9–16. doi:10.5194/se-2-9-2011.

Juhlin C, Dehghannejad M, Lund B, Malehmir A, Pratt G (2010) Reflection seismic imaging of the end-glacial Pärvie Fault system, northern Sweden. J Appl Geophys 70:307–316. doi:10.1016/j.jappgeo.2009.06.004.

Kelson, K.I., Kang, K.-H., Page, W.D., Lee, C.-T., Cluff, L.S., 2001, Representative styles of deformation along the Chelungpu fault from the 1999 Chi-Chi (Taiwan) earthquake: Geomorphic characteristics and responses of man-made structures, Bull. Seismol. Soc. Am. 91(5): 930-952.

King, T.R., 2019, GEOLOGIC EXPRESSIONS OF FAULTING AND EARTHQUAKE STRONG GROUND MOTIONS IN INTRAPLATE BEDROCK TERRAINS. PhD dissertation, School of Earth Sciences, University of Melbourne, December 2019, 336 p.

King, T.R., Quigley, M. and Clark, D., 2019a, Surface-rupturing earthquakes in Australia and their environmental effects; New insights from re-analyses of observational data. Geosciences 9, 408, doi:10.3390/geosciences9100408, 34 p.

King, T.R.; Quigley, M.; Clark, D., 2019b, Review paper: The 14th October 1968 Mw 6.6 Meckering surface rupturing earthquake, Australia. EarthArXiv Prepr. 2019, 1–25.

King, T.R.; Quigley, M.C.; Clark, D., 2019c, Review paper: The 10th March 1970 Mw 5.0 Calingiri surface rupturing earthquake, Australia. EarthArXiv Prepr.

King, T.R.; Quigley, M.C.; Clark, D., 2019d, Review paper: The 2nd June 1979 Mw 6.1 Cadoux surface rupturing earthquake, Australia. EarthArXiv Prepr. 2019, 1–19.

King, T.R.; Quigley, M.C.; Clark, D, 2019e, Review paper: The 30th March 1968 Mw 5.7 Marryat Creek surface rupturing earthquake, Australia. EarthArXiv Prepr. 2019, 1–17.

King, T.R.; Quigley, M.; Clark, D., 2019f, Review paper: The 23rd March 2012 Mw 5.2 Pukatja surface rupturing earthquake, Australia. EarthArXiv Prepr. 2019, 1–13.

King, T.R.; Quigley, M.; Clark, D., 2019g, Review paper: The 20th May 2016 Mw 6.1 Petermann surface rupturing earthquake, Australia. EarthArXiv Prepr. 2019, 1–16.

King, T.R.; Quigley, M.C.; Clark, D.; Valkaniotis, S.; Mohammadi, H.; Barnhart,W.D., 2019h, The 1987 to 2019 Tennant Creek, Australia, earthquake sequence: A protracted intraplate multi-mainshock sequence. EarthArXiv Prepr. 2019.

Kutu, J.M., Anami, C.Y., Asiedu, D.K., Manu, J., Hayford, E. And Oppong, I., 2013, Recent seismicity of southern Ghana and re-interpretation of the 1939 Accra earthquake; Implications for recurrence of major earthquake. Int. Jour. Basic and Appl. Sci. 2(4): 322-331.Lagerbäck, R. and Witschard, F, 1983, Neotectonics in northern Sweden- geological investigations. SKBF/KBS Tech. Report 83-58, 58 p.

Lagerbäck, R., 1988a, Periglacial phenomena in the wooded areas of Northern Sweden - relicts from the Tarendo Interstadial. Boreas, 17, 487-499, doi.org/10.1111/j.l502-3885 .1988. tb00563 .X.

Lagerbäck, R., 1988b, The Veiki moraines in northern Sweden - widespread evidence of an Early Weichselian deglaciation. Boreas, 17, 469-486, doi.org/10.1111/j.1502-3885.1988.tb00562.x.

Lagerbäck, R. and Robertsson, A.-M., 1988, Kettle holes - stratigraphical archives for Weichselian geology and palaeoenvironment in northernmost Sweden. Boreas, 17,439-468, doi.org/10.lllllj.1502-3885.1988.tb0056l.x.

Lagerbäck, R., 1990, Late Quaternary faulting and-paleoseismicity in northern Fennoscandia, with particular reference to the Lansjarv area, northen Sweden. Geol. Foren. I Stockholm Forhand. 112(4): 333-354.

Lagerbäck, R., 1992, Dating of Late Quaternary faulting in northen Sweden. Jour. Geol. Soc. London 149: 285-291.

Lagerbäck, R. and Sundh, M., 2008, Early Holocene Faulting and Paleoseismicity in Northern Sweden. Research Paper C 836, Geological Survey of Sweden.

Langer, C.J., Bonilla, M.G. and Bollinger, G.A., 1985, The Guinea, West Africa, earthquake of December 22, 1983; Reconnaissance geologic and seismologic field studies. U.S. Geol. Survey, Open-File Rept. 85-282, 28 p.

Lei, Q. and Loew, S., 2021, Modelling coseismic displacements of fracture systems in crystalline rock during large earthquakes: Implications for the safety of nuclear waste repositories: Inter. Jour. Rock Mech. & Mining Sci., 138, 104590.

Lei, Q. and Loew, S., 2022, Reply to Comment by Fälth et al on ”Modelling coseismic displacements of fracture systems in crystalline rock during large earthquakes:

Implications for the safety of nuclear waste repositories". International Journal of Rock Mechanics & Mining Sciences 150, 105014.

Leonard, M., Ripper, I.D. and Yue, L., 2002, Australian earthquake fault plane solutions. Geoscience Australia, Record 2002/19, Canberra.

Leonard, M., 2008, One hundred years of earthquake recording in Australia. Bull. Seismol. Soc. Amer. 98(3): 1458-1470.

Leonard, M., 2010, Earthquake fault scaling: Self-consistent relating of rupture length, width, average displacement, and moment release. Bull. Seismol. Soc. Amer. 100(5A): 1971-1988.

Leonard. M., 2014, Self-consistent earthquake fault-scaling relations; Update and extension to Stable Continental strike-slip faults. Bull. Seismol. Soc. Amer. 104(6): 2953-2965.

Lindblom, E., Lund, B., Tryggvason, A., Uski, M., Bödvarsson, R., Juhlin, C., and Roberts, R., 2015, Microearthquakes illuminate the deep structure of the endglacial Pärvie fault, northern Sweden. Geophys J Int. 201: 1704-1716.

Malehmir, A., Andersson, M., Mehta, S., Brodic, B., Munier, R., Place, J., Maries, G., Smith, C., Kamm, J., Bastani, M., Mikko, H., and Lund, B., 2016, Post-glacial reactivation of the Bollnäs fault, central Sweden –a multidisciplinary geophysical investigation: EGU Solid Earth, 7, 509–527, doi:10.5194/se-7-509-2016

Markusic, S., Stanko, D, Penava, D., Ivancic, I., Orsulic, O.B., Korbar, T. and Sarhosis, V, 2021, Destructive M6.2 Petrinja earthquake (Croatia) in 2020- Preliminary multidisciplinary research. Remote Sensing 13(6): 1095.

Martin, C.D., 2007, Quantifying in situ stress magnitudes and orientations for Forsmark. Forsmark state 2.2., SKB R-07-26, Swedish Nuclear Fuel and Waste Management Co.

Mattila, J., Ojala, A. E. K., Ruskeeniemi, T. et al., 2019, Evidence of multiple slip events on postglacial faults in northern Fennoscandia. Quaternary Science Reviews, 215, 242–252, doi.org/10.1016/j.quascirev.2019.05.022.

McCalpin, J.P. (ed.), 2009a, Paleoseismology, 2nd Edition: Academic Press, San Diego, 613 p.

McCalpin, J.P., 2009b, Application of paleoseismic data to seismic hazard assessment and neotectonic research, Chapter 9 *in* McCalpin, J.P. (ed.), 2009, Paleoseismology, 2nd Edition: Academic Press, San Diego, p. 15.

McCalpin, J.P., 2013, Seismology: Post-glacial seismicity and paleoseismology at Forsmark, Initial Review Phase: Stral sakerhets myndigheten (Swedish Radiation Safety Authority), Stockholm, Sweden, Technical Note 2013:34, 66 p. Available at https://www.stralsakerhetsmyndigheten.se/publikationer/rapporter/avfall--transport--fysiskt-skydd/2013/201334/

McCalpin, J.P. and Nishenko, S.P., 1996, Holocene paleoseismicity, temporal clustering, and probabilities of future large (M>7) earthquakes on the Wasatch fault zone, Utah: Journal of Geophysical Research, v. 101(B3), p. 6233-6253.

Mikko, H., Smith, C. A., Lund, B., Ask, M. V. S. and Munier, R., 2015, LiDAR-derived inventory of post-glacial fault scarps in Sweden. GFF, 137, 334–338, doi.org/10.1080/11035897.2015.1036360.

Mörner, N.-A., 2003. Paleoseismicity of Sweden - a novel paradigm. Contribution to INQUA from its Sub-commission on Paleoseismology. Printed by JOFO Grafiska AB for Institute of Paleogeophysics & Geodynamics, Stockholm University, 320 pp. ISBN-91-631-4072-1, 320 pp, (hard cover, colour print)

Moss, R.E.S. and Ross, Z. E., 2011, Probabilistic fault displacement hazard analysis for reverse faults: Bull. Seismol. Soc. Amer., v. 101, no. 4, p. 1542-1553.

Moss, R. E. S., K. V. Stanton, and M. I. Buelna, 2013, The impact of material stiffness on the likelihood of fault rupture propagating to the ground surface, Seismol. Res. Lett. 84, no. 3, 485–488.

Moss, R.E.S., Thompson, S., Kuo, C-H., Younesi, K., and Chao, S-H., 2022, Reverse Fault PFDHA. Report GIRS-2022-05, DOI: 10.34948/N3F595, Natural Hazards Risk & Resiliency Research Center, B. John Garrick Institute for the Risk Sciences. Univ. of California-Los Angeles, 124 p. (https:\\risksciences.ucla.edu/girs-reports/2022/05)

Nandan, S., Ouillon, G. and Sornette, D., 2022, Are large earthquakes preferentially triggered by other large events? JGR Solid Earth, https://doi.org/10.1029/2022JB024380.

Nurminen, F.-C., 2018, Probabilistic model of fault displacement hazard for reverse faults: M.S. Thesis, Oulu Mining School, University of Oulu, FINLAND, August 2018, 83 p.

Nurminen, F.-C., P. Boncio, F. Visini, B. Pace, A. Valentini, S. Baize, and O. Scotti, 2020, Probability of occurrence and displacement regression of distributed surface rupturing for reverse earthquakes: Front. Earth Sci. 8, doi: 10.3389/feart.2020.581605.

Nurminen, F., F. Visini, S. Baize, P. Boncio, B. Pace, O. Scotti, and A. Valentini, 2021, Probability of distributed surface rupturing occurrence and displacement regression for normal and reverse earthquakes (abs.): Seismological Research Letters, Volume 92, Number 2B, April 2021 • www.srl-online.org; Fall AGU Meeting.

Nurminen, F., Baize, S., Boncio, P., Blumetti, A.M., Cinti, F.R., Civico, R. and Guerrieri, L., 2022, SURE 2.0- New release of the worldwide database of surface ruptures for fault displacement hazard analyses. Nature Scientific Data, 9, article number 729 (2022) • www.srl-online.org;

Öhrling, C., Peterson, G. and Mikko, H., 2018, Detailed geomorphological analysis of LiDAR derived elevation data; Searching for indicatives of late- and postglacial seismic activity: SKB Report R-18-10, Swedish Nuclear Fuel and Waste Management Co., Stockholm, 35 p.

Öhrling, C. and Smith, C., 2020, Sedimentologisk undersökning av misstänkt glacialt inducerad förkastningsbrant: SGU Report 200:21, 16 p. (in Swedish).

Ojala, A. E. K., Mattila, J., Ruskeeniemi, T. et al., 2017, Postglacial seismic activity along the Isovaara-Riikonkumpu fault complex. Global and Planetary Change, 157, 59–72, doi.org/10.1016/j.gloplacha.2017.08.015.

Ojala, A. E. K., Mattila, J., Ruskeeniemi, T. et al., 2019, Postglacial Faults in Finland – A Review of PGSdyn Project Results. POSIVA Report 2019-01. Posiva Oy, Eurajoki.

Ojala, A. E. K., Mattila, J., Middleton, M. et al., 2020, Earthquake-induced deformation structures in glacial sediments – evidence on fault reactivation and instability at the Vaalajärvi fault in northern Fennoscandia. Journal of Seismology, 24(3), doi.org/10.1007/s10950-020-09915-6.

Olesen, L., Olesen, O., Dehls, J. and Tassis, G., 2018, Late-/postglacial age and tectonic origin of the Nordmannvikdalen Fault, northern Norway. Norwegian Journal of Geology, 98, 483–500, doi.org/10.17850/njg98-3-09.

Olesen, O., Olsen, L., Gibbons, S., Ruud, B.O., Johansen, T.A., and Kværna, T., 2021, Postglacial Faulting in Norway; Large Magnitude Earthquakes of the Late Holocene Age, in Steffen, H., Olesen, O., and Sutinen, R. (eds.), Glacially-Triggered Faulting: Cambridge Univ. Press, Cambridge, UK, p. 198-217.

Pedersen, R., Jonsson, S., Arnadottir, T., Sigmundsson, F., and Feigl, K.L., 2003, Fault slip distribution of two June 2000 Mw6.5 earthquakes in South Iceland estimated from joint inversion of InSAR and GPS measurements. Earth Plan. Sci. Lett. 213: 487-502.

Petersen, M., Dawson, T. E., Chen, R., Cao, T., Wills, C. J., Schwartz, D. P., and Frankel, A. D., 2011, Fault displacement hazard for strike-slip faults: Bull. Seismol. Soc. Am., 101, 805–825.

Pizza, M., Ferrario, M.F., Thomas, F., Tringali, G. and Livio, F., 2023, Likelihood of Primary surface faulting; Updating empirical regressions. Bull. Seismol. Soc. Amer., 113(5): 2106-2118.

Polcari, M., Albano, M., Atzori, S., Bignami, C. and Starmondo, S., 2018, The causative fault of the 2016 Mwp 6.1 Petermann Ranges intraplate earthquake (central Australia) retrieved by C- and L-band InSAR data. Remote Sensing 10: 1311, doi:10.3390/rs10081311.

Redfield, T. F. And Osmundsen, P.T., 2014, Some remarks on the earthquakes of Fennoscandia; A conceptual seismological model drawn from the perspective of hyperextension. Norwegian Jour. Geol., 94(4):233-262.

Sarmiento, A. and 14 others, 2021, Fault Displacement Hazard Initiative Database: Natural Hazards Risk & Resiliency Research Center, B. John Garrick Institute for the Risk Sciences, Report GIRS-2021-08, University of California, Los Angeles, DOI: 10.34948/N36P48, 94 p. plus Supplemental data files.

Schulte, S.M. and Mooney, W.D., 2005, An updated global earthquake catalogue for stable continental regions: Reassessing the correlation with ancient rifts. Geophys. Jour. Int. 161: 707-721.

Shaw, B.E., 2011, Surface-slip gradients of large earthquakes. Bull. Seismol. Soc. Amer. 101(2): 792-804.

Sigfusdottir, T., 2013, A Sedimentological and Stratigraphical Study of Veiki Moraine in Northernmost Sweden. Dissertations in Geology at Lund University.

SKB, 2011, Long-term safety for the final repository for spent nuclear fuel at Forsmark. Svensk Kärnbränslehantering AB (SKB); [SKB TR-11, 3 volumes].

Smith, C. A., Sundh, M. and Mikko, H., 2014, Surficial geology indicates early Holocene faulting and seismicity, central Sweden. International Journal of Earth Sciences, 103(6), 1711–1724, doi.org/10.1007/s00531-014-1025-6.

Smith, C. A., Grigull, S. and Mikko, H., 2018, Geomorphic evidence of multiple surface ruptures of the Merasjärvi “postglacial fault”, northern Sweden. GFF, 140(4), 318–322, doi.org/10.1080/11035897.2018.1492963.

Smith, C.A., Ojala, A., Grigull, S. and Mikko, H., 2022a, Dating of Postglacial Faults in Fennoscandia, Chapter 8 *in* Steffen, H., Olesen, O. and Sutinen, R. (eds.), 2022, Glacially-Triggered Faulting: Cambridge Univ. Press, Cambridge, UK, p. 133-150.

Smith, C.A., Mikko, H., and Grigull, S., 2022b, Glacially Induced Faults in Sweden: The Rise and Reassessment of the Single-Rupture Hypothesis, Chapter 12 in Steffen, H., Olesen, O. and Sutinen, R. (eds.), 2022, Glacially-Triggered Faulting: Cambridge Univ. Press, Cambridge, UK, p. 218-230.

Stanfors, R. and Ericsson, L.O., 1993, Post-glacial faulting in the Lansjärv area, Northern Sweden; Comments from the expert group on a field visit at the Molberget post-glacial fault area, 1991: SKB Technical Report 93-11, 93 p.

Stein, S., Liu, M., Calais, E. and Li, Q., 2009, Mid-continent earthquakes as a complex system, Seismol. Res. Lett., 80(4), 551–553.

Sun, T., Wang, K., Fujiwara, T, Kodaira, S. and He, J., 2017, Large fault slip peaking at trench in the 2011 Tohoku-oki earthquake. Nature Communications, vol. 8, article 14044.

Takao, M., J. Tsuchiyama, T. Annaka, and T. Kurita, 2013, Application of probabilistic fault displacement hazard analysis in Japan, J. Jpn. Assoc. Earthq. Eng. 13, 17–36, doi: 10.5610/jaee.13.17. (in Japanese)

Takao, M., K. Ueta, T. Annaka, T. Kurita, H. Nakase, T. Kyoya, and J. Kato, 2014, Reliability improvement of probabilistic fault displacement hazard analysis, J. Jpn. Assoc. Earthq. Eng. 14, 2_16–2_36, doi: 10.5610/jaee.14.2_16. (in Japanese)

Takao, M., T. Tani, T. Oshima, T. Annaka, and T. Kurita, 2016, Maximum likelihood estimation of the parameters regarding displacement evaluation of distributed fault in PFDHA, J. Jpn. Assoc. Earthq. Eng. 16, 2_96–2_101, doi: 10.5610/jaee.16.2_96. (in Japanese)

Torvela, T. and Ehlers, C., 2010, From ductile to brittle deformation: structural development and strain distribution along a crustal-scale shear zone in SW Finland. Int J Earth Sci (Geol Rundsch) (2010) 99:1133–1152; DOI 10.1007/s00531-009-0451-3.

Warage, A., 2007, Seismotectonics in central Sudan and local site effect in western Khartoum. M.S. thesis, Dept. of Earth Sci., Univ. of Bergen, Norway, 183 p.

Yoon, J.S., Stephansson, O. and Min, K.-B., 2014, Relation between earthquake magnitude, fracture length and fracture shear displacement in the KBS-3 repository at Forsmark; Main review phase. Stral Sakerhets Myndigheten (SSM) Report 2014-59, 220 p.

Yoon, J.S. and Zang, A., 2019, 3D thermo-mechanical coupled modelling of thermo-seismic response of a fractured rock mass related to the final disposal of spent nuclear fuel and nuclear waste in hard rock. Stral Sakerhets Myndigheten (SSM) Report 2019-15, Stockholm, Sweden, 105 p.

Youngs, R. R., Arabasz, W. J., Anderson, R. E., Ramelli, A. R., Ake, J. P., Slemmons, D. B., McCalpin, J. P., Doser, D. I., Fridrich, C. J., Swan III, F. H., Rogers, A. M., Yount, J. C., Anderson, L. W., Smith, K. D., Bruhn, R. L., Knuepfer, L. K., Smith, R. B., dePolo, C. M., O'Leary, D.W., Coppersmith, K. J., Pezzopane, S. K., Schwartz, D. P., Whitney, J.W., Olig, S. S., and Toro, G. R., 2003, A methodology for probabilistic fault displacement hazard analysis (PFDHA). Earthq. Spectra, 19, 191–219.

# Appendix A

Other surface ruptures in Australia, aside from Meckering (see Fig. 3-12)

10-MARCH-1970, Calingiri, Australia rupture (M5.03); King et al, 2019c

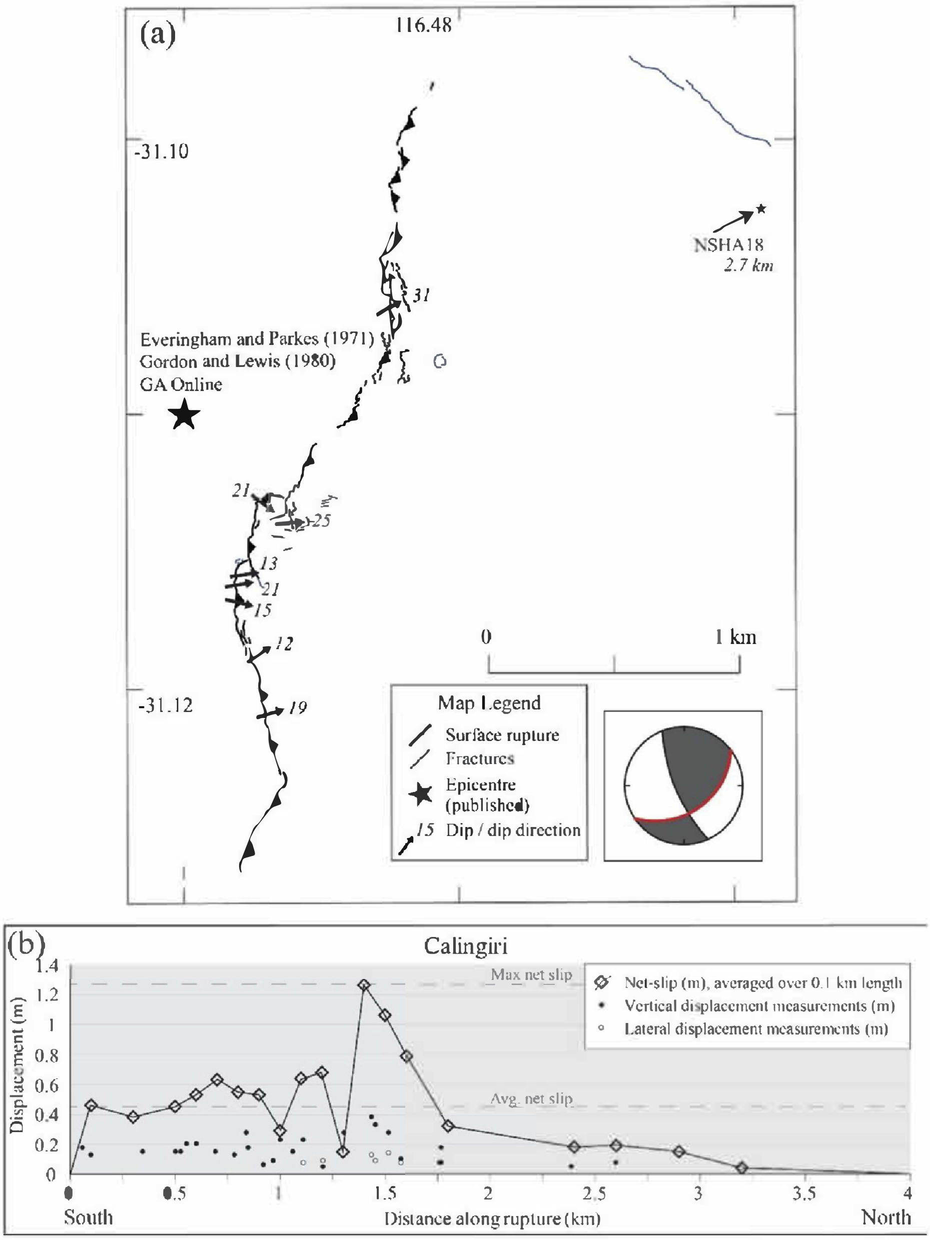

Figure A-1. 1970 Mw 5.0 Calingiri earthquake (a) rupture and fracture map of Calingiri (Gordon and Lewis, (1980)) showing published epicenter locations and dip measurements of scarp (Gordon and Lewis, (1980)), focal mechanism (red line shows preferred plane from original publication) from Fitch et al. (1973) (b) graph of along-rupture vertical and lateral displacement measurements (Gordon and Lewis, (1980)) and net slip calculated from available data averaged over 0.1 km increments (this study).

## 2-JUNE-1979, Cadoux, Australia rupture (M6.1); King et al., 2019d

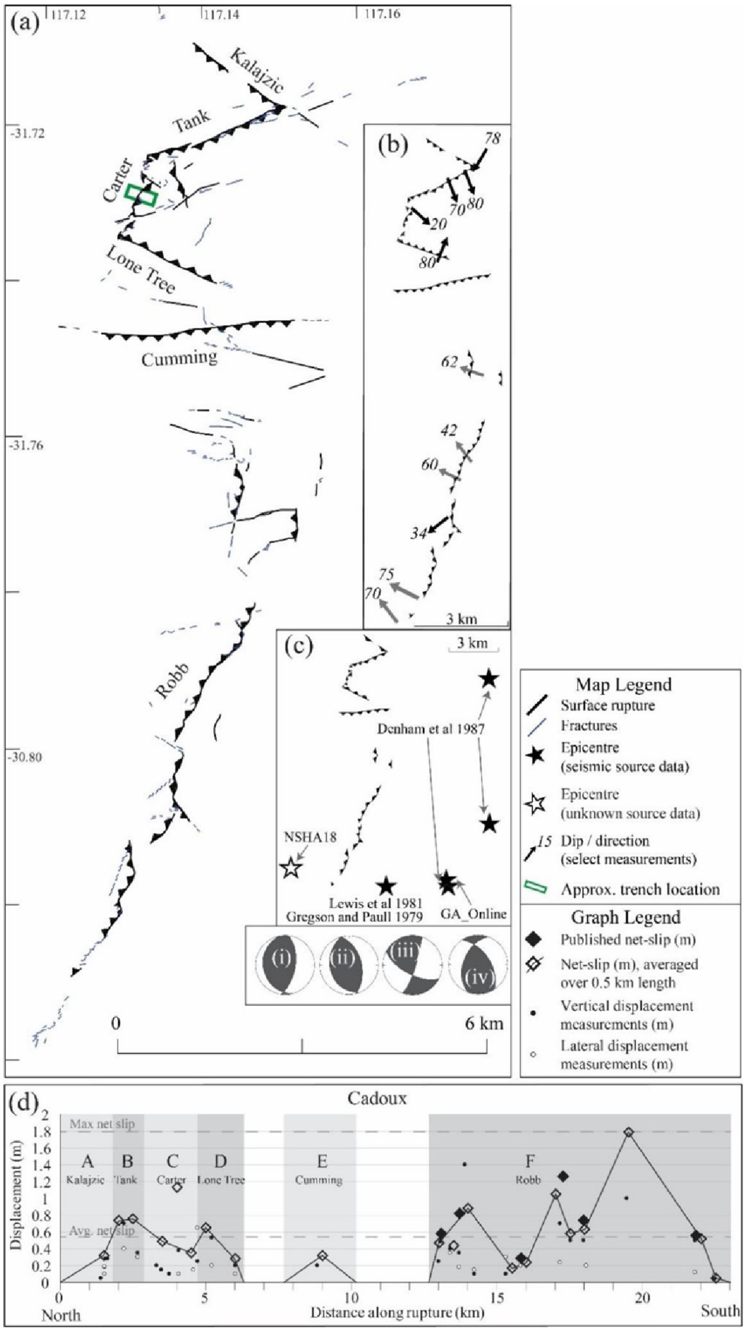

Figure A-2. 1979 Mw 6.1 Cadoux earthquake (a) rupture scarps and fracturing involved in the Cadoux rupture with named faults (Lewis et al., (1981)), focal mechanisms from (i) Denham et al. 1987 (ii) Fredrich et al. (1988) (iii) Everingham and Smith (unpublished, Lewis et al. (1981)) (iv) CMT (b) available dip measurements, black where directly measured and grey were calculated based on available displacement measurements (Lewis et al., (1981)) (c) published epicenter locations (d) graph along-rupture of vertical and lateral displacement measurements and calculated net slip (Lewis et al., (1981)) and net slip calculated from available data averaged over 0.5 km increments (King et al, 2019a).

## 30-MARCH-1986, Marryat Creek, Australia rupture (M5.7); King et al., 2019e

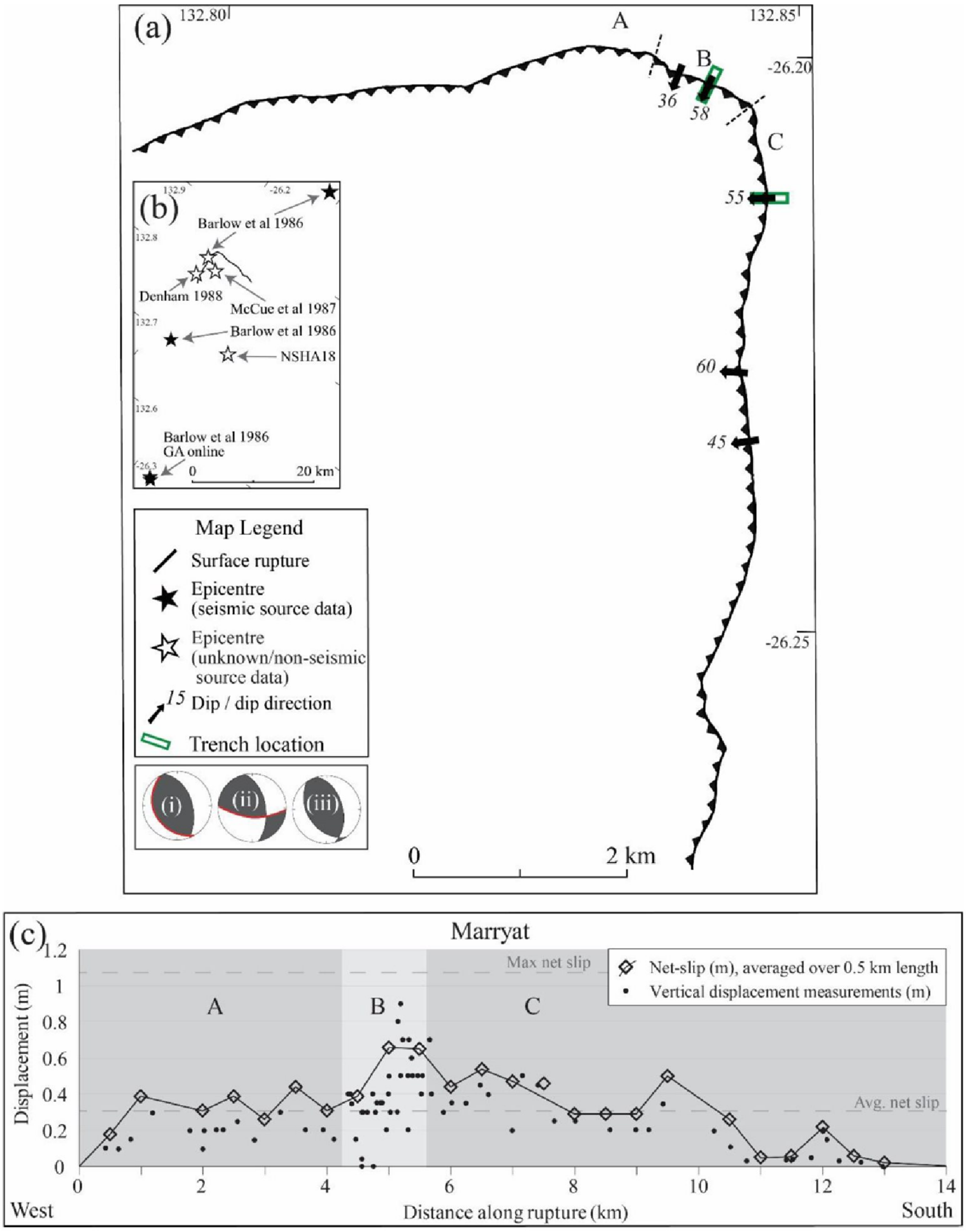

Figure A-3. 1986 Mw 5.7 Marryat Creek earthquake (a) rupture and fracture map of Marryat Creek scarp and available dip measurements (Bowman and Barlow, (1991); Machette et al., (1993)) with faults labelled as per displacement graphs, focal mechanisms (red line shows preferred plane from original publication) from (i) Fredrich et al. (1968), (ii) Barlow et al. (1986), (iii) CMT, trench location from (Machette et al., (1993)), (b) published epicenter locations, and (c) graph of along-rupture vertical and lateral displacement measurements (Bowman and Barlow, (1991)) and net slip calculated from available data averaged over 0.5 km increments (King, 2019).

## 22-JANUARY-1988, Tennant Creek (Kunayungk u), Australia; 3 ruptures of M6.27, 6.44, 6.58; King et al., 2019h

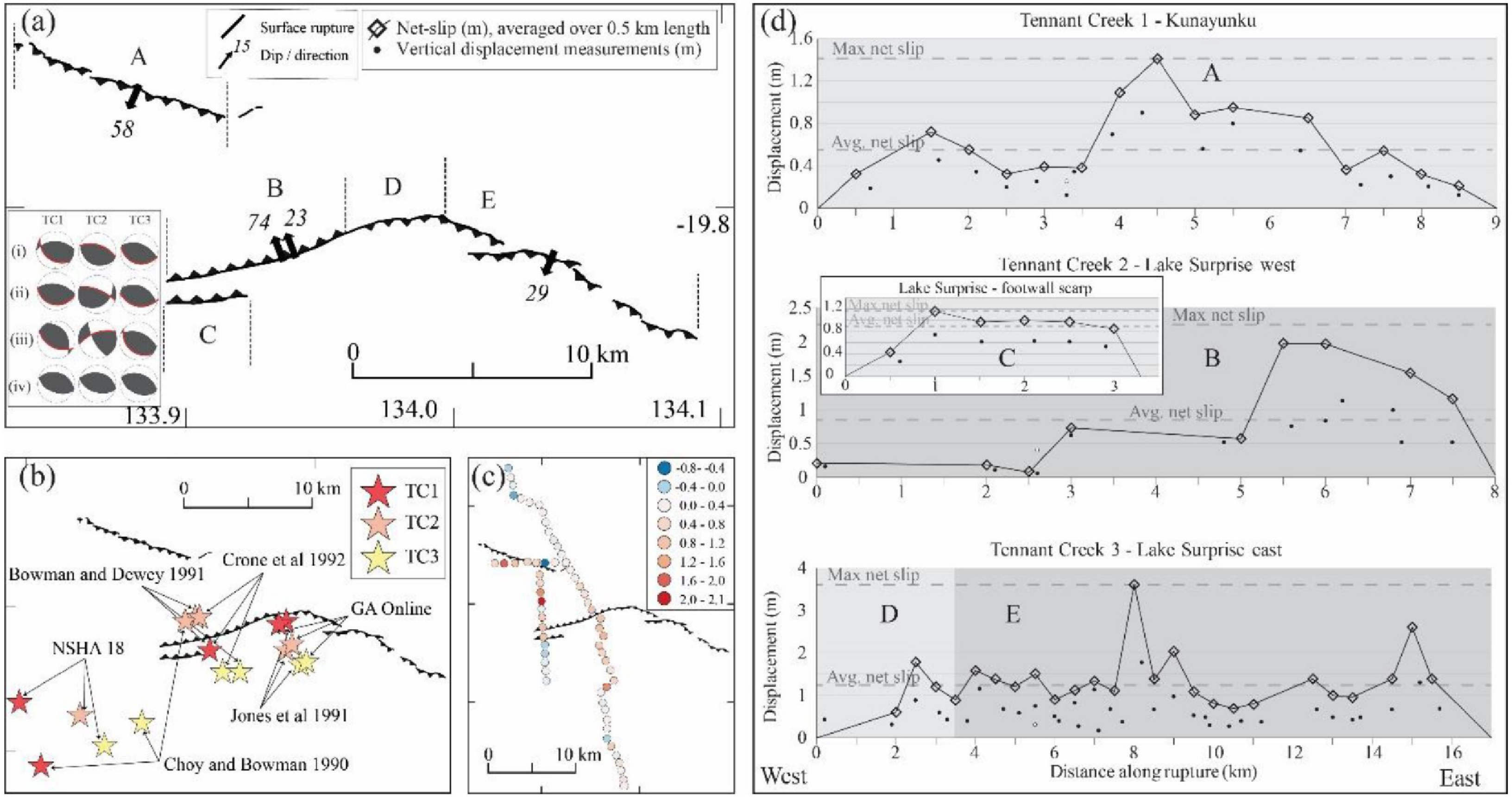

Figure A-4. 1988 Mw 6.3 (TC1), 6.4 (TC2) and 6.6 (TC3) Tennant Creek earthquakes (a) rupture and cracking map of Kunayungku and Lake Surprise scarps with available dip measurements also the locations of trenches from Crone et al. (1992) with faults labelled as per displacement graphs, focal mechanisms (red line shows preferred plane from original publication) from (i) McCaffrey (1989), (ii) Choy & Bowman (1990), (iii) Jones et al. (1991), (iv) CMT, (b) published epicenter locations of all three mainshocks (c) resurveyed benchmark offsets (Crone et al., (1992)) uncertainties as discussed in text, and (d) graphs of along-rupture vertical and lateral displacement measurements (Crone et al., (1992)) and net slip calculated from available data averaged over 0.5 km increments (King, 2019). NOTE: TC2 rupture is on a conjugate fault that dips in opposite direction from other two faults (Bowman, 1991, Geophys. J. Int.)

## 10-OCTOBER-2007, Katanning, Australia rupture (M4.7); King et al., 2019a

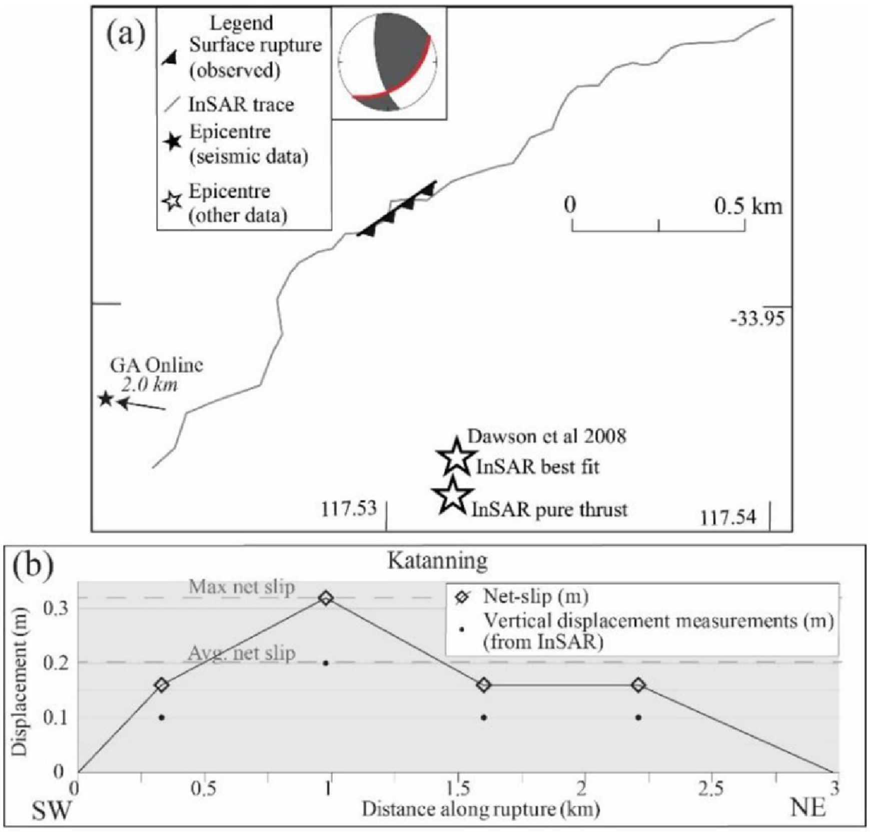

Figure A-5. 2008 Mw 4.7 Katanning earthquake (a) approximate visible rupture and InSAR trace (digitized from Dawson et al. (2008)), published epicenter locations and focal mechanism (Dawson et al., (2008)) (b) graph of along-rupture vertical and displacement taken from InSAR data (Dawson et al., (2008)) and net slip calculated from InSAR data (King, 2019).

## 23-MARCH-2012, Pukatja, Australia rupture (M5.18); King et al., 2019f

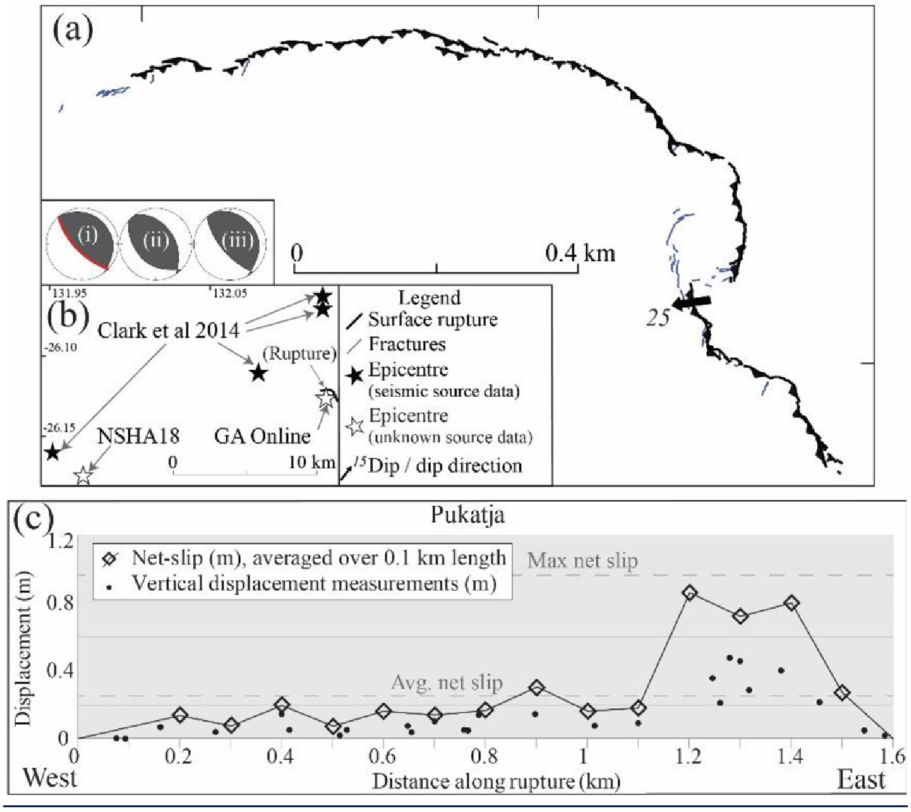

Figure A-6. 2012 Mw 5.2 Pukatja / Ernabella earthquake (a) rupture and fracture map of Pukatja scarp and available dip measurements also the location of hand-dug trench (Clark et al., (2014)), focal mechanisms as described in Clark et al. (2014) from (i) Clark et al. (2014), (ii) GCMT, (iii) St Louis University; (b) graph of along-rupture vertical displacement measurements (Clark et al., (2014)) and net slip calculated from available data averaged over 0.1 km increments (King, 2019a).

## 20-MAY-2016, Petermann, Australia rupture (M6.0); King et al., 2019g

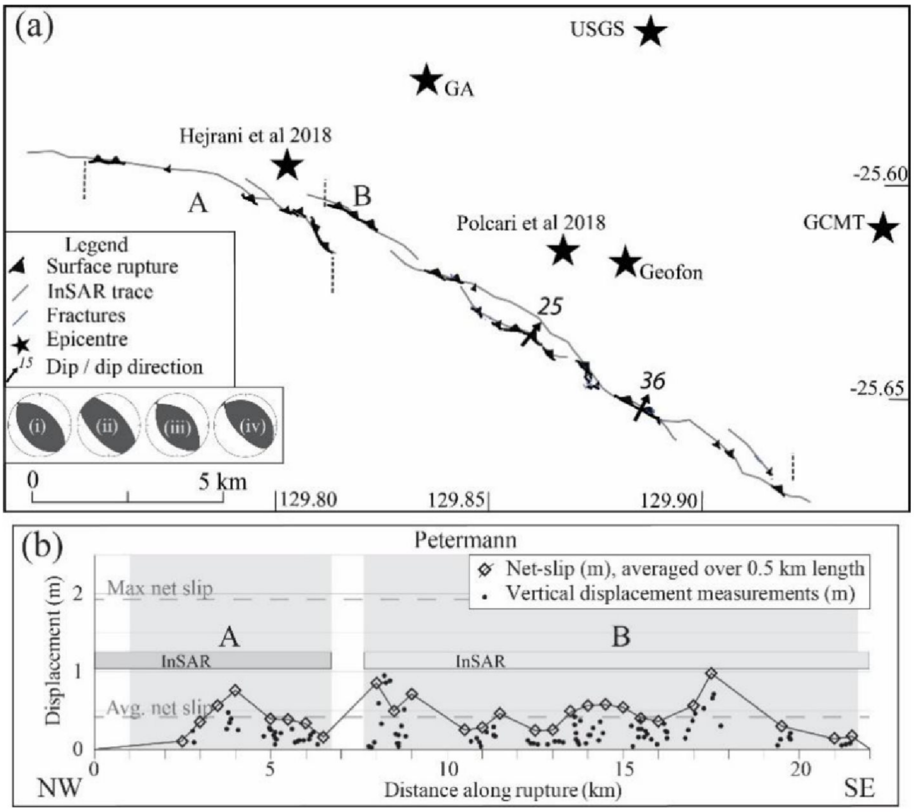

Figure A-7. 2016 Mw 6.1 Petermann earthquake rupture and fracture map of Petermann scarp (King et al., (2018)) showing published epicenter locations and dip measurements of rupture (also the location of hand-dug trenches), focal mechanisms (i–iii) as described in King et al. (2018), (i) USGS, (ii) GCMT, (iii) Geofon, and (iv) from Hejrani & Tkalcic (2018); (b) graph of along-rupture vertical displacement measurements and net slip calculated from available data averaged over 0.5 km increments.

# Appendix B

FIGURES describing the frequency of distributed faulting (DF) as a function of distance from the principal REVERSE fault (PF), based on the SURE 1.0 database.

Fig. B-1

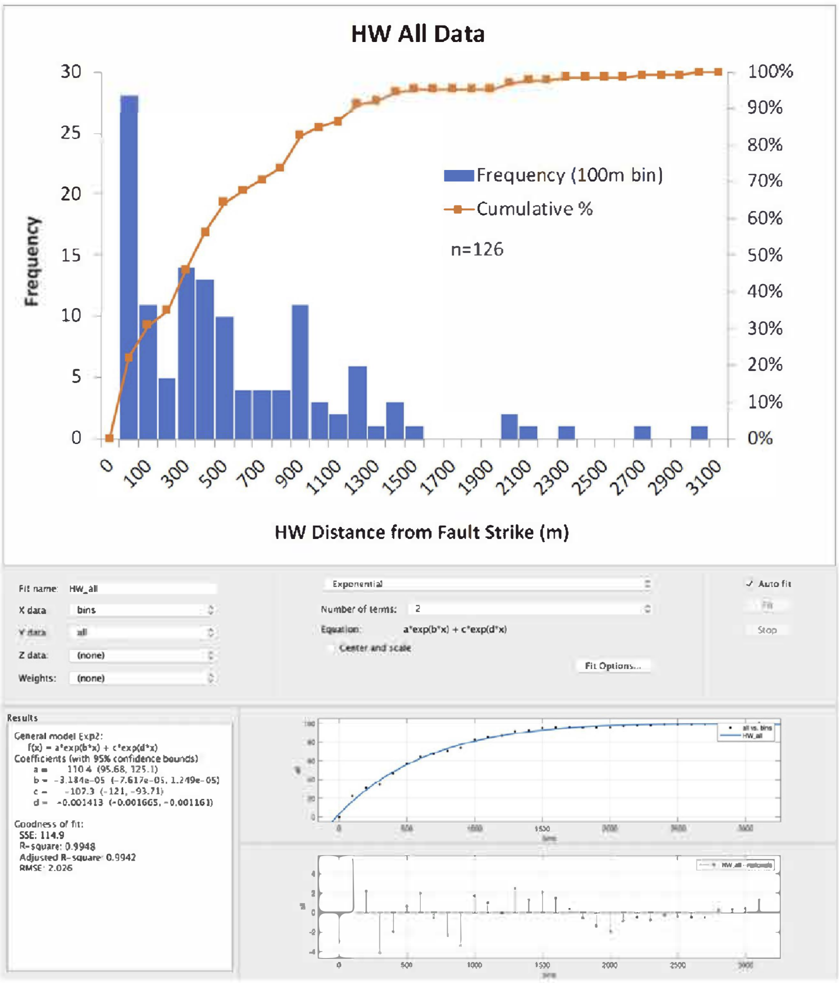

Fit name: HW_all
X data: bins
Y data: all
Z data: (none)
Weights: (none)

Exponential
Number of terms: 2
Equation: a*exp(b*x) + c*exp(d*x)

Results

```
General model Exp2:
    f(x) = a*exp(b*x) + c*exp(d*x)
Coefficients (with 95% confidence bounds)
       a =       110.4  (95.68, 125.1)
       b =  -3.184e-05  (-7.617e-05, 1.249e-05)
       c =      -107.3  (-121, -93.71)
       d =   -0.001413  (-0.001665, -0.001161)

Goodness of fit:
  SSE: 114.9
  R-square: 0.9948
  Adjusted R-square: 0.9942
  RMSE: 2.026
```

Fig. B-2.

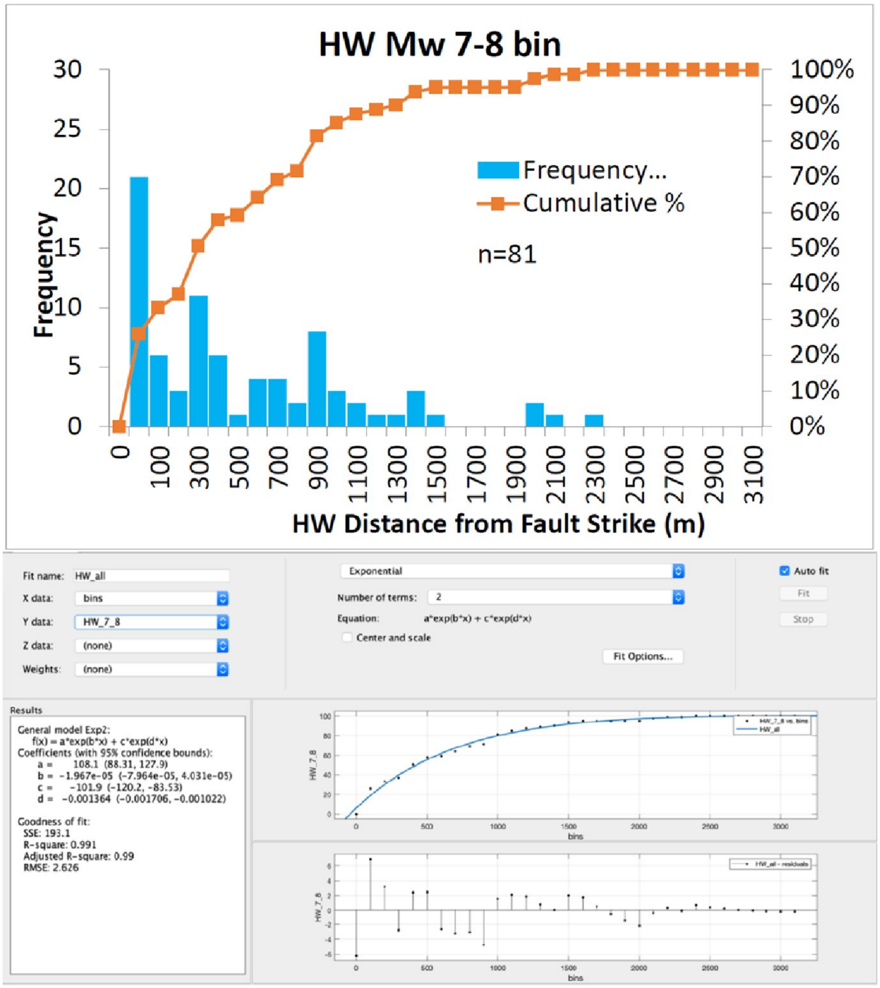

Fit name: HW_all
X data: bins
Y data: HW_7_8
Z data: (none)
Weights: (none)

Exponential
Number of terms: 2
Equation: a*exp(b*x) + c*exp(d*x)
☐ Center and scale
☑ Auto fit

Results

```
General model Exp2:
    f(x) = a*exp(b*x) + c*exp(d*x)
Coefficients (with 95% confidence bounds):
      a =       108.1  (88.31, 127.9)
      b =  -1.967e-05  (-7.964e-05, 4.031e-05)
      c =      -101.9  (-120.2, -83.53)
      d =   -0.001364  (-0.001706, -0.001022)

Goodness of fit:
  SSE: 193.1
  R-square: 0.991
  Adjusted R-square: 0.99
  RMSE: 2.626
```

Fig. B-3. (also used as an illustrative example in text, Fig. 3-23)

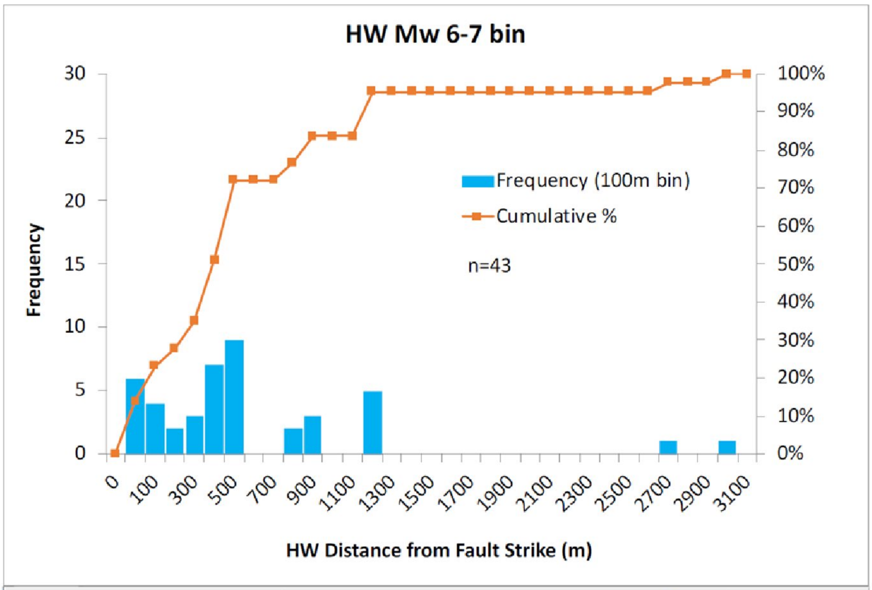

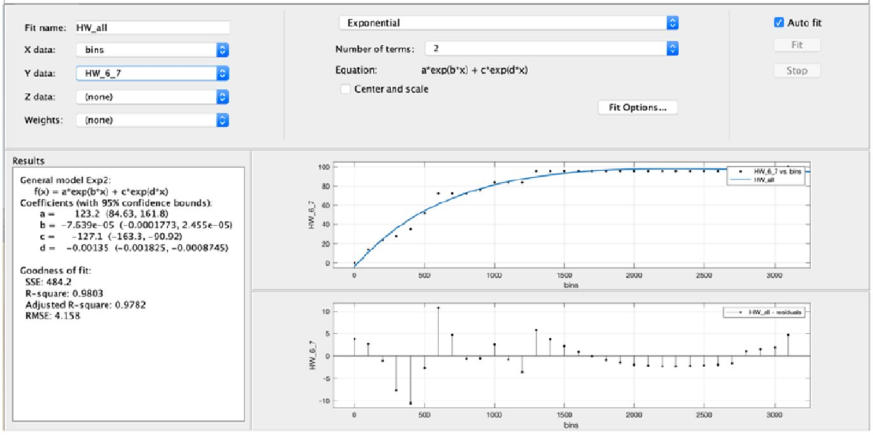

Fit name: HW_all
X data: bins
Y data: HW_6_7
Z data: (none)
Weights: (none)
Exponential
Number of terms: 2
Equation: a*exp(b*x) + c*exp(d*x)
☐ Center and scale
☑ Auto fit

Results

```
General model Exp2:
    f(x) = a*exp(b*x) + c*exp(d*x)
Coefficients (with 95% confidence bounds):
      a =       123.2  (84.63, 161.8)
      b =  -7.639e-05  (-0.0001773, 2.455e-05)
      c =      -127.1  (-163.3, -90.92)
      d =    -0.00135  (-0.001825, -0.0008745)

Goodness of fit:
  SSE: 484.2
  R-square: 0.9803
  Adjusted R-square: 0.9782
  RMSE: 4.158
```

Fig. B-4.

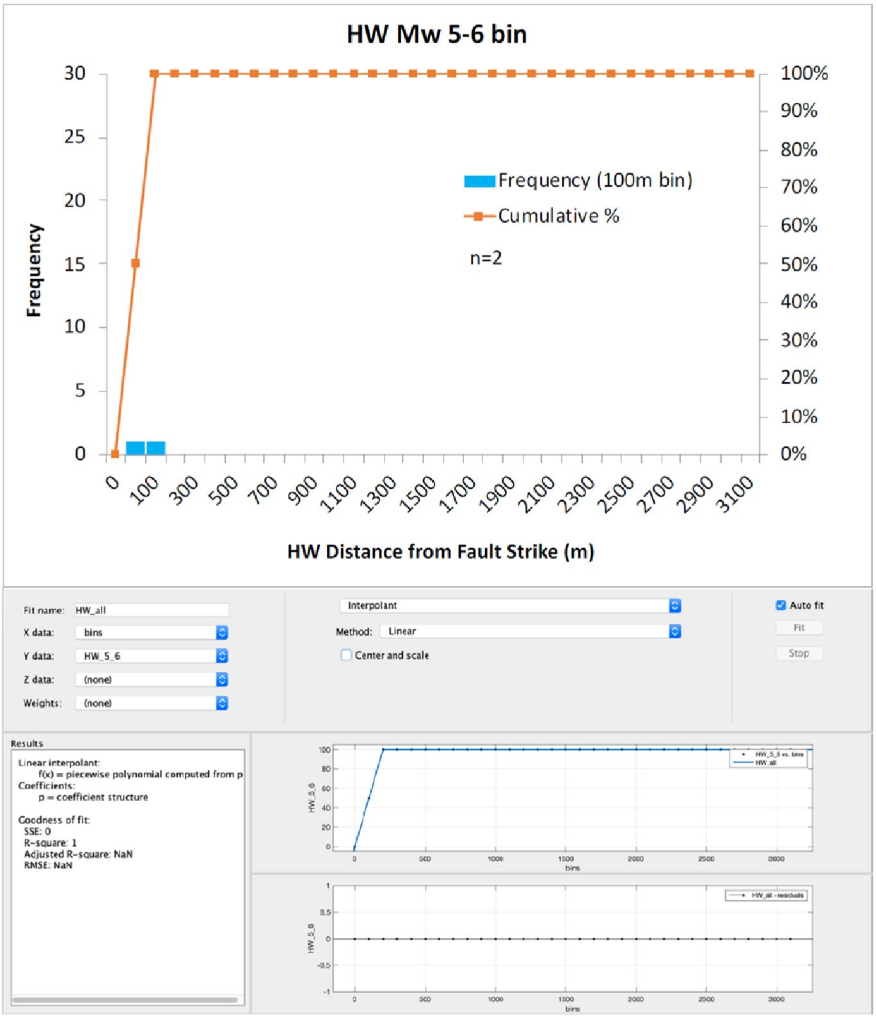

Fit name: HW_all
X data: bins
Y data: HW_5_6
Z data: (none)
Weights: (none)

Interpolant
Method: Linear
☐ Center and scale
☑ Auto fit

Results

```
Linear interpolant:
     f(x) = piecewise polynomial computed from p
Coefficients:
     p = coefficient structure

Goodness of fit:
  SSE: 0
  R-square: 1
  Adjusted R-square: NaN
  RMSE: NaN
```

Fig. B-5

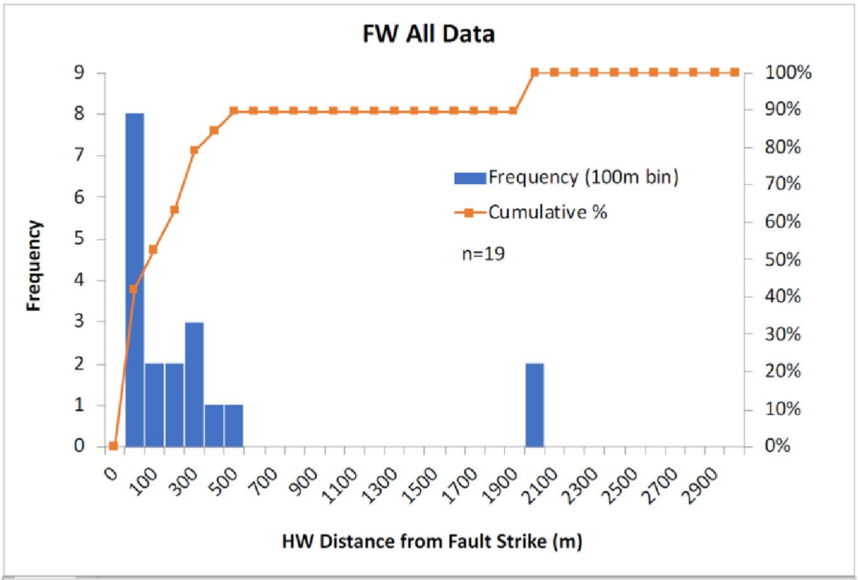

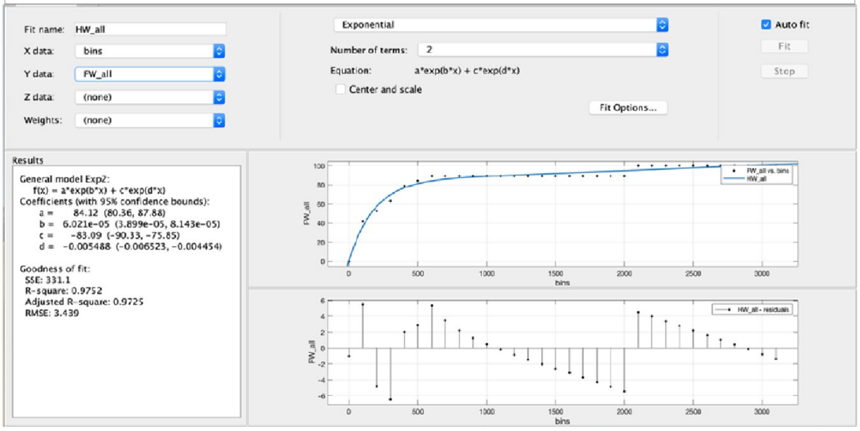

Fit name: HW_all
X data: bins
Y data: FW_all
Z data: (none)
Weights: (none)

Exponential
Number of terms: 2
Equation: a*exp(b*x) + c*exp(d*x)
☐ Center and scale

☑ Auto fit

Results

```
General model Exp2:
   f(x) = a*exp(b*x) + c*exp(d*x)
Coefficients (with 95% confidence bounds):
      a =       84.12  (80.36, 87.88)
      b =   6.021e-05  (3.899e-05, 8.143e-05)
      c =      -83.09  (-90.33, -75.85)
      d =   -0.005488  (-0.006523, -0.004454)

Goodness of fit:
  SSE: 331.1
  R-square: 0.9752
  Adjusted R-square: 0.9725
  RMSE: 3.439
```

# Appendix C

FIGURES describing the probability of distributed faulting (DF) as a function of distance from the principal REVERSE fault (PF), based on the FHDI database.

Fig. C-1

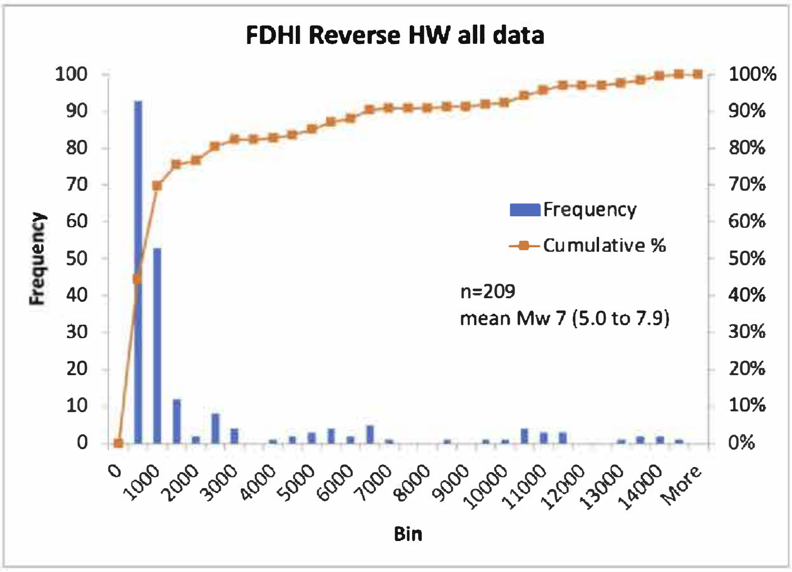

Fig. C-2

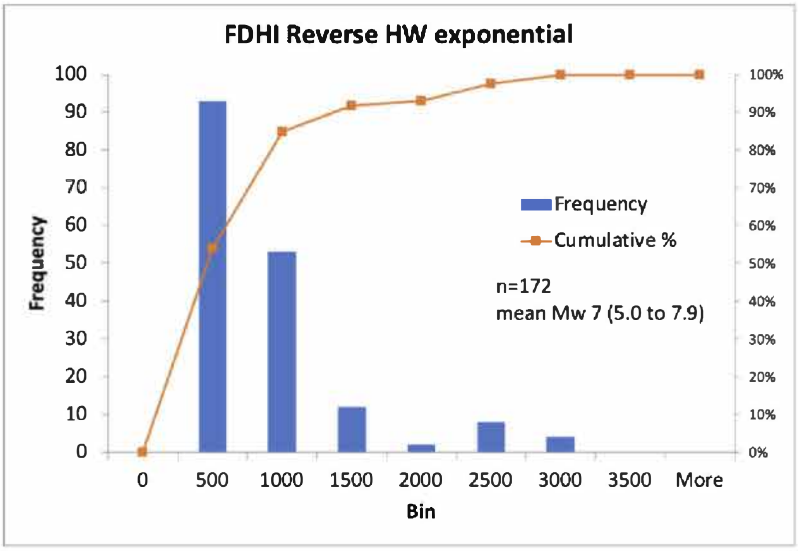

Fig. C-3

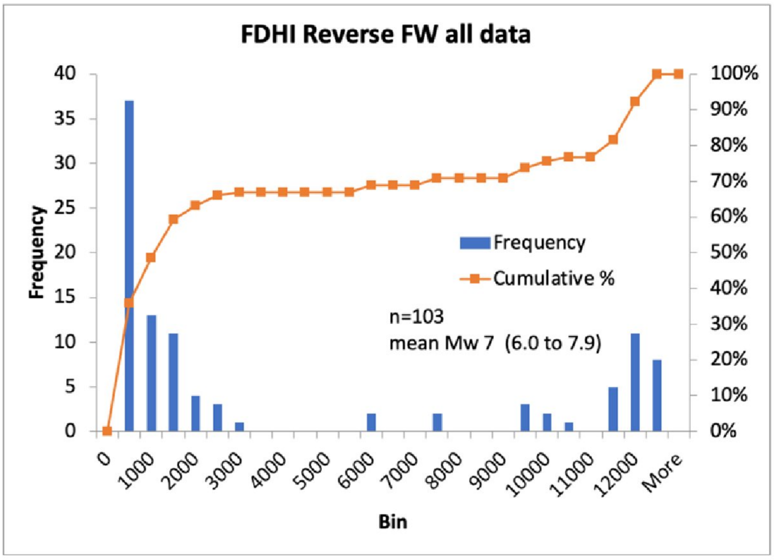
FDHI Reverse FW all data
Frequency
Cumulative %
n=103
mean Mw 7 (6.0 to 7.9)
Frequency
Bin
0
5
10
15
20
25
30
35
40
0%
10%
20%
30%
40%
50%
60%
70%
80%
90%
100%
0
1000
2000
3000
4000
5000
6000
7000
8000
9000
10000
11000
12000
More

Fig. C-4

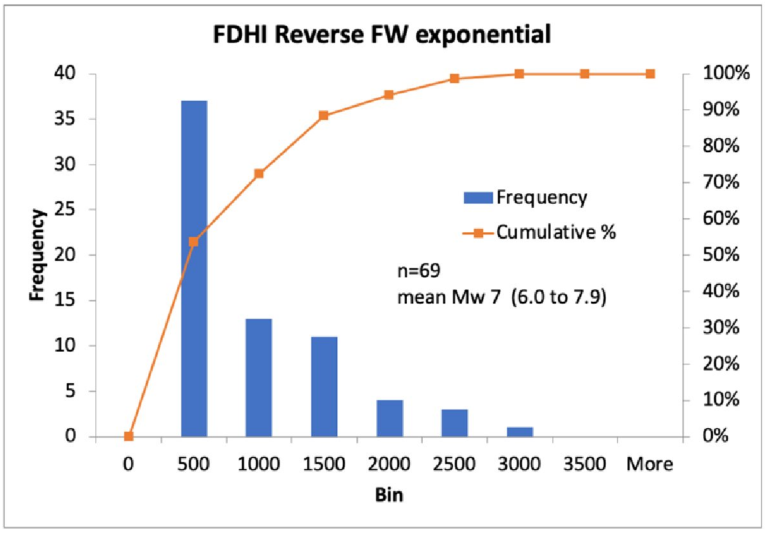
FDHI Reverse FW exponential
Frequency
Cumulative %
n=69
mean Mw 7 (6.0 to 7.9)
Frequency
Bin
0
5
10
15
20
25
30
35
40
0%
10%
20%
30%
40%
50%
60%
70%
80%
90%
100%
0
500
1000
1500
2000
2500
3000
3500
More

Fig. C-5

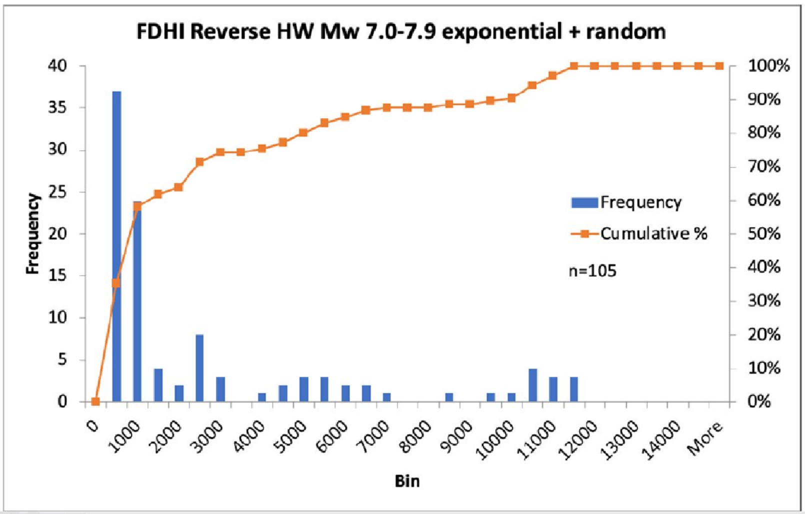

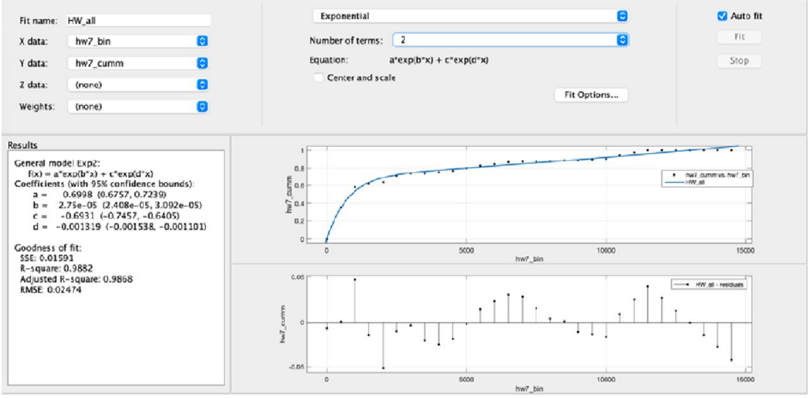

Fit name: HW_all
X data: hw7_bin
Y data: hw7_cumm
Z data: (none)
Weights: (none)
Exponential
Number of terms: 2
Equation: a*exp(b*x) + c*exp(d*x)
☐ Center and scale
☑ Auto fit

Results

```
General model Exp2:
    f(x) = a*exp(b*x) + c*exp(d*x)
Coefficients (with 95% confidence bounds):
      a =      0.6998  (0.6757, 0.7239)
      b =    2.75e-05  (2.408e-05, 3.092e-05)
      c =     -0.6931  (-0.7457, -0.6405)
      d =   -0.001319  (-0.001538, -0.001101)

Goodness of fit:
  SSE: 0.01591
  R-square: 0.9882
  Adjusted R-square: 0.9868
  RMSE: 0.02474
```

Fig. C-6

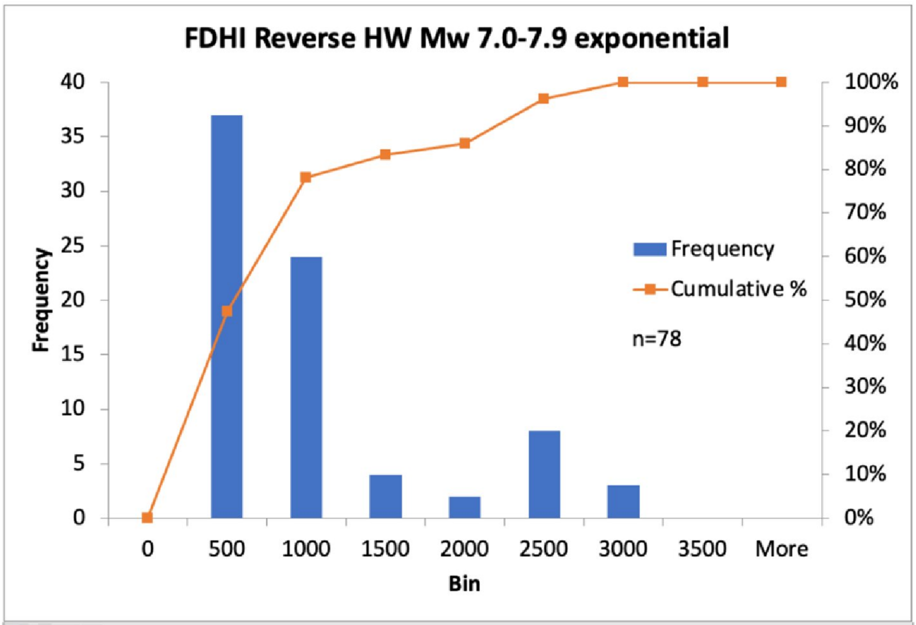

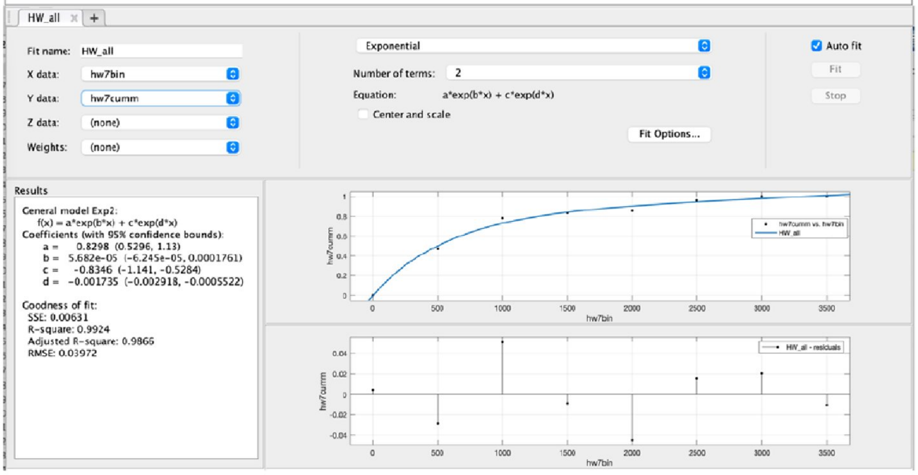

Fit name: HW_all
X data: hw7bin
Y data: hw7cumm
Z data: (none)
Weights: (none)

Exponential
Number of terms: 2
Equation: a*exp(b*x) + c*exp(d*x)
☐ Center and scale
☑ Auto fit

```
General model Exp2:
    f(x) = a*exp(b*x) + c*exp(d*x)
Coefficients (with 95% confidence bounds):
      a =      0.8298  (0.5296, 1.13)
      b =   5.682e-05  (-6.245e-05, 0.0001761)
      c =     -0.8346  (-1.141, -0.5284)
      d =   -0.001735  (-0.002918, -0.0005522)

Goodness of fit:
  SSE: 0.00631
  R-square: 0.9924
  Adjusted R-square: 0.9866
  RMSE: 0.03972
```

Fig. C-7

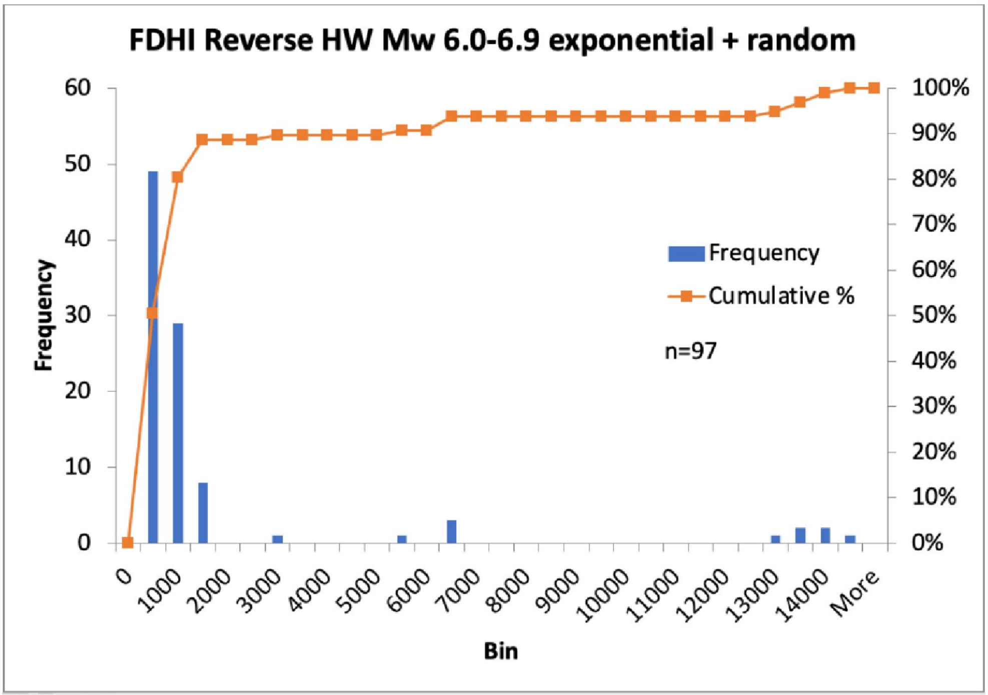

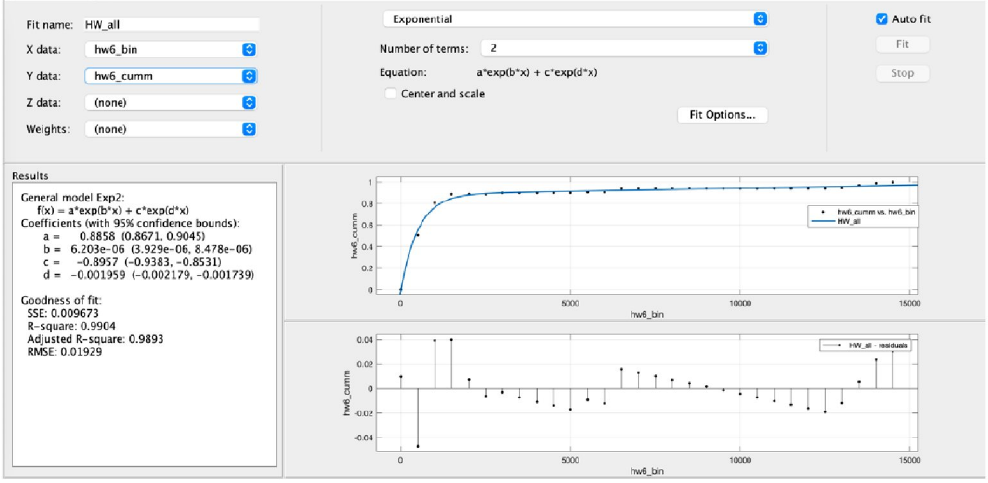

Fit name: HW_all
X data: hw6_bin
Y data: hw6_cumm
Z data: (none)
Weights: (none)

Exponential
Number of terms: 2
Equation: a*exp(b*x) + c*exp(d*x)
☐ Center and scale
☑ Auto fit

Results

```
General model Exp2:
    f(x) = a*exp(b*x) + c*exp(d*x)
Coefficients (with 95% confidence bounds):
      a =      0.8858  (0.8671, 0.9045)
      b =   6.203e-06  (3.929e-06, 8.478e-06)
      c =     -0.8957  (-0.9383, -0.8531)
      d =   -0.001959  (-0.002179, -0.001739)

Goodness of fit:
  SSE: 0.009673
  R-square: 0.9904
  Adjusted R-square: 0.9893
  RMSE: 0.01929
```

Fig. C-8

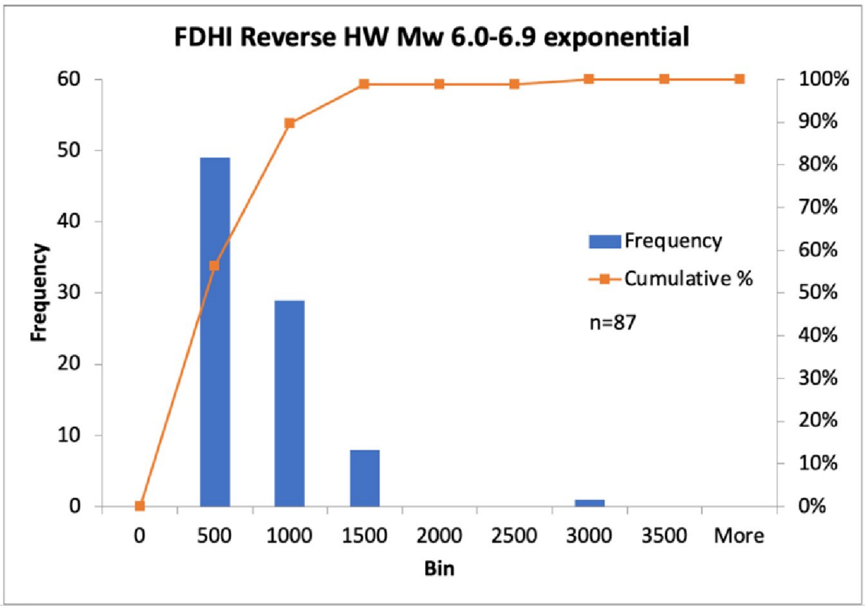

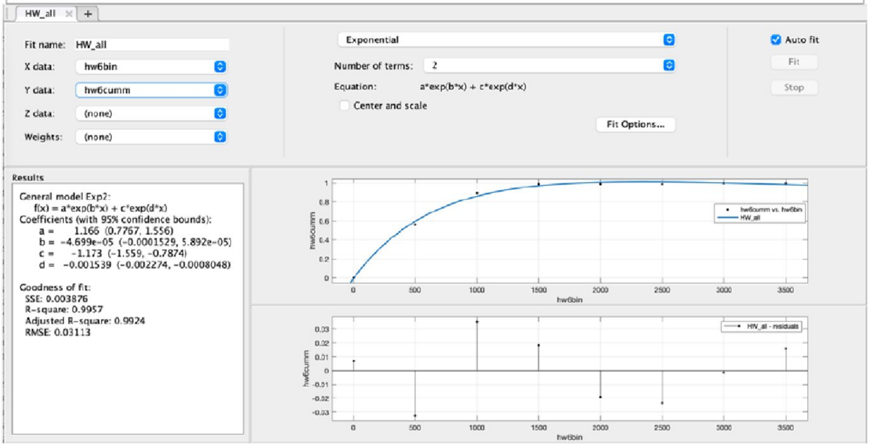

Fit name: HW_all
X data: hw6bin
Y data: hw6cumm
Z data: (none)
Weights: (none)

Exponential
Number of terms: 2
Equation: a*exp(b*x) + c*exp(d*x)
☐ Center and scale
☑ Auto fit

Results

```
General model Exp2:
    f(x) = a*exp(b*x) + c*exp(d*x)
Coefficients (with 95% confidence bounds):
      a =       1.166  (0.7767, 1.556)
      b =  -4.699e-05  (-0.0001529, 5.892e-05)
      c =      -1.173  (-1.559, -0.7874)
      d =   -0.001539  (-0.002274, -0.0008048)

Goodness of fit:
  SSE: 0.003876
  R-square: 0.9957
  Adjusted R-square: 0.9924
  RMSE: 0.03113
```

Fig. C-9

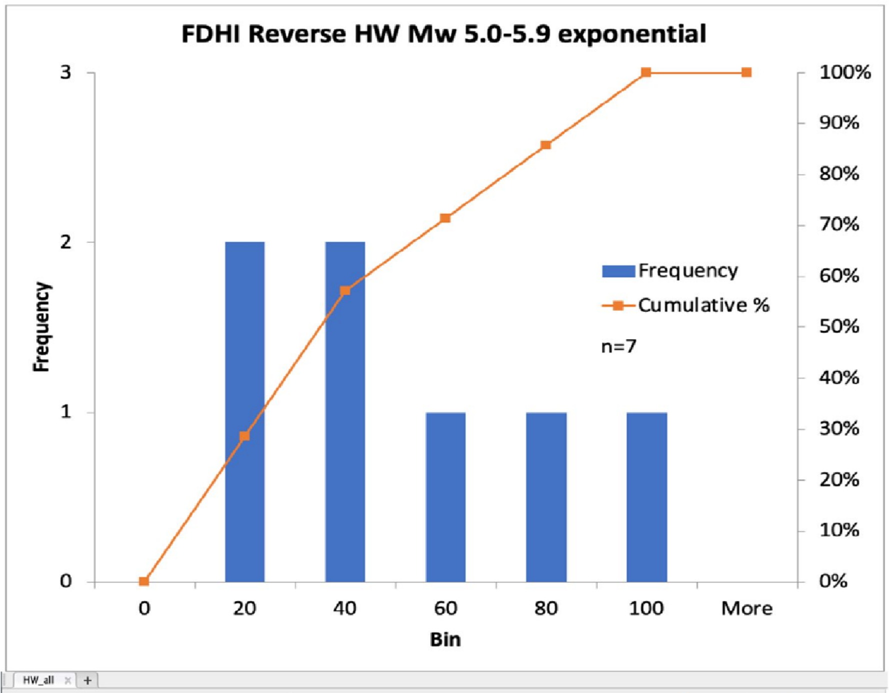

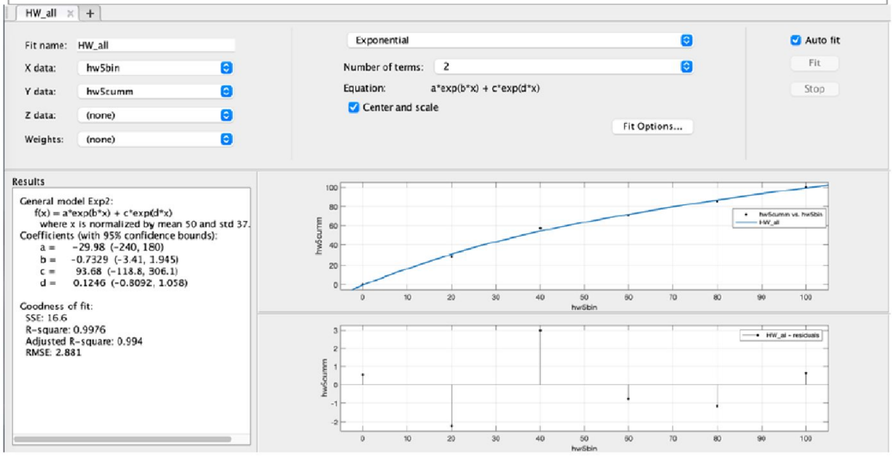

Fit name: HW_all
X data: hw5bin
Y data: hw5cumm
Z data: (none)
Weights: (none)

Exponential
Number of terms: 2
Equation: a*exp(b*x) + c*exp(d*x)
☑ Center and scale
☑ Auto fit

Results

```
General model Exp2:
   f(x) = a*exp(b*x) + c*exp(d*x)
     where x is normalized by mean 50 and std 37.
Coefficients (with 95% confidence bounds):
     a =     -29.98  (-240, 180)
     b =    -0.7329  (-3.41, 1.945)
     c =      93.68  (-118.8, 306.1)
     d =     0.1246  (-0.8092, 1.058)

Goodness of fit:
  SSE: 16.6
  R-square: 0.9976
  Adjusted R-square: 0.994
  RMSE: 2.881
```

Fig. C-10

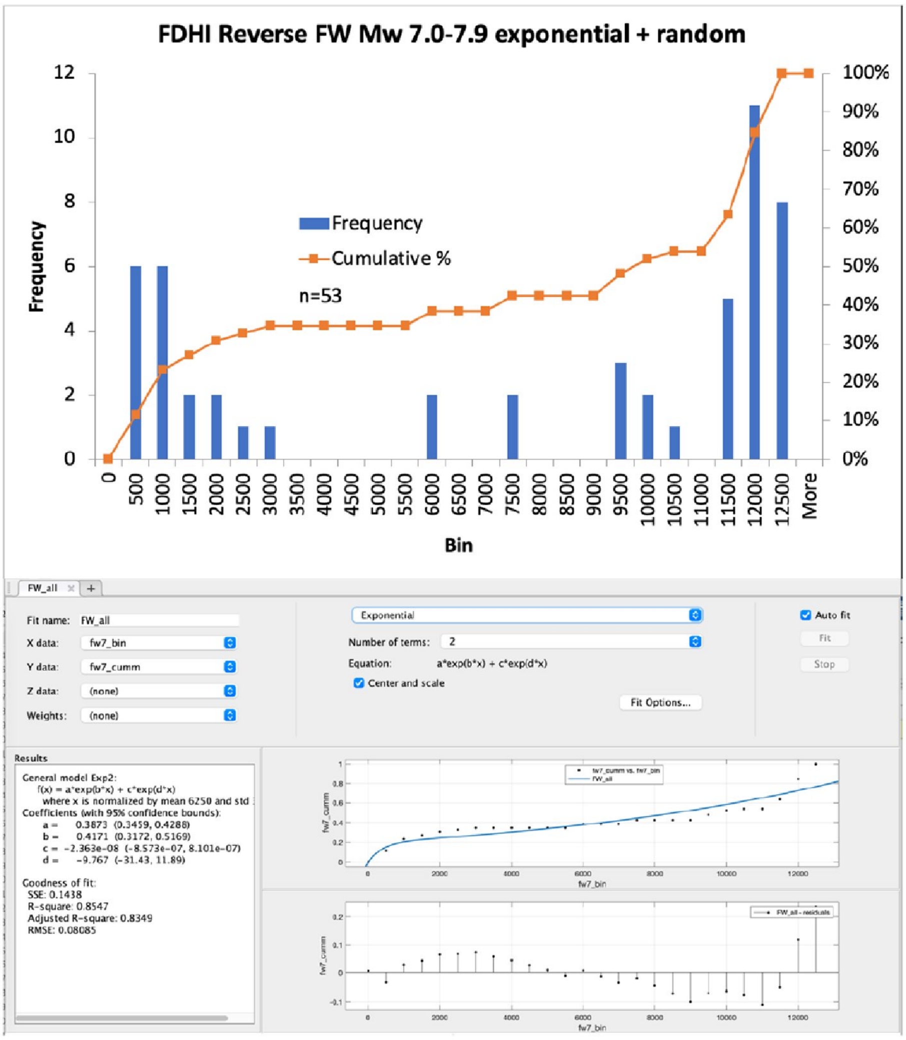

Fit name: FW_all
X data: fw7_bin
Y data: fw7_cumm
Z data: (none)
Weights: (none)

Exponential
Number of terms: 2
Equation: a*exp(b*x) + c*exp(d*x)
☑ Center and scale
☑ Auto fit

Results

```
General model Exp2:
    f(x) = a*exp(b*x) + c*exp(d*x)
      where x is normalized by mean 6250 and std
Coefficients (with 95% confidence bounds):
      a =      0.3873  (0.3459, 0.4288)
      b =      0.4171  (0.3172, 0.5169)
      c =  -2.363e-08  (-8.573e-07, 8.101e-07)
      d =      -9.767  (-31.43, 11.89)

Goodness of fit:
  SSE: 0.1438
  R-square: 0.8547
  Adjusted R-square: 0.8349
  RMSE: 0.08085
```

Fig. C-11

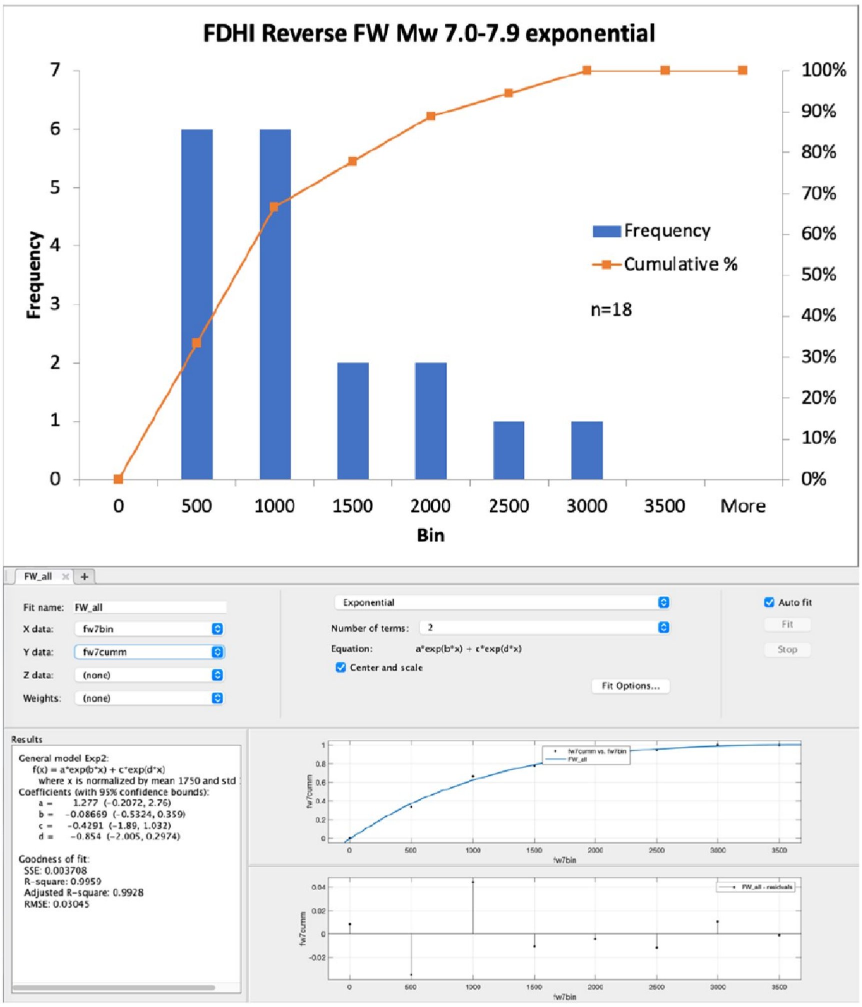

Fit name: FW_all
X data: fw7bin
Y data: fw7cumm
Z data: (none)
Weights: (none)

Exponential
Number of terms: 2
Equation: a*exp(b*x) + c*exp(d*x)
☑ Center and scale

Results

```
General model Exp2:
    f(x) = a*exp(b*x) + c*exp(d*x)
      where x is normalized by mean 1750 and std
Coefficients (with 95% confidence bounds):
      a =       1.277  (-0.2072, 2.76)
      b =    -0.08669  (-0.5324, 0.359)
      c =     -0.4291  (-1.89, 1.032)
      d =      -0.854  (-2.005, 0.2974)

Goodness of fit:
  SSE: 0.003708
  R-square: 0.9959
  Adjusted R-square: 0.9928
  RMSE: 0.03045
```

Fig. C-12

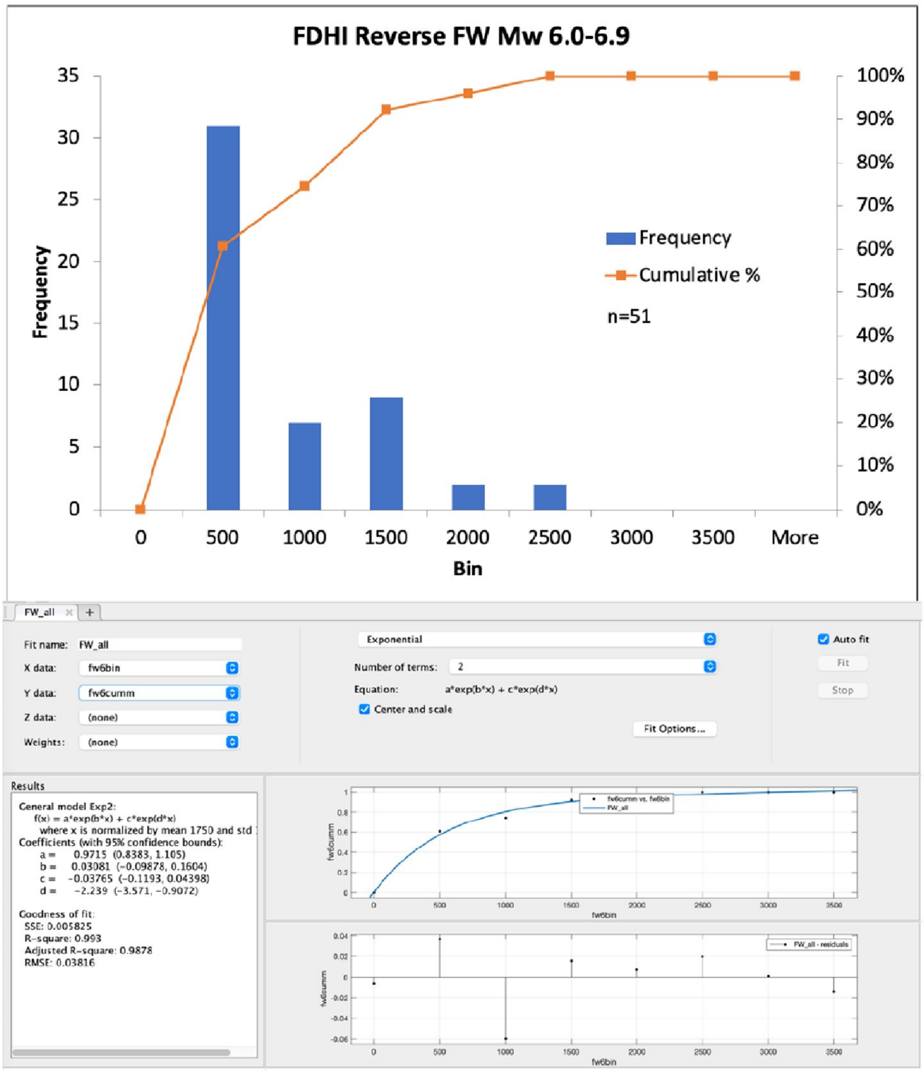

Fit name: FW_all

X data: fw6bin

Y data: fw6cumm

Z data: (none)

Weights: (none)

Exponential

Number of terms: 2

Equation: a*exp(b*x) + c*exp(d*x)

☑ Center and scale

☑ Auto fit

Results

```
General model Exp2:
    f(x) = a*exp(b*x) + c*exp(d*x)
      where x is normalized by mean 1750 and std
Coefficients (with 95% confidence bounds):
      a =      0.9715  (0.8383, 1.105)
      b =     0.03081  (-0.09878, 0.1604)
      c =    -0.03765  (-0.1193, 0.04398)
      d =      -2.239  (-3.571, -0.9072)

Goodness of fit:
  SSE: 0.005825
  R-square: 0.993
  Adjusted R-square: 0.9878
  RMSE: 0.03816
```

# Appendix D

from file ”*spreadsheet for Nurminen equation 6 Falth 2015 M56 INPUT.xls*”

DISTRIBUTED FAULTING VERTICAL DISPLACEMENTS (Y, in m) PREDICTED BY NURMINEN ET AL (2020, simple ruptures) AT VARIOUS DISTANCES (s, in m)

AWAY FROM THE PRINCIPAL REVERSE FAULT on the FW. Red cells indicate predicted vertical displacement > 5 cm (0.05 m)

**D1: M5.6 earthquake on fault ZFMA2 (Repository is on FW of ZFMA2); Assuming Dn equals Falth et al. (2015) Davg=0.97 m OR Dmax=1.7 m**

Using the absurd Dmax and Davg of Falth et al 2015

**Nurm. All simple ruptures**

| sigma | |
|---|---|
| FW | 0.8812 |

**Falth and Hokmark 2015 give example of M5.6 EQ on ZFMA2 FW and HW**

**FW, Davg= 0.97 m**

INPUTS for M5.6 on example fault

| | | | | | | | | | OUTPUTS | Y=vd | ln(Y) | | ln(Y) | | ln(Y) | | ln(Y) | |
|---|---|---|---|---|---|---|---|---|---|---|---|---|---|---|---|---|---|---|
| | | | | | | | | | ln(Y) | Y (m) | med. Plus | | med. Plus | | med. Minus | | med. Minus | |
| a | b1 | s | ln(s) | c1 | Dn | ln(Dn) | d1 | m | | | 1 sigma | Y (m) | 2 sigma | Y (m) | 1 sigma | Y (m) | 2 sigma | Y (m) |
| -5.1043 | -0.6483 | 200.00 | 5.30 | 0.1983 | 0.97 | -0.03 | 0.9461 | 5.60 | -3.2471 | 0.0389 | -2.3659 | 0.0939 | -1.4847 | 0.2266 | -4.1283 | 0.0161 | -5.0095 | 0.0067 |
| -5.1043 | -0.6483 | 400.00 | 5.99 | 0.1983 | 0.97 | -0.03 | 0.9461 | 5.60 | -3.6964 | 0.0248 | -2.8152 | 0.0599 | -1.9340 | 0.1446 | -4.5776 | 0.0103 | -5.4588 | 0.0043 |
| -5.1043 | -0.6483 | 600.00 | 6.40 | 0.1983 | 0.97 | -0.03 | 0.9461 | 5.60 | -3.9593 | 0.0191 | -3.0781 | 0.0460 | -2.1969 | 0.1111 | -4.8405 | 0.0079 | -5.7217 | 0.0033 |
| -5.1043 | -0.6483 | 1200.00 | 7.09 | 0.1983 | 0.97 | -0.03 | 0.9461 | 5.60 | -4.4087 | 0.0122 | | | | | | | | |
| -5.1043 | -0.6483 | 1400.00 | 7.24 | 0.1983 | 0.97 | -0.03 | 0.9461 | 5.60 | -4.5086 | 0.0110 | | | | | | | | |

**FW, Dmax= 1.7 m**

INPUTS for M5.6 on example

| | | | | | | | | | OUTPUTS | Y=vd | | | | | | | | |
|---|---|---|---|---|---|---|---|---|---|---|---|---|---|---|---|---|---|---|
| | | | | | | | | | ln(Y) | Y (m) | | | | | | | | |
| a | b1 | s | ln(s) | c1 | Dn | ln(Dn) | d1 | m | | | | | | | | | | |
| -5.1043 | -0.6483 | 200.00 | 5.30 | 0.1983 | 1.70 | 0.53 | 0.9461 | 5.60 | -3.1358 | 0.0435 | -2.2546 | 0.1049 | -1.3734 | 0.2532 | -4.0170 | 0.0180 | -4.8982 | 0.0075 |
| -5.1043 | -0.6483 | 400.00 | 5.99 | 0.1983 | 1.70 | 0.53 | 0.9461 | 5.60 | -3.5852 | 0.0277 | -2.7040 | 0.0669 | -1.8228 | 0.1616 | -4.4664 | 0.0115 | -5.3476 | 0.0048 |
| -5.1043 | -0.6483 | 600.00 | 6.40 | 0.1983 | 1.70 | 0.53 | 0.9461 | 5.60 | -3.8480 | 0.0213 | -2.9668 | 0.0515 | -2.0856 | 0.1242 | -4.7292 | 0.0088 | -5.6104 | 0.0037 |
| -5.1043 | -0.6483 | 1200.00 | 7.09 | 0.1983 | 1.70 | 0.53 | 0.9461 | 5.60 | -4.2974 | 0.0136 | | | | | | | | |
| -5.1043 | -0.6483 | 1400.00 | 7.24 | 0.1983 | 1.70 | 0.53 | 0.9461 | 5.60 | -4.3973 | 0.0123 | | | | | | | | |

from file ”*spreadsheet for Nurminen equation 6 Falth 2015 M56 INPUT.xls*”

DISTRIBUTED FAULTING VERTICAL DISPLACEMENTS (Y, in m) PREDICTED BY NURMINEN ET AL (2020, simple ruptures) AT VARIOUS DISTANCES (s, in m) AWAY FROM THE PRINCIPAL REVERSE FAULT on the FW. Red cells indicate predicted vertical displacement > 5 cm (0.05 m)

**D2: M5.6 earthquake on fault ZFMA2 (Repository is on FW of ZFMA2); Assuming Dn equals W&C (1994) Davg=0.22 m OR Dmax=0.61 m**

Using the empirical Dmax and Davg for M5.6 from W&C94

**Nurm. All simple ruptures**

sigma FW 0.8812

**Falth and Hokmark 2015 give example of M5.6 EQ on ZFMA2 FW and HW**

**FW, Davg= 0.22 m**

INPUTS for M5.6 on example fault

| a | b1 | S (m) | ln(s) | c1 | Dn | ln(Dn) | d1 | m | OUTPUTS ln(Y) | Y=vd Y (m) | ln(Y) med. Plus 1 sigma | Y (m) | ln(Y) med. Plus 2 sigma | Y (m) | ln(Y) med. Minus 1 sigma | Y (m) | ln(Y) med. Minus 2 sigma | Y (m) |
|---|---|---|---|---|---|---|---|---|---|---|---|---|---|---|---|---|---|---|
| -5.1043 | -0.6483 | 200.00 | 5.30 | 0.1983 | 0.22 | -1.51 | 0.9461 | 5.60 | -3.5413 | 0.0290 | -2.6601 | 0.0699 | -1.7789 | 0.1688 | -4.4225 | 0.0120 | -5.3037 | 0.0050 |
| -5.1043 | -0.6483 | 400.00 | 5.99 | 0.1983 | 0.22 | -1.51 | 0.9461 | 5.60 | -3.9907 | 0.0185 | -3.1095 | 0.0446 | -2.2283 | 0.1077 | -4.8719 | 0.0077 | -5.7531 | 0.0032 |
| -5.1043 | -0.6483 | 600.00 | 6.40 | 0.1983 | 0.22 | -1.51 | 0.9461 | 5.60 | -4.2535 | 0.0142 | -3.3723 | 0.0343 | -2.4911 | 0.0828 | -5.1347 | 0.0059 | -6.0159 | 0.0024 |
| -5.1043 | -0.6483 | 1200.00 | 7.09 | 0.1983 | 0.22 | -1.51 | 0.9461 | 5.60 | -4.7029 | 0.0091 | | | | | | | | |
| -5.1043 | -0.6483 | 1400.00 | 7.24 | 0.1983 | 0.22 | -1.51 | 0.9461 | 5.60 | -4.8028 | 0.0082 | | | | | | | | |

**FW, Dmax= 0.61 m**

INPUTS for M5.6 on example

| a | b1 | s | ln(s) | c1 | Dn | ln(Dn) | d1 | m | OUTPUTS ln(Y) | Y=vd Y (m) | | | | | | | | |
|---|---|---|---|---|---|---|---|---|---|---|---|---|---|---|---|---|---|---|
| -5.1043 | -0.6483 | 200.00 | 5.30 | 0.1983 | 0.61 | -0.49 | 0.9461 | 5.60 | -3.3391 | 0.0355 | -2.4579 | 0.0856 | -1.5767 | 0.2067 | -4.2203 | 0.0147 | -5.1015 | 0.0061 |
| -5.1043 | -0.6483 | 400.00 | 5.99 | 0.1983 | 0.61 | -0.49 | 0.9461 | 5.60 | -3.7884 | 0.0226 | -2.9072 | 0.0546 | -2.0260 | 0.1319 | -4.6696 | 0.0094 | -5.5508 | 0.0039 |
| -5.1043 | -0.6483 | 600.00 | 6.40 | 0.1983 | 0.61 | -0.49 | 0.9461 | 5.60 | -4.0513 | 0.0174 | -3.1701 | 0.0420 | -2.2889 | 0.1014 | -4.9325 | 0.0072 | -5.8137 | 0.0030 |
| -5.1043 | -0.6483 | 1200.00 | 7.09 | 0.1983 | 0.61 | -0.49 | 0.9461 | 5.60 | -4.5007 | 0.0111 | | | | | | | | |
| -5.1043 | -0.6483 | 1400.00 | 7.24 | 0.1983 | 0.61 | -0.49 | 0.9461 | 5.60 | -4.6006 | 0.0100 | | | | | | | | |

from file ”*spreadsheet for Nurminen equation 6 Falth 2015 M56 INPUT.xls*”

DISTRIBUTED FAULTING VERTICAL DISPLACEMENTS (Y, in m) PREDICTED from SCR five-rupture Subset from FDHI, using a NURMINEN-style equation at VARIOUS DISTANCES (s, in m) AWAY FROM THE PRINCIPAL REVERSE FAULT on the FW. Red cells indicate predicted vertical displacement > 5 cm (0.05 m)

**D3: M5.6 earthquake on fault ZFMA2 (Repository is on FW of ZFMA2); Assuming Dn equals W&C (1994) Davg=0.22 m OR Dmax=0.61 m**

$\ln(Y) = a1 + (b1 * \ln(s)) + (c1 * (\ln DN)) + d1m$

$\ln(Y) = (-4.3070) + (-0.1852 * \ln(s)) + (0.3435 * (\ln DN)) + 0.6708m$

Using the empirical Dmax and Davg for M5.6 from W&C94 **Nurm. SCR subset** sigma FW 0.6719

**Falth and Hokmark 2015 give example of M5.6 EQ on ZFMA2 FW and HW**

**FW, Davg= 0.22 m**

INPUTS for M5.6 on example fault

| | | | | | | | | | OUTPUTS | Y=vd | ln(Y) | | ln(Y) | | ln(Y) | | ln(Y) | |
|---|---|---|---|---|---|---|---|---|---|---|---|---|---|---|---|---|---|---|
| | | | | | | | | | ln(Y) | Y (m) | med. Plus | | med. Plus | | med. Minus | | med. Minus | |
| a | b1 | s | ln(s) | c1 | Dn | ln(Dn) | d1 | m | | | 1 sigma | Y (m) | 2 sigma | Y (m) | 1 sigma | Y (m) | 2 sigma | Y (m) |
| -17.5973 | -0.0831 | 200.00 | 5.30 | -0.3999 | 0.22 | -1.51 | 2.5916 | 5.60 | -2.9191 | 0.0540 | -2.2472 | 0.1057 | -1.5753 | 0.2069 | -3.5910 | 0.0276 | -4.2629 | 0.0141 |
| -17.5973 | -0.0831 | 400.00 | 5.99 | -0.3999 | 0.22 | -1.51 | 2.5916 | 5.60 | -2.9767 | 0.0510 | -2.3048 | 0.0998 | -1.6329 | 0.1954 | -3.6486 | 0.0260 | -4.3205 | 0.0133 |
| -17.5973 | -0.0831 | 600.00 | 6.40 | -0.3999 | 0.22 | -1.51 | 2.5916 | 5.60 | -3.0104 | 0.0493 | -2.3385 | 0.0965 | -1.6666 | 0.1889 | -3.6823 | 0.0252 | -4.3542 | 0.0129 |
| -17.5973 | -0.0831 | 1200.00 | 7.09 | -0.3999 | 0.22 | -1.51 | 2.5916 | 5.60 | -3.0680 | 0.0465 | | | | | | | | |
| -17.5973 | -0.0831 | 1400.00 | 7.24 | -0.3999 | 0.22 | -1.51 | 2.5916 | 5.60 | -3.0808 | 0.0459 | | | | | | | | |

**FW, Dmax= 0.61 m**

INPUTS for M5.6 on example

| | | | | | | | | | OUTPUTS | Y=vd | | | | | | | | |
|---|---|---|---|---|---|---|---|---|---|---|---|---|---|---|---|---|---|---|
| | | | | | | | | | ln(Y) | Y (m) | | | | | | | | |
| a | b1 | s | ln(s) | c1 | Dn | ln(Dn) | d1 | m | | | | | | | | | | |
| -17.5973 | -0.0831 | 200.00 | 5.30 | -0.3999 | 0.61 | -0.49 | 2.5916 | 5.60 | -3.3270 | 0.0359 | -2.6551 | 0.0703 | -1.9832 | 0.1376 | -3.9989 | 0.0183 | -4.6708 | 0.0094 |
| -17.5973 | -0.0831 | 400.00 | 5.99 | -0.3999 | 0.61 | -0.49 | 2.5916 | 5.60 | -3.3846 | 0.0339 | -2.7127 | 0.0664 | -2.0408 | 0.1299 | -4.0565 | 0.0173 | -4.7284 | 0.0088 |
| -17.5973 | -0.0831 | 600.00 | 6.40 | -0.3999 | 0.61 | -0.49 | 2.5916 | 5.60 | -3.4183 | 0.0328 | -2.7464 | 0.0642 | -2.0745 | 0.1256 | -4.0902 | 0.0167 | -4.7621 | 0.0085 |
| -17.5973 | -0.0831 | 1200.00 | 7.09 | -0.3999 | 0.61 | -0.49 | 2.5916 | 5.60 | -3.4759 | 0.0309 | | | | | | | | |
| -17.5973 | -0.0831 | 1400.00 | 7.24 | -0.3999 | 0.61 | -0.49 | 2.5916 | 5.60 | -3.4887 | 0.0305 | | | | | | | | |

# Appendix E

**Moss et al (2002) method of computing ”d” (vertical distributed displacement) as a function of M (magnitude) and ”r” (distance from Principal Fault), for distances of 0 to 6.5 km from the PF. In this range ”d/MD” decreases exponentially away from the PF.**

**Case 4: M5.6 reverse fault earthquake, where repository is on FW.**

Note: the Moss equation (blue font) outputs the quantity d/MD (where MD= maximum displacement on principal fault). So calculating ”d” is a 3-step process. In Step 1 we calculate d/MD based on given distance ”r” of 200, 400, and 600 m (Columns 1-5). In Step 2 we compute MD given the earthquake magnitude 5.6, using the equation of Moss et al. 2022 (Column 7; MD values shown in Column 3). In step 3 we multiply the d/MD ratio (Column 5) by the MD value to compute ”d”. See text in Sec. 5.2.1.2.

Moss et al. 2022 Method of calculating "d" as a function of M and "r"

| Column number | 1 | 2 | 3 | 4 | 5 | 6 | log10MD=-2.5 + 0.415Mag |
|---|---|---|---|---|---|---|---|
| | Moss 2022 Equations fit to the footwall DF displacements are: | | | | | | Moss et al 2022 page 40 |
| | For $r\ from\ 0\ km\ to\ 6.5\ km$: | | | | | | |
| | $d/MD = 0.58 * exp(-0.26 * r)$ | | | **THIS YIELDS THE 95%-ile VALUE** | | | |
| Row number | EQ Mag. | log 10 MD | MD Moss 2022 | r (km) | d/MD | d | |
| 1 | 5.6 | -0.176 | 0.666806769 | 0.2 | 0.550610743 | 0.367151 | **uses Moss 2022 MD for M5.6** |
| 2 | 5.6 | -0.176 | 0.666806769 | 0.4 | 0.522710673 | 0.348547 | |
| 3 | 5.6 | -0.176 | 0.666806769 | 0.6 | 0.49622433 | 0.330886 | |
| | | | | SOLVE FOR the distance where "d" becomes <0.05m | | | |
| 4 | 5.6 | -0.176 | 0.666806769 | 7 | 0.093974936 | 0.062663 | |
| 5 | 5.6 | -0.176 | 0.666806769 | 7.5 | 0.082518962 | 0.055024 | |
| 6 | 5.6 | -0.176 | 0.666806769 | 7.8 | 0.076327104 | 0.050895 | |
| 7 | 5.6 | -0.176 | 0.666806769 | 8 | 0.072459523 | 0.048317 | |
| 8 | 5.6 | -0.176 | 0.666806769 | 9 | 0.05587003 | 0.037255 | |

| | | | | | | | |
|---|---|---|---|---|---|---|---|
| 9 | 5.6 | -0.176 | 0.666806769 | 10 | 0.043078675 | 0.028725 | |
| 10 | 5.6 | | 1.7 | 0.2 | 0.550610743 | 0.936038 | uses Falth et al 2015 MD for M5.6 |
| 11 | 5.6 | | 1.7 | 0.4 | 0.522710673 | 0.888608 | |
| 12 | 5.6 | | 1.7 | 0.6 | 0.49622433 | 0.843581 | |

.

# Appendix F

DISTRIBUTED FAULTING DISPLACEMENTS PREDICTED BY Nurminen et al. (2020) AT VARIOUS DISTANCES AWAY FROM THE PRINCIPAL REVERSE FAULT. Red cells indicate predicted vertical displacement > 5 cm (0.05 m)

**Case 5: Example reverse-fault earthquakes of M5.5 (MD=0.61 m), 6.2 (MD=1.18 m), and 7.5 (MD=4.1 m)**

NOTE: distributed fault vertical displacements (d) are computed in the same manner as explained in Appendix D.

**Falth and Hokmark 2010 give example of M5.5 EQ on PF, and DR displ at 200, 600, 1000, 1250, 1500 on FW**

| | | | | | | | | | | |
|---|---|---|---|---|---|---|---|---|---|---|
| **FW, Dmax= 0.61 m MOSS 2022** | | | | | | | | | OUTPUTS | Y=vd |
| INPUTS | for M5.5 on example fault | | | | | | | | ln(Y) | Y (m) |
| INPUTS | for M5.5 on example fault | | | | | | | | ln(Y) | Y (m) |
| a | b1 | s | ln(s) | c1 | Dn | ln(Dn) | d1 | m | | |
| -5.1043 | -0.6483 | 200.00 | 5.30 | 0.1983 | 0.61 | -0.49 | 0.9461 | 5.50 | -3.4337 | 0.0323 |
| -5.1043 | -0.6483 | 600.00 | 6.40 | 0.1983 | 0.61 | -0.49 | 0.9461 | 5.50 | -4.1459 | 0.0158 |
| -5.1043 | -0.6483 | 1000.00 | 6.91 | 0.1983 | 0.61 | -0.49 | 0.9461 | 5.50 | -4.4771 | 0.0114 |
| -5.1043 | -0.6483 | 1250.00 | 7.13 | 0.1983 | 0.61 | -0.49 | 0.9461 | 5.50 | -4.6217 | 0.0098 |
| -5.1043 | -0.6483 | 1500.00 | 7.31 | 0.1983 | 0.61 | -0.49 | 0.9461 | 5.50 | -4.7399 | 0.0087 |

**Falth and Hokmark 2010 give example of M6.2 EQ on PF, and DR displ at 200, 600, 1000, 1250, 1500 m on FW**

| | | | | | | | | | | |
|---|---|---|---|---|---|---|---|---|---|---|
| **FW, Dmax= 1.18 m MOSS 2022** | | | | | | | | | OUTPUTS | Y=vd |
| INPUTS | for M5.5 on example fault | | | | | | | | ln(Y) | Y (m) |
| a | b1 | s | ln(s) | c1 | Dn | ln(Dn) | d1 | m | | |
| -5.1043 | -0.6483 | 200.00 | 5.30 | 0.1983 | 1.18 | 0.17 | 0.9461 | 6.20 | -2.6406 | 0.0713 |
| -5.1043 | -0.6483 | 600.00 | 6.40 | 0.1983 | 1.18 | 0.17 | 0.9461 | 6.20 | -3.3528 | 0.0350 |
| -5.1043 | -0.6483 | 1000.00 | 6.91 | 0.1983 | 1.18 | 0.17 | 0.9461 | 6.20 | -3.6840 | 0.0251 |
| -5.1043 | -0.6483 | 1250.00 | 7.13 | 0.1983 | 1.18 | 0.17 | 0.9461 | 6.20 | -3.8286 | 0.0217 |

|  |  |  |  |  |  |  |  |  |  |  |
|---|---|---|---|---|---|---|---|---|---|---|
| -5.1043 | -0.6483 | 1500.00 | 7.31 | 0.1983 | 1.18 | 0.17 | 0.9461 | 6.20 | -3.9468 | 0.0193 |

**Falth and Hokmark 2010 give example of M7.5 EQ on PF, and DR displ at 200, 600, 1000, 1250, 1500 on FW**

**FW, Dmax= 4.1 m MOSS 2022**

| INPUTS | for M5.5 on example fault |  |  |  |  |  |  |  | OUTPUTS | Y=vd |
|---|---|---|---|---|---|---|---|---|---|---|
|  |  |  |  |  |  |  |  |  | ln(Y) | Y (m) |
| a | b1 | s | ln(s) | c1 | Dn | ln(Dn) | d1 | m |  |  |
| -5.1043 | -0.6483 | 200.00 | 5.30 | 0.1983 | 4.10 | 1.41 | 0.9461 | 7.50 | -1.1637 | 0.3123 |
| -5.1043 | -0.6483 | 600.00 | 6.40 | 0.1983 | 4.10 | 1.41 | 0.9461 | 7.50 | -1.8759 | 0.1532 |
| -5.1043 | -0.6483 | 1000.00 | 6.91 | 0.1983 | 4.10 | 1.41 | 0.9461 | 7.50 | -2.2070 | 0.1100 |
| -5.1043 | -0.6483 | 1250.00 | 7.13 | 0.1983 | 4.10 | 1.41 | 0.9461 | 7.50 | -2.3517 | 0.0952 |
| -5.1043 | -0.6483 | 1500.00 | 7.31 | 0.1983 | 4.10 | 1.41 | 0.9461 | 7.50 | -2.4699 | 0.0846 |

# Appendix G

DISTRIBUTED FAULTING DISPLACEMENTS PREDICTED BY MOSS ET AL (2020) AT VARIOUS DISTANCES AWAY FROM THE PRINCIPAL REVERSE FAULT. This exponential equation (blue font) is only recommended up to 6.5 km away from the PF, beyond which Moss says ”d” remains constant. Red cells indicate predicted vertical displacement > 5 cm (0.05 m)

**Case 5: Example reverse-fault earthquakes of M5.5 (MD=0.61 m), 6.2 (MD=1.18 m), and 7.5 (MD=4.1 m)**

NOTE: distributed fault vertical displacements (d) are computed in the same manner as explained in Appendix E.

| | | | | |
|---|---|---|---|---|
| Moss et al 2022 | Mag | 5.5 | 6.2 | 7.5 |
| Eq is for 95%-ile curve | MD (m) | 0.61 | 1.18 | 4.1 |

d/MD=0.58*exp(-0.26*r)

| | | | | MAG | 5.5 | MAG | 6.2 | MAG | 7.5 |
|---|---|---|---|---|---|---|---|---|---|
| r (km) | (-0.26)*r | exp(-0.26*r) | d/MD | MD | d | MD | d | MD | d |
| 0.2 | -0.052 | 0.949328867 | 0.550611 | 0.61 | 0.335873 | 1.18 | 0.649721 | 4.1 | 2.257504 |
| 0.4 | -0.104 | 0.901225297 | 0.522711 | 0.61 | 0.318854 | 1.18 | 0.616799 | 4.1 | 2.143114 |
| 0.6 | -0.156 | 0.85555919 | 0.496224 | 0.61 | 0.302697 | 1.18 | 0.585545 | 4.1 | 2.03452 |
| 1 | -0.26 | 0.771051586 | 0.44721 | 0.61 | 0.272798 | 1.18 | 0.527708 | 4.1 | 1.833561 |
| 1.5 | -0.39 | 0.677056874 | 0.392693 | 0.61 | 0.239543 | 1.18 | 0.463378 | 4.1 | 1.610041 |
| 2 | -0.52 | 0.594520548 | 0.344822 | 0.61 | 0.210341 | 1.18 | 0.40689 | 4.1 | 1.41377 |
| 3 | -0.78 | 0.458406011 | 0.265875 | 0.61 | 0.162184 | 1.18 | 0.313733 | 4.1 | 1.090089 |
| 4 | -1.04 | 0.353454682 | 0.205004 | 0.61 | 0.125052 | 1.18 | 0.241904 | 4.1 | 0.840515 |
| 5 | -1.3 | 0.272531793 | 0.158068 | 0.61 | 0.096422 | 1.18 | 0.186521 | 4.1 | 0.648081 |
| 6 | -1.56 | 0.210136071 | 0.121879 | 0.61 | 0.074346 | 1.18 | 0.143817 | 4.1 | 0.499704 |
| 7 | -1.82 | 0.162025751 | 0.093975 | 0.61 | 0.057325 | 1.18 | 0.11089 | 4.1 | 0.385297 |
| 8 | -2.08 | 0.124930212 | 0.07246 | 0.61 | 0.0442 | 1.18 | 0.085502 | 4.1 | 0.297084 |
| 9 | -2.34 | 0.096327638 | 0.05587 | 0.61 | 0.034081 | 1.18 | 0.065927 | 4.1 | 0.229067 |
| 0 | 0 | 1 | 0.58 | 0.61 | 0.3538 | 1.18 | 0.6844 | 4.1 | 2.378 |

| | | | | | | | | | |
|---|---|---|---|---|---|---|---|---|---|
| 12 | -3.12 | 0.044157168 | 0.025611 | 0.61 | 0.015623 | 1.18 | 0.030221 | 4.1 | 0.105006 |
| 14 | -3.64 | 0.026252344 | 0.015226 | 0.61 | 0.009288 | 1.18 | 0.017967 | 4.1 | 0.062428 |
| 16 | -4.16 | 0.015607558 | 0.009052 | 0.61 | 0.005522 | 1.18 | 0.010682 | 4.1 | 0.037115 |
| 18 | -4.68 | 0.009279014 | 0.005382 | 0.61 | 0.003283 | 1.18 | 0.006351 | 4.1 | 0.022065 |
| 20 | -5.2 | 0.005516564 | 0.0032 | 0.61 | 0.001952 | 1.18 | 0.003776 | 4.1 | 0.013118 |
| 25 | -6.5 | 0.001503439 | 0.000872 | 0.61 | 0.000532 | 1.18 | 0.001029 | 4.1 | 0.003575 |
| 30 | -7.8 | 0.000409735 | 0.000238 | 0.61 | 0.000145 | 1.18 | 0.00028 | 4.1 | 0.000974 |
| 35 | -9.1 | 0.000111666 | 6.48E-05 | 0.61 | 3.95E-05 | 1.18 | 7.64E-05 | 4.1 | 0.000266 |
| 40 | -10.4 | 3.04325E-05 | 1.77E-05 | 0.61 | 1.08E-05 | 1.18 | 2.08E-05 | 4.1 | 7.24E-05 |

The Swedish Radiation Safety Authority (SSM) works proactively and preventively with nuclear safety, radiation protection, nuclear security, and nuclear non-proliferation to protect people and the environment from the harmful effects of radiation, now and in the future.

**Strålsäkerhetsmyndigheten**
SE-171 16 Stockholm
+46 (0) 8-799 40 00
www.stralsakerhetsmyndigheten.se
registrator@ssm.se

E-print AB, 2024